Preparation and Characterization of Doped CdS and ZnS Nanostructures

A

Thesis

Submitted for the award of degree of

Doctor of Philosophy

By

Shivani Jindal

(Registration No. 901512008)

Under the supervision of

Dr. Puneet Sharma

Professor

School of Physics & Materials Science

Thapar Institute of Engineering & Technology, Patiala-147004

Punjab (INDIA)

August, 2021

DEDICATED

TO

MY

FAMILY

CERTIFICATE

This is to certify that the thesis entitled **"Preparation and Characterization of Doped CdS and ZnS Nanostructures"** which is being submitted by Shivani Jindal in the fulfilment of the requirement for the award of the degree Doctor of Philosophy in the School of Physics & Materials Science, Thapar Institute of Engineering & Technology (TIET), is an authentic record of candidate's own work carried out by her under my supervision and guidance. The matter presented in this thesis has not been submitted in part or full for the award of any degree in any other University or Institute.

Date: 28|10|2021

Place: Patiala

Dr. Puneet Sharma
(Professor)
School of Physics & Materials Science
Thapar Institute of Engineering & Technology
Patiala-147004

Acknowledgement

In my journey towards this degree firstly, I would like to express my deep and sincere gratitude to my supervisor **Dr. Puneet Sharma**, Professor, Thapar Institute of engineering & Technology (TIET) Patiala, Punjab for giving me opportunity to carry out the research work under his supervision. He has been there providing his heartfelt support, invaluable guidance, inspiration, constant encouragement and valuable suggestion throughout the journey without whom the work would not have been crowned with success. Without his able guidance, this thesis would not be possible and I shall be eternally grateful to him for his assistance.

I offer my special thanks to **Dr. O. P. Pandey**, Head, School of Physics & Materials Science, Thapar Institute of Engineering & Technology (TIET), Patiala, for providing all the necessary facilities in the department. I extend my gratitude to my doctoral committee members and all faculty members of the SPMS who supported and encouraged me especially, **Dr. Kulvir Singh, Dr. D.P. Singh and Dr. B.C Mohanty.**

I am thankful to my labmates **Dr. Chhavi Pahwa**, **Dr. Santhoshkumar Mahadevan**, **Anoop Pratap Singh, Parminder Singh, Sonal Singh and Anupriya** for their kind support in experimental activities during my research.

I am grateful to all teaching, non-teaching staff and research scholars of School of Physics and Materials Science who never turn me down whenever I approached for any help.

I would like to thank SAI Lab, Thapar Institute of Engineering & Technology for SEM and XRD facility.

I gratefully acknowledge Thapar Institute of Engineering & Technology (TIET) for providing me fellowship throughout my work.

I gratefully acknowledge DST-FIST for providing magnetic measurement and Atomic force microscope facilities.

I would like to convey my sincere gratitude to my friend **Dr. Chhavi Pahwa** for creating cheerful atmosphere during my stay. I express my deep gratitude to **Dr. Kamaldeep Kaur and Dr. Neetu Bansal** for the joyful company during my work.

Most of all, I would like to thank my husband **Mr. Hiteshwar Singh Pahwa** who provided me relentless encouragement, prayers that made this work to reach its destination. Further I like to extend my gratitude my mother in law **Mrs. Shaweta Pahwa** for her immense support, love and blessings during the course of writing this thesis. Last but not least, I am also greatly indebted to my parents (**Mr. Rakesh Jindal** and **Mrs. Rajni Jindal**) for their unconditional love, constant inspiration, moral support and blessings at every step of my life. Special thanks to my loving brother **Siddhant Jindal** who have always been a source of incessant support.

And above all, I pay my profound gratitude to The Almighty GOD for giving me strength, love and blessings.

Shivani

Shivani Jindal

List of Publications

1. **Shivani Jindal**, Puneet Sharma, "Magnetic and optical properties of transition metal (Fe, Co) and rare-earth (Tb, Dy) doped ZnS nanoparticles", Journal of Alloys and Compounds 879 (2021) 160383.

2. **Shivani Jindal**, Puneet Sharma, "Ferromagnetic transition metal-doped CdS nanoparticles: a comparative study", Journal of Materials Science: Materials in Electronics 31 (2020) 20295–20302.

3. **Shivani Jindal**, Puneet Sharma, "Optical and magnetic properties of Dy^{3+} doped CdS dilute magnetic semiconductor nanoparticles", Materials Science in Semiconductor Processing 108 (2020) 104884.

Others:

Shivani Jindal, Kamaldeep, N.K Verma & Puneet Sharma, "Effect of Tb^{3+} ion substitution on structural, optical and magnetic properties of CdS nanoparticles", Journal of Materials Science: Materials in Electronics, 29 (2018) 86-90.

List of conferences and workshop

1. **Shivani Jindal**, Puneet Sharma, "Structural, Optical and Magnetic Properties of Iron Doped CdS Nanoparticles" 1st National conference on Innovation in Applied Science and Engineering **(NCIASE-2019)** April 27-28, 2019.

2. **Shivani Jindal**, Puneet Sharma, "Enhanced Ferromagnetic and Optical Properties in Dy^{3+} Doped CdS Nanoparticles" International Conference on Magnetism and Magnetic Materials **(ICMAGMA- 2018)** December 09-13, 2018.

3. **Shivani Jindal**, Puneet Sharma, "Optical and Structural Properties of Dy^{3+} Doped CdS Nanoparticles", International Conference on Nanomaterials: Synthesis, Characterization and Applications **(ICN -2018)** May 11-13, 2018.

4. National Workshop on Advanced Techniques for surface characterization, Thapar University, Oct 28-30, 2015.

5. Workshop on Thin films and processing technology (ICTP) at National Physical Laboratory, Delhi (2017).

6. Workshop on Vacuum, Plasma & Thin Film Depostion/Processing Technologies and their Metrological Implication, TIET (2018).

List of Figures

List of Tables

List of Symbols

$\boldsymbol{M}$	Magnetization
$\boldsymbol{M_s}$	Saturation magnetization
$\boldsymbol{H_c}$	Coercivity
$\boldsymbol{M_r}$	Remanent magnetization
$\boldsymbol{T_c}$	Curie Temperature
Oe	Oerested
T	Tesla
$\boldsymbol{\mu_B}$	Bohr magneton
Ω	Ohm
K	Kelvin
$\boldsymbol{h}$	Planck's constant
$\boldsymbol{m_e^*}$	Effective mass of electron
$\boldsymbol{m_h^*}$	Effective mass of holes
$\boldsymbol{\varepsilon}$	Dielectric constant
e	Electronic charge
Å	Angstrom
$\boldsymbol{D}$	Crystallite size
$\boldsymbol{E_g}$	Bandgap

Abbreviations used

DMS	Dilute magnetic semiconductors
LED	Light emitting diodes
WZ	Wurtzite
ZB	Zinc blend
HCP	Hexagonal close packing
CCP	Cubic close packing
VB	Valence band
CB	Conduction band
TM	Transition metal
RE	Rare earth
RKKY	Ruderman–Kittel–Kasuya–Yosida
BMP	Bound magnetic polarons
M-H	Magnetic hysteresis loop
RT	Room temperature
CBD	Chemical bath deposition
PL	Photo luminescence
XRD	X-ray diffraction
FESEM	Field emission scanning electron microscopy
HR-TEM	High-resolution transmission electron microscopy
SAED	Selected area electron diffraction
VSM	Vibrating sample magnetometer
UV	Ultra violet
EDS	Energy dispersive microscopy
AFM	Atomic force microscope
EMA	Effective mass approximation

FC	Field cooled
ZFC	Zero field cooled
ml	Millilitre
nm	Nanometre
M	Mole
eV	Electron volt
keV	Kilo-electron volt
a.u.	arbitrary units

Preface

Owing to unique size dependent optical, electronic and magnetic properties, CdS and ZnS have gained considerable attention in various optoelectronic and spintronic applications. Also, their wide band gap in visible range makes them suitable for solar cell application. At nanoscale, these materials exhibit entirely different properties as compared to their bulk counterpart due to large surface to volume ratio and quantum-confinement effect. Further, the properties of these materials can be altered by tailoring the particle size and suitable cationic doping. Therefore, the main focus of this work is to understand the size effect and to systematically investigate transition metal (*TM*) (Fe^{3+}, Co^{2+}) and rare earth (*RE*) (Dy^{3+}, Tb^{3+}) doped CdS and ZnS nanostructures with an emphasis to their optical and magnetic properties. The carried out work is organized into five chapters and the content of each chapter is given below.

Chapter 1 (Introduction)

Chapter 1 briefly introduces the semiconductors and the dilute magnetic semiconductors (DMS). The different theories of origin of magnetism in DMS are summarized. The important applications of DMS have been paragraphed.

Chapter 2 (Literature review)

The important work carried out on DMS, particularly CdS and ZnS nanostructures (nanoparticles/thin films) are reviewed with a focus to their structural, optical and magnetic properties. The detail description of the effect of various dopants (*TM* and *RE*) and processing methods are discussed. The comparative study on optical and magnetic properties of CdS and ZnS nanoparticles/films by various researchers has been tabulated. The chapter is concluded with motivation and objectives of the present work.

Chapter 3 (Experimental procedure & characterization techniques)

The details of adopted processing method for synthesis of *TM* (Fe^{3+}, Co^{2+}) and *RE* (Tb^{3+}, Dy^{3+}) doped CdS and ZnS nanoparticles are provided. The deposition of CdS and ZnS thin film using chemical bath deposition method is also given. The various characterization techniques used to study structural, morphological, elemental, optical and magnetic properties are given.

Chapter 4 (Results and discussion)

This chapter reports the structural, optical and magnetic properties of undoped and doped (*TM* and *RE*) CdS and ZnS nanostructures. The results are divided into three sections, firstly the effect of annealing on undoped CdS and ZnS nanoparticles has been discussed. Secondly, the effect of *TM* and *RE* doping on CdS and ZnS nanoparticles is reported. Finally, the structural and optical properties of CdS and ZnS films at selected doping concentration are investigated and discussed.

Chapter 5 (Conclusions)

The important outcomes obtained from various experiments are mentioned. The effects of annealing temperature on CdS and ZnS nanoparticles are outlined. The results of *TM* (Fe^{3+}, Co^{2+}) and *RE* (Dy^{3+}, Tb^{3+}) doped CdS and ZnS nanoparticles are summarized. Finally, the studies on CdS and ZnS films at selected doping concentration are concluded. The comparative results obtained from the comprehensive studies are provided in tabular form. In the end, future scope of present work is given.

Contents

Chapter 1

Introduction

Overview

This chapter gives general introduction classification of semiconductor materials. A brief description of dilute magnetic semiconductors (DMS) and theories related to origin of magnetism are summarized. The important applications of DMS materials are paragraphed.

1.1 Introduction

Semiconductors have drawn significant attention with the discovery of transistors at Bell Laboratory in 1947 [1]. Afterwards, an enormous growth in semiconductor industry were seen as their potential use in solar cells, light-emitting diodes (LED), photo detectors, photocatalysis, biomedical and spintronic applications [2–7]. Later, the focus has been shifted to miniaturized semiconductor devices in order to improve functionality, increase integration and reduce energy consumption. With the continuous efforts, the size of semiconductor devices has been reduced from millimeter to micrometer range. The newer approach exploits electric charge and its spin degree of freedom for novel magneto-opto-electronic devices, which emerges out as a new area of spintronics. The spin manipulation facilitated faster devices with low energy consumption [8]. For the advancement of microelectronics, wide variety of semiconductors has been explored and their fundamental properties were investigated. On the basis of constituents, these are classified as elemental and compound semiconductors. The elemental semiconductors include group IV elements while III-V and II-VI belongs to compound semiconductors as shown in Table 1.1.

Table 1.1 Various types of semiconductor materials.

Group	Types
IV	Ge, Sn, Te, Si, Se etc.
III-V	GaN, GaAs, GaP, InP, InN, InAs etc
II-VI	ZnSe, ZnS, ZnO, ZnTe, CdSe, CdS, CdTe etc.

Among the various groups of semiconductors, Group IV elements *i.e.* Silicon and Germanium became the leading candidate in electronic components. The group III-V and II-VI compounds are widely used in gas sensors, laser/infra-red detector and solar cells. In the recent years, II–VI semiconductors have progressively attracted attention of researchers due to their relatively higher bandgap (E_g), large ionicity, high effective mass of carriers, small radiative carrier lifetime and short carrier diffusion in comparison to III–V compounds [9]. The wavelength of the emitted radiation depends on the E_g of the semiconductor. Largely, III–V semiconductors do not have sufficiently large E_g to fabricate light emitting diodes or laser diodes in the blue and green region. However, a few exception *i.e.* GaN (E_g = 3.7 eV) which can be used for blue LEDs [10,11].

In II-VI semiconductor category, zinc sulphide (ZnS) and cadmium sulphide (CdS) are of greater interest because of their wide E_g of 2.42 eV and 3.67 eV that can be exploited for window layer in solar cells. The CdS and ZnS exist in two types of crystal

structures; namely wurtzite (WZ) and zinc blend (ZB). The WZ crystallizes in hexagonal close packing (HCP) while, ZB has cubic close packing (CCP). In ZB structure sulphur atoms occupies the FCC positions and Zn/Cd atoms occupy half of tetrahedral interstitial positions of FCC unit cell as indicated in Fig. 1.1 (a). Basically, this structure consists of two interpenetrating FCC lattices, one for zinc and other for sulphur, with their origins displaced by one quarter of body diagonal. In WZ structure sulphur atoms occupy HCP positions and Zn/Cd atoms are present at half of tetrahedral interstitial positions of HCP unit cell as shown in Fig. 1.1 (b).

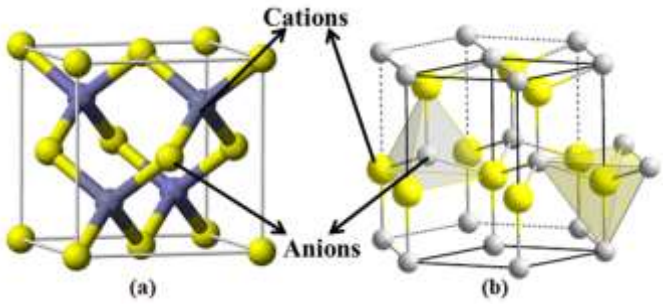

Fig. 1.1 Unit cell of CdS/ ZnS (a) zinc blend (CCP) and (b) wurtzite (HCP) [12].

Owing to unique size dependent optical, electronic and magnetic properties, group II-VI semiconductors exhibit entirely different properties at nanoscale as compared to their bulk counterpart. When the dimensions of semiconductor materials approach to Bohr-exciton radius, the excitons are confined *i.e.* motion in the crystal is restricted. Such confinement increases the separation between conduction (CB) and valence band (VB) that changes the energy spectrum of semiconductor. The widening of E_g with decreasing size is shown in Fig. 1.2.

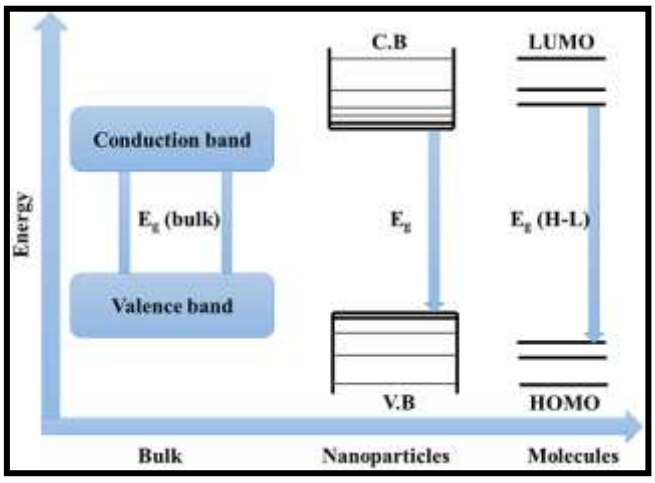

Fig. 1.2 Comparative energy level diagrams of semiconductors at bulk, nano and molecular level [13].

Doping of small concentration in III-V and II-VI semiconductors; which is responsible for dilute magnetism are classified as new class of semiconductors *i.e.* dilute magnetic semiconductors (DMS). A brief description of DMS materials is given below.

1.2 Dilute magnetic semiconductors

Dilute magnetic semiconductors (DMS) are lightly doped semiconductors wherein a small amount of host cations are substituted by rare earth (*RE*) and transition metals (*TM*) ions. The *TM* (Fe, Co, Ni, etc.) and *RE* (Eu, Gd, Er, etc.) have partially filled *d* and *f* states respectively, that facilitates spin-spin exchange interaction between delocalized CB electrons with localized magnetic moments of dopant which are responsible for magnetism in DMS material [14,15].

The origin of magnetism in DMS materials is interpreted by various researchers and different theoretical models were proposed. In early 1951, Zener proposed first theoretical interpretation on exchange interaction between carriers and localized magnetic ion spins in GaN and ZnO [16]. The result indicated that direct exchange interaction between magnetic ions is not ferromagnetic while indirect exchange mediated by carrier is ferromagnetic. Later, Dietl *et al.* modified this model and describes hole mediated ferromagnetism in doped *p*-type semiconductors (GaMnAs) [17]. In earlier attempts, few models were based on Ruderman–Kittel–Kasuya–Yosida (RKKY) type exchange interaction, exchange coupling between magnetic ions and CB electrons. The conduction electrons get magnetized by magnetic ion and polarization decays with distance from magnetic ion in oscillatory manner. The interaction is ferromagnetic at smaller distance and oscillates between positive and negative value. Due to this oscillation there is ferromagnetic or antiferromagnetic exchange coupling as shown in Fig. 1.3 [18–20]. When there is large number of conduction electrons in CB then this kind of interaction become prominent. Such kind of interactions is observable when two ferromagnetic thin films are separated by a non-magnetic conductor/insulator layer, where ferromagnetic to antiferromagnetic transition occurs with spacer layer thickness. Such interactions are well described as Giant magnetoresistance (GMR) and Tunnel magnetoresistance (TMR) in magnetic heterostructures. However, the application of RKKY theory is not realistic because of low carrier concentration in DMS [21].

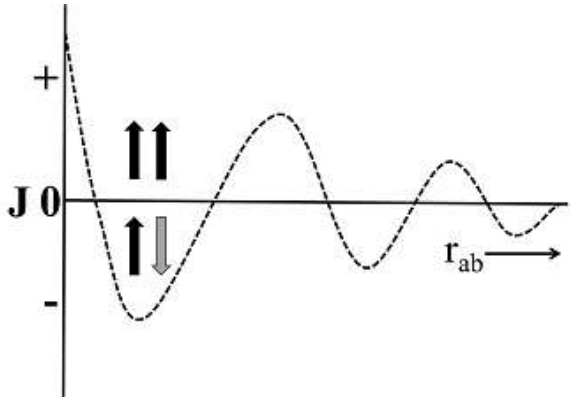

Fig. 1.3 RKKY exchange parameter (*J*) *vs.* distance between interacting magnetic ions (r_{ab}) [22].

Sato *et al.* proposed double exchange interaction for carrier mediated ferromagnetism in *TM* doped ZnO [23]. The interaction occurs with movement of free electrons from one magnetic ion to another because oxidation state of two nearest neighbor ions differs by one (Fig. 1.4) called as Zener exchange interaction [22].

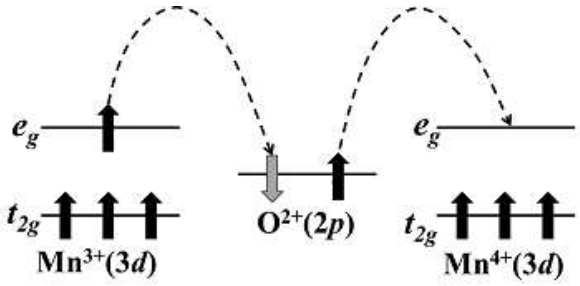

Fig. 1.4 Double exchange interaction in MnO system [22].

The presence of ferromagnetism in DMS has also been described via bound magnetic polarons (BMP) [24]. In this, polarons interact via virtual carrier hopping and interact with magnetic ions in interstitial sites. The direct anti-ferromagnetic interactions get dominated by indirect ferromagnetic interactions that cause the alignment of magnetic polarons. The BMP are formed due *sd-pd* exchange interactions between doped *TM* and bound carriers that contributes to ferromagnetism in DMS [25,26]. The idea of BMP is illustrated in Fig. 1.5. According to few theoretical interpretations the formation of clusters of doped atoms are found responsible for ferromagnetism in DMS. The crystal field splitting and Hund's rule filling of *d*-levels are models that depicts the existence of ferromagnetism [27–29]. It is also reported that presence of secondary phases and defects contributes to ferromagnetism.

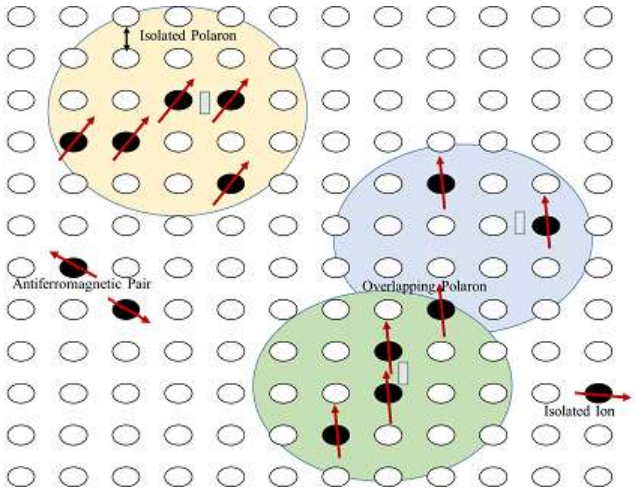

Fig. 1.5 Schematic representation of bound magnetic polaron [26].

Apart from changing the magnetic properties, the dopant has an added advantage of tuning electronic and optical properties. The dopants have ability to alter the position of Fermi energy level which results in tailoring the E_g and conduction type. The donor creates states near CB while acceptors create states near VB as shown in (Fig. 1.6).

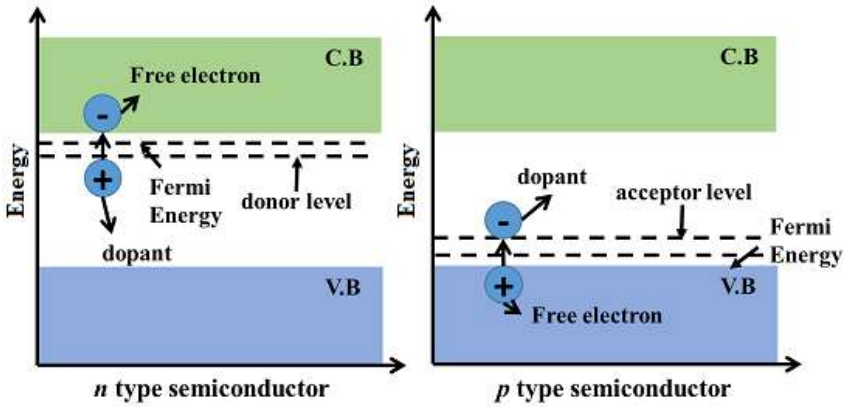

Fig. 1.6 Electronic band structure of doped semiconductor (*n*–type and *p*–type).

Also, luminescent properties such as emission intensities and wavelength of band to band edge transitions/defect site emissions found to depend on the type and concentration of dopants. The luminescence of these materials is based on the radiative recombination of delocalized CB electrons with localized hole that results in broad bandwidth, long exciton life time and large Stoke's shift.

1.3 Applications of DMS

DMS governs a new area of research known as spintronics in which both the

semiconducting and magnetic properties are combined in a single material. Spintronic materials leads to faster storage and transfer of information for quantum computation, magnetotronics, communication and electronics [5,30]. Further, these materials also found applications in magnetic field sensors, magnetic random access memory and magnetic recording disks [31,32]. Also, II-VI group semiconductors CdS and ZnS are potentially used in light emitting diodes, photoresistors, photodetectors, photocatalyst and gas sensors [3,33–35]. They are also used as window layer in solar cells because of their optical E_g (ZnS 3.67 eV and CdS 2.42 eV) is in visible range. The E_g of this range allows high energy incident photons on window-absorber junction that enhances the blue response and thus contribute to better cell performance [2].

1.4 Motivation

Among various II-VI group semiconductors, CdS and ZnS are suitable for various scientific and technological applications. The preparation and characterization of these materials in nano form is an exciting area of materials research because of their size tunable properties. A fraction of *TM* and *RE* doping in semiconductors leads to dilute magnetic semiconductors that offer spin based characteristics along with semiconducting properties that may increase the storage and processing capabilities of devices to make them more compact and multifunctional. Considering the interesting optical and magnetic properties of CdS and ZnS useful for wide variety of applications has given motivation to explore their properties further with novel *TM* and *RE* dopants. After the detailed literature review in Chapter 2, the objectives of the study are defined and listed.

Chapter 2

Literature review

Overview

In this chapter, the important work carried out on DMS, particularly CdS and ZnS nanostructures are reviewed for their structural, optical and magnetic properties. The detail description of the effect of various dopants (*TM* and *RE*) and processing methods are discussed. The emphasis is given to CdS and ZnS based doped nanoparticles and thin films. The comparative study on optical and magnetic properties of CdS and ZnS nanoparticles/films by various researchers has been tabulated. The chapter is concluded with motivation and objectives of the present work.

2.1 Preamble

The idea of Dilute magnetic semiconductors (DMS) was appealing due to coexistence of semiconducting and ferromagnetic properties in it. Over a decade (1970-1980), the research was mainly focused on group IV elements, III-V and II-VI compound semiconductors [15,36,37]. The importance of each group semiconductor has already been mentioned in introduction. In the present review the focus has been made on II-VI group semiconductors with an emphasis to CdS and ZnS nanostructures. These semiconductors are largely investigated for nanoparticles and nanocrystalline thin films. In general, nanoparticles are defined as particle between 1-100 nm in diameter. This term is also used for larger particle size upto 500 nm. Whereas, nanofilms are referred as thin layer of material from fraction of nm to several micrometer in thickness [38]. The reasonable E_g and high photoconductivity in the visible region makes them to use as buffer layer in solar cells and electroluminescence/photoluminescence (PL) device applications [39–41]. The extraordinary size dependent tunable properties and wide range of cationic doping *i.e.* transition (*TM*) and rare earth (*RE*) metal further allows to tailor their ferromagnetic and optical properties.

Subjected to their size and dopant dependent properties, the following section reviews the major work carried out on CdS and ZnS material. In general, nanopowders were mainly synthesized by sol-gel, solvo/hydrothermal method, chemical colloidal method, micro-emulsion and one-pot synthesis etc. [42–46]. Whereas, thin films were deposited by vacuum evaporation, spray pyrolysis, chemical bath deposition (CBD), sputtering and electro-deposition etc. [47–51]. The review has been categorized in CdS and ZnS nanostructures (nanoparticles and thin films) with *TM* and *RE* doping irrespective to their processing methodology.

2.2 CdS based nanostructures

The first report on bulk CdS dates back to 1926 when the valence electronic distribution and crystal structure was theoretically explained by M. L Huggins [52]. Thereafter, the crystal structure of CdS and phase transformation with respect to temperature and pressure was investigated by various researchers. It has been found that bulk CdS remain in wurtzite phase with band gap (E_g) of 2.42 eV and melting point of 1600 °C [53]. At high pressure, wurtzite phase found to transform to cubic rock salt structure [54]. After the fundamental studies on CdS crystal structure and phase transformation the attention was shifted to size and shape dependent properties. The various morphologies of CdS

nanostructures that has been investigated are nanowires, nanospheres, nano dendrites, nanorods, and sea urchin like shape [55–59]. It has been observed that shape also play a major role in deciding optical and magnetic properties [60–62].

However, the main focus of the work was to investigate the size and dopant dependent properties. Therefore, in the following section the important work on size dependent properties of undoped CdS nanostructures and effect of dopants are reviewed.

In literature various studies reported the size effect on structural, magnetic and optical properties. Banerjee *et al.* has tuned the particle size using capping agent. It has been observed that particle size decreased from 10 to 0.7 nm with increasing amount of capping agent. The transformation from hexagonal to cubic phase was obtained with corresponding increase in E_g from 2.59 to 3.85 eV [63]. Kotkata *et al.* studied the size induced optical properties and showed that the growth of nanocrystals depends upon aging period, capping agent and prior filtration of reacting agent [64]. Later, Sivasubramanian *et al.* observed zinc-blend to wurtzite phase transformation with annealing of CdS nanoparticles in temperature range of 473-773 K for 2h in Ar atmosphere. The emission intensities for particles annealed at 773 K found to be higher [65]. Zhang *et al.* has investigated effect of CTAB on CdS nanoparticle. The decreasing the amount of CTAB particle size found to increase from 4 to 8 nm. With increase in particle size, absorbance edge found to shift towards higher wavelength and emission intensities were quenched. Further, effect of refluxing time was also studied and emission intensities found to enhanced as consequence of crystal growth [66]. Singh *et al.* studied the size tunebility of CdS nanoparticles by controlling the amount of capping agent as well as annealing temperature. The high PL intensity and smallest particle size of 3 nm was achieved using 0.6ml of thioglycerol. The annealing temperature causes the growth in particle size and emission intensity found to get quenched with rise in temperature upto 350 °C [67]. Heiba *et al.* synthesized CdS nanoparticles by varying the nucleation temperature from 150 to 500 °C. The results showed the CdS nanoparticles exhibit hexagonal phase at 150 °C that transforms to cubic phase with rise in temperature. The E_g found to decrease from 2.77 to 2.56 eV. Also, PL intensities found to vary with temperature [68]. Apart from size dependent properties of CdS nanoparticles, size dependent properties of CdS thin films has also been studied by several researchers by varying the deposition time, bath temperature, annealing temperature and thickness of films. The change in optical properties of Co doped CdS thin films deposited via CBD technique by varying the deposition time was studied by M. Muthusamy *et al*. The

deposited films had hexagonal phase and E_g found to increase from 2.44 to 2.66 eV with rising deposition time from 10 to 30h. The PL spectra showed emission peaks in blue, red and green region [69]. S. Butt *et al.* investigated the effect of thickness (250 to 940 nm) on optical properties of In doped CdS films. With increasing thickness the transmittance of films reduces from 80 to 60 % and correspond decreases in E_g from 2.44 to 2.35 eV was observed [70]. The effect of bath temperature on thickness of CdS films was investigated by S. Rondiya *et al*. The result showed that on raising the bath temperature form 65 to 80 °C, thickness of films increases from 73.84 to 117.28 nm. This increasing thickness reduces the film transmittance from 80 to 70% and thus E_g reduces from 2.89 to 2.59 eV [71].

After the size dependent studies, the focus of researchers was shifted to doping of CdS nanoparticles. The first Fe doped single crystal of CdS compound ($Cd_{1-x}Fe_xCr_2S_4$) was prepared by Barraclough *et al*. and remarkable change in electrical resistivity and Curie temperature (T_c) suggests doping is an effective way to tune the properties of such compounds [72]. The effect of Fe (0-5%) on optical and electrical properties of CdS nanocrystals was carried out by B. Tripathi *et al.* The results showed hexagonal phase of nanocrystals and reduction in E_g from 3.54 eV to 3.27 eV with doping content. Also, electrical conductivity found to enhanced from 0.819×10^{-6} to $3.326\times10^{-6}\ \Omega^{-1}m^{-1}$ for 5% Fe [73–75]. Further, M. Thambidurai *et al.* investigated structural and optical properties of Fe, Co (0-7%) doped CdS nanoparticles of size 2.8-4.5 nm. The E_g found to decrease with doping of Fe and Co [76,77]. Later, they extended their work to Cr doped CdS nanoparticles with average size of 2.2-3.8 nm. The results depict reduction in E_g with Cr doping from 3.77-3.97 eV [78]. The spectroscopic studies on $Cd_{1-x}Fe_xS$ nanoparticles at higher doping concentration upto x = 0.20 was done by H. Sekhar *et al.* and observed higher emission peaks at lower doping (x = 0.05 and 0.10), whereas peaks get quenched for higher doping (x = 0.20) [79]. Recently, N. Jeevanantham *et al.* also reported reduction in E_g from 2.49 to 2.19 eV in Co doped CdS nanoparticles [80].

The *RT* ferromagnetism in Fe (2 and 3%) doped CdS nanocrystals was observed by G. Murali *et al.* However, at higher Fe (4 and 5%) content there is transition from ferromagnetic to paramagnetic state due to increased iron-iron super exchange interactions with doping. There results also showed the presence of both cubic and hexagonal phases in doped nanocrystals [81]. Further, they extended their work on Mn doped CdS nanowires and observed increase in ferromagnetism with doping of Mn. PL spectra showed quenched emissions with increasing Mn concentration without any Mn

related transitions [82]. On contrary A. Nag *et al.* showed Mn^{2+} related *d* emissions [83]. Their co-workers studied the optical and magnetic properties of doped $Cd_{1-x}Co_xS$ (x = 2 to 8%) having particle size of 3 nm. The results showed the red shift in absorption edge with increasing Co concentration and in PL spectra the green emission was observed for all samples due to transition of trapped electron from donor level to valence band (VB) edge. The magnetic studies confirmed ferromagnetism with increase in magnetic saturation (M_s) upto 4% of Co content. However, at higher doping content; M_s reduces due dominant antiferromagnetic coupling arises from decrease in Co-Co separation [84]. They also observed similar trend in Co-Mn co-doped and Cr doped CdS nanoparticles (0-7%) [85,86].

On contrary, R. Sathyamoorthy *et al.* observed *RT* ferromagnetism in all $Cd_{1-x}Co_xS$ (x = 0.10, 0.20 and 0.30) nanoclusters having hexagonal phase. The maximum M_s value of 0.076 emu/g was observed for x = 0.30 [87]. Also, L. Saravanan *et al*. reported ferromagnetism without any antiferromagnetic coupling at 6% of Co content [88]. Later, T. Lavanya *et al.* reported the transition from para to ferromagnetism with increasing Co concentration from 1-5% [89]. K. Kaur *et al.* synthesized Co doped (3-15%) CdS nanorods. The results showed hexagonal phase of nanorods and E_g (2.46 to 2.72 eV) lie in visible region between. The magnetic analysis reflect the ferromagnetism in undoped and doped samples [90]. A. Ghosh *et al.* has calculated the Curie-Weiss temperature for wurtzite and cubic phase of Fe doped CdS. The results showed that doped wurtzite CdS exhibits higher Curie-Weiss temperature (~320 K) as compared to cubic CdS (~384 K) nanoparticles [91]. Later, they extended their work to temperature dependent magnetic properties of $Cd_{1-x}Fe_xS$ (x ~ 0.0017-0.033) nanoparticles. The results showed that in temperature range of 160-300 K, inverse magnetic susceptibility follows linear Curie-Weiss equation with transition from anti-ferromagnetic to ferromagnetic behavior with increasing Fe doping [92].

S. Muruganandam *et al.* prepared 1, 5 and 10% Co doped CdS nanoparticles of size 6-14 nm. The blue shift in optical absorption was attributed to quantum confinement effect [93]. N. H. Patel *et al.* observed paramagnetism in Ni (10, 15, 20%) as well as in Co doped CdS nanoparticles at similar doping concentration [94,95]. Recently, M. B. Leena *et al.* observed weak ferromagnetism in Fe and Co doped CdS nanoparticles having cubic phase. The E_g found to decrease from 2.70 eV to 2.43 eV and 2.47 eV with Co and Fe doping, respectively [96]. On contrary, F. Ibraheem *et al*. reported paramagnetism in Co doped (2-10%) CdS. Also, E_g found to increase from 2.50 eV to 2.76 eV with doping

[97].

S. Khajuria *et al.* studied the Co^{2+} and Co^{2+}–Gd^{3+}, Co^{2+}–Er^{3+}, Co^{2+}–Tb^{3+} co-doped CdS nanoparticles having particle size in the range of 40-50 nm. The fluorescence intensities of co-doped samples were found to be higher [98]. In the same year, P. Elavarthi *et al*. observed the transition from cubic phase for undoped to mixed phase (cubic and hexagonal) for Cr doped CdS nanoparticles. The magnetic analysis showed ferromagnetism in doped nanoparticles whereas undoped CdS was diamagnetic. Also, M_s was found to increase upto 3% Cr doping which further diminishes with increasing concentration [86]. Z. Zhang *et al*. also, reported the similar trend in magnetic properties of Cr doped (3-7%) CdS nanoparticles [99]. B. S. Rao *et al.* investigated optical properties of Ni (2-10%) doped CdS nanoparticles. The result showed decrease in E_g from 3.54 eV to 3.14 eV [100]. The similar reduction in E_g with Ni doping was confirmed by A. Firdous *et al.* [101]. On contrary, I. F. Ertis *et al.* observed nearly constant E_g from 2.25 to 2.26 eV with Ni doping [102].

Apart from experimental studies extensive theoretical and numerical calculation on optical and magnetic properties of *TM* doped CdS nanoparticles have also been carried out by various researchers. Pan *et al.* uses first principal calculation and reported that carrier mediated (hole) double-exchange interactions exhibit ferromagnetism in carbon doped CdS nanoparticles [103]. Bogle *et al.* have combined both experimental and theoretical studies on Co doped CdS nanoparticles. The weak magnetism was observed that found to decrease with Co content. The first principal calculations were carried out in order to study this magnetic behavior and confirmed that the formation of defects with Co doping effects its magnetic properties [104]. Hu *et al.* uses first-principle calculations and theoretically confirms the presence of ferromagnetism in Co doped CdS nanocrystals attributed to Cd vacancies [105]. Y. Han *et al.* gave the theoretical analysis on optical properties of Co doped CdS and investigated the effect of doping concentration on absorption coefficient, optical conductivity, dielectric function, reflective index, transmittance and reflectivity. The results showed reduction in E_g and found that 7.26% Co concentration is best suited for light operated switch, photovoltaic cells and fiber optic communication [106]. Later, R. Iqbal *et al.* performed density functional calculations to study the structural, optical, magnetic and electronic properties of Co doped CdS. The results showed significant decrease in E_g from 2.56 to 1.6 eV [107]. W. Benstaali *et al.* carried out the theoretical analysis of Ni doped CdS and showed that 6.25% Ni doped CdS is an intrinsic semiconductor, whereas 12.5% of Ni is half-metallic and

ferromagnetic material [108]. Li *et al.* investigated the magnetic behavior of Cu doped CdS and showed that doped CdS have magnetic moment of 1.0 μ_B per super cell. The observed ferromagnetism was attributed to coupling chain and estimated T_c of Cu doped CdS was 400 K. [109].

Along with the *TM* based CdS nanostructures, a parallel investigations on *RE* doped CdS were also reported, though the studies are limited. C. Tiseanu *et al.* carried out time resolved PL properties of Tb doped CdS and ZnS nanocrystals. The results showed that in comparison to CdS nanocrystals; ZnS nanocrystals exhibit strong luminescence [110]. In later years, P. V. Jyothy *et al.* and S. Rai *et al.* reported enhancement in luminescent properties with doping of Tb in CdS nanoparticles [111,112]. They also observed enhanced blue emission of Dy doped CdS nanoparticles embedded in silica xerogel annealed upto 100 °C [113]. Y. Hanifehpour *et al.* synthesize Tb doped CdS nanoparticles via sonochemical method and studied their sonocatalytic performance. The results indicated that doped samples showed higher de-colorization efficiency than undoped [114].

L. Saravanan *et al*. reported hexagonal and cubic phase in Ce and Sm doped nanoparticles, respectively [115,116]. Later, they investigated the effect of Sm^{3+} and Nd^{3+} on structural and optical properties of CdS nanocrystals having cubic phase. The results showed decrease in E_g as compared to undoped one. Also, emission intensities get enhanced with doping [117].

M. Thambidurai *et al.* synthesized Gd doped CdS nanoparticles with hexagonal phase. The E_g found to decrease from 3.93 to 3.76 eV with Gd doping (1.82-5.83%) [118]. Recently, A. Khan *et al.* observed increase in electrical conductivity with frequency in Gd doped (1-5%) CdS nanoparticles. The E_g found to be varied with doping in the range of 2.31 to 2.41 eV and emission intensity get quenched with Gd doping [119]. R. Zhao *et al.* observed ferromagnetism in Eu doped (0.08, 0.19 and 0.26%) CdS nanoparticles attributed to dopant atoms and Cd vacancies. The M_s found to increase with Eu doping from 0.017 emu/g to 0.032 emu/g that further reduces to 0.008 emu/g at higher Eu (0.26%) content. Also, for higher doping amount temperature dependent magnetic properties has been carried out. It was observed that M_s increases to 0.029 emu/g with decreasing temperature upto 10 K [120].

The decrease in E_g from 2.30 to 2.24 eV with Gd doping was reported by B. Poornaprakash *et al*. Also, transition from diamagnetic to superparamagnetic state was

observed in undoped with Gd doping [121]. They also obtained room temperature (*RT*) ferromagnetism and enhanced E_g from 3.1 to 3.3 eV for Eu doped CdS quantum dots. The doped quantum dots showed enhanced photocatalytic activity as compared to undoped CdS [122]. Recently in 2021, the similar transition from diamagnetic to ferromagnetic state was reported for Er doped CdS nanoparticles [123]. The theoretical studies on *RE* doped CdS are rare. One of the studies was carried out on Pd doped CdS using first principles calculation. The result verifies that sample becomes spin polarized and act as a DMS material. A formation of hybridized chain was found to be responsible for the long-range ferromagnetic coupling [124].

The effect of *TM* and *RE* doping was also investigated on CdS thin films deposited by various methods. Apart from doped nanoparticles, doped CdS thin films systems were also extensively investigated. The Cu doped CdS thin films have been prepared by pulsed laser deposition and annealed at 300 °C. It was observed Cu doping enhances optical transmission [125]. A. Jafari *et al.* showed transmittance of CdS films improves at low doping concentration of Sn that make them suitable for use as buffer layer in solar cells [126]. Chandramohan *et al.* fabricated Co doped CdS thin films and showed that presence of Co ions marginally reduces the E_g [127]. M. E. Hagary *et al.* investigated magnetic properties of $Cd_{1-x}Fe_xS$ ($0.05 \leq x \leq 0.2$) films. The presence of *RT* ferromagnetism was confirmed from magnetic domains using magnetic force microscopy. The existence of RKKY exchange interactions between localized spin of Fe^{3+} ions and conductive electrons was responsible for observed ferromagnetism [128]. R. Premarani *et al*. reported *RT* ferromagnetism in Ni doped CdS films with maximum M_s of 51.34×10^{-6} emu/g for 10% Ni. The E_g values reduced from 2.62 to 2.28 eV by increasing Ni content [129]. In other study of Ni doped CdS films red shift in absorption edge was observed [130]. The same group has also studied optical properties of Co doped CdS nanofilms and revealed that the presence of Co ions causes reduction in E_g from 2.88 eV to 2.43 eV. The urbach energy and structure disordered parameter found to increase with doping. The narrowing of E_g was due to *sp-d* exchange interaction between free CB electrons of CdS and *d* electrons of Co ions [131]. Further they extended their work to study the magnetic properties of Co doped CdS films. The magnetic analysis confirmed the ferromagnetism in doped CdS while undoped CdS showed diamagnetism. This transition in magnetic behavior was attributed to phase separation, induced lattice defects, and *sp–d* exchange interactions [132]. S. Saravanakumar *et al.* also confirms the ferromagnetic behavior in

Co doped CdS with corresponding reduction in E_g from 2.40 to 2.27 eV with increasing doping concentration [133]. On contrary, M. Tomakin *et al.* have found increase in E_g from 2.36 eV to 2.39 eV Co doping in CdS films. The results also showed *RT* ferromagnetism [134].

H. Khallaf *et al*. have deposited Ga doped CdS thin films and a minimum E_g of 2.32 eV has been observed at maximum concentration of Ga. The annealing of Ga doped CdS films showed a phase transition and increase in lattice defect as evident from Micro-Raman spectroscopy [135]. K. Zou *et al.* deposited Dy doped CdS films via CBD method and observed the transition from cubic to mixed (hexagonal and cubic) phase. The uniformity, transmittance and compactness of films were improved with doping [136]. Later, S. Yilmaz *et al.* reported Dy doping has no significant effect on E_g of CdS thin films [137].

2.3 ZnS based nanostructures

Zinc sulphide (ZnS) with n-type conductivity and wide E_g of ~ 3.67 eV is also widely investigated by researchers for optoelectronic device applications. The first report on luminescence properties in bulk ZnS was given by T. Sidot in 1866 and observed that it exhibit phosphorescence [138]. During the period of 1940 to 1970 the main focus of research was on luminescence properties of bulk ZnS. However, the report on ZnS nanocrystals was firstly given in 1994 by R. Bhargava *et al.*, where luminescence and lifetime shortening of Mn doped ZnS nanoparticles were investigated [139]. Since then, there has been lot of studies on doped ZnS nanostructures. To induce optimal magnetization along with suitable E_g could be of prime importance for various applications based on magnetic and optical properties. The major approach to tune optical E_g and magnetization is by particle size variation/film thickness and suitable doping.

The previous investigation on ZnS nanoparticles revealed size induced modification in structural and optical properties. The role of particle size variation on optical properties of ZnS nanoparticles was reported by Borah *et al*. The result showed that with increasing particle size from 4.9 to 6.6 nm, the E_g decreases from 4.2 to 3.6 eV [140]. Rathore *et al.* also synthesize the ZnS nanoparticles of size 2.2 to 3.2 nm and observed decrease in E_g from 4.10 to 3.8 eV [141]. There are many reports in the literature dealing with particle size variation by changing annealing temperature. Murali *et al.* induce the particle size from 2.66 to 34.6 nm by varying the annealing temperature. Also transformation from cubic to hexagonal phase was found and also absorption edge

shifts towards higher wavelength with annealing temperature. The E_g found to vary with increasing temperature [142]. Several studies have reported the transformation from cubic to hexagonal phase with varying the particles size by increasing the annealing temperature [143,144]. Recently, Prasad *et al.* investigated the cubic and hexagonal ZnS nanoparticles. The E_g of hexagonal ZnS was found higher than cubic ZnS by 0.12 eV. Also, the emission behavior of both the phases was not identical due to change in crystallite size, structure and orientation [145]. The effect of processing parameters on growth and quality of films was investigated by Q. Li. The transmittance of deposited film was around 90% with E_g of 3.15 eV [146].

Over the past years, other than size induced structural and optical properties, considerable efforts have been made to evolve ZnS with *TM* and *RE* doping which has been summarized below:

In early years, the role of Fe, Ni and Mn on structural, optical and magnetic properties of ZnS were investigated. It was found that the doping of Ni and Fe in ZnS nanoparticles quenches the emission intensities in PL spectra [147]. The magnetism in Mn and Eu doped ZnS nanocrystals was reported by N. Tsujii *et al.* [148]. Later, H. Yuan *et al*. observed the paramagnetic behavior in Mn doped ZnS nanowires [149]. The phase change from hexagonal to cubic with Mn doping (0-20%) was observed by S. Biswas *et al.* Also the presence of magnetic dipole interaction in higher Mn concentration doped ZnS was confirmed by electron paramagnetic resonance [150]. C.S. Pathak *et al*. carried out optical analysis of Ni and Co doped ZnS nanoparticles. The E_g found to decrease with doping from 4.93 to 3.93 eV (Ni) and 4.30 to 4.03 eV (Co) [151,152]. In the same year, S. Kumar *et al*. studied the magnetic properties of Ni doped (1-5%) ZnS. The results depicted that nanoparticle with lower Ni content exhibit saturated *M-H* loop indicating ferromagnetism. Whereas, samples having higher Ni content, *M-H* loops are non-saturating due to appearance of antiferromagnetic coupling arising from decreased Ni-Ni distance with doping [153]. The optical properties *TM* (Mn, Co, Ni, Cu, Ag and Cd) doped ZnS nanoparticles were investigated by V. Ramasamy *et al.* The absorption spectra of all samples found to be blue shifted as compared to bulk ZnS. A significant enhancement in emission intensity of Mn and Ni doped ZnS nanoparticles was observed [154]. R. Sarkar *et al.* observed increase in emission intensities by ~35 times in Co doped ZnS [155]. Thereafter, the optical properties of Cu and Fe doped ZnS nanoparticles was studied by T. M. Hammad *et al.* The blue shift in absorption wavelength was observed and PL intensity found to get quenched with increasing doping content of Fe and Cu

[156].

The magnetic properties of Fe doped (1-5%) ZnS nanoparticles was investigated by Bhattacharya *et al*. The results showed decrease in magnetization due to anti ferromagnetic coupling between Fe^{3+} and Fe^{2+} ions as observed by magnetization *vs* temperature curve [157]. Thereafter, S. Sambasivam *et al.* and Eryong *et al*. prepared 3-7 nm size nanoparticles and observed superparamagnetism upto 20% Fe that changes to ferromagnetic state at higher concentration. The maximum M_s of 0.70 emu/g was observed for 60% of Fe concentration. The optical studies showed blue shift in absorption edge [158–160]. Further, Sambasivam *et al*. also investigated the magnetic properties of Co doped ZnS and observed *RT* ferromagnetism in all samples. The M_s found to decreases with increasing Co content from 10 to 30% attributed to anti ferromagnetic coupling in doped nanoparticles. Also, blue shift in absorption edge was reported [161]. On contrary, K. Patel reported paramagnetism in 15% Co doped ZnS nanoparticles [162].

B. Poornaprakash *et al.* reported paramagnetism in Fe doped (1, 3and 5%) ZnS nanoparticles due to decrease in Fe-Fe distance with increasing Fe concentration that results in antiferromangnetic interaction between Fe-Fe ions [163]. The similar paramagnetic behavior was reported by Y. Li *et al*. and D. Saikia *et al* [164–166]. Later, B. Poornaprakash *et al.*, also studied the effect of Fe, Co, and Ni doping on ZnS nanoparticles. The results showed cubic phase of all samples and estimated E_g values were around 3.70, to 3.98 eV with doping. The magnetic analysis indicated diamagnetic nature of undoped and paramagnetic behavior of Fe doped ZnS. Whereas, Co and Ni showed ferromagnetic behavior at similar concentration [167]. They also investigated concentration dependent optical and magnetic properties of Co doped (1-5%) ZnS nanoparticles (~10 nm). The *RT* ferromagnetism was observed in all samples with an increase in M_s with Co content. Also, emission intensity found to enhance with doping with slight increase in E_g [168]. The group further extended their work to Ni doped (1-5%) ZnS nanoparticles. The results showed all doped samples exhibit ferromagnetism and maximum magnetization was obtained for 3% Ni doping. Also, decrease in E_g was observed with increasing Ni content [169]. In Co, Sm and Co-Sm co-doped ZnS nanoparticles they observed that Sm-Co co-doped sample showed enhanced ferromagnetism as compared to individually doped [170].

S. Kumar *et al.* reported transformation from ferromagnetic to paramagnetic state in ZnS with Co doping content. The results also showed decrease in E_g from 4.59 to 4.80 eV with doping [171]. The similar reduction in E_g from 3.32 to 2.65 eV with Co doping

upto 22.49% was reported by R. Wang *et al.* [172]. Further, the same group extended their work on Co doped ZnS nanorods and reported ferromagnetism in all samples [173]. The *RT* ferromagnetism in Ni and Co co-doped nanorods and Ni doped nanoparticles was confirmed by W. Zhao *et al*. [174]. They also observed increase in M_s with increasing Ni content upto 3% that further diminishes at 5 and 7% Ni, whereas, decrease in magnetization was reported for Cr doped ZnS nanoparticles synthesized via hydrothermal method [175,176].

P. C. Patel *et al.* carried out the concentration dependent magnetic properties of Fe doped (2-15%) nanoparticles. The results showed the hexagonal phase of nanoparticles with average particle size of 4-10 nm. The *RT* ferromagnetism was observed in all samples with highest value of magnetization for 8% Fe, that further decrease with increasing doping concentration due to enhanced antiferromagnetic interaction between Fe-Fe ions [177]. They also studied the optical and magnetic properties of Co doped ZnS (0-10%) nanoparticles. The reduction in magnetization was observed at higher concentration attributed to antiferromagnetic coupling and E_g also found to decrease with doping from 3.45 to 2.80 eV due to *s-d* and *p-d* interactions [178]. Later, they also investigated temperature dependent (300 K and 5 K) ferromagnetic behavior of Ni doped ZnS nanoparticles. At 5 K well saturated *M-H* loop was observed and M_s found to increase with Ni doping concentration at both temperature. The ZFC-FC curves showed strongly coupled nanoparticles by magnetic interactions. Optical studies showed decrease in E_g because of the presence of surface defects and sulphur/zinc vacancies [179].

Recently, S. Kumar *et al.* observed cubic phase in Co doped ZnS with weak signature of hexagonal phase. The magnetic measurements confirmed *RT* ferromagnetism in all samples. The ZFC and FC curves suggested that ferromagnetic character is due to formation of various defects/vacancies with doping. Also, the blue shift was observed in absorption spectra [180]. On contrary, V. V. Jadhavar *et al.* reported paramagnetic behavior in pristine and Co doped ZnS nanoparticles. Also, the E_g found to decrease from 3.33 to 2.71 eV with increasing Co content [181].

The theoretical studies were also carried out in doped ZnS. To investigate the magnetic behavior, Y. Li *et al*. performed DFT studies on Cr doped ZnS nanowires. The results confirmed the presence of ferromagnetism attributed to double exchange interaction arising from hybridization between 3*d* (Cr) and 3*p* (S) states [182]. The similar role of hybridization in the development of induced magnetic moments was studied by H. Chen *et al.* by using first-principal calculations on *TM* doped ZnS

nanowires. They reported antiferromagnetic interaction in Cr doped and ferromagnetic interaction in Mn, Co, Fe and Ni doped samples [183]. G. Gurung *et al.* carried out theoretical analysis of *TM* doped ZnS and results showed that doping of Ni enhances optical absorption in comparison to Mn and Co doped samples [184].

Apart from *TM* doping, *RE* doped ZnS has also been explored by various research groups. A. Bol *et al.* used two different techniques to synthesize Eu and Tb doped ZnS nanoparticles. The luminescence measurements showed that *RE* ions were not incorporated in the host nanoparticles even upto 800 °C [185]. Later, X. Tian *et al*. studied the Dy (1-3%) doped ZnS nanoparticles and reported that E_g of nanoparticles varies with doping in the range from 3.27 to 3.41 eV. They also observed that PL emissions were related to zinc vacancies and Dy due to $^4F_{9/2}$-$^6H_{15/2}$ transition [186]. The optical analysis of *RE* doped ZnS has been carried out by several other researchers [187–189].The extensive studies on effect of *RE* (Dy, Eu, Gd, Nd and Tb) doping on magnetic and optical properties of ZnS nanostructures have been carried out by B. Pooranprakash *et al*. They gave first *RT* magnetic report on Dy (2 and 4%) and Eu (1-4%) doped ZnS nanoparticles synthesized via refluxing and hydrothermal technique, respectively. The results revealed cubic phase of nanoparticles with average particles size of 2-4 nm for Dy and 4-8 nm for Eu doped samples. The ferromagnetism was observed in all doped nanoparticles and magnetization increases with increasing doping content. The observed ferromagnetism was due to contribution of magnetic moment from unpaired 4*f* electrons of *RE* ions. In Dy doped samples, E_g found to decrease from 3.85 to 3.70 eV [190,191]. They also observed *RT* ferromagnetism in Gd (3-5%) doped ZnS nanoparticles prepared by hydrothermal process. The magnetization found to increase upto 3% of Gd content with value of 0.063 emu/g that further reduces to 0.049 emu/g for 5% Gd due to antiferromagnetic coupling between Gd-Gd ions [192]. Whereas, P. Kaur *et al.* observed increase in magnetization with doping of Gd from 2% to 4% [193]. In the same year, B. Pooranprakash *et al.* also studied Nd doping (2 and 4%) effect on ZnS nanoparticles. All Nd doped samples exhibited ferromagnetism [194]. The optical properties ZnS quantum dots doped with Tb was also studied and observed that PL emissions exhibit $^5D_4 \rightarrow {}^7F_6$, $^5D_4 \rightarrow {}^7F_3$, $^5D_4 \rightarrow {}^7F_4$ and $^5D_4 \rightarrow {}^7F_5$ electron transition of Tb^{3+} ions [195]. The transformation from ferromagnetism to superparamagnetism with increasing Tb concentration (1, 3 and 5%) was also reported [196]. On contrary, Ramu *et al.* reported paramagnetism in Tb doped ZnS synthesized via co-precipitation method [197].

According to some recent reports, M. Salim *et al.* has obtained remarkable enhancement on the luminescence intensity with 6% Tb doped ZnS quantum dots and also reported three distinctive light emission *i.e.* green, blue and red [198]. Recently, *RT* ferromagnetism in Mn, Dy and Mn-Dy co doped ZnS nanoparticles was shown by S. Rajesh *et al.* and highest value of magnetization was found for Dy doped sample [199].

The ZnS thin films systems were also extensively investigated and reported. Initially ZnS thin films were studied by various researches for use as window layer to increase the efficiency of solar cells [200,201]. Qi Liu and Guobing carried out the comparative study of CdS and ZnS thin films deposited by CBD having E_g of 2.41 eV for CdS and 3.51 eV for ZnS [202]. The role of substrate temperature (T_s) on magnetic properties of Co doped ZnS films was firstly given by S.P Patel *et al.* The result revealed ferromagnetism in all samples and magnetization enhances with increasing T_s [203]. Further, they studied effect of heavy ions on magnetic properties of these films and observed that samples irradiated at fluence of 1×10^2 ion/cm^2 showed paramagnetic behavior [204]. M. S. Akhtar *et al.* carried out both experimental and theoretical investigation on Fe-doped ZnS (0-15%) thin films prepared by a CBD method. The results showed cubic phase of deposited films and the presence of *RT* ferromagnetism. Also, theoretical investigations found to be consistent with experimental data with addition to observed half-metallicity in Fe doped ZnS clusters [205]. In the same year, A. Goktas *et al.* deposited Fe doped ZnS thin films by varying doping concentration from 1-20% and observed paramagnetic behavior at low doping concentration which transforms to ferromagnetism at higher Fe content. The E_g found in range of 3.59-2.08 eV [206]. They also investigated the effect of Co doping (0-5%) and film thickness on optical and magnetic properties. Compared to undoped ZnS; the reduced E_g was obtained for doped ZnS while refractive index, dielectric constants and excitation coefficient were enhanced with Co doping as well as film thickness. In temperature dependence magnetic properties, the ferromagnetism was observed at 5 K and 100 K while samples exhibit paramagnetic behavior at 200 K and 300 K [207]. The optical properties of 398-412 nm thick Ni doped ZnS thin films was investigated by R. Sahraei *et al.* and results showed that the E_g varies between 3.65 to 3.76 eV [208]. K. S. Wanjala *et al*. reported the concentration dependent optical and electrical properties of Sn doped ZnS film and obtained maximum transmittance of 78% in doped films with E_g in the range of 3.91eV to 4.12 eV [209]. The increased E_g from 3.70 to 3.75 eV with Cu doping was reported by A. Jrad *et al.*[210].

Recently, I. L. Quintas *et al.* deposited 10% Co doped thin films of thickness 43-66 nm via Pulsed laser deposition technique. The emission peaks were observed in green and red region attributed to native defects and impurities [211].

Comparison of CdS and ZnS nanoparticles and thin films:

From literature, it is found *TM* and *RE* doping is widely investigated for structural, optical and magnetic properties. However, there are ambiguities associated to different processing methods, conditions and dopant concentration adopted by researchers. The Table 2.1 summarizes the reported optical and magnetic properties of *TM* and *RE* doped ZnS/CdS nanostructures.

Table 2.1 Summarized reported properties of ZnS and CdS nanostructures.

Authors	Dopant	Synthesis Technique	Phase	Doping (%)	Crystallite size (*D*)/Thickness (d)	Magnetization	E_g (eV)/ Absorbance (nm)
K. Patel *et al.* [162]	ZnS:Co	Microwave irradiation	Cubic	0	6.73 nm	Paramagnetic	4.79
				5	4.99 nm		5.00
				15	4.20 nm		5.42
S. Kumar *et al.* [171]	ZnS:Co	Solvo-thermal	Cubic	0	~ 9.38 nm	Diamagnetic	270 nm
				1		Ferromagnetic	267 nm
				5		Paramagnetic	262 nm
S. Sambasivama *et al.* [161]	ZnS:Co	Co-precipitation	Cubic	0	13-16 nm	Diamagnetic	3.78
				10		0.7 emu/g	3.81
				20		0.5 emu/g	3.85
				30		0.4 emu/g	3.93
P.C. Patel *et al.* [178]	ZnS:Co	Co-precipitation	Cubic	1 to 10	3-5 nm	Ferromagnetic	2.8 to 3.5
G. Giribabu *et al.* [84]	CdS:Co	Co-precipitation	Cubic	0	2-3 nm	Diamagnetic	N.P
				4		$87.69x10^{-4}$	
				6		$27.4x10^{-4}$	
				8		Diamagnetic	
F. Ibraheem *et al.* [97]	CdS:Co	Co-precipitation	Cubic	0	5-10 nm	Diamagnetic	2.50
				2		Paramagnetic	2.61
				5			2.68
				10			2.76
N.H Patel *et al.* [95]	CdS:Co	Co-precipitation		0	N.P	Diamagnetic	3.23
				10		Paramagnetic	3.21
				15			3.19
G. Murali *et al.* [81]	CdS: Fe	Co-precipitation	Cubic and hexagonal	0	1.2-2 nm	Diamagnetic	N.P
				3		Ferromagnetic	
				5		Paramagnetic	
M. Leena *et al.* [96]	CdS:Fe, Co	Co-precipitation	Cubic	0	N.P	Diamagnetic	2.7
				Fe		Ferromagnetic	2.47
				Co			2.43
Y. Li *et al.* [164]	ZnS:Fe	Micro-emulsion	Cubic	0	4-7 nm	Paramagnetic	335nm
				1		Ferromagnetic	279 nm
				30	Amorphous	Paramagnetic	

S. Kumar *et al.* [212]	ZnS:Fe	Solvo-thermal	Hexagonal	0	~ 10.38 nm	Diamagnetic	3.86
				1		Ferromagnetic	3.91
				5		Paramagnetic	3.94
S. Sambasivam *et al.* [158]	ZnS:Fe	Co-precipitation	Cubic	0	6.70-7.40 nm	Diamagnetic	3.7
				10		Superparamagnetism	3.8
				40		0.70 emu/g	4.1
N. Eryong *et al.* [213]	ZnS:Fe	Co-precipitation	Cubic	0	3-5 nm	Diamagnetic	N.P
				10		Superparamagnetism	
D. Saikia *et al*. [166]	ZnS:Fe^{3+}	Co-precipitation	Cubic	0		Diamagnetic	N.P
				1	2.74 nm	Ferromagnetic	
				3	2.72 nm	Superparamagnetism	
				10	2.59 nm	paramagnetic	
B. Poornaprakash *et al.* [167]	ZnS:Fe, Co, Ni	Chemical refluxing	Cubic	0	3-7 nm	Diamagnetic	3.92
				2% Fe		Paramagnetic	3.70
				2% Co		Ferromagnetic	3.98
				2% Ni		Ferromagnetic	3.76
B. Poornaprakash *et al.* [196]	ZnS:Tb	Hydro-thermal	Cubic	0	2-5 nm	Diamagnetic	N.P
				1		0.0006 emu/g	
				3		0.0006 emu/g	
				5		Superparamagneti	
S. Ramu *et al.* [197]	ZnS:Tb	Co-precipitation	Cubic	0	5 nm	Diamagnetic	N.P
				6	8 nm	Paramagnetic	
S. P. Patel *et al.* [214]	ZnS:Co	PLD at 200^o, 400^o and 600^o C	Hexagonal	0	N.P	Ferromagnetism	3.90
				2.5			3.45
				5			3.32
M. S. Akhtar *et al.* [215]	Multi layer deposition	Chemical bath deposition (CBD)	Cubic	0	4 nm (*D*) 5µm (d)	N.P	3.78 eV
I. L. Quintas *et al.* [211]	ZnS:Co	Pulsed laser deposition (PLD)	Cubic & Hexagonal	10	43-66 nm (d)	N.P	N.P

From the comparative table it can be observed that reported magnetic behavior of ZnS nanostructures is contradictory. For instance, fundamentally ZnS should not show size or doping dependent magnetic transitions *i.e.* diamagnetic to paramagnetic or to ferromagnetic. Yes, it can be superparamagnetic below a critical diameter. The other contradiction that Co doped ZnS shows higher magnetization than Fe doped ZnS despite its lower magnetic moment than Fe, even at low doping concentration. The similar contradictory results have been observed for CdS nanostructures. In order to understand this, a comparative study of CdS and ZnS nanostructure is required at similar doping concentration and processing parameters. Therefore, the main focus of this work is to systematically investigates the *TM* (Fe^{3+}, Co^{2+}) and *RE* (Dy^{3+}, Tb^{3+}) doped CdS and ZnS

nanostructures synthesized under similar concentration and processing parameters. The main objectives of the study are

- To investigate size effect of CdS and ZnS nanostructures.
- To investigate effect of transition and rare earth doped CdS and ZnS on structural, optical and magnetic properties.

Chapter 3

Experimental procedure & characterization techniques

Overview

In this chapter, details of processing method adopted for synthesis of transition metal (Fe^{3+}, Co^{2+}) and rare earth (Tb^{3+}, Dy^{3+}) doped cadmium sulphide (CdS) and zinc sulphide (ZnS) nanostructures has been explained. A brief description of CdS and ZnS thin film deposition using chemical bath deposition is also given. The various characterization techniques used to analyze structural, morphological, elemental, optical and magnetic properties are given.

3.1 Synthesis of nanopowders

Nanopowders of cadmium sulphide (CdS) and zinc sulphide (ZnS) were synthesized by hydrothermal method. Laboratory grade (> 99.9% purity, Sigma-Aldrich) cadmium chloride monohydrate ($CdCl_2 \cdot H_2O$), sodium sulphide (Na_2S), zinc chloride ($ZnCl_2$), cobalt chloride hexahydrate ($CoCl_2 \cdot 6H_2O$), ferric chloride hexahydrate ($FeCl_3 \cdot 6H_2O$), dysprosium (III) nitrate hydrate ($Dy(NO_3)_3 \cdot xH_2O$) and terbium chloride hexahydrate ($TbCl_3 \cdot 6H_2O$) were used as precursors. Firstly, 0.25 mole (M) of $CdCl_2 \cdot xH_2O$/$ZnCl_2 \cdot xH_2O$ with appropriate concentration of dopant was dissolved in distilled water. Then, 0.25 M of Na_2S was added slowly to the above solution. The mixture was stirred continuously for 1 hour at room temperature (*RT*) till the homogeneous solution was formed. After that solution was transferred into 100 ml autoclave with 80% of the total volume. Thereafter, autoclave with CdS and ZnS solutions were placed in oven at 160 ℃ for 5 hours and 170 ℃ for 6 hours respectively. The autoclaves were allowed to cool at *RT* and obtained precipitates were firstly washed with ethanol followed by distilled water for two-three times to remove impurities. Finally, samples were dried in hot air oven at 60 ℃ and grinded to obtain the fine powder. Further, the powders were annealed at 300 ℃ in argon atmosphere for 1 hour.

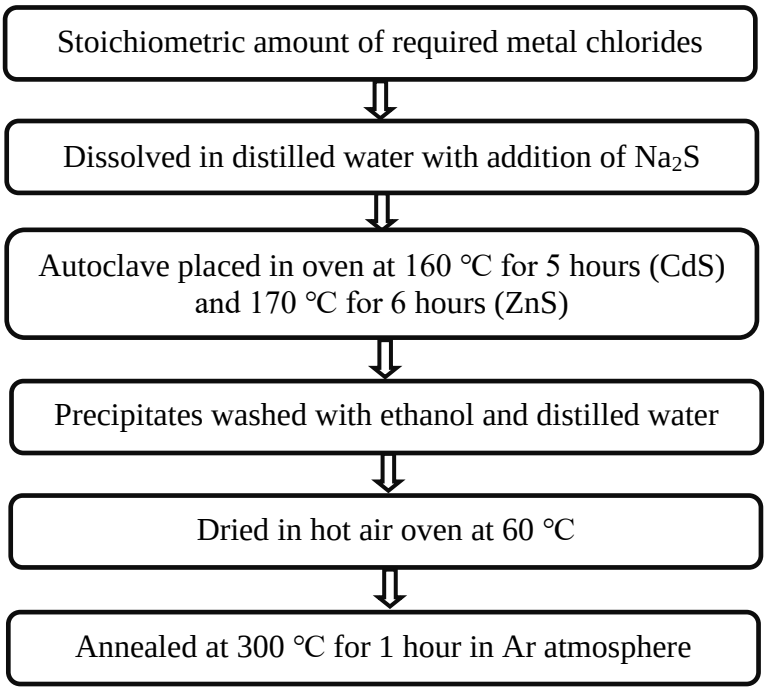

Fig. 3.1 Process flowchart of hydrothermal synthesis of CdS and ZnS nanoparticles.

The following doped and undoped series of CdS and ZnS nanoparticles were synthesized:

1. $Cd/Zn_{1-x}Fe_xS$ for x = 0, 0.05, 0.10 and 0.15
2. $Cd/Zn_{1-x}Co_xS$ for x = 0, 0.05, 0.10 and 0.15
3. $Cd/Zn_{1-x}Dy_xS$ for x = 0, 0.05, 0.10 and 0.15
4. $Cd/Zn_{1-x}Tb_xS$ for x = 0, 0.05, 0.10 and 0.15

3.2 Deposition of Thin films

In the present work, CdS, $Cd_{0.9}X_{0.1}S$, ZnS and $Zn_{0.9}X_{0.1}S$ (X = Fe^{3+} and Dy^{3+}) thin films were deposited using chemical bath deposition (CBD) technique.

Prior to the deposition of films, the glass substrate was ultrasonically cleaned with soap solution (Labolene) followed by distilled water. After that substrates were soaked in chromic acid solution for 30 minutes. The substrate was again washed with distilled water for several times and ultrasonically degreased with acetone. Finally, the glass slides were cleaned with isopropyl alcohol and dried in oven.

3.2.1 Deposition of CdS thin films

Firstly, precursor solutions were individually prepared with distilled water as solvent. 25 ml of 0.1 M $CdCl_2 \cdot H_2O$ solution, 5 ml of 1 M KOH, 20 ml of 1 M tri-sodium citrate $Na_3C_6H_5O_7.2H_2O$ and 20 ml buffer NaOH (pH~10) solution were mixed in 150 ml beaker under continuous stirring along with appropriate concentration of dopants. Thereafter, distilled water was added to above solution to make a total volume of 90 ml. The bath temperature was raised to 60 ℃ (with an accuracy of ±1°C) then 10 ml of 1 M thiourea was added. A pre-cleaned glass substrate was immersed vertically in the bath solution. The substrate was kept in solution for 1 hour under continuous stirring. After that, the substrate was taken out and ultrasonically washed in distilled water to remove loosely adhered particles. The precursor films thus obtained were dried in air. Multiple coating (max of 2) was carried out to acquire the suitable thickness. The systematic diagram for film deposition is given in Fig. 3.2.

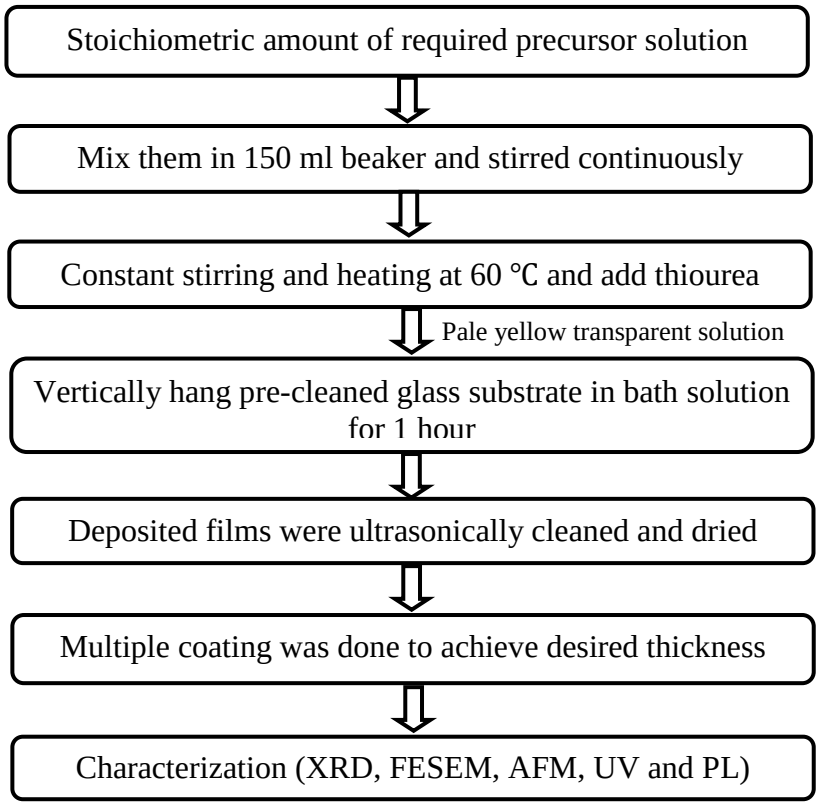

Fig. 3.2 Process flowchart for chemical bath deposition of CdS films.

3.2.2 Deposition of ZnS thin films

In this CBD process, zinc acetate (Zn $(CH_3COO)_2$) and thiourea SC $(NH_2)_2$ were used as source of Zn and S. 0.2 M Zinc acetate solution, 0.6 M of SC $(NH_2)_2$, 0.13 M tri-sodium citrate solutions were mixed. The mixture was continuously stirred with addition of appropriate amount of dopant. The total volume of bath solution was made 100 ml by adding requisition amount of distilled water. After that, ammonia (NH_3) solution was added to maintain the pH~ 10. The glass substrates were immersed in the prepared solution for 3 hours at constant temperature 70 °C (with an accuracy of ±1 °C). Thereafter coated substrate was ultrasonically cleaned with distilled water followed by air drying. Subsequent 2 layers were deposited by following the as mentioned procedure.

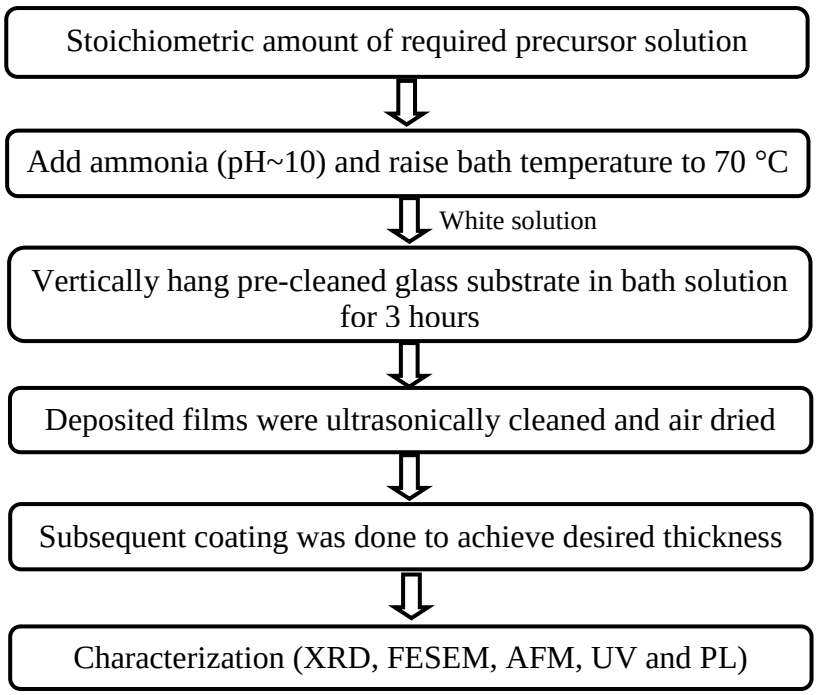

Fig. 3.3 Process flowchart for chemical bath deposition of ZnS films.

3.3 Material characterization:

The structural analysis of nanopowders/thin films was carried out by X-ray diffractometer (XRD). The High resolution transmission electron microscopy (HR-TEM) was used to study the morphology of nanoparticles, whereas the surface morphology of thin films was analyzed by Field emission scanning electron microscopy (FE-SEM) and Atomic force microscopy (AFM). The elemental composition was determined using energy dispersive spectroscopy (EDS). The optical properties were measured by *UV*–visible and photoluminescence (PL) spectroscopy. The *RT* magnetic properties of nanopowders were measured by vibrating sample magnetometer (VSM). The brief description of above mentioned characterization measurements are given below:

3.3.1 X-ray Diffractometer (XRD)

X-ray diffractometer (XRD) model X'PERT Pro-Panalytical (PANalytical) with Cu-K_α (λ = 1.5405 Å) was used to confirm the formation of phase. The diffraction data was recorded at *RT* in the range of $20° \leq 2\theta \leq 80°$ with step size of 0.05°. The observed diffraction peaks were matched with JCPDS card no. 41-1049 for hexagonal CdS (space group $P6_3mc$) and 00-002-0564 for cubic ZnS (space group F-43*m*). The crystallite size (*D*) was calculated by Scherrer equation [216] defined as:

$$D = \frac{0.9\lambda}{\beta Cos\theta} \quad (3.1)$$

where λ is wavelength of X-ray used, θ is the Bragg's angle in degree and β is full width at half maximum.

3.3.2 Energy dispersive spectroscopy (EDS)

The elemental analysis was carried using energy dispersive spectroscopy (EDS) model JEOL (JSM-1T100).

3.3.3 High-resolution transmission electron microscopy (HR-TEM)

The microstructural features and selected area electron diffraction (SAED) patterns of nanopowders were examined by High-resolution transmission electron microscopy (HR-TEM) model Hitachi H-7650. Prior to the measurements, the particles were sonicated in ethanol for 1 hour to disperse them. Then, a drop of dispersed nanoparticles was spread on copper coated TEM grids (3mm diameter and 200 mesh). The size of nanoparticles was determined using axio vision software.

3.3.4 Field emission scanning electron microscopy (FE-SEM)

The surface morphology and cross-sectional of thin films has been observed by Field emission scanning electron microscope (FE-SEM).

3.3.5 Atomic force microscopy (AFM)

Atomic force microscopy (AFM) model (ND-MDT Solver Next) was used to examine surface morphology and roughness of the films. These features were determined using fine tip/probe of AFM that raster scan the surface of sample in non-contact mode. The two and three dimensional image of surface is taken by monitoring the motion of probe as it is scanned across surface.

3.3.6 *UV*–visible spectroscopy

UV-visible spectrometer of PerkinElmer Lambda 45 was used to measure absorbance spectra for nanoparticles and thin films. Prior to measurement particles were dispersed in ethanol and for thin films the measurement was carried out with glass substrate. The absorbance of glass substrate has been subtracted from the absorbance spectra of films. The optical E_g was determined from Tauc's relation using the following equation [217]

$$\alpha h\nu = A(h\nu - E_g)^n \quad (3.2)$$

where, v is frequency, α is absorption coefficient, constant A is function of electronic transition probability, h is Plank's constant and n is type of transition (for direct transition $n = 1/2$).

3.3.7 Photoluminescence spectroscopy

The emission spectra of nanoparticles and films were carried out by fluorescence spectrophotometer (Agilent Carry Eclipse-G9800A) equipped with Xenon lamp. All emission spectra were recorded at *RT* in the range of 300-600 nm with 5 nm slit width. Prior to the measurements, the powdered samples were sonicated for 1 h to disperse them in ethanol. However, for films measurements were done using solid assembly of spectrophotometer.

3.3.8 Vibrating sample magnetometer (VSM)

The *RT* magnetic measurements were carried out by Lake Shore model 7404 magnetometer with maximum field of +1 Tesla to -1 Tesla. The magnetic properties (M_s, M_r and H_c) were measured from obtained hysteresis (M-H) loops. The paramagnetic contribution has been subtracted from obtained magnetization (M) using M-χH relation where χ is susceptibility of the material.

Chapter 4

Results and discussion

Overview

In this chapter, the structural, optical and magnetic properties of CdS and ZnS nanostructures are discussed. The results are divided into three parts, firstly the effect of annealing on CdS and ZnS nanoparticles has been studied. Secondly, the effect of *TM* and *RE* doped CdS and ZnS nanoparticles is reported. Finally, the structural and optical properties of CdS and ZnS films at selected doping concentration are investigated.

The main objectives of the study were to investigate the size and doping (transition metal (*TM*) & rare earth (*RE*)) effect on structural, optical and magnetic properties of CdS and ZnS nanoparticles. To accomplish this study, first the CdS and ZnS nanopowders were synthesized using hydrothermal method and size effect was induced by varying the annealing temperature. Thereafter at selected processing condition, the effect of *TM* (Fe^{3+}, Co^{2+}) and *RE* (Tb^{3+}, Dy^{3+}) metal ion doping was investigated. Finally, doped CdS and ZnS films were deposited using CBD method and their properties were investigated. The structural and morphological studies were carried out by XRD, FESEM, HRTEM and AFM, for optical studies *UV*-visible and PL spectroscopy and *RT* magnetic studies were carried out by VSM. The results as obtained from the mentioned studies are discussed below.

4.1 Effect of annealing temperature

4.1.1 X-ray diffraction

Fig. 4.1 (a & b) represents the X-ray diffraction pattern of CdS and ZnS nanoparticles annealed in the temperature range of 200-400 °C. It is observed that with rise in annealing temperature intensity of diffraction peaks is increasing reflecting better crystallinity and larger crystallite size (Table 4.1). In Fig. 4.1 (a) all diffraction peaks corresponds to hexagonal wurtzite phase with space group $P6_3mc$ (JCPDS file no. 41-1049). No phase change has been observed within studied temperature range.

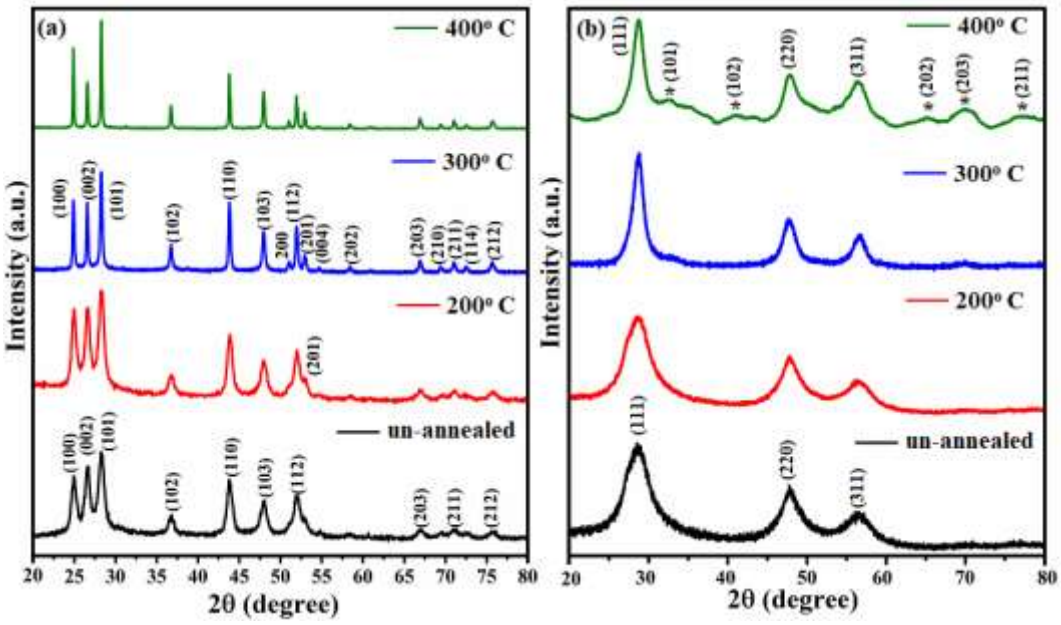

Fig. 4.1 XRD patterns of (a) CdS and (b) ZnS nanoparticles annealed at 200-400 °C.

In Fig. 4.1 (b), as-synthesized ZnS nanoparticles have diffraction peaks at (111), (220) and (311) planes that corresponds to cubic ZnS with space group *F*-43*m* (JCPDS file no. 00-002-0564). Upto 300 °C all samples showed cubic phase, while minor peaks of hexagonal phase emerges out at 400 °C as reported earlier [143,144]. The crystallite size (*D*) given in Table 4.1 was calculated using the Scherrer formula. The lattice parameters (*a*, *c*) were calculated by following relation:

For CdS nanoparticles

$$\frac{1}{d_{hkl}^2} = \frac{4}{3}\left[\frac{h^2+hk+k^2}{a^2}\right] + \frac{l^2}{c^2} \quad (4.1)$$

And for ZnS nanoparticles

$$\frac{1}{d_{hkl}^2} = \left[\frac{h^2+k^2+l^2}{a^2}\right] \quad (4.2)$$

where, *d* is inter-planar spacing and (*hkl*) are miller indices of plane.

The crystallite size of as synthesized CdS is relatively higher than ZnS nanoparticles. With annealing temperature CdS crystallite size increased from 12.18 nm to 49.56 nm, whereas no remarkable change in ZnS has been observed. No obvious change in lattice parameters has been observed.

Table 4.1 Structural parameters of CdS and ZnS nanoparticles.

Annealing temperature (°C)	CdS			ZnS	
	Lattice parameters *(Å)*		Crystallite Size *D (nm)*	Lattice parameter *(Å)*	Crystallite Size *D (nm)*
	a	*c*		*a*	
Un-annealed	4.13	6.70	12.18	5.32	3.91
200	4.13	6.71	12.99	5.33	4.02
300	4.14	6.72	29.67	5.39	4.80
400	4.14	6.72	49.56	5.41	5.20

4.1.2 *UV*- visible spectra

Fig. 4.2 (a & b) represents the *UV*-visible absorption spectra of CdS and ZnS nanoparticles recorded from 400 to 650 nm and 250 to 600 nm, respectively annealed in the temperature range of 200 to 400 °C. The optical E_g was determined using the following Tauc's equation

$$\alpha h\nu = A(h\nu - E_g)^n \quad (4.3)$$

where, α is absorption coefficient, ν is frequency, constant A is function of electronic transition probability, h is Plank's constant and n is type of transition (for direct transition n =1/2). E_g was determined by extrapolating the plot of $(\alpha h\nu)^2$ *vs.* $h\nu$ as shown in Fig.

4.2 (c & d). With the rise in annealing temperature the optical E_g (Table 4.2) found to decrease and absorption edge shifts towards higher wavelength. In case of CdS, measured crystallite size is quite higher than Bohr exciton radii (5nm), therefore, the variation in E_g may largely ascribed to change in crystallite [142,218,219]. However, the comparable crystallite size of ZnS to Bohr exciton radii (2.5 nm), increases the separation between valence and conduction bands that consequently increases the optical E_g.

Table 4.2 E_g of CdS and ZnS nanoparticles.

Annealing temperature (°C)	CdS E_g (eV)	ZnS E_g (eV)
Un annealed	2.51	3.78
200	2.50	3.77
300	2.48	3.74
400	2.43	3.69

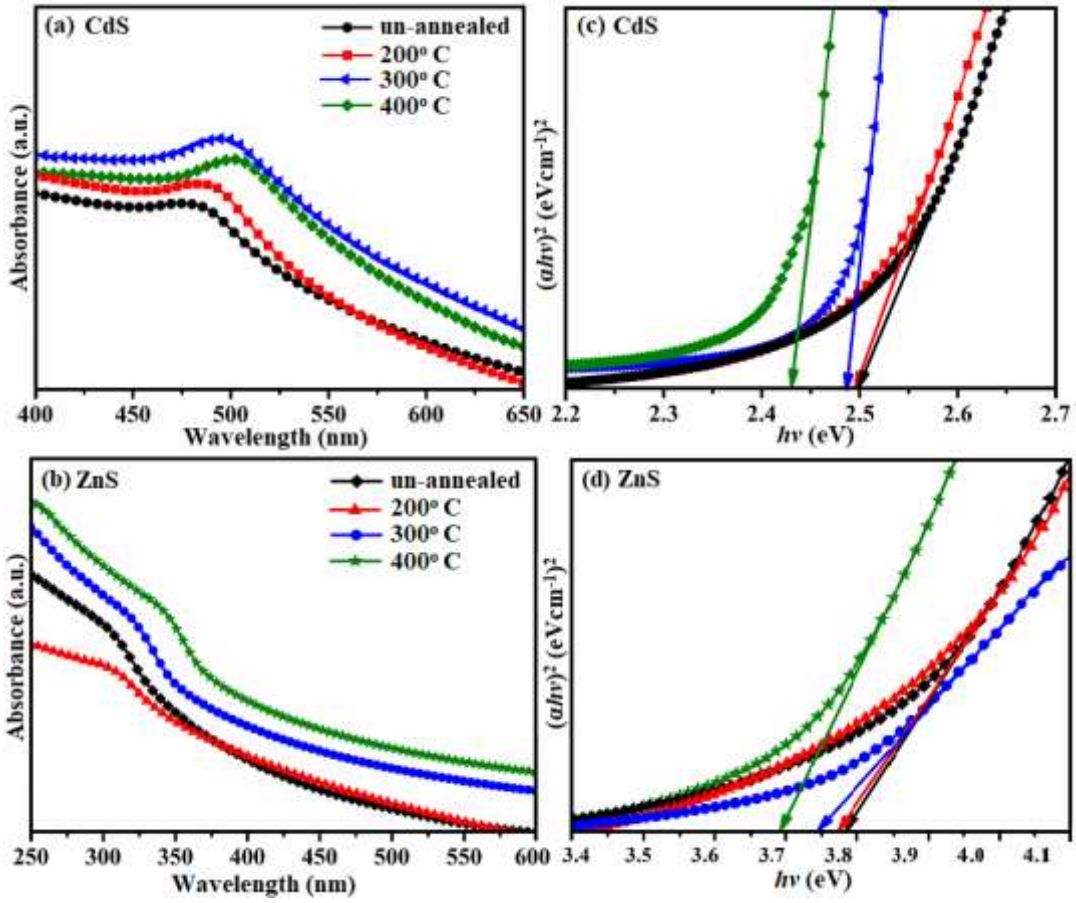

Fig. 4.2 (a & b) *UV*-visible absorption spectra, (c & d) Tauc's plot of CdS and ZnS nanoparticles.

4.1.3 Photoluminescence spectra

Fig. 4.3 (a & b) shows the *RT*-photoluminescence spectra of CdS and ZnS nanoparticles obtained at excitation wavelength of 380 and 260 nm, respectively. In Fig. 4.3 (a) four peaks are observed at 490 nm, 529 nm, 540 nm and 571 nm in as synthesized sample. The peak at 490 nm corresponds to blue emissions. The main emission band at around 529 nm is due to green emission, which can be attributed to surface donor-acceptor pair recombination. After excitation across band-edge, the electrons and holes trickle down non-radiatively to deep-traps where two recombination processes occurs in *d-d* intra ion transitions. Firstly, recombination of trapped holes in acceptor level with free electrons from conduction band and secondly, with electrons from donor level that results in green emission [220]. The two small humps at 540 nm and 571 nm are due to presence of surface traps. The intensity of emission peaks enhances with annealing temperature this can be due to formation of clusters with annealing [221,222]. The peak at 529 nm slightly shifts to 535 nm at 400 °C indicating the red shift.

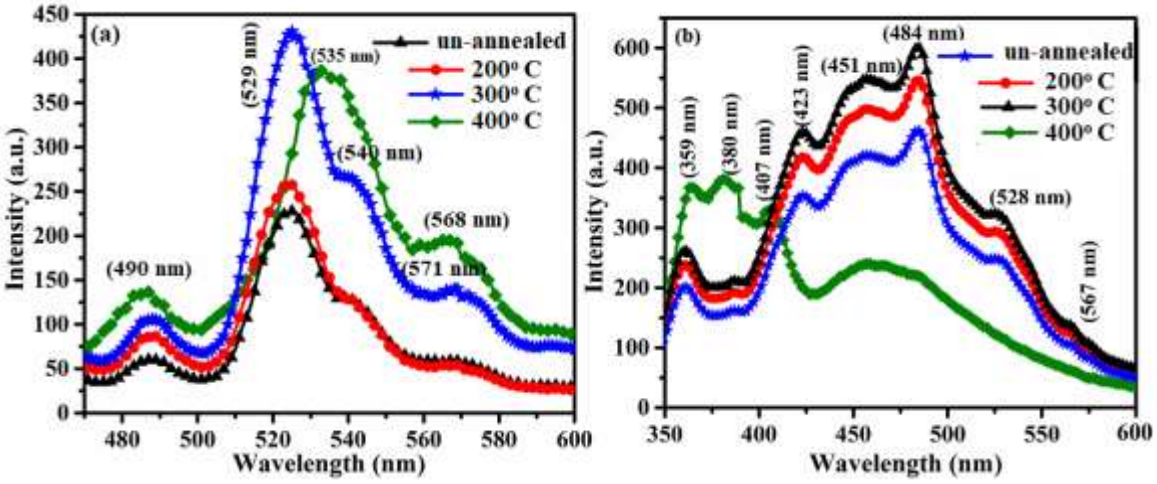

Fig. 4.3 PL spectra of (a) CdS and (b) ZnS nanoparticles.

In Fig. 4.3 (b) as synthesized ZnS sample showed peaks at ~ 359 nm, 423 nm, 451 nm, 484 nm, 528 nm and 567 nm. The peak at 359 nm is band to band edge transitions originating from the recombination of free excitons of ZnS nanoparticles [162]. The PL emission consist of two parts: first zinc vacancy (V_{Zn}) and sulphur atoms (I_S) as acceptor states located closer to valance band edge, and second sulphur vacancies (V_S) and interstitial zinc atoms (I_{Zn}) as donor states located closer to conduction band edge. The violet emission at 423 nm is attributed to transition from V_S to valence band edge of ZnS [223]. The two peaks at 451 nm and 484 nm are blue emissions associated with

recombination of free charge carriers in shallow traps, at the surface of nanoparticles [224]. The two small humps at 528 nm and 567 nm are related to native defects of pure ZnS such as V_{Zn} [225,226]. The emission intensity increases with rise in annealing temperature upto 300 °C [144]. However, for samples annealed at 400 °C, the emission spectra is different due to existence of mixed phase in ZnS nanoparticles.

4.1.4 Magnetic analysis

The *RT* magnetic behavior (*M-H*) of CdS and ZnS nanoparticles annealed at 200-400 °C is shown in Fig. 4.4 (a & b). All samples exhibit ferromagnetic behavior without much variation in saturation magnetization (M_s). The origin of ferromagnetism in dilute magnetic semiconductors (DMS) can be ascribed to two reasons firstly; the formation of ion vacancies and defects [227]. Secondly; the higher surface to volume ratio of nanoparticles causes larger number of magnetic moment; the exchange interaction between them favors their parallel alignment that results in higher M_s [22].

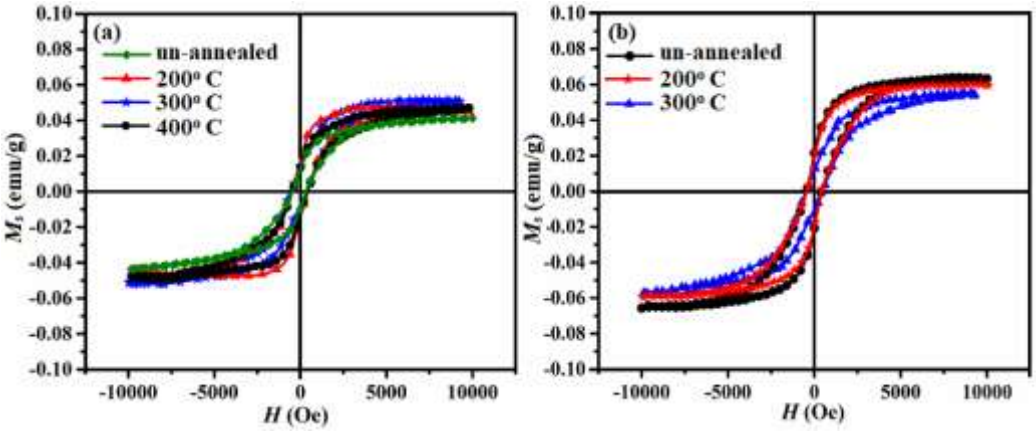

Fig. 4.4 *M-H* loops of (a) CdS and (b) ZnS nanoparticles.

From above discussion, it is evident that within studied temperature range the enhanced PL emissions and optimal E_g were obtained at 300 °C which make them suitable for optoelectronics and solar cell applications. Henceforth, the 300 °C annealing temperature has been chosen for further investigations. The effect of *TM* and *RE* doping on CdS and ZnS has been discussed below.

4.2 Transition metal doped nanoparticles

Among the transition metals, Fe and Co have been chosen as dopants. The doping of Fe^{3+} and Co^{2+} in CdS and ZnS nanoparticles may further enhance magnetization due to their

ferromagnetic nature. A dilute concentration of x = 0.05, 0.10 and 0.15 were doped in nanoparticles and their properties has been investigated.

4.2.1 Transition metal doped CdS nanoparticles

4.2.1.1 X-ray diffraction

The X-ray diffraction (XRD) patterns of $Cd_{1-x}Fe_xS$ and $Cd_{1-x}Co_xS$ nanoparticles have been illustrated in Fig. 4.5 (a & b), respectively. All diffraction peaks corresponds to hexagonal wurtzite phase with space group $P6_3mc$ (JCPDS file no. 41-1049).

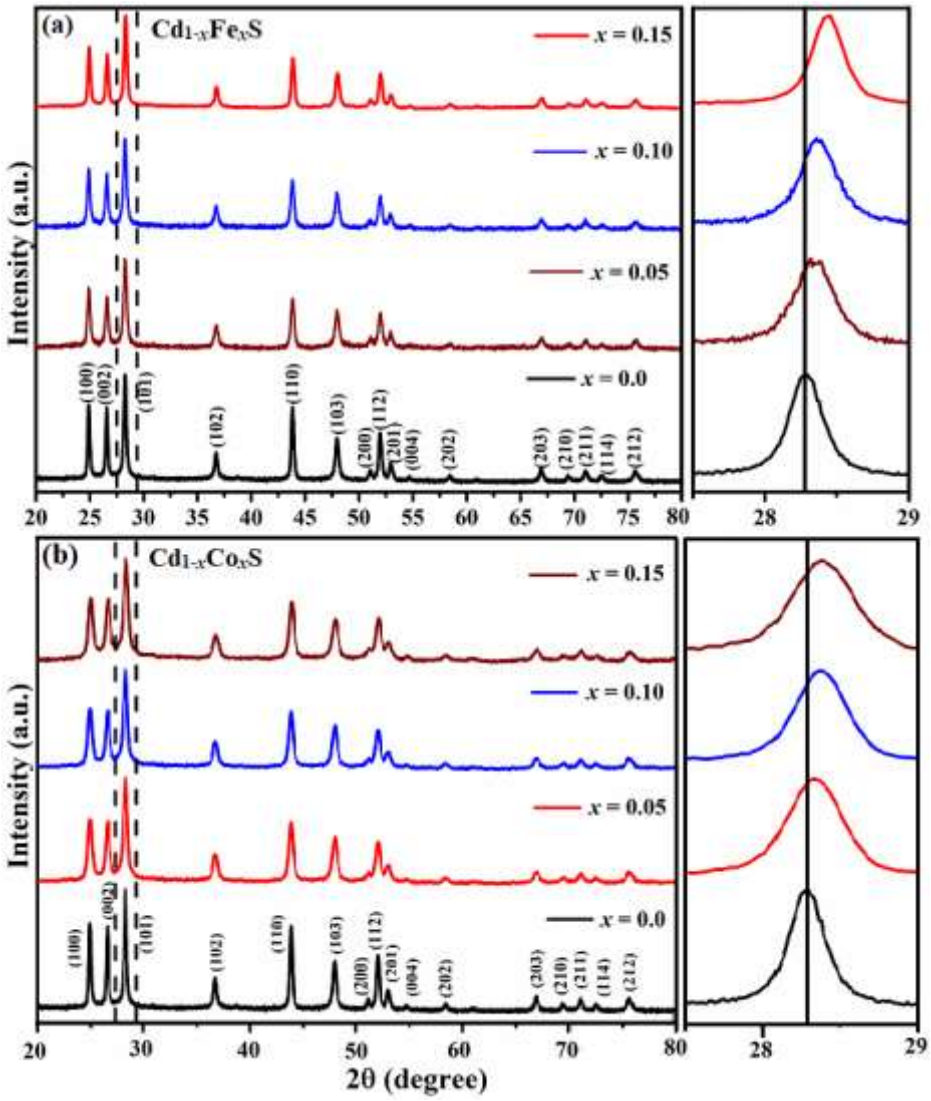

Fig. 4.5 XRD patterns of (a) $Cd_{1-x}Fe_xS$ and (b) $Cd_{1-x}Co_xS$ nanoparticles with magnified plot depicting peak shift.

The peak shift towards higher diffraction angle is due to stresses in the lattice as a consequence of smaller ionic radii of Fe^{3+} ion (0.64Å) and Co^{2+} ion (0.74Å) compared to

Cd^{2+} ion (0.97Å) [79,84]. A consistent decrease in *D* (Table 4.3) with doping concentration confirms that cationic sites are well substituted in host CdS lattice. While the presence of dopant showed no significant effect on lattice parameter (*a* & *c*). The c/a ratio is 1.63 which confirms the hexagonal symmetry of nanoparticles.

Table 4.3 Structural parameters and E_g of $Cd_{1-x}Fe_xS$ and $Cd_{1-x}Co_xS$ nanoparticles.

Sample	Concentration (*x*)	Lattice parameters *(Å)*		Crystallite Size *D (nm)*	E_g (eV)
		a	*c*		
CdS	0.0	4.14	6.72	29.67	2.48
$Cd_{1-x}Fe_xS$	0.05	4.13	6.71	14.81	2.53
	0.10	4.13	6.71	13.80	2.55
	0.15	4.13	6.70	11.50	2.56
$Cd_{1-x}Co_xS$	0.05	4.13	6.71	17.07	2.49
	0.10	4.13	6.71	15.53	2.51
	0.15	4.13	6.71	13.88	2.53

4.2.1.2 Morphological analysis

HR-TEM micrographs of undoped and doped nanoparticles are shown in Fig. 4.6 (a-c).

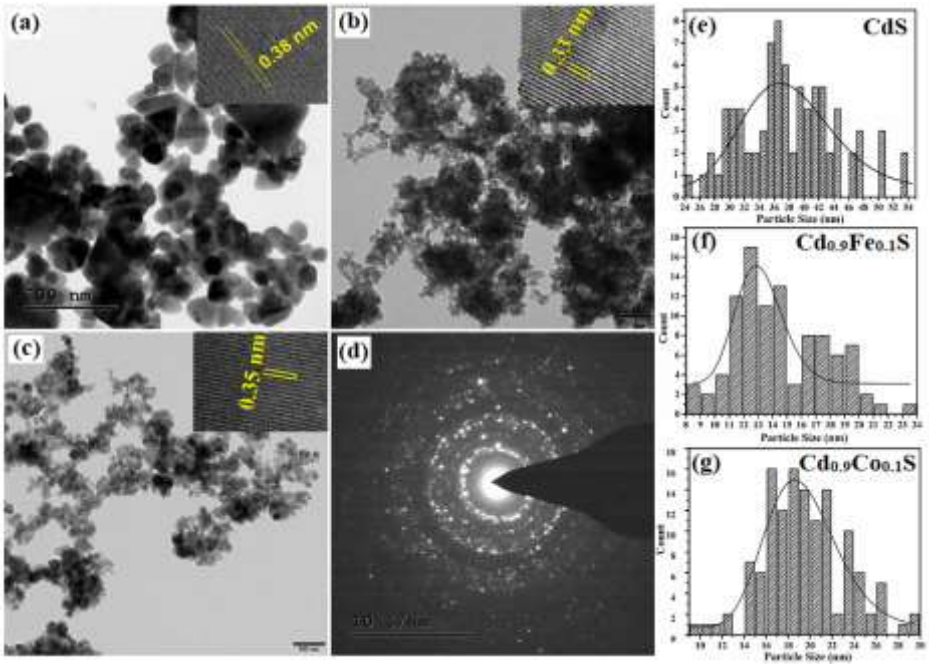

Fig. 4.6 TEM micrographs of (a) CdS, (b) $Cd_{0.9}Fe_{0.1}S$, (c) $Cd_{0.9}Co_{0.1}S$, (d) SAED pattern for CdS and (e-g) are particle size distribution histogram. Inset shows lattice fringe pattern.

The particle size distribution and corresponding Gaussian curve fitting of samples are

represented in Fig. 4.6 (e-g). The average particle diameter of undoped CdS is 37.69 nm which decreased to 13.06 nm (Fe) and 19.14 nm (Co). The measured *d*-spacing value from lattice fringe pattern is ~ 0.38 nm, 0.33 nm and 0.35 nm as shown in inset, corresponds to (002) plane of hexagonal structure of CdS. The decrease in *d*-spacing can be ascribed to lattice shrinkage with doping. The SAED pattern for CdS (Fig. 4.6 (d)) is not sharp indicating the nano-crystalline nature of nanoparticles. Fig. 4.7 represent EDS spectra of $Cd_{1-x}Fe_xS$ and $Cd_{1-x}Co_xS$ (x = 0.10) nanoparticles that confirms the presence of Cd, S, Fe and Co without any other elements.

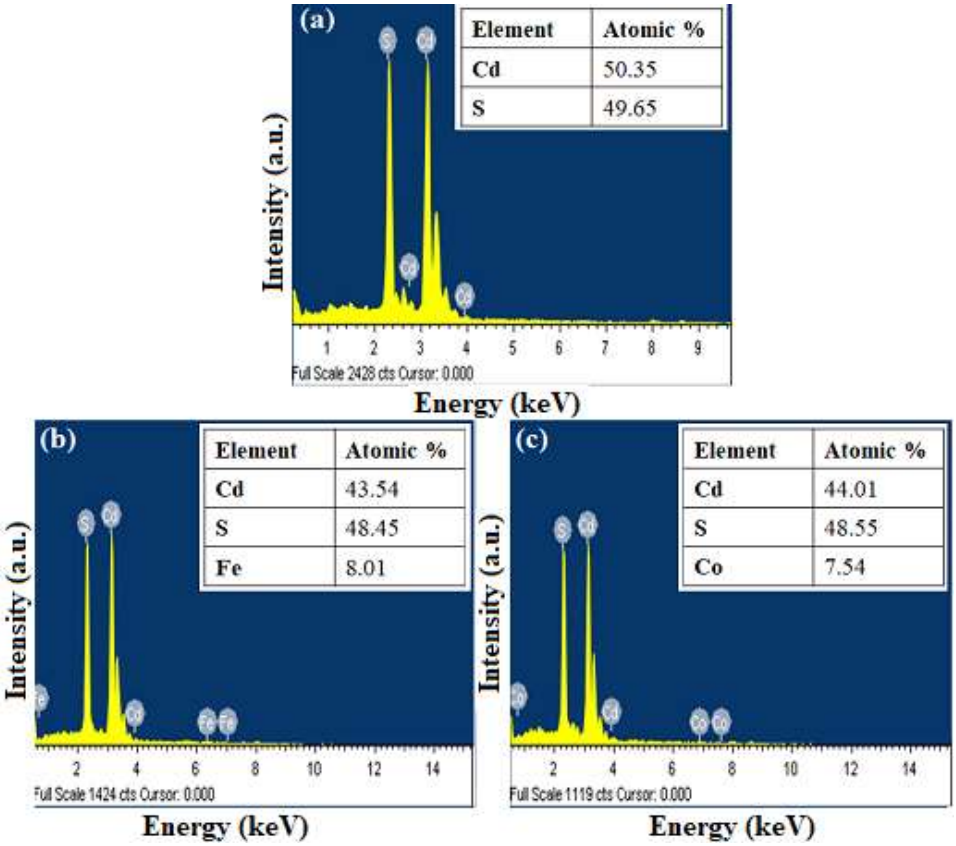

Fig. 4.7 EDS spectra of (a) CdS, (b) $Cd_{0.9}Fe_{0.1}S$ and (c) $Cd_{0.9}Co_{0.1}S$ nanoparticles.

4.2.1.3 *UV*- visible spectra

Fig. 4.8 (a & b) depicts the *UV*-visible absorbance spectra of $Cd_{1-x}Fe_xS$ and $Cd_{1-x}Co_xS$ nanoparticles recorded from 400 to 850 nm. The blue shift in absorbance wavelength was observed with doping. The variation in E_g with Fe^{3+} and Co^{2+} doping is shown in Fig. 4.8 (c & d) and tabulated in Table 4.3. The E_g for undoped CdS is 2.48 eV increased with doping to 2.56 eV (Fe^{3+}) and 2.53 eV (Co^{2+}). The change in E_g can be attributed to various factors such as formation of defects, quantum confinement effect etc. Since, the size of nanoparticles in our system is much higher than Bohr-exciton radii (5nm)

therefore the size effect has no role in the modification of E_g. The widening of E_g with doping content can be ascribed to Burstein-Moss effect. According to which, when excess carriers are introduced in host lattice, the Fermi level shifts towards conduction band (CB) because of *sp-d* exchange interaction between CB electrons and localized spin of Co^{2+} and Fe^{3+} [228]. This exchange interaction produces excess carriers which occupy the states closer to Fermi level in CB, resulting in shifting of E_g to higher levels. Further, formation of various sulphur related defects with doping, tends to change the electronic band structure of host lattice [229].

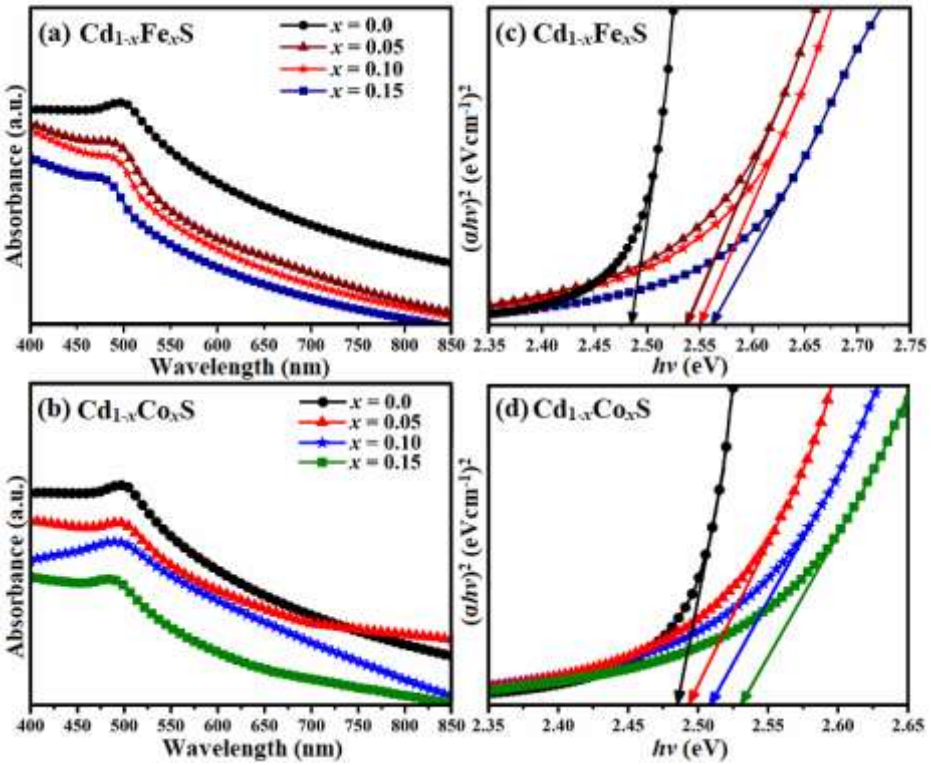

Fig. 4.8 (a & b) *UV*-visible absorption spectra, (c & d) Tauc's plot of $Cd_{1-x}Fe_xS$ and $Cd_{1-x}Co_xS$ nanoparticles.

4.2.1.4 Photoluminescence spectra

The representative *RT* photoluminescence spectra obtained at excitation wavelength of 380 nm are shown in Fig. 4.9. Four peaks are observed at 490 nm, 529 nm, 540 nm and 571 nm in all compositions. The reason for emergence of these emissions has already been discussed in section 4.1.3. No dopant related peaks has been observed. However, the intensity of peaks gets quenched with doping. The quenching of PL intensity can be attributed to formation of deep centers or defects that inhibit more number of electrons/holes to get excited and give rise to non-radiative transitions. However, intensity

of Fe^{3+}-doped CdS is higher than Co^{2+}, as doping of Fe^{3+} may create more Cd^{2+} vacancies as compared to Co^{2+} to maintain the charge neutrality. This causes high donor-acceptor pair recombination in Fe^{3+} doped CdS than in Co^{2+} doped CdS. Similar type of quenching has been reported in literature [84,230].

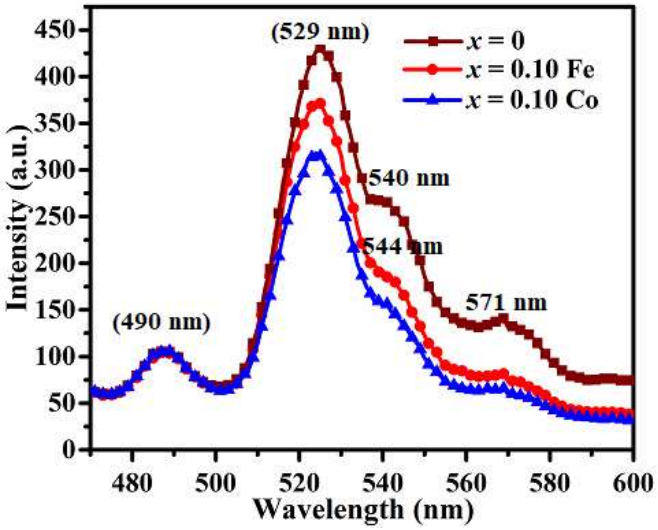

Fig. 4.9 Representative PL spectra of $Cd_{0.9}Fe_{0.1}S$ and $Cd_{0.9}Co_{0.1}S$ nanoparticles.

4.2.1.5 Magnetic analysis

The *M-H* loops of Fe^{3+} and Co^{2+} doped CdS nanoparticles are shown in Fig. 4.10. All composition shows measurable coercivity (H_c) and residual magnetization (M_r) (inset Fig. 4.10) which confirms ferromagnetic ordering.

The observed ferromagnetism in undoped CdS has already discussed in section 4.1.4. Beside the own magnetization of CdS nanoparticles, doping with Fe and Co further contribute to ferromagnetism, which is well evident from Fig. 4.10. The M_s is linearly increasing with doping concentration. Also, as reflected from PL spectra due to higher surface donor-acceptor pair recombination, $Cd_{1-x}Fe_xS$ should have a weak magnetism. However, the higher M_s in Fe doped nanoparticles is due to higher magnetic moment of Fe^{3+} ion compared to Co^{2+} ion that may have obscure the weak magnetism caused by donor-acceptor pair recombination in Fe doped CdS nanoparticles. The decrease in H_c with doping is consequence of soft magnetic nature of *TM* ions (Fe^{3+}, Co^{2+}) (Table 4.4). Comparing the magnetic nature of Fe and Co; Co is hexagonal in nature and magnetization vector remain along c axis, whereas Fe is cubic with magnetization vector along <100> direction [231,232]. Moreover, relative higher magnetocrystalline anisotropy of Co results in higher H_c. Hence Co doped CdS shows higher H_c than Fe

doped nanoparticles. The observed M_s values are comparable to highest reported in the literature for given compositions [81,84].

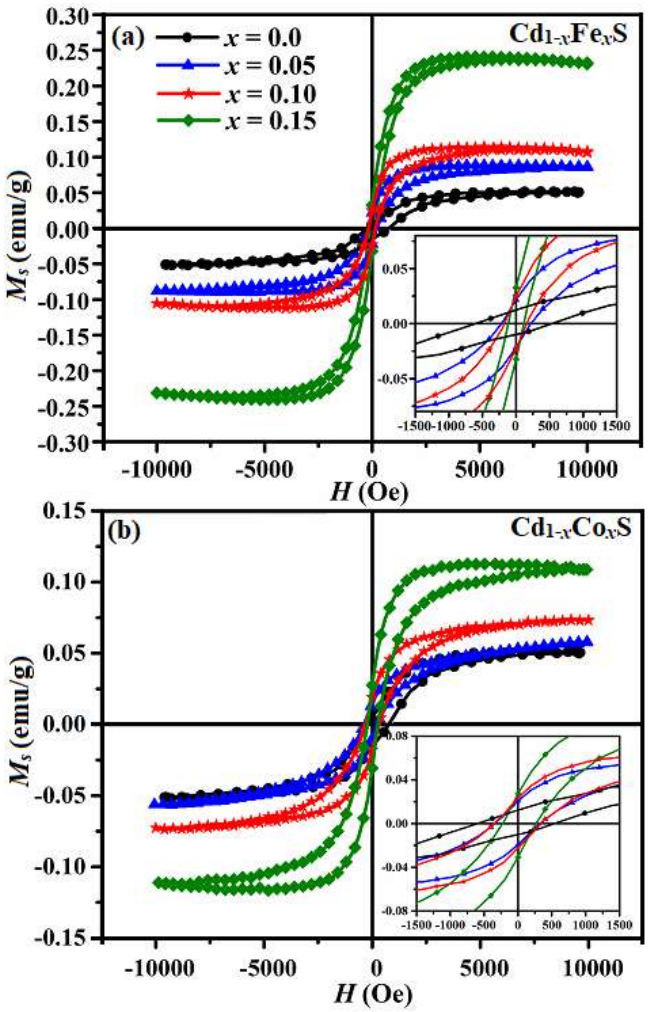

Fig. 4.10 *M-H* loops of (a) $Cd_{1-x}Fe_xS$ and (b) $Cd_{1-x}Co_xS$ nanoparticles. Inset shows the magnified view of *M-H* loop.

Table 4.4 Magnetic properties of $Cd_{1-x}Fe_xS$ and $Cd_{1-x}Co_xS$ nanoparticles.

Concentration (x)	$Cd_{1-x}Fe_xS$			$Cd_{1-x}Co_xS$		
	M_s (emu/g)	M_r (emu/g)	H_c (Oe)	M_s (emu/g)	M_r (emu/g)	H_c (Oe)
0.0	0.049	0.010	433.5	0.049	0.010	433.5
0.05	0.087	0.020	222.0	0.057	0.019	332.2
0.10	0.108	0.023	160.2	0.072	0.022	338.7
0.15	0.236	0.032	114.2	0.109	0.028	263.7

4.2.2 Transition metal doped ZnS nanoparticles

4.2.2.1 X-ray diffraction

The XRD patterns of $Zn_{1-x}Fe_xS$ and $Zn_{1-x}Co_xS$ nanoparticles are shown in Fig. 4.11 (a & b) corresponds cubic phase with space group F-43*m* (JCPDS file no. 00-002-0564).

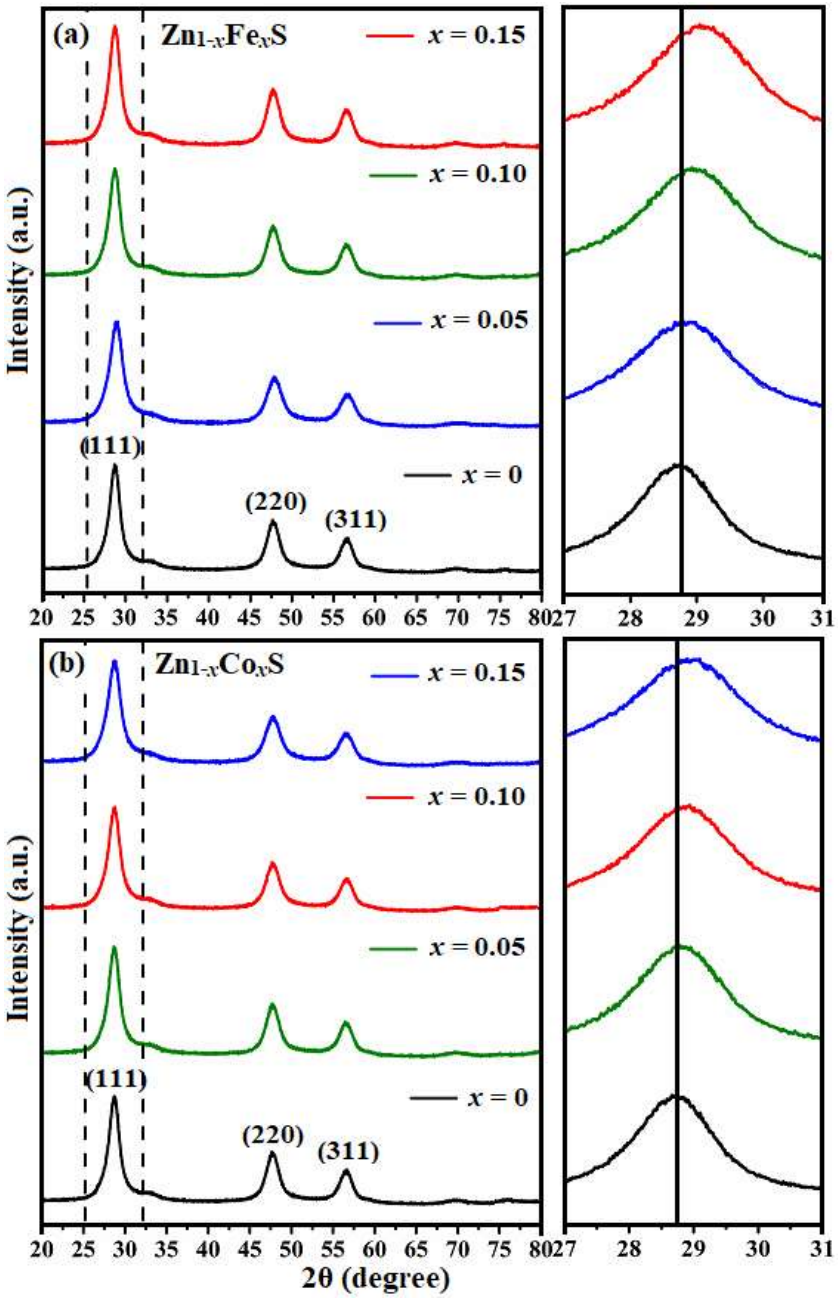

Fig. 4.11 XRD patterns of (a) $Zn_{1-x}Fe_xS$ and (b) $Zn_{1-x}Co_xS$ nanoparticles with magnified plot depicting peak shift.

The crystallite size also found to decrease due to smaller ionic radii of dopants compared to Zn^{2+} (0.74Å) which also causes peak shift. The change in lattice constant '*a*' with

dopants is (Table 4.5) ascribed to different ionic radii of dopant and in agreement with the crystallite size variation.

Table 4.5 Structural parameters and E_g of $Zn_{1-x}Fe_xS$ and $Zn_{1-x}Co_xS$ nanoparticles.

Sample	Concentration (x)	Lattice parameter (a) Å	Crystallite/Particle Size (nm)			E_g (eV)
			XRD	TEM	*UV*- Vis	
ZnS	0	5.39	4.80	6.77	6.76	3.74
$Zn_{1-x}Fe_xS$	0.05	5.32	4.08	-	4.77	3.80
	0.10	5.31	3.67	5.02	4.27	3.83
	0.15	5.30	3.61	-	3.90	3.86
$Zn_{1-x}Co_xS$	0.05	5.34	4.25	-	5.52	3.77
	0.10	5.33	4.01	5.09	4.99	3.79
	0.15	5.32	3.90	-	4.42	3.82

4.2.2.2 Morphological analysis

HR-TEM micrographs of $Zn_{1-x}Fe_xS$ and $Zn_{1-x}Co_xS$ (x = 0 and 0.10) along with particle size distribution histogram of nanoparticles are shown in Fig. 4.12 (a-g). All doped nanoparticles showed spherical morphology irrespective to type of dopant. A broad particle size distribution (4-11 nm) was observed for ZnS, which become narrower with doping. The average particle diameter of nanoparticles given in Table 4.5 is comparable to crystallite size. It is clear that with Fe^{3+} and Co^{2+} doping particle size shrinks. The d-spacing value measured from lattice fringe pattern (inset Fig. 4.12 (a-c)) are about ~ 0.34 nm that corresponds to (111) plane of ZnS cubic structure. Fig. 4.12 (d) shows the representative SAED pattern for undoped ZnS nanoparticle that depicts continuous diffraction rings of (111), (220) and (311) planes, and in lines with XRD result. The similar SAED pattern has been observed for other samples. EDS spectra of synthesized nanoparticles shown in Fig. 4.13 confirms the presence of Zn, S, Co and Fe without any contamination.

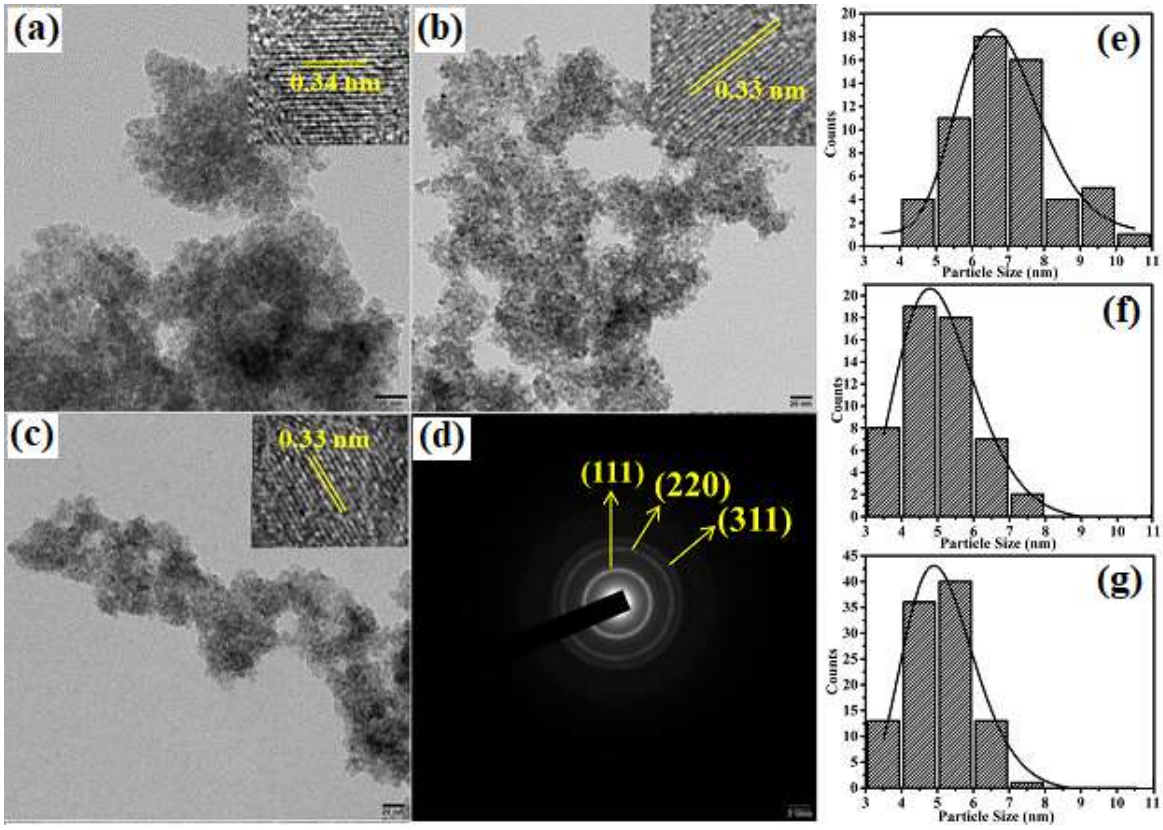

Fig. 4.12 TEM micrographs of (a) ZnS, (b) $Zn_{0.9}Fe_{0.1}S$, (c) $Zn_{0.9}Co_{0.1}S$, (d) SAED pattern of ZnS nanoparticles and (e-g) are particle size distribution histogram. Inset shows the lattice fringe patterns.

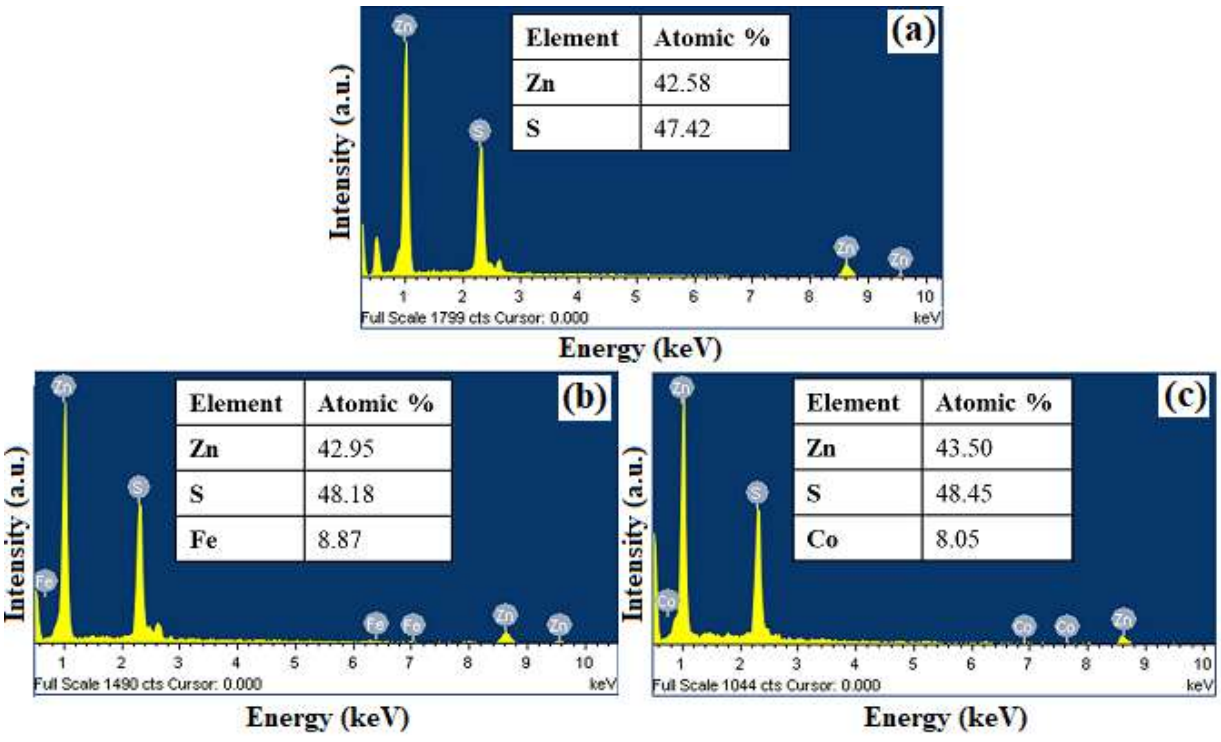

Fig. 4.13 EDS spectra of (a) ZnS, (b) $Zn_{0.9}Fe_{0.1}S$ and (c) $Zn_{0.9}Co_{0.1}S$ nanoparticles.

4.2.2.3 *UV*- visible spectra

Fig. 4.14 (a & b) depicts the *UV*- visible absorbance spectra of $Zn_{1-x}Fe_xS$ and $Zn_{1-x}Co_xS$ nanoparticles recorded in the wavelength range of 250-500 nm. The estimated E_g from Tauc's plot (Fig. 4.14 (c & d)) are given in Table 4.5.

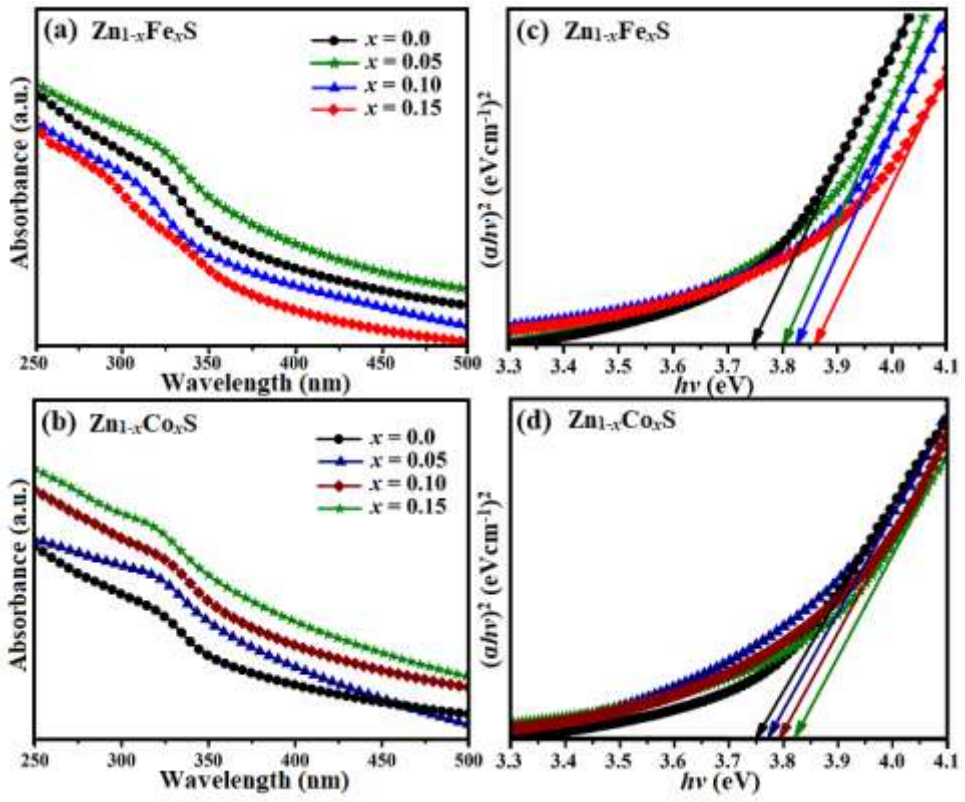

Fig. 4.14 (a & b) *UV*-visible absorption spectra, (c & d) Tauc's plot of $Zn_{1-x}Fe_xS$ and $Zn_{1-x}Co_xS$ nanoparticles.

The observed slight increase in E_g of undoped ZnS (3.74 eV) nanoparticles than its bulk (3.67 eV) counterpart can be ascribed to quantum confinement effect. The E_g found to increase with Fe^{3+} and Co^{2+} doping with the maximum value of 3.86 eV for Fe^{3+} doped (x = 0.15) nanoparticles. This variation in E_g is due to defect induced intermediate bands originated from different ionic radii and valance state of dopants that tune the electronic band structure of ZnS nanoparticles. Using the obtained E_g, the particle size was further confirmed by Brus effective mass approximations (*EMA*) formula [233].

$$\Delta E_g = E_g^{nano} - E_g^{bulk} = \frac{h^2}{8R^2}\left(\frac{1}{m_e^*} + \frac{1}{m_h^*}\right) - \frac{1.8e^2}{\varepsilon R} \quad (4.4)$$

Where E_g^{nano} and E_g^{bulk} are optical band gap energy of nanoparticles and bulk in Joules,

respectively. h is the plank's constant, R is radius of nanoparticle, m_e^*= 0.34 m_0 and m_h^*= 0.23 m_0 are effective mass of electrons and holes, respectively, where m_0 is free electron mass, e is the electronic charge and ε is dielectric constant of ZnS *i.e.* 8.76 [234]. The calculated particle size using Brus formula (Table 4.5) is in good agreement with XRD and TEM.

4.2.2.4 Photoluminescence spectra

The representative PL spectra of x = 0.10 obtained at excitation wavelength of 260 nm are represented in Fig. 4.15. All samples showed the peaks at ~ 359 nm, 423 nm, 451 nm, 484 nm, 528 nm and 567 nm with varied intensity. The reason for emergence of these peaks has already discussed in section 4.1.3. No peaks related to dopant has been observed, however intensity of peaks get quenched with doping of Fe^{3+} and Co^{2+}.

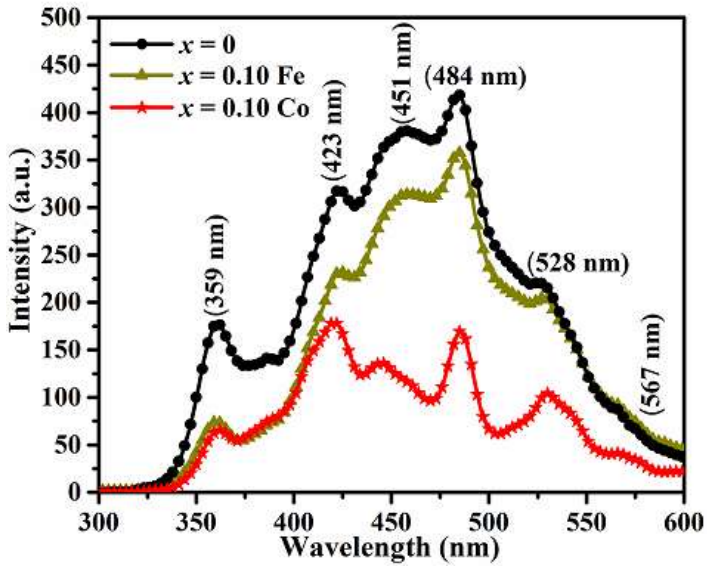

Fig. 4.15 Representative PL spectra of $Zn_{0.9}Fe_{0.1}S$ and $Zn_{0.9}Co_{0.1}S$ nanoparticles.

4.2.2.5 Magnetic analysis

RT magnetization (*M-H*) loops of $Zn_{1-x}Fe_xS$ and $Zn_{1-x}Co_xS$ nanoparticles are shown in Fig. 4.16. The obtained measurable H_c and M_r (inset Fig. 4.16) confirms the presence of ferromagnetism in all samples. In previous studies undoped ZnS showed diamagnetic and paramagnetic behavior. The observed ferromagnetic behavior in ZnS can be ascribed to the presence of sulphur vacancies and higher surface to volume ratio of nanoparticles which causes large number of uncompensated magnetic moments [22].

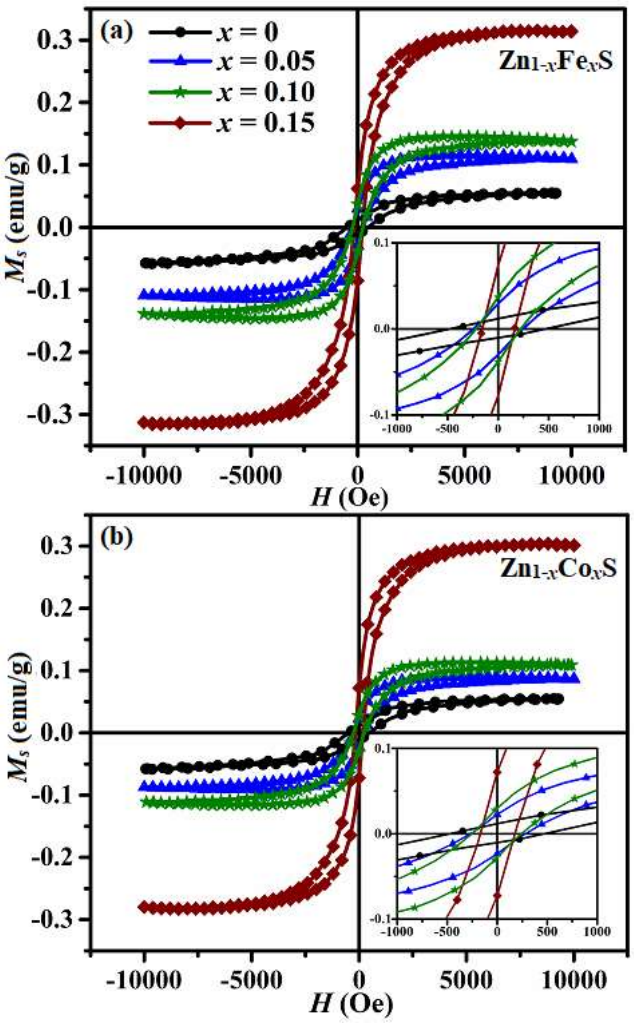

Fig. 4.16 *M-H* loops of (a) $Zn_{1-x}Fe_xS$ and (b) $Zn_{1-x}Co_xS$ nanoparticles. Inset shows the magnified view of *M-H* loop.

Table 4.6 shows that M_s and M_r are increasing with doping concentration for both Fe and Co doped ZnS nanoparticle. However, the higher M_s of Fe^{3+} doped nanoparticles is due to higher magnetic moment of Fe^{3+} ion compared to Co^{2+} ion. The lower H_c in doped nanoparticles suggest that inherit moment of Fe and Co contributes to swift demagnetization at lower magnetic field despite smaller particles. Basically, the magnetic properties of DMS materials are interplay of particle size and type of dopant and its concentration. It has been observed that with decreasing particle size magnetization increases, however below a critical particle diameter, the ferromagnetism disappear and particle acquire superparamagnetism [223]. To understand the role of dopants, it is mandatory to isolate the size effect by keeping size distribution in narrow range. As discussed in literature, *TM* doped ZnS showed different magnetization behavior. A few

studies showed that with increasing *TM* concentration, initially M_s increases and then decreases, due to dominant antiferromagnetic coupling at higher concentration [161]. In another study, Bhattacharya *et al.* has reported the signature of Fe^{2+} formation by magnetization *vs.* temperature curve and showed the decrease in M_s due to anti ferromagnetic coupling between Fe^{3+} and Fe^{2+} ions. In the present work, M_s found to increase gradually which suggest that no antiferromagnetic coupling is present due to low doping concentration. The presence of any Fe^{2+} ion formation is also ignored due observed decrease in lattice parameter [157].

Table 4.6 Magnetic properties of $Zn_{1-x}Fe_xS$ and $Zn_{1-x}Co_xS$ nanoparticles.

Sample	Concentration (x)	M_s at 1 T (emu/g)	M_r (emu/g)	H_c (Oe)
ZnS	0	0.057	0.011	471.1
$Zn_{1-x}Fe_xS$	0.05	0.112	0.029	246.2
	0.10	0.137	0.037	243.5
	0.15	0.322	0.077	172.0
$Zn_{1-x}Co_xS$	0.05	0.090	0.023	248.4
	0.10	0.108	0.029	247.5
	0.15	0.290	0.074	192.4

4.3 Rare earth doped nanoparticles

Among the rare earth ions, Dy^{3+} and Tb^{3+} have been chosen as dopants due to their excellent luminescent properties. Tb^{3+} ions reportedly showed sharp emission in green region that can be used for display application. On the other hand, Dy^{3+} ions exhibit strong luminescence in blue and yellow region of visible spectra. The studies pertaining to the doping of these rare earth are limited. Therefore, the effect of dilute (x = 0.05, 0.10 and 0.15) doping of Tb^{3+} and Dy^{3+} on structural, optical and magnetic properties of CdS and ZnS nanoparticles has been investigated.

4.3.1 Rare earth doped CdS nanoparticles

4.3.1.1 X-ray diffraction

The XRD patterns of $Cd_{1-x}Dy_xS$ and $Cd_{1-x}Tb_xS$ nanoparticles have been illustrated in Fig. 4.17 (a & b). All the diffraction peaks corresponds to the hexagonal wurtzite phase with space group $P6_3mc$ (JCPDS file no. 41-1049).

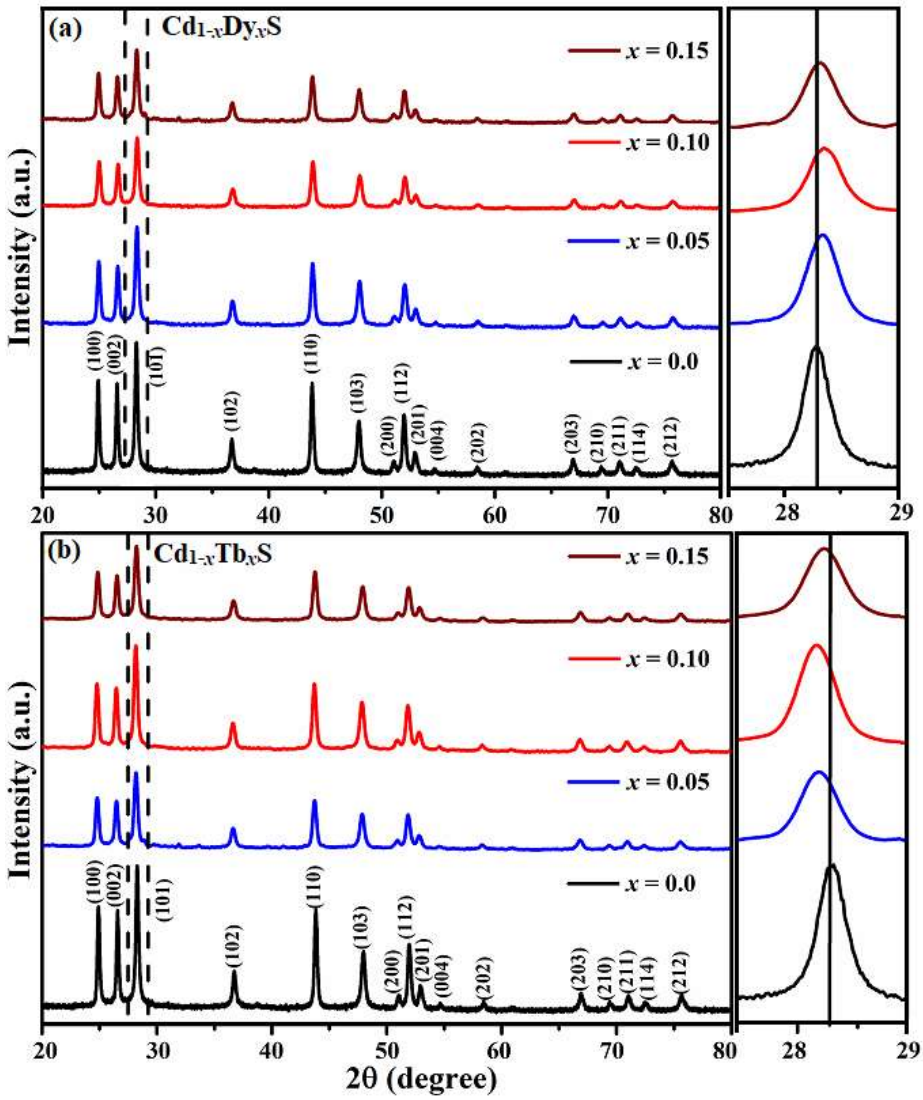

Fig. 4.17 XRD patterns of (a) $Cd_{1-x}Dy_xS$ and (b) $Cd_{1-x}Tb_xS$ nanoparticles with magnified plot depicting peak shift.

In Dy doped nanoparticles, the 2θ values are shifting towards higher diffraction angle upto $x = 0.10$ due to smaller ionic radii of Dy^{3+} ion (0.91Å) as compared to Cd^{2+} ion (0.97Å) [235]. For higher doping content ($x = 0.15$) 2θ shifts towards lower diffraction angle suggests that excess of Dy^{3+} ions causes stress compensation in crystal. However, for Tb^{3+} doping the shift in 2θ values (inset (b)) are towards lower diffraction angle, which is a consequence of larger ionic radii of Tb^{3+} ion (1.25Å) compared to Cd^{2+} ion [236]. Further, for $x = 0.15$, reverse trend is observed *i.e.*, peak shift towards higher diffraction angle, which suggest that at higher doping amount, the excess Tb^{3+} remained unsubstituted and creates a pinning action to lattice expansion. To verify doping effect, lattice parameters (*a, c*) have been calculated (Table 4.7). In Dy doped nanoparticles, *D*

(Table 4.7) initially found to decrease upto x = 0.10, then increases. No measurable change in lattice parameters has been observed.

Table 4.7 Structural parameters and E_g of $Cd_{1-x}Dy_xS$ and $Cd_{1-x}Tb_xS$ nanoparticles.

Sample	Concentration (x)	Lattice parameters *(Å)*		Crystallite Size *D (nm)*	E_g (eV)
		a	*c*		
CdS	0.0	4.14	6.72	29.67	2.48
$Cd_{1-x}Dy_xS$	0.05	4.13	6.71	22.14	2.54
	0.10	4.13	6.71	19.91	2.55
	0.15	4.13	6.71	25.80	2.49
$Cd_{1-x}Tb_xS$	0.05	4.14	6.72	33.34	2.43
	0.10	4.14	6.72	35.65	2.42
	0.15	4.14	6.72	32.40	2.44

4.3.1.2 Morphological analysis

HR-TEM micrographs and SAED pattern of $Cd_{1-x}Dy_xS$ and $Cd_{1-x}Tb_xS$ nanoparticles for x = 0.0 and 0.10 are shown in Fig. 4.18 (a-d). The particle size distribution and corresponding Gaussian curve fitting of samples are represented in Fig. 4.18 (e-g). Nanopowder shows spherical morphology with uniform particle size. The average particle diameter of undoped CdS is 37.69 nm which changes to ~30 nm (Dy) and ~ 40 nm (Tb). The change in particle size with doping may ascribed to different reasons. The different ionic radii of Dy^{3+} and Tb^{3+} than Cd^{2+} causes shrinkage/expansion in the unit cell which resulted in different particle size. The other reason could be the different thermodynamic conditions of crystal growth of doped and undoped one. The *d*-spacing for (002) plane (inset) is nearly constant in Tb^{3+} doped nanoparticles, whereas with Dy^{3+} doping shrinkage in *d*-spacing from ~ 0.38 nm to 0.33 nm is measured. The SAED pattern for CdS (Fig. 4.18 (d)) is not sharp, depicting the nano-crystalline nature of particles. Fig. 4.19 depicts EDS spectra of $Cd_{1-x}Dy_xS$ and $Cd_{1-x}Tb_xS$ for x = 0 and 0.10 that confirms the presence of Cd, S, Dy and Tb in synthesized nanoparticles without any contamination.

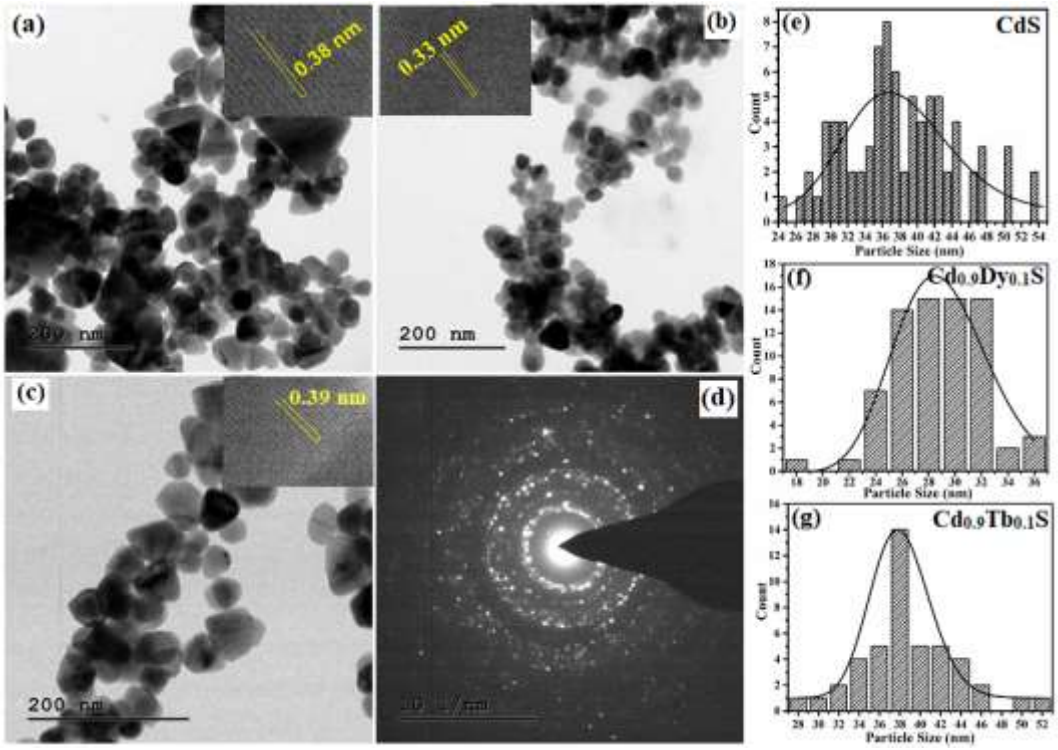

Fig. 4.18 TEM micrographs of (a) CdS, (b) $Cd_{0.9}Dy_{0.1}S$, (c) $Cd_{0.9}Tb_{0.1}S$, (d) SAED pattern for CdS and (e-g) are particle size distribution histogram. Inset shows lattice fringe pattern.

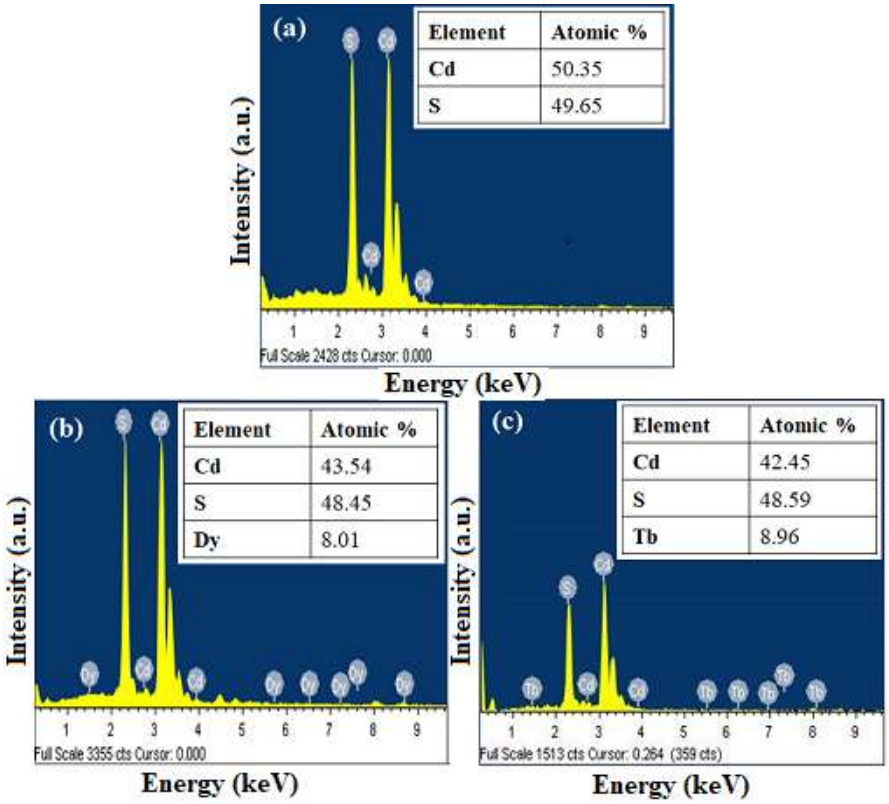

Fig. 4.19 EDS spectra of (a) CdS, (b) $Cd_{0.9}Dy_{0.1}S$ and (c) $Cd_{0.9}Tb_{0.1}S$ nanoparticles.

4.3.1.3 *UV*- visible spectra

Fig. 4.20 depicts the *UV*-visible absorbance spectra recorded and corresponding Tauc's plot of Dy and Tb doped CdS nanoparticles. Table 4.7 shows the obtained E_g of doped nanoparticles.

The optical E_g found to enhance from 2.48 eV to 2.55 eV with Dy^{3+} doping upto x = 0.10. Further, for x = 0.15 absorption edge slightly shifts towards higher wavelength and E_g decreased to 2.49 eV. However, for Tb doping there is decrease in E_g values upto x = 0.10 showing the red shift and consequently the absorption edge shifts towards the higher wavelength indicates the increase in particle size, which corroborate with XRD [237]. Also, this decrease in E_g values can be attributed to the introduction of new energy levels in the host lattice upon Tb^{3+} doping [238]. At x = 0.15, more defect centers may be produced due to decrease in crystallite size to 32.40 nm which in turn increase E_g to 2.44 eV. The change in E_g can be attributed to various factors such as formation of defects and sulphur vacancies.

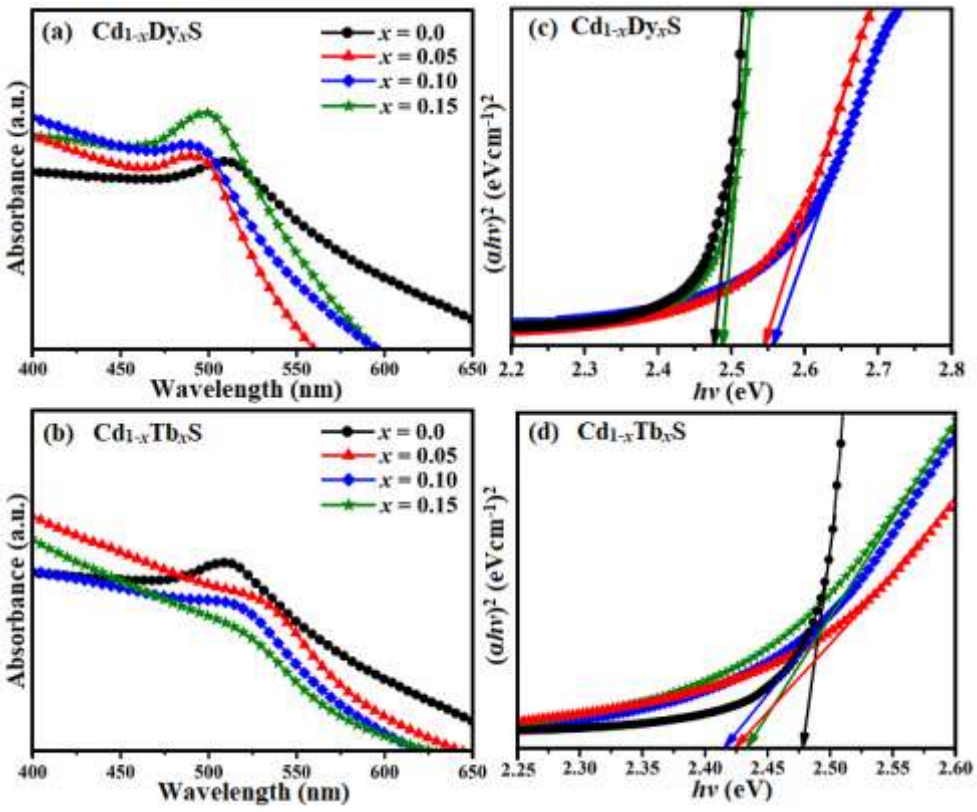

Fig. 4.20 (a & b) *UV*-visible absorption spectra, (c & d) Tauc's plot of $Cd_{1-x}Dy_xS$ and $Cd_{1-x}Tb_xS$ nanoparticles.

4.3.1.4 Photoluminescence spectra

The representative PL spectra of $Cd_{1-x}Dy_xS$ and $Cd_{1-x}Tb_xS$ nanoparticles with excitation wavelength of 380 nm are shown in Fig. 4.21. Four peaks are observed at 490 nm, 529 nm, 540 nm and 571 nm in all compositions. The reason for emergence of these emissions has already discussed in section 4.1.3. In doped CdS; the peak at 540 nm (x = 0) slightly shifted to ~545 nm due to sulphur vacancies which easily forms in CdS. These sulphur vacancies acts as trap states for photogenerated electrons resulting in yellow emission [239]. The doping of Dy^{3+} in CdS shows two transitions. Firstly, $^4F_{9/2} \rightarrow {}^6H_{13/2}$ (yellow emission) magnetic dipole transitions at ~570 nm and secondly, at 486 nm due to force electric dipole $^4F_{9/2} \rightarrow {}^6H_{15/2}$ (blue emission) transition [240]. In our system, these transitions are getting overlapped with defect states and band to band edge transition, respectively.

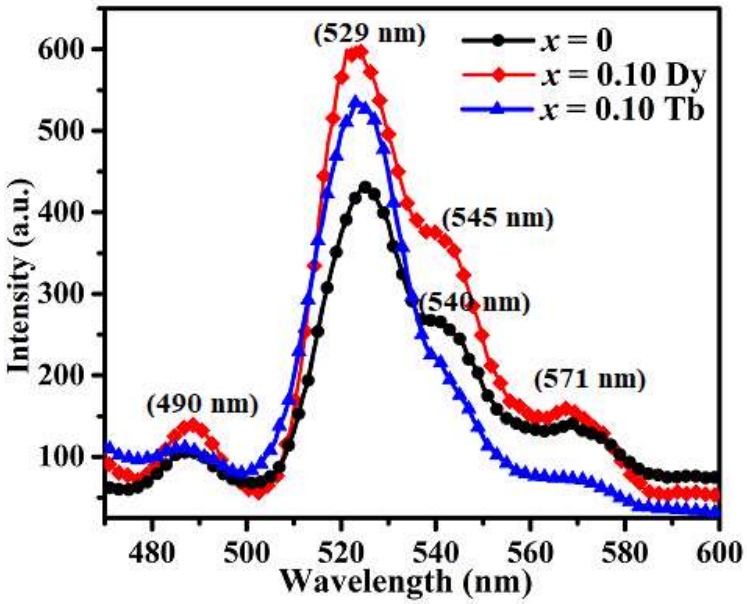

Fig. 4.21 Representative PL spectra of $Cd_{0.9}Dy_{0.1}S$ and $Cd_{0.9}Tb_{0.1}S$ nanoparticles.

4.3.1.5 Magnetic analysis

Fig. 4.22 (a & b) shows *RT* magnetic behavior of $Cd_{1-x}Dy_xS$ and $Cd_{1-x}Tb_xS$ nanoparticles. The magnified image of *M-H* loop (inset-II (a & b)) shows the presence of M_r and H_c in CdS nanoparticles. The measured magnetic properties of nanoparticles are given in Table 4.8. The observed ferromagnetism in undoped CdS has already discussed in section 4.1.4.

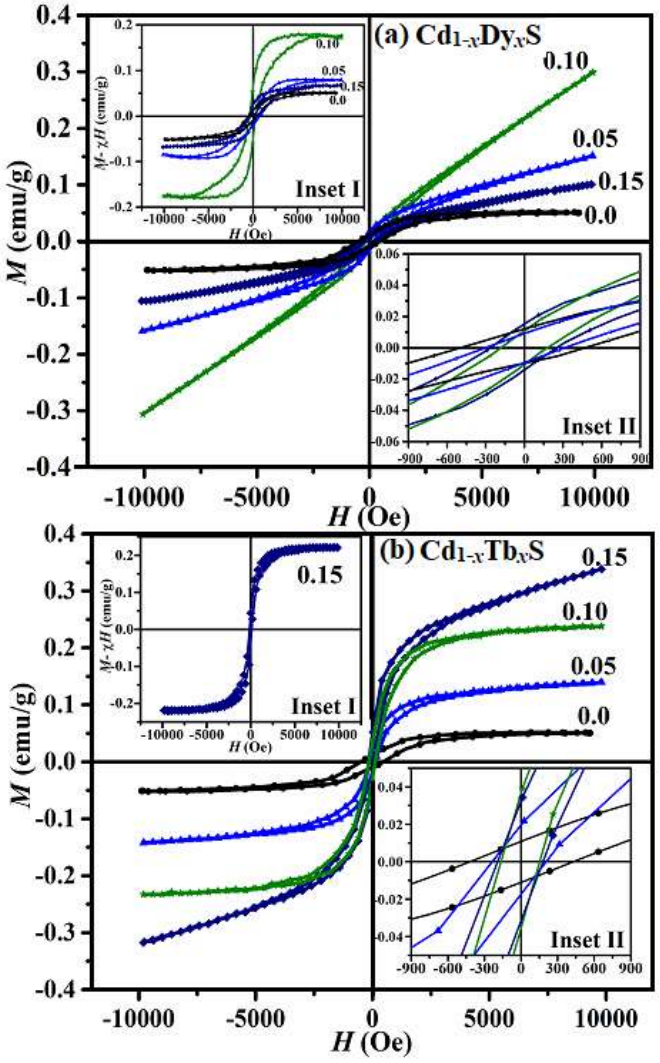

Fig. 4.22 *M-H* loops of (a) $Cd_{1-x}Dy_xS$ and (b) $Cd_{1-x}Tb_xS$ nanoparticles. Inset I shows (*M-χH*) *vs. H* loop and Inset II shows magnified view of *M-H* loop.

In Dy^{3+} and Tb^{3+} doped nanoparticles, *M* found to increase that can be attributed to formation of various defects and vacancies with doping [227]. However *M-H* loop are non-saturating in nature at higher doping concentration. The non-saturating *M-H* behavior is a characteristic feature of paramagnetic, anti-ferromagnetic or superparamagnetic contributions. Since the particle size in our case is higher than the Bohr exciton radii, therefore, the possibility of superparamagnetic contribution can be neglected. Similar, non-saturating behavior was observed in Co doped ZnO nanostructures, where fine nanoclusters of Co contributed to superparamagnetism [241,242]. Also antiferromagnetic coupling between neighboring ferromagnetic ions showed non saturating behavior [243]. Since Dy^{3+} and Tb^{3+} are paramagnetic at *RT* with Curie temperature of 85 K and 220 K, respectively [244], therefore their nanoclusters will not contribute to

superparamagnetism. Hence, non-saturation of *M-H* curve may ascribe to paramagnetic contribution from dopant ions. Subtracting paramagnetic contribution from magnetization (*M-χH*, *χ* is susceptibility); well saturated *M-H* loops were observed. The representative figure (x = 0.10 and 0.15) is shown in inset-I Fig. 4.23 (a & b). The observed low magnetization in x = 0.15 given in Table 4.8 justifies the presence of anti-ferromagnetic coupling arising from dopant ion exchange interactions within the lattice.

Table 4.8 Magnetic properties of $Cd_{1-x}Dy_xS$ and $Cd_{1-x}Tb_xS$ nanoparticles.

Concentration (x)	$Cd_{1-x}Dy_xS$			$Cd_{1-x}Tb_xS$		
	M_s (emu/g)	M_r (emu/g)	H_c (Oe)	M_s (emu/g)	M_r (emu/g)	H_c (Oe)
0.0	0.049	0.010	433.5	0.049	0.010	433.5
0.05	0.080	0.015	258.4	0.13	0.012	268.5
0.10	0.172	0.050	179.4	0.23	0.016	201.1
0.15	0.068	0.012	309.3	0.21	0.016	210.4

4.3.2 Rare earth doped ZnS nanoparticles

4.3.2.1 X-ray diffraction

The XRD patterns of $Zn_{1-x}Dy_xS$ and $Zn_{1-x}Tb_xS$ also corresponds to cubic phase (Fig. 4.23 (a & b). The marginal increase (4.80 to 5.23 nm) in crystallite size with *RE* doping is due to larger Tb^{3+} (1.25 Å) and Dy^{3+} (0.91 Å) ions compared to Zn^{2+} (0.74Å). The change in lattice constant '*a*' with dopants is (Table 4.9) ascribed to different ionic radii of dopant and in agreement with the crystallite size variation.

Table 4.9 Structural parameters and E_g of doped $Zn_{1-x}Dy_xS$ and $Zn_{1-x}Tb_xS$ nanoparticles.

Sample	Concentration (x)	Lattice parameter (a) Å	Crystallite/Particle Size (nm)			E_g (eV)
			XRD	TEM	*UV*- Vis	
ZnS	0	5.39	4.80	6.77	6.76	3.74
$Zn_{1-x}Dy_xS$	0.05	5.38	4.85		7.40	3.73
	0.10	5.40	4.92	6.82	8.27	3.72
	0.15	5.41	4.97		9.56	3.71
$Zn_{1-x}Tb_xS$	0.05	5.39	5.17		9.56	3.71
	0.10	5.41	5.21	8.16	11.70	3.70
	0.15	5.42	5.23		16.55	3.69

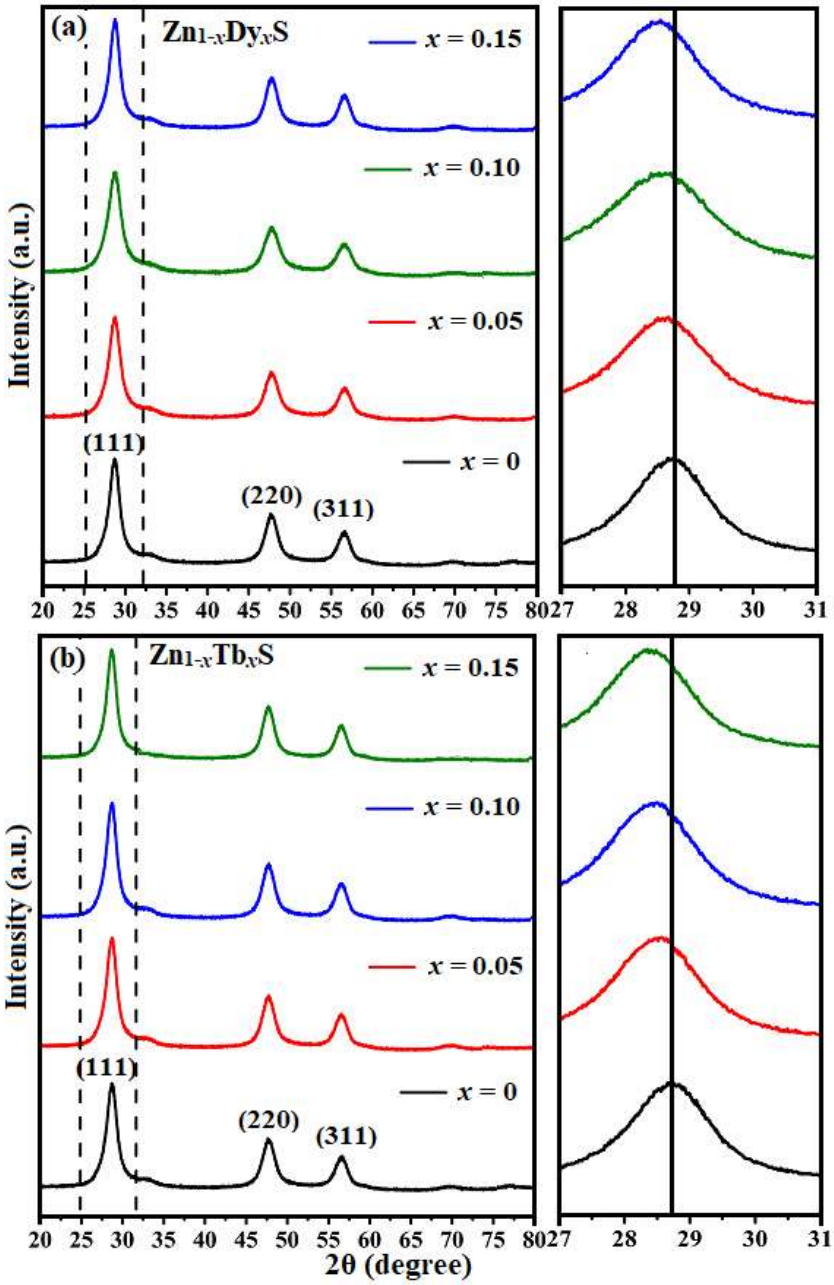

Fig. 4.23 XRD patterns of (a) $Zn_{1-x}Dy_xS$ and (b) $Zn_{1-x}Tb_xS$ doped nanoparticles with magnified plot depicting peak shift.

4.3.2.2 Morphological analysis

HR-TEM micrographs along with particle size distribution histogram of nanoparticles are shown in Fig. 4.24 (a-g). The average particle diameter of nanoparticles is given in Table 4.9. The *d*-spacing value measured from lattice fringe pattern (inset Fig. 4.24 (a-c)) are about ~ 0.34 nm that corresponds to (111) plane of ZnS cubic structure. Fig. 4.24 (d) shows the representative SAED pattern for undoped ZnS nanoparticle that depicts continuous diffraction rings of (111), (220) and (311) planes, and in lines with XRD

result. The similar SAED pattern has been observed for other samples. EDS spectra of synthesized nanoparticles shown in Fig. 4.25 confirms the presence of Zn, S, Dy and Tb without any contamination.

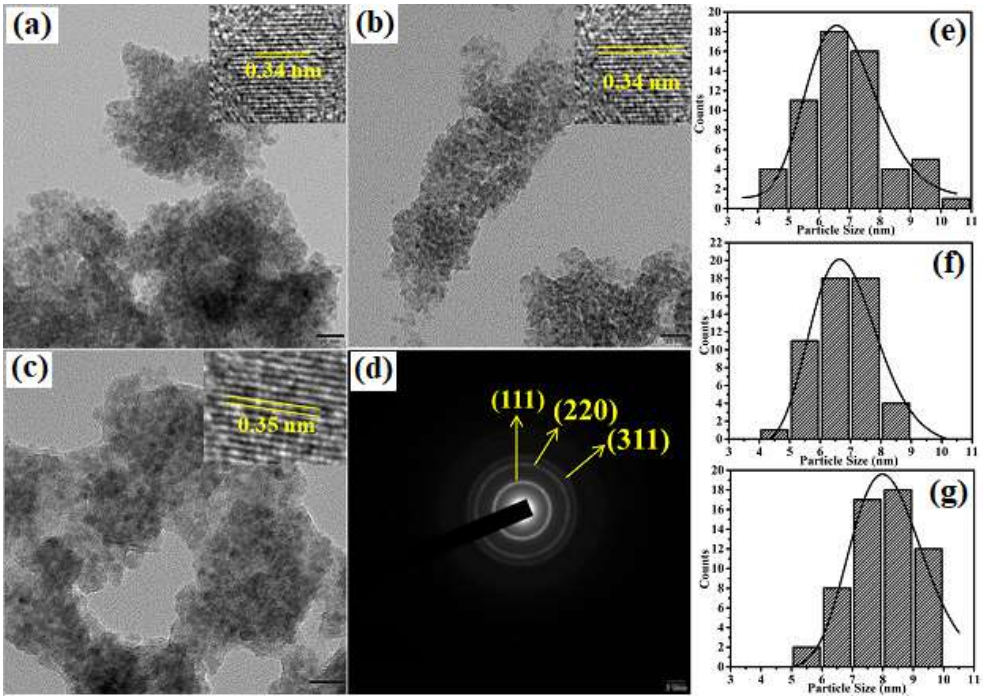

Fig. 4.24 TEM micrographs of (a) ZnS, (b) $Zn_{0.9}Dy_{0.1}S$, (c) $Zn_{0.9}Tb_{0.1}S$, (d) SAED pattern of ZnS nanoparticles and (e-g) are particle size distribution histogram. Inset shows the lattice fringe patterns.

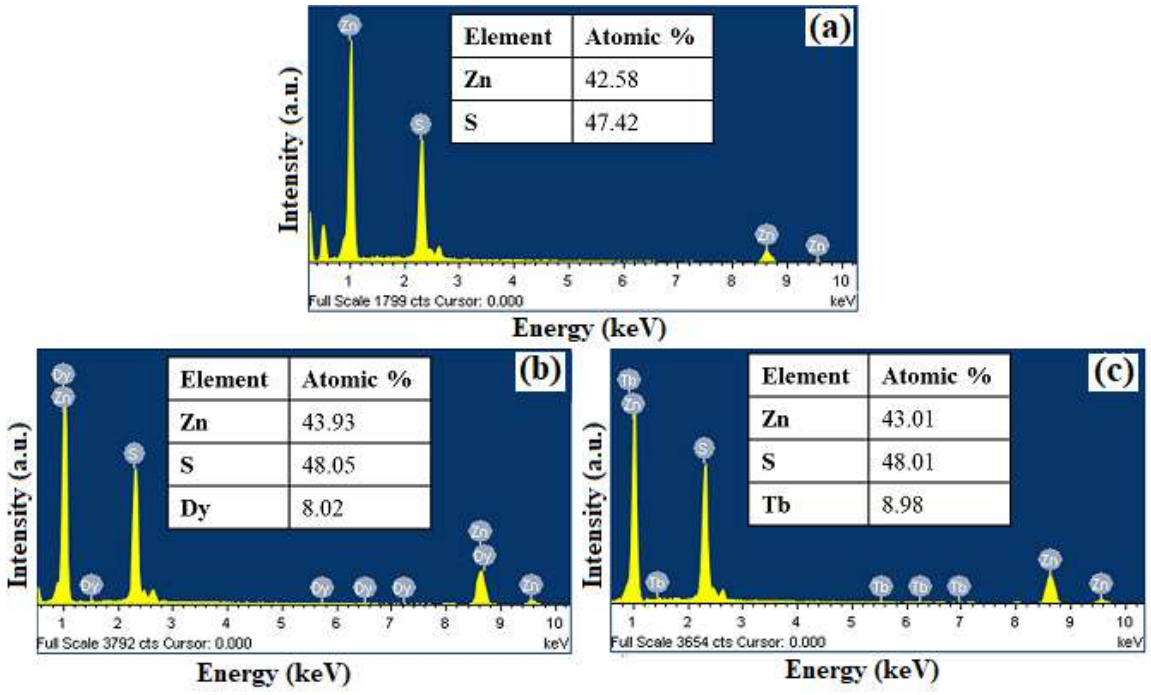

Fig. 4.25 EDS spectra of (a) ZnS, (b) $Zn_{0.9}Dy_{0.1}S$ and (c) $Zn_{0.9}Tb_{0.1}S$ nanoparticles.

4.3.2.3 *UV*- visible spectra

Fig. 4.26 (a & b) represents the *UV*- visible absorbance spectra recorded in the wavelength range of 250-500 nm.

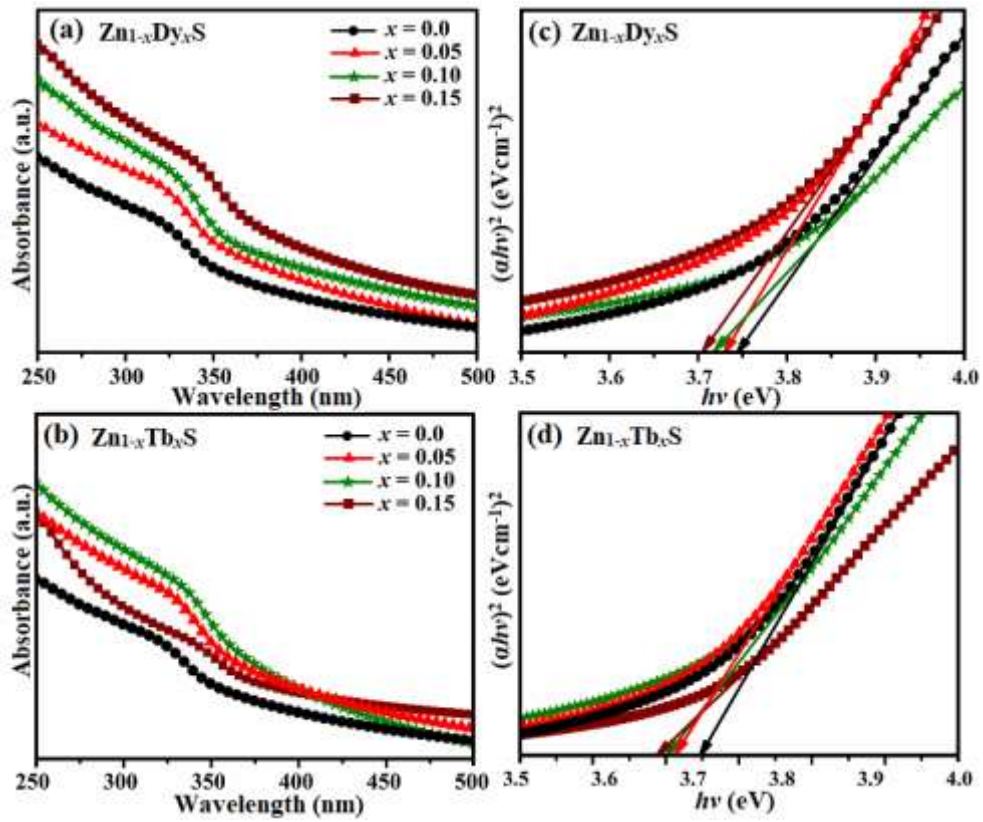

Fig. 4.26 (a & b) *UV*-visible absorption spectra, (c & d) Tauc's plot of $Zn_{1-x}Dy_xS$ and $Zn_{1-x}Tb_xS$ nanoparticles.

The E_g found to decreases marginally to 3.71 eV (Dy^{3+}) and 3.69 eV (Tb^{3+}) with doping (Table 4.9). This variation in E_g is due to defect induced intermediate bands originated from different ionic radii and valance state of dopants that tune the electronic band structure of ZnS nanoparticles [220]. The calculated particle size using Brus formula (Table 4.9) is in good agreement with XRD and TEM.

4.3.2.4 Photoluminescence spectra

The representative PL spectra of Dy^{3+} and Tb^{3+} doped nanoparticles (x = 0.10) obtained at excitation wavelength of 260 nm are represented in Fig. 4.27. All samples showed the peaks at ~ 359 nm, 423 nm, 451 nm, 484 nm, 528 nm and 567 nm with varied intensity. The reason for emergence of these peaks as already discussed in section 4.13. No peaks related to dopant has been observed. The *RE* doped ZnS showed higher emission intensity

than undoped ZnS, which is favorable for their potential use in light emitting diodes [245].

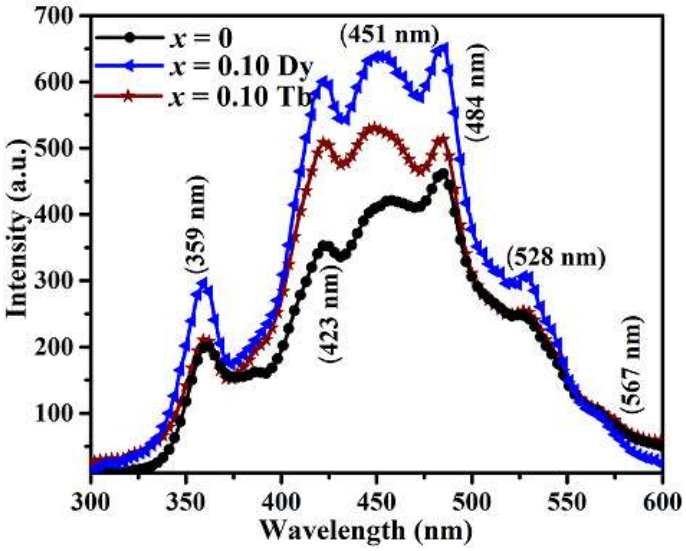

Fig. 4.27 Representative PL spectra of $Zn_{0.9}Dy_{0.1}S$ and $Zn_{0.9}Tb_{0.1}S$ nanoparticles.

4.3.2.5 Magnetic analysis

RT magnetization (*M-H*) loops of $Zn_{1-x}Dy_xS$ and $Zn_{1-x}Tb_xS$ (x = 0, 0.05, 0.10 and 0.15) nanoparticles are shown in Fig. 4.28. The obtained measurable H_c and M_r (inset Fig. 4.28) confirms the presence of ferromagnetism in all samples. The observed ferromagnetism in undoped ZnS has already discussed in section 4.1.4. Beside own magnetization of ZnS; doping of Dy^{3+} and Tb^{3+} further contribute to ferromagnetism, which is well evident from Fig 4.28. The obtained magnetic parameters are tabulated in Table 4.10. M_s and M_r were found to increase for both Dy^{3+} and Tb^{3+} doped ZnS nanoparticle. The low H_c of doped ZnS than undoped nanoparticle is due higher particle size (Table 4.10).

Table 4.10 Magnetic properties of $Zn_{1-x}Dy_xS$ and $Zn_{1-x}Tb_xS$ nanoparticles.

Sample	Concentration (x)	M_s at 1 T (emu/g)	M_r (emu/g)	H_c (Oe)
ZnS	0	0.057	0.011	471.1
$Zn_{1-x}Dy_xS$	0.05	0.072	0.022	350.0
	0.10	0.084	0.028	367.7
	0.15	0.092	0.032	369.9
$Zn_{1-x}Tb_xS$	0.05	0.061	0.019	432.0
	0.10	0.078	0.026	443.4
	0.15	0.083	0.027	449.1

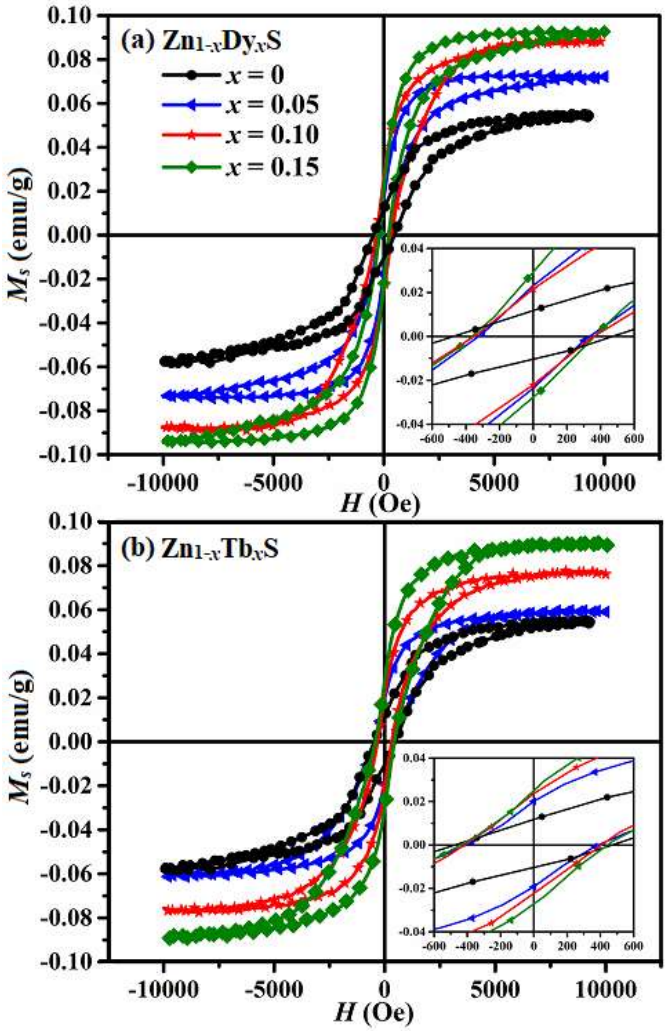

Fig. 4.28 *M-H* loops of (a) $Zn_{1-x}Dy_xS$ and (b) $Zn_{1-x}Tb_xS$ nanoparticles. Inset shows the magnified view of *M-H* loop.

4.4 CdS and ZnS thin films

Recently, thin films of CdS and ZnS are potentially used in solar cells, photo sensors and light emitting diodes. Therefore, an attempt has been made to investigate the dopant induced properties in CdS and ZnS films. As observed, Fe^{3+} doped nanoparticles showed higher optical E_g and M_s. Whereas, doping of Dy^{3+} enhances the luminescent properties in both CdS and ZnS nanoparticles and also exhibit higher M_s at $x = 0.10$ in doped CdS and ZnS. Therefore, among the studied concentration range and type of dopant, the concentration of $x = 0.10$ and Fe^{3+}, Dy^{3+} dopants have been chosen for CdS and ZnS films. The films have been prepared by chemical bath deposition technique and the effect of dopants on structural, morphological and optical properties are investigated.

4.4.1 Effect of Fe^{3+} and Dy^{3+} doping on CdS and ZnS thin films

4.4.1.1 X-ray diffraction

The Fig. 4.29 represents XRD patterns of doped CdS and ZnS films. In Fig. 4.29 (a) the diffraction peaks shows preferential growth along (002) plane of hexagonal CdS, whereas, CdS nanoparticles have showed multiple diffraction peaks from other planes. Similar to ZnS nanoparticles, three peaks at (111), (220) and (311) plane of cubic phase has been obtained in films. The variation in crystallite size (Table 4.11) with doping is similar to nanoparticles.

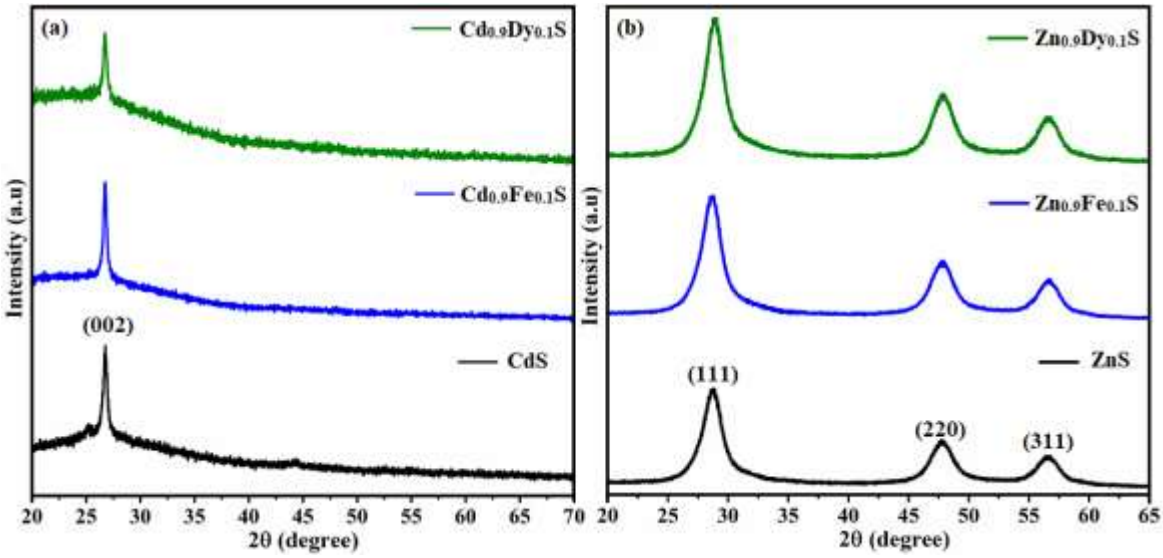

Fig. 4.29 XRD patterns of (a) CdS and (b) ZnS thin films.

Table 4.11 Crystallite size, thickness and E_g of CdS and ZnS films.

Sample	Crystallite size (nm)	Thickness (nm)	E_g (eV)
CdS	22.46	356	2.46
$Cd_{0.9}Fe_{0.1}S$	17.90	342	2.49
$Cd_{0.9}Dy_{0.1}S$	21.92	350	2.47
ZnS	6.45	566	3.71
$Zn_{0.9}Fe_{0.1}S$	4.98	440	3.75
$Zn_{0.9}Dy_{0.1}S$	7.30	664	3.69

4.4.1.2 Microstructural analysis

FESEM surface morphology of CdS and ZnS film shown in Fig. 4.30 and Fig. 4.31 depicts that films are densely packed with low porosity.

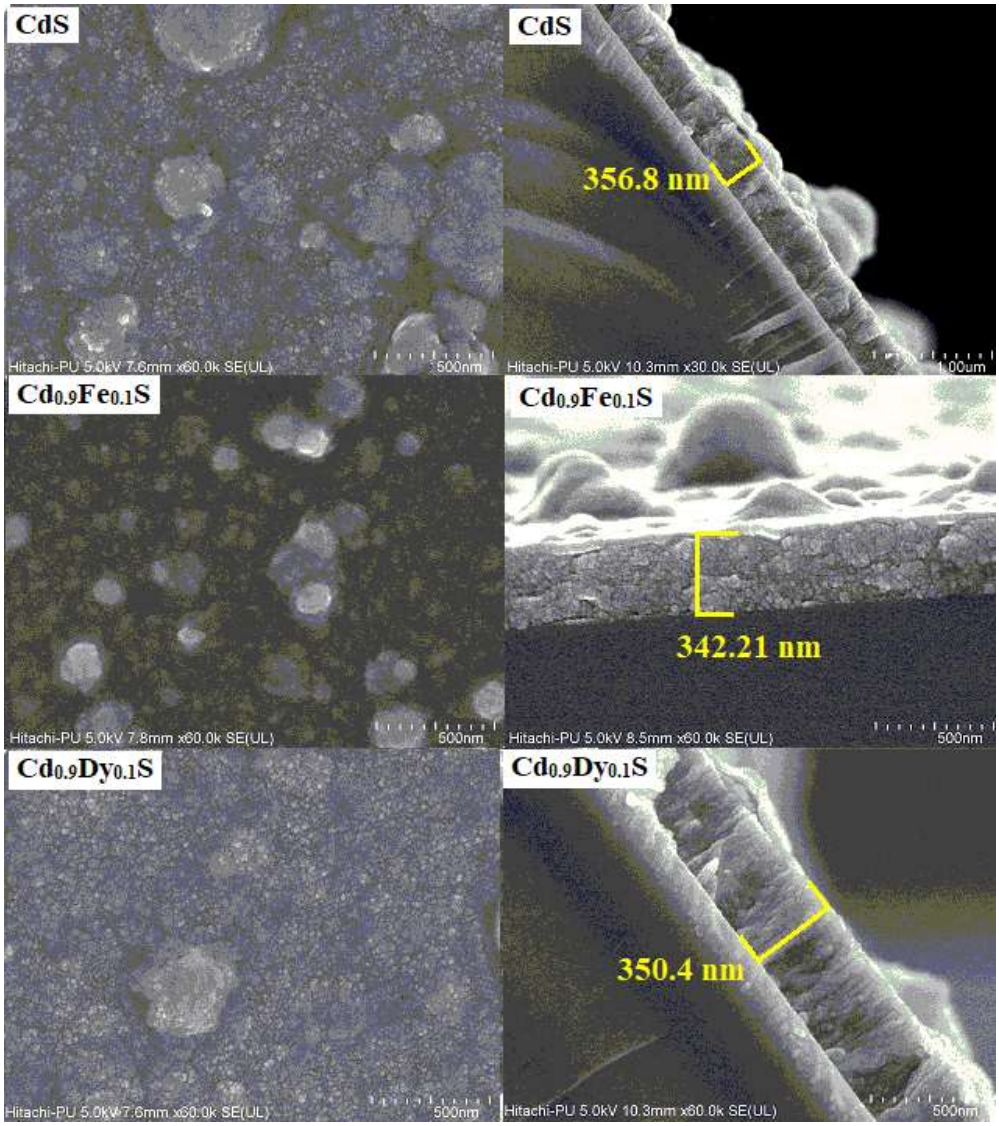

Fig. 4.30 Surface morphology and corresponding cross-section images of doped CdS films.

The surface of the films shows cluster formation due to agglomeration of constituent particles. The cross-sectional image of CdS films depicted in Fig. 4.30 shows an average thickness of ~350 ± 10 nm. For ZnS films (Fig. 4.31) average thickness is ~556.03 nm which increases to 664.25 nm with doping of Dy^{3+} that can be attributed to higher growth rate with Dy^{3+} substitution contrary to Fe^{3+} doping which reduces thickness to 440.06 nm.

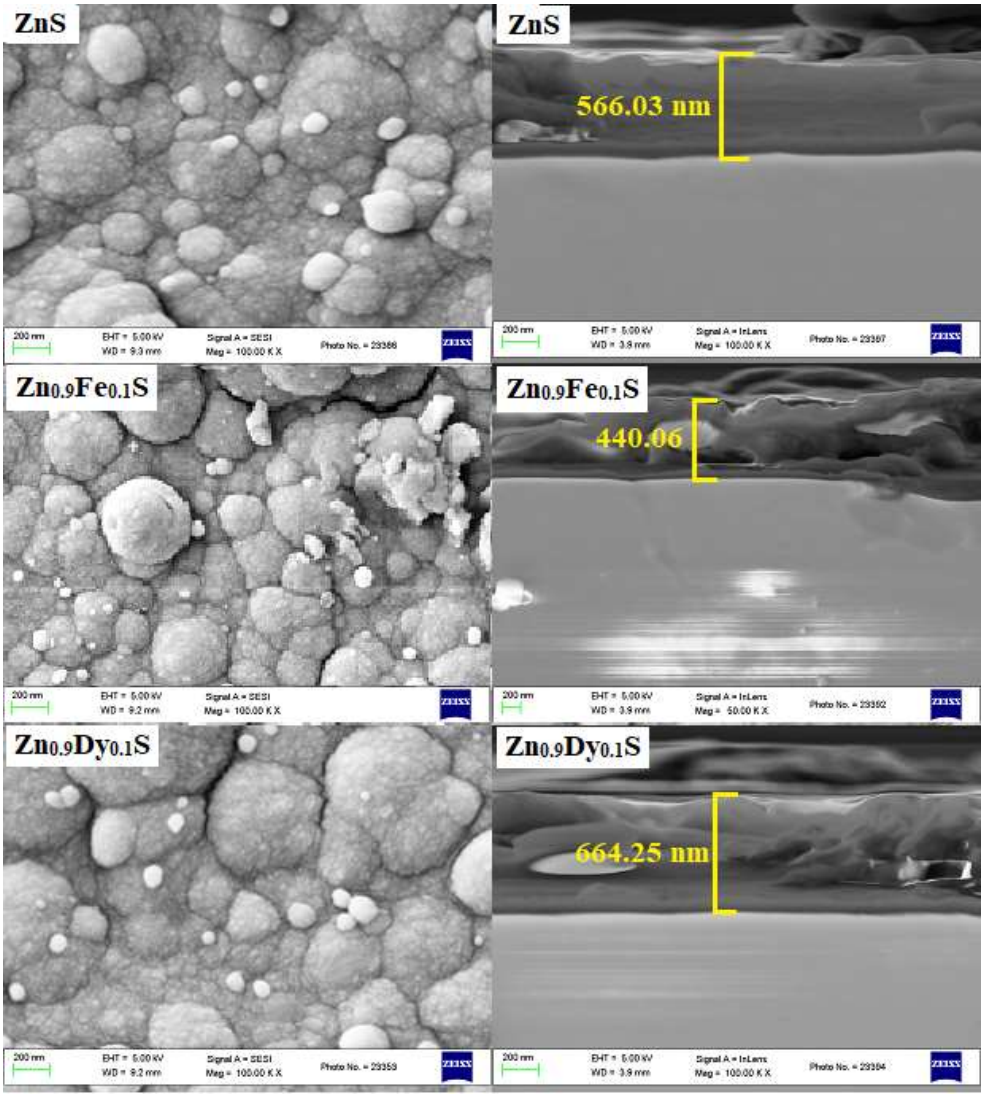

Fig. 4.31 Surface morphology and corresponding cross-section images of doped ZnS films.

The Fig. 4.32 represents AFM images ($10\times10\mu m^2$) of undoped and doped CdS and ZnS films. The image verifies the presence of agglomerated particles on surface of both CdS and ZnS films as observed in FESEM. The average root mean square roughness (S_q) found to decrease from 150.13 nm (CdS) to 116.38 nm (Fe^{3+}) and 135.20 nm (Dy^{3+}). Whereas for ZnS, S_q values are 117.87 nm (ZnS), 100.45 nm (Fe^{3+}) and 146.45 nm (Dy^{3+}).

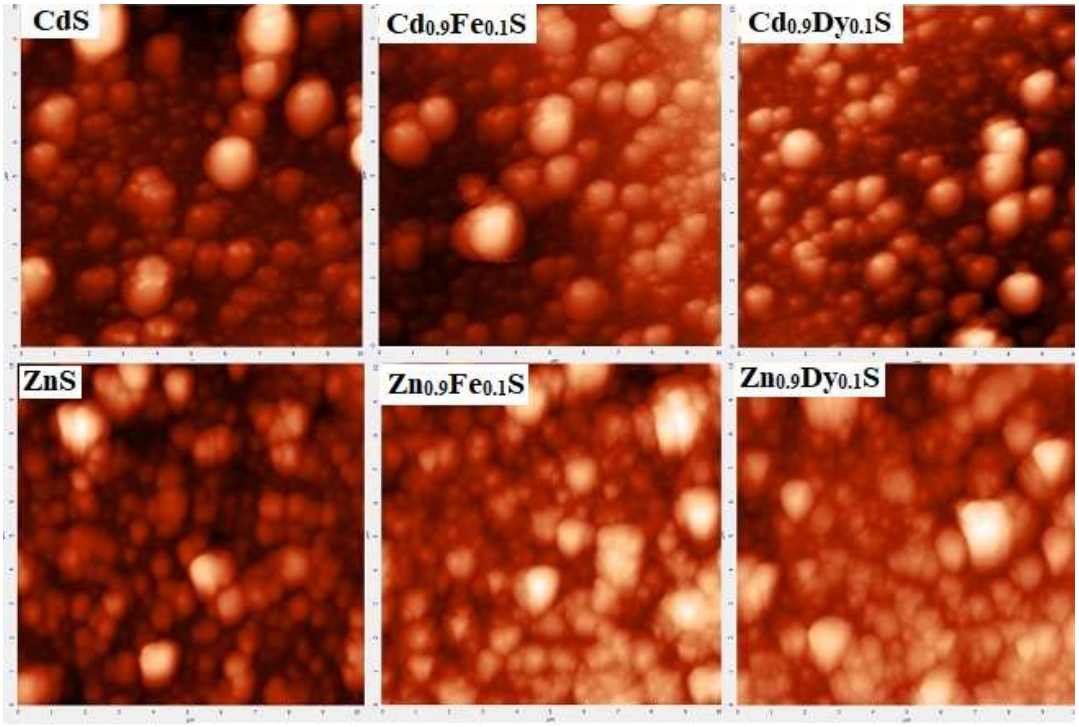

Fig. 4.32 AFM images of doped CdS and ZnS thin films.

4.4.1.3 Optical studies

The *UV*-visible absorption spectra of deposited films are shown in Fig. 4.33. The absorption edge found to shift with dopants indicating the change in optical E_g.

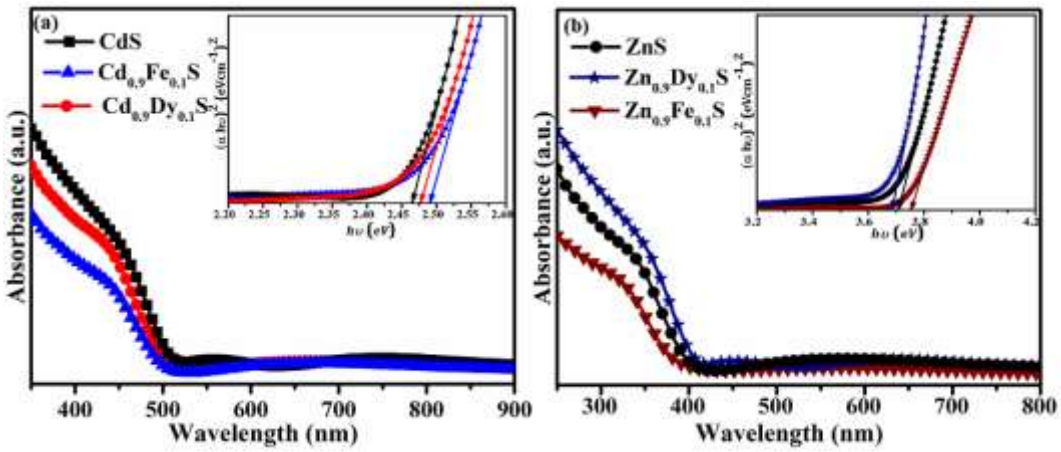

Fig. 4.33 *UV*-visible spectra of (a) CdS and (b) ZnS films. Inset depicts corresponding Tauc's plot.

The estimated E_g from Tauc's plot (Inset) are given in Table 4.11. A marginal increase in optical E_g from 2.46 eV to 2.49 eV (Fe^{3+}) and 2.47 eV (Dy^{3+}) has been observed for CdS films [246]. On contrary, nanoparticle at same doping content showed enhanced E_g. The

reason may ascribe to percentage reduction in crystallite size which is higher for doped nanoparticles as compared to films. The E_g of ZnS found to vary from 3.71 eV to 3.75 eV (Fe^{3+}) and 3.69 eV (Dy^{3+}). The obtained change in E_g with doping was similar to doped ZnS nanoparticles.

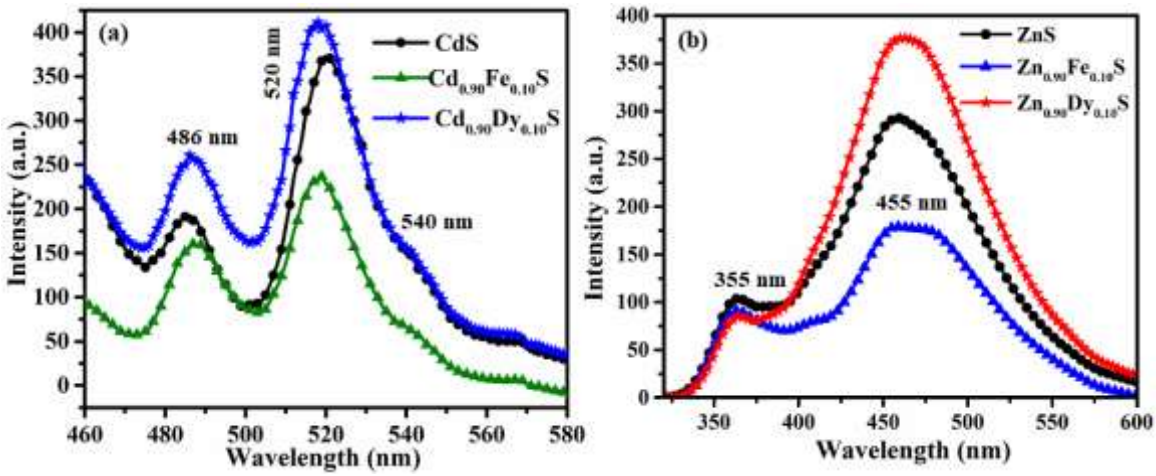

Fig. 4.34 PL spectra of (a) CdS and (b) ZnS films.

The representative PL spectra of doped CdS and ZnS films with excitation wavelength of 380 nm and 230 nm, respectively are shown in Fig. 4.34. Similar to CdS nanoparticles, the emission peaks at ~486 nm, 520 nm and 540 nm were obtained. The small hump at 571 nm as observed in CdS nanoparticles is absent. The emission spectra of ZnS films are different form nanoparticles. In nanoparticles, well distinguished peaks at 423 nm, 451 nm, 484 nm, 528 nm and 567 nm have been observed. Whereas, in films peaks appeared to get merged together in the form of one broad peak centered at 455 nm. This emission is due to transition of donor acceptor pair to valence band [154,247]. With Dy^{3+} doping the intensity of emission peak is relatively higher.

Chapter 5

Conclusions

Overview

In this chapter, the outcomes of the various experiments are summarized. The effects of annealing temperature on CdS and ZnS nanoparticles are outlined. Further, effect of *TM* (Fe^{3+}, Co^{2+}) and *RE* (Dy^{3+}, Tb^{3+}) doping on structural, optical and magnetic properties of CdS and ZnS nanoparticles/thin films are concluded and tabulated. Finally, the future scope of present work is given at the end of this chapter.

In the present work, CdS and ZnS nanoparticles were synthesized via hydrothermal method. The particle size variation in undoped CdS and ZnS was induced by annealing temperature. Thereafter, the series (x = 0, 0.05, 0.10 and 0.15) of *TM* (Fe^{3+}, Co^{2+}) and *RE* (Dy^{3+}, Tb^{3+}) doped CdS and ZnS nanoparticles were synthesized. At chosen doping concentration of x = 0.10, Fe^{3+} and Dy^{3+} doped CdS and ZnS thin films were deposited using chemical bath deposition technique. Effect of doping on structural, morphological, optical and magnetic properties were investigated and compared. The important findings and conclusions drawn from the work are as follows:

- Firstly, the synthesized CdS and ZnS nanoparticles were annealed in the temperature range of 200-400 °C. The XRD patterns confirmed wurtzite phase of CdS and cubic phase in ZnS nanoparticles. The marginal decrease in E_g has been observed with annealing. In PL spectra, emission intensities enhances with annealing ascribed to cluster formation. No major variation in magnetization was found with annealing.
- The XRD pattern confirmed wurtzite phase in *TM* doped CdS nanoparticles. The crystallite size of Fe^{3+} doped CdS (~11.50 nm) was relatively smaller than Co^{2+} doping (~13.88 nm). The TEM images confirmed spherical morphology with average particle size of 37.69 nm which found to decrease with *TM* doping. The E_g was increased from 2.48 eV to 2.56 eV (Fe^{3+}) and 2.53 eV (Co^{2+}). *M-H* loops confirm *RT* ferromagnetism in all the compositions with a maximum value of M_s (0.236 emu/g) in Fe^{3+} doped nanoparticles.
- The XRD pattern of Fe^{3+} and Co^{2+} doped ZnS nanoparticles confirmed cubic phase. The Fe^{3+} (~3.61 nm) doped nanoparticles have relatively smaller crystallite size as compared to Co^{2+} (3.90 nm) doped ZnS. The average size of ZnS spherical nanoparticles was ~ 6.77 nm that further reduces with Fe^{3+} and Co^{2+} doping. The optical E_g found to increase from 3.74 eV to 3.86 eV (Fe) and 3.82 eV (Co) with doping. *M-H* loops confirm *RT* ferromagnetism in all samples with a maximum M_s of 0.332emu/g for Fe^{3+} doped ZnS.

  This study revealed that Fe^{3+} doped CdS and ZnS nanoparticles showed enhanced optical and magnetic properties.
- The XRD patterns of Dy^{3+} and Tb^{3+} doped CdS nanoparticles confirmed wurtzite phase for all compositions. The crystallite size found to decrease from 29.67 nm to 19.91 nm with Dy^{3+} doping, whereas for Tb^{3+} doped nanoparticles it increases

to 35.65 nm. HR-TEM micrographs revealed the spherical morphology of the nanoparticles. The optical E_g enhanced from 2.48 eV to 2.55 eV with Dy^{3+} doping and it reduces to 2.42 eV for Tb^{3+} doped CdS. PL spectra exhibited enhanced emission peaks in blue, green and yellow region of visible spectra with Dy^{3+} and Tb^{3+} doping. The *M-H* loop of doped CdS nanoparticles showed enhanced magnetization with an evidence of paramagnetic contribution.

- Series of Dy^{3+} and Tb^{3+} doped ZnS nanoparticles exhibit cubic phase with spherical morphology. The crystallite size found to increase from 4.80 nm to 4.97 nm (Dy^{3+}) and 5.23 nm (Tb^{3+}) with doping. The optical E_g of Dy^{3+} doped (3.71 eV) ZnS was relatively higher than Tb^{3+} doped (3.96 eV). In PL spectra, emission intensities enhances with doping. *M-H* loops confirm *RT* ferromagnetism in all samples.
- The XRD pattern confirmed the wurtzite and cubic phase in CdS and ZnS thin films, respectively. The FESEM micrograph depicts that films are densely packed with the presence of clusters at surface. The thickness of CdS films found to be ~ 350 nm, whereas, ZnS film are ~ 556 nm thick. The highest E_g of 3.75 eV was obtained for Fe^{3+} doped ZnS thin film.

Table 5.1 Comparative properties of studied doped CdS and ZnS nanoparticles.

Doping Concentration (x)			Crystallite Size D *(nm)*	E_g (eV)	M_s (emu/g)
CdS	Undoped	0.0	29.67	2.48	0.049
	Fe	0.05	14.81	2.53	0.087
		0.10	13.80	2.55	0.108
		0.15	11.50	2.56	0.236
	Co	0.05	17.07	2.49	0.057
		0.10	15.53	2.51	0.072
		0.15	13.88	2.53	0.109
	Dy	0.05	22.14	2.54	0.080
		0.10	19.91	2.55	0.172
		0.15	25.80	2.49	0.068
	Tb	0.05	33.34	2.43	0.130
		0.10	35.65	2.42	0.230
		0.15	32.40	2.44	0.210
ZnS	Undoped	0.0	4.80	3.74	0.057
	Fe	0.05	4.08	3.80	0.112
		0.10	3.67	3.83	0.137
		0.15	3.61	3.86	0.322
	Co	0.05	4.25	3.77	0.090
		0.10	4.01	3.79	0.108
		0.15	3.90	3.82	0.290
	Dy	0.05	4.85	3.73	0.072
		0.10	4.92	3.72	0.084
		0.15	4.97	3.71	0.092
	Tb	0.05	5.17	3.71	0.061
		0.10	5.21	3.70	0.078
		0.15	5.23	3.69	0.083

Future Scope

The present study revealed that optical and magnetic properties are remarkably affected by *TM* and *RE* doping. An extensive investigation of various deposition conditions, different thickness and annealing temperature are required for *RE* and *TM* doped films. Moreover, these doped films must be explored as buffer layer of solar cells and sensors applications. In addition, the study can be extended to the co-doping of *TM* and *RE* doped CdS and ZnS nanostructures. The optical and magnetic properties of other nanostructures such as nanorods, nano tubes, nano wires and quantum dots of doped CdS and ZnS can also be carried out. The magnetic studies can be further explored by analysis at low as well as high temperatures.

References

[1] M. Riordan, L. Hoddeson, C. Herring, The invention of the transistor, Rev. Mod. Phys. 71 (1999). https://doi.org/10.1103/revmodphys.71.s336.

[2] A.A. Ojo, I.M. Dharmadasa, 15.3 % efficient graded bandgap solar cells fabricated using electroplated CdS and CdTe thin films, Sol. Energy. 136 (2016) 10–14. https://doi.org/10.1016/j.solener.2016.06.067.

[3] F. Li, C. Nie, L. You, X. Jin, Q. Zhang, Y. Qin, White light emitting device based on single-phase White light emitting device based on single- phase CdS quantum dots, Nanotechnology. 29 (2018).

[4] Y. Liu, K. Ai, Q. Yuan, L. Lu, Fluorescence-enhanced gadolinium-doped zinc oxide quantum dots for magnetic resonance and fluorescence imaging, Biomaterials. 32 (2011) 1185–1192. https://doi.org/10.1016/j.biomaterials.2010.10.022.

[5] S. Das Sarma, E.H. Hwang, A. Kaminski, How to make semiconductors ferromagnetic : a first course on spintronics, Solid State Commun. 127 (2003) 99–107. https://doi.org/10.1016/S0038-1098(03)00337-5.

[6] C. Soci, A. Zhang, B. Xiang, S.A. Dayeh, D.P.R. Aplin, J. Park, X.Y. Bao, Y.H. Lo, D. Wang, ZnO nanowire UV photodetectors with high internal gain, Nano Lett. 7 (2007) 1003–1009. https://doi.org/10.1021/nl070111x.

[7] S.S. Ghosh, C. Choubey, A. Sil, Photocatalytic response of Fe, Co, Ni doped ZnO based diluted magnetic semiconductors for spintronics applications., Superlattices Microstruct. 125 (2019) 271–280. https://doi.org/10.1016/j.spmi.2018.10.028.

[8] I. Zutic, J. Fabian, S. Das Sarma, Spintronics : Fundamentals and applications, Rev. Mod. Phys. 76 (2004) 323–410.

[9] T.L. Chu, S.S. Chu, Thin film II-VI photovoltaics, Solid State Electron. 38 (1995) 533–549. https://doi.org/10.1016/0038-1101(94)00203-R.

[10] K. Pinardi, U. Jain, S.C. Jain, H.E. Maes, R. Van Overstraeten, M. Willander, Critical thickness and strain relaxation in lattice mismatched II-VI semiconductor layers, J. Appl. Phys. 83 (1998) 4724–4733. https://doi.org/10.1063/1.367261.

[11] K.V.R.M. Murali, V.B. Naik, D. Datta, Gallium-Nitride-Based Light-Emitting Diodes, Resonance. 20 (2015) 605–616.

[12] T. Zhai, X. Fang, H. Zeng, X. Xu, Y. Bando, D. Golberg, Vapor-phase synthesis of one-dimensional ZnS, CdS, and $Zn_xCd_{1-x}S$ nanostructures, Pure Appl. Chem. 82

(2010) 2027–2053. https://doi.org/10.1351/PAC-CON-09-09-18.

[13] Adlim, Review: Preparations and Application of Metal Nanoparticles., Indo. J. Chem. 6 (2006) 1–10.

[14] C. Liu, F. Yun, H. Morkoc, Ferromagnetism of ZnO and GaN : A Review, J. Mater. Sci. Mater. Electron. 16 (2005) 555–597.

[15] J.K. Furdyna, Diluted magnetic semiconductors: Issues and opportunities, J. Vac. Sci. Technol. A. 4 (1986) 2002–2009. https://doi.org/10.1116/1.574016.

[16] C. Zener, Interaction between the d shells in the transition metals, Phys. Rev. 81 (1951) 440–444. https://doi.org/10.1103/PhysRev.81.440.

[17] T. Dietl, Zener Model Description of Ferromagnetism in Zinc-Blende Magnetic Semiconductors, 1019 (2012). https://doi.org/10.1126/science.287.5455.1019.

[18] M.A. Ruderman, C. Kittel, Indirect exchange coupling of nuclear magnetic moments by conduction electrons, Phys. Rev. 96 (1954) 99–102. https://doi.org/10.1103/PhysRev.96.99.

[19] K. Yosida, Magnetic properties of Cu-Mn alloys, Phys. Rev. 106 (1957) 893–898. https://doi.org/10.1103/PhysRev.106.893.

[20] T. Kasuya, A Theory of Metallic Ferro- and Antiferromagnetism on Zener's Model, Prog. Theor. Phys. 16 (1956) 45–57. https://doi.org/10.1143/ptp.16.45.

[21] T. Story, R.R. Gafqzka, R.B. Frankel, P.A. Wolff, Carrier-Concentration-Induced Ferromagnetism in PbSnMnTe, Phys. Rev. Lett. 56 (1986) 7–9.

[22] R. Singh, Unexpected magnetism in nanomaterials, J. Magn. Magn. Mater. 346 (2013) 58–73. https://doi.org/10.1016/j.jmmm.2013.07.005.

[23] K. Sato, H. Katayama-Yoshida, Material design for transparent ferromagnets with ZnO-based magnetic semiconductors, Japanese J. Appl. Physics, Part 2 Lett. 39 (2000) 555–558. https://doi.org/10.1143/jjap.39.l555.

[24] A.C. Durst, A.C. Durst, R.N. Bhatt, P.A. Wolff, Bound magnetic polaron interactions in insulating doped diluted magnetic semiconductors, Phys. Rev. B - Condens. Matter Mater. Phys. 65 (2002) 2352051–23520510. https://doi.org/10.1103/PhysRevB.65.235205.

[25] T. Dietl, F. Matsukura, F. Matsukura, H. Ohno, Ferromagnetism of magnetic semiconductors: Zhang-Rice limit, Phys. Rev. B - Condens. Matter Mater. Phys. 66 (2002) 332031–332034. https://doi.org/10.1103/PhysRevB.66.033203.

[26] J.M.D. Coey, M. Venkatesan, C.B. Fitzgerald, Donor impurity band exchange in dilute ferromagnetic oxides, Nat. Mater. 4 (2005) 173–179.

https://doi.org/10.1038/nmat1310.

[27] M. van Schilfgaarde, O.N. Mryasov, Anomalous exchange interactions in III-V dilute magnetic semiconductors, Phys. Rev. B - Condens. Matter Mater. Phys. 63 (2001) 2–5. https://doi.org/10.1103/PhysRevB.63.233205.

[28] J. Cui, U. Gibson, Thermal modification of magnetism in cobalt-doped ZnO nanowires grown at low temperatures, Phys. Rev. B - Condens. Matter Mater. Phys. 74 (2006) 1–8. https://doi.org/10.1103/PhysRevB.74.045416.

[29] T. Dietl, Origin of ferromagnetic response in diluted magnetic semiconductors and oxides, J. Phys. Condens. Matter. 19 (2007). https://doi.org/10.1088/0953-8984/19/16/165204.

[30] S.A. Wolf, D.D. Awschalom, R.A. Buhrman, J.M. Daughton, S. Von Molnár, M.L. Roukes, A.Y. Chtchelkanova, D.M. Treger, Spintronics: A spin-based electronics vision for the future, Science (80). 294 (2001) 1488–1495. https://doi.org/10.1126/science.1065389.

[31] A. Fert, Nobel lecture: Origin, development, and future of spintronics nobel lecture: Origin, development, and future of spintronics, Rev. Mod. Phys. 80 (2008) 1517–1530. https://doi.org/10.1103/RevModPhys.80.1517.

[32] E.E. Fullerton, I.K. Schuller, The 2007 nobel prize in physics: Magnetism and transport at the nanoscale, ACS Nano. 1 (2007) 384–389. https://doi.org/10.1021/nn700422j.

[33] T. Arai, S.I. Senda, Y. Sato, H. Takahashi, K. Shinoda, B. Jeyadevan, K. Tohji, Cu-doped ZnS hollow particle with high activity for hydrogen generation from alkaline sulfide solution under visible light, Chem. Mater. 20 (2008) 1997–2000. https://doi.org/10.1021/cm071803p.

[34] J. Kundu, B.K. Satpathy, D. Pradhan, Composition-Controlled CdS/ZnS Heterostructure Nanocomposites for Efficient Visible Light Photocatalytic Hydrogen Generation, Ind. Eng. Chem. Res. 58 (2019) 22709–22717. https://doi.org/10.1021/acs.iecr.9b03764.

[35] S. Premkumar, D. Nataraj, G. Bharathi, S. Ramya, T.D. Thangadurai, Highly Responsive Ultraviolet Sensor Based on ZnS Quantum Dot Solid with Enhanced Photocurrent, Sci. Rep. 9 (2019) 1–14. https://doi.org/10.1038/s41598-019-55097-8.

[36] V.A. Ivanov, Diluted Magnetic Semiconductors and Spintronics, Bull. Russ. Acad. Sci. Phys. 71 (2007) 1651–1653. https://doi.org/10.3103/S1062873807110433.

[37] J.A. Gaj, Semimagnetic Semiconductors, ACTA Phys. Pol. A. 96 (1999) 95–124. https://doi.org/10.1016/B978-0-44-453153-7.00064-X.

[38] A. Ranzoni, M.A. Cooper, The Growing Influence of Nanotechnology in Our Lives, Elsevier Inc., 2017. https://doi.org/10.1016/B978-0-323-39981-4.00001-4.

[39] L. Yujie, Y. Liping, Synthesis of CdS nanowire networks and their optical and electrical properties, Nanotechnology. 18 (2007). https://doi.org/10.1088/0957-4484/18/20/205605.

[40] Y. Yang, J. Huang, J. Shen, Preparation , characterization and electroluminescence of ZnS nanocrystals in a polymer matrix, J. Mater. Chem. 7 (1997) 131–133.

[41] K. Matsune, H. Oda, T. Toyama, 15 % Efficiency CdS/CdTe thin film solar cells using CdS layers doped with metal organic compounds, Sol. Energy Mater. Sol. Cells. 90 (2006) 3108–3114. https://doi.org/10.1016/j.solmat.2006.06.030.

[42] D.U. Saenger, G. Jung, M. Mennig, Optical and Structural Properties of Doped ZnS Nanoparticles Produced by the Sol-Gel Method, 639 (1998) 635–639.

[43] H. Villavicencio, O. Sanchez, Hydrothermal growth of CdS and ZnS Nanoparticles in MOR-type zeolites, (2001) 101–104.

[44] B.S. Rao, B.R. Kumar, V.R. Reddy, T.S. Rao, Preparation and characterization of cds nanoparticles by chemical co-precipitation technique, Chalcogenide Lett. 8 (2011) 177–185.

[45] A.I. Iorgu, D. Berger, L. Alexandrescu, B.S. Vasile, C. Matei, Synthesis of Photoluminescent pure and doped cadmium sulfide by reverse Microemulsion method, Chalcogenide Lett. 10 (2013) 525–531.

[46] A.H. Davis, E. Hofman, K. Chen, Z.J. Li, A. Khammang, H. Zamani, J.M. Franck, M.M. Maye, R.W. Meulenberg, W. Zheng, Exciton Energy Shifts and Tunable Dopant Emission in Manganese-Doped Two-Dimensional CdS/ZnS Core/Shell Nanoplatelets., Chem. Mater. 31 (2019) 2516–2523. https://doi.org/10.1021/acs.chemmater.9b00006.

[47] S. Aksu, E. Bacaksiz, M. Parlak, S. Yılmaz, I. Polat, M. Altunbas, M. Türksoy, R. Topkaya, Structural, optical and magnetic properties of Mn diffusion-doped CdS thin films prepared by vacuum evaporation, Mater. Chem. Phys. 130 (2011) 340–345. https://doi.org/10.1016/j.matchemphys.2011.06.046.

[48] M.A. Islam, F. Haque, K.S. Rahman, N. Dhar, M.S. Hossain, Y. Sulaiman, N. Amin, Effect of oxidation on structural , optical and electrical properties of CdS thin films grown by sputtering, Opt. - Int. J. Light Electron Opt. 126 (2015) 3177–

3180. https://doi.org/10.1016/j.ijleo.2015.07.078.

[49] N. Badera, B. Godbole, S.B. Srivastava, P.N. Vishwakarma, L.S.S. Chandra, D. Jain, M. Gangrade, T. Shripathi, V.G. Sathe, V. Ganesan, Quenching of photoconductivity in Fe doped CdS thin films prepared by spray pyrolysis technique, Appl. Surf. Sci. 254 (2008) 7042–7048. https://doi.org/10.1016/j.apsusc.2008.05.218.

[50] M. Muthusamy, S. Muthukumaran, Effect of Cu-doping on structural, optical and photoluminescence properties of CdS thin films, Opt.- Int. J. Light Electron Opt. 126 (2015) 5200–5206. https://doi.org/10.1016/j.ijleo.2015.09.186.

[51] J. Nishino, S. Chatani, Y. Uotani, Y. Nosaka, Electrodeposition method for controlled formation of CdS films from aqueous solutions, J. Electroanal. Chem. 473 (1999) 217–222. https://doi.org/10.1016/S0022-0728(99)00250-8.

[52] M.L. Huggins, Evidence from crystal structures in regard to atomic structures, Phys. Rev. 27 (1926) 286–297. https://doi.org/10.1103/PhysRev.27.286.

[53] A.N. Goldstein, C.M. Echer, A.P. Alivisatos, Melting in semiconductor nanocrystals, Science (80). 256 (1992) 1425–1427. https://doi.org/10.1126/science.256.5062.1425.

[54] C.C. Chen, A.B. Herhold, C.S. Johnson, A.P. Alivisatos, Size dependence of structural metastability in semiconductor nanocrystals, Science (80) 276 (1997) 398–401. https://doi.org/10.1126/science.276.5311.398.

[55] W. Qingqing, X. Gang, H. Gaorong, Solvothermal synthesis and characterization of uniform CdS nanowires in high yield, J. Solid State Chem. 178 (2005) 2680–2685. https://doi.org/10.1016/j.jssc.2005.06.005.

[56] R.S. Ganesh, S.K. Sharma, E. Durgadevi, M. Navaneethan, H.S. Binitha, S. Ponnusamy, C. Muthamizhchelvan, Y. Hayakawa, D.Y. Kim, Surfactant free synthesis of CdS nanospheres, microstructural analysis, chemical bonding, optical properties and photocatalytic activities, Superlattices Microstruct. 104 (2017) 247–257. https://doi.org/10.1016/j.spmi.2017.02.029.

[57] Q. Pan, K. Huang, S. Ni, Q. Wang, F. Yang, D. He, Fabrication and photoluminescence properties of large-scale hierarchical CdS dendrites, Mater. Lett. 61 (2007) 4773–4776. https://doi.org/10.1016/j.matlet.2007.03.025.

[58] Y.D. Li, H.W. Liao, Y. Ding, Y.T. Qian, L. Yang, G.E. Zhou, Nonaqueous Synthesis of CdS Nanorod Semiconductor, Chem. Mater. 10 (1998) 2301–2303. https://doi.org/10.1021/cm970789l.

[59] N. Zhang, X. Ma, J. Han, S. Ruan, Y. Chen, H. Zhang, C. Li, Synthesis of sea urchin-like microsphere of CdS and its gas sensing properties, Mater. Sci. Eng. B Solid-State Mater. Adv. Technol. 243 (2019) 206–213. https://doi.org/10.1016/j.mseb.2019.04.006.

[60] B. Ahmed, S. Kumar, S. Kumar, A.K. Ojha, Shape induced (spherical, sheets and rods) optical and magnetic properties of CdS nanostructures with enhanced photocatalytic activity for photodegradation of methylene blue dye under ultra-violet irradiation, J. Alloys Compd. 679 (2016) 324–334. https://doi.org/10.1016/j.jallcom.2016.03.295.

[61] Y. Al-Douri, A.A. Odeh, Y.A. Wahab, C.H. Voon, Correlation Between Magnetization and Particle Size of CdS Nanostructures by Solvothermal Method, J. Supercond. Nov. Magn. 32 (2019) 283–289. https://doi.org/10.1007/s10948-018-4947-6.

[62] L. Meng, J.M.D. Lane, L. Baca, J. Tafoya, T. Ao, B. Stoltzfus, M. Knudson, D. Morgan, K. Austin, C. Park, P. Chow, Y. Xiao, R. Li, Y. Qin, H. Fan, Shape Dependence of Pressure-Induced Phase Transition in CdS Semiconductor Nanocrystals., J. Am. Chem. Soc. 142 (2020) 6505–6510. https://doi.org/10.1021/jacs.0c01906.

[63] R. Banerjee, R. Jayakrishnan, P. Ayyub, Effect of the size-induced structural transformation on the band gap in CdS nanoparticles, J. Phys. Condens. Matter. 12 (2000) 10647–10654. https://doi.org/10.1088/0953-8984/12/50/325.

[64] M.F. Kotkata, A.E. Masoud, M.B. Mohamed, E.A. Mahmoud, Synthesis and structural characterization of CdS nanoparticles, Phys. E Low-Dimensional Syst. Nanostructures. 41 (2009) 1457–1465. https://doi.org/10.1016/j.physe.2009.04.020.

[65] V. Sivasubramanian, A.K. Arora, M. Premila, C.S. Sundar, V.S. Sastry, Optical properties of CdS nanoparticles upon annealing, Phys. E Low-Dimensional Syst. Nanostructures. 31 (2006) 93–98. https://doi.org/10.1016/j.physe.2005.10.001.

[66] J. Zhang, L. Sun, C. Liao, C. Yan, Size control and photoluminescence enhancement of CdS nanoparticles prepared via reverse micelle method, 124 (2002) 45–48.

[67] V. Singh, P.K. Sharma, P. Chauhan, Synthesis of CdS nanoparticles with enhanced optical properties, Mater. Charact. 62 (2010) 43–52. https://doi.org/10.1016/j.matchar.2010.10.009.

[68] Z.K. Heiba, M.B. Mohamed, N.G. Imam, Structural tuning of CdS nanoparticles with nucleation temperature and its reflection on the optical properties, J. Mol. Struct. 1094 (2015) 91–97. https://doi.org/10.1016/j.molstruc.2015.04.003.

[69] M. Muthusamy, Muthukumaran, Effect of deposition time on optical, structural and photoluminescence properties of $Cd_{0.6}Co_{0.4}$ S thin films by chemical bath deposition method, (2013) 2277–2286. https://doi.org/10.1007/s10854-013-1090-9.

[70] S. Butt, N. Abbas, A. Nazir, Z. Ali, A. Maqsood, Influence of film thickness and In-doping on physical properties of CdS thin films, J. Alloys Compd. 587 (2014) 582–587. https://doi.org/10.1016/j.jallcom.2013.10.221.

[71] S. Rondiya, A. Rokade, B. Gabhale, S. Pandharkar, Effect of bath temperature on optical and morphology properties of CdS thin films grown by chemical bath deposition, Energy Procedia. 110 (2017) 202–209. https://doi.org/10.1016/j.egypro.2017.03.128.

[72] K.G. Barraclough, A. Meyer, H. Schafer, L. Treitincer, Preparation , Electrical and Magnetic Properties of Cd_{1-x} $Fe_xCr_2S_4$ Single Crystals, Phys. Stat. Sol. 22 (1974).

[73] S. Chandramohan, A. Kanjilal, S.N. Sarangi, S. Majumder, R. Sathyamoorthy, T.Som, Effect of Fe-ion implantation doping on structural and optical properties of CdS thin films, Appl Phys A. 99 (2010) 837–842. https://doi.org/10.1007/s00339-010-5598-z.

[74] K. Liu, J.Y. Zhang, X. Wu, B. Li, B. Li, Y. Lu, X. Fan, D. Shen, Fe-doped and (Zn, Fe) co-doped CdS films:Could the Zn doping affect the concentration of Fe^{2+} and the optical properties?, Phys. B. 389 (2007) 248–251. https://doi.org/10.1016/j.physb.2006.06.157.

[75] B. Tripathi, F. Singh, D.K. Avasthi, A.K. Bhati, D. Das, Y.K. Vijay, Structural , optical , electrical and positron annihilation studies of CdS:Fe system, J. Alloys Compd. 454 (2008) 97–101. https://doi.org/10.1016/j.jallcom.2007.01.016.

[76] M. Thambidurai, N. Muthukumarasamy, S. Agilan, N. Murugan, N.S. Arul, S. Vasantha, R. Balasundaraprabhu, Studies on optical absorption and structural properties of Fe doped CdS quantum dots, Solid State Sci. 12 (2010) 1554–1559. https://doi.org/10.1016/j.solidstatesciences.2010.06.020.

[77] M. Thambidurai, N. Muthukumarasamy, D. Velauthapillai, S. Agilan, Structural , Optical , and Electrical Properties of Cobalt-Doped CdS Quantum Dots, 41 (2012). https://doi.org/10.1007/s11664-012-1900-5.

[78] M. Thambidurai, N. Muthukumarasamy, D. Velauthapillai, N. Murugan, J.

Chaudhuri, S. Parameswaran, A. Marathe, S. Agilan, R. Balasundaraprabhu, Effect of Cr-doping on the structural and optical properties of CdS nanoparticles prepared by chemical precipitation method, (2012) 618–624. https://doi.org/10.1007/s10854-011-0454-2.

[79] H. Sekhar, D.N. Rao, Spectroscopic studies on Fe^{3+} doped CdS nanopowders prepared by simple coprecipitation method, J. Alloys Compd. 517 (2012) 103–110. https://doi.org/10.1016/j.jallcom.2011.12.039.

[80] N. Jeevanantham, O.N. Balasundaram, High-performance visible light photocatalytic activity of cobalt (Co) doped CdS nanoparticles by wet chemical route, J. Iran. Chem. Soc. 16 (2019) 243–251. https://doi.org/10.1007/s13738-018-1499-4.

[81] G. Murali, D.A. Reddy, B. Poornaprakash, R.P. Vijayalakshmi, B.K. Reddy, R. Venugopal, Room temperature magnetism of Fe doped CdS nanocrystals, Phys. B Phys. Condens. Matter. 407 (2012) 2084–2088. https://doi.org/10.1016/j.physb.2012.02.011.

[82] G. Murali, D.A. Reddy, G. Giribabu, R.P. Vijayalakshmi, R. Venugopal, Room temperature ferromagnetism in Mn doped CdS nanowires, J. Alloys Compd. 581 (2013) 849–855. https://doi.org/10.1016/j.jallcom.2013.08.004.

[83] A. Nag, S. Sapra, C. Nagamani, A. Sharma, N. Pradhan, S. V. Bhat, D.D. Sarma, A study of Mn^{2+} doping in CdS nanocrystals, Chem. Mater. 19 (2007) 3252–3259. https://doi.org/10.1021/cm0702767.

[84] G. Giribabu, G. Murali, D.A. Reddy, C. Liu, R.P. Vijayalakshmi, Structural, optical and magnetic properties of Co doped CdS nanoparticles, J. Alloys Compd. (2013). https://doi.org/10.1016/j.jallcom.2013.07.082.

[85] G. Giribabu, G. Murali, R.P. Vijayalakshmi, Structural, magnetic and optical properties of cobalt and manganese codoped CdS nanoparticles, Mater. Lett. 117 (2014) 298–301. https://doi.org/10.1016/j.matlet.2013.12.024.

[86] P. Elavarthi, A. Anil, G. Murali, D.A. Reddy, K.R. Gunasekhar, Room temperature ferromagnetism and white light emissive CdS : Cr nanoparticles synthesized by chemical co-precipitation method, J. Alloys Compd. 656 (2016) 510–517. https://doi.org/10.1016/j.jallcom.2015.09.244.

[87] R. Sathyamoorthya, P. Sudhagara, A. Balernab, C. Balasubramanianc, S. Belluccib, A.I. Popovd, K. Asokanf, Surfactant-assisted synthesis of $Cd_{1-x}Co_xS$ nanocluster alloys and their structural, optical and magnetic properties, J. Alloys

Compd. 493 (2010) 240–245.

[88] L. Saravanan, A. Pandurangan, R. Jayavel, Synthesis of cobalt-doped cadmium sulphide nanocrystals and their optical and magnetic properties, J Nanopart Res.13 (2011) 1621–1628. https://doi.org/10.1007/s11051-010-9915-4.

[89] T. Lavanya, K. Satheesh, N. V Jaya, Ferromagnetic behaviour at room temperature of Co doped CdS nanoparticles by chemical precipitation method : Synthesis , optical and electrical properties, IOP Conf. Ser. Mater. Sci. Eng. 73 (2015). https://doi.org/10.1088/1757-899X/73/1/012114.

[90] K. Kaur, G.S. Lotey, N.K. Verma, Optical and magnetic properties of Fe-doped CdS dilute magnetic semiconducting nanorods, (2014) 2605–2610. https://doi.org/10.1007/s10854-014-1918-y.

[91] A. Ghosh, S. Paul, S. Raj, High-temperature ferromagnetism in Fe-doped wurtzite and zincblende CdS nanoparticles, Phys. Status Solidi B. 1362 (2015) 1355–1362. https://doi.org/10.1002/pssb.201451524.

[92] A. Ghosh, S. Paul, S. Raj, Magnetic properties of zinc-blende $Cd_{1-x}Fe_xS$ nanoparticles Temperature and Fe-content dependence studies, J. Magn. Magn. Mater. 405 (2016) 238–243.

[93] S. Muruganandam, G. Anbalagan, G. Murugadoss, Optical, electrochemical and thermal properties of Co^{2+}-doped CdS nanoparticles using polyvinylpyrrolidone, Appl Nanosci. 5 (2015) 245–253. https://doi.org/10.1007/s13204-014-0313-6.

[94] N.H. Patel, M.P. Deshpande, S.H. Chaki, Study on structural, magnetic properties of undoped and Ni doped CdS nanoparticles, Mater. Sci. Semicond. Process. 31 (2015) 272–280. https://doi.org/10.1016/j.mssp.2014.11.039.

[95] N.H. Patel, M.P.D.S.H. Chaki, Influence of Co-doping on the optical and magnetic properties of CdS nanoparticles, J. Mater. Sci. Mater. Electron. 0 (2018) 0. https://doi.org/10.1007/s10854-018-9230-x.

[96] M. Bernadette, A. Leena, K. Raji, Room Temperature Ferromagnetism in Fe Doped CdS and Cobalt Doped CdS Nano Particles, Mater. Today Proc. 8 (2019) 362–370. https://doi.org/10.1016/j.matpr.2019.02.124.

[97] F. Ibraheem, M.A. Mahdy, E.A. Mahmoud, J.E. Ortega, C. Rogero, I.A. Mahdy, A. El-sayed, Tuning Paramagnetic effect of Co-Doped CdS diluted magnetic semiconductor quantum dots, J. Alloys Compd. 834 (2020) 155196. https://doi.org/10.1016/j.jallcom.2020.155196.

[98] S. Khajuria, S. Sanotra, J. Ladol, H. Nawaz, Synthesis, characterization and optical

properties of cobalt and lanthanide doped CdS nanoparticles, J. Mater. Sci. Mater. Electron. 26 (2015) 7073–7080. https://doi.org/10.1007/s10854-015-3328-1.

[99] Z. Zhang, L. Han, G. Xie, Q. Liao, B. Zhong, Room-temperature ferromagnetic and optical properties of Cr-doped CdS nanoparticles via a solvothermal preparation, J. Mater. Sci. Mater. Electron. 27 (2016) 12940–12946. https://doi.org/10.1007/s10854-016-5432-2.

[100] B.S. Rao, B.R. Kumar, V.R. Reddy, T.S. Rao, G.V. Chalapathi, Influence on optical properties of nickel doped cadmium sulfide, Chalcogenide Lett. 8 (2011) 39–44.

[101] A. Firdous, D.Singh, M.M. Ahmad, Electrical and optical studies of pure and Ni-doped CdS quantum dots, Appl Nanosci (2013) 13–18. https://doi.org/10.1007/s13204-012-0065-0.

[102] I.F. Ertis, I. Boz, Synthesis and Characterization of Metal-Doped (Ni, Co, Ce, Sb) CdS Catalysts and Their Use in Methylene Blue Degradation under Visible Light Irradiation, Mod. Res. Catal. 6 (2017) 1–14. https://doi.org/10.4236/mrc.2017.61001.

[103] H. Pan, Y.P. Feng, Q.Y. Wu, Z.G. Huang, J. Lin, Magnetic properties of carbon doped CdS: A first-principles and Monte Carlo study, Phys. Rev. B. 77 (2008) 3–6. https://doi.org/10.1103/PhysRevB.77.125211.

[104] K.A. Bogle, S. Ghosh, S.D. Dhole, V.N. Bhoraskar, L. Fu, M. Chi, N.D. Browning, D. Kundaliya, G.P. Das, O. B, Co:CdS Diluted Magnetic Semiconductor Nanoparticles: Radiation Synthesis , Dopant - Defect Complex Formation, and Unexpected Magnetism, Chem. Mater. 20 (2008) 440–446.

[105] T. Hu, M. Zhang, S. Wang, Q. Shi, G. Cui, S. Sun, CdS:Co diluted magnetic semiconductor nanocrystals: Synthesis and ferromagnetism study, Cryst. Eng. Comm. 13 (2011) 5646–5649. https://doi.org/10.1039/c1ce05593c.

[106] Y. Han, C. Yang, Y. Sun, M. Wang, X. Ma, The novel optical properties of CdS caused by concentration of impurity Co, J. Alloys Compd. 585 (2014) 503–509. https://doi.org/10.1016/j.jallcom.2013.09.198.

[107] R. Iqbal, I. Khan, H.A.R. Aliabad, Z. Ali, I. Ahmad, Density functional studies of magneto-optic properties of CdCoS, J. Magn. Magn. Mater. 351 (2014) 60–64. https://doi.org/10.1016/j.jmmm.2013.09.016.

[108] W. Benstaali, S. Bentata, H.A. Bentounes, A. Abbad, B. Bouadjemi, Materials Science in Semiconductor Processing Influence of Ni–Ni separation on the

optoelectronic and magnetic properties of Ni-doped cubic cadmium sulphide, Mater. Sci. Semicond. Process. 17 (2014) 53–58. https://doi.org/10.1016/j.mssp.2013.08.007.

[109] P. Li, C. Zhang, J. Lian, S. Gao, X. Wang, First-principles study on electronic and magnetic properties of Cu-doped CdS, Solid State Commun. 151 (2011) 1712–1715. https://doi.org/10.1016/j.ssc.2011.07.042.

[110] C. Tiseanu, R.K. Mehra, R. Kho, M. Kumke, Comparative Study of Time-Resolved Photoluminescence Properties of Terbium-Doped Thiosalicylic-Capped CdS and ZnS Nanocrystals, J. Phys. Chem. 107 (2003) 12153–12160. https://doi.org/10.1021/jp035322e.

[111] P. V Jyothy, K.A. Amrutha, J. Gijo, Fluorescence Enhancement in Tb^{3+}/ CdS Nanoparticles Doped Silica Xerogels, J Fluoresc. (2009) 165–168. https://doi.org/10.1007/s10895-008-0398-y.

[112] S. Rai, L. bokatial Effect of CdS nanoparticles on photoluminescence spectra of Tb^{3+} in sol–gel-derived silica glasses, Bull. Mater. Sci. 34 (2011) 227-231.

[113] P. V Jyothy, K.A. Amrutha, J. Xavier, N.V.Ã. Unnikrishnan, Journal of Physics and Chemistry of Solids Fluorescence characteristics of Dy^{3+}/ CdS nanocrystals doped silica xerogel, J. Phys. Chem. Solids. 70 (2009) 927–930. https://doi.org/10.1016/j.jpcs.2009.04.017.

[114] Y. Hanifehpour, N. Hamnabard, B. Mirtamizdoust, S.W. Joo, Sonochemical Synthesis , Characterization and Sonocatalytic Performance of Terbium-Doped CdS Nanoparticles Sonochemical Synthesis, Characterization and Sonocatalytic, J. Inorg. Organomet. Polym. Mater. (2016). https://doi.org/10.1007/s10904-016-0352-4.

[115] R. Jayavel, Synthesis and luminescence enhancement of Cerium doped CdS nanoparticles, Mater. Lett. 66 (2012) 343–345. https://doi.org/10.1016/j.matlet.2011.09.006.

[116] L. Saravanan, R. Jayavel, A. Pandurangan, L. Jih-hsin, M. Hsin-yuan, Influence of Sm doping on the microstructural properties of CdS nanocrystals, Powder. 266 (2014) 407–411. https://doi.org/10.1016/j.powtec.2014.06.051.

[117] L. Saravanan, R. Jayavel, A. Pandurangan, L. Jih-hsin, M. Hsin-yuan, Synthesis , Structural and Optical properties of Sm^{3+} and Nd^{3+} doped Cadmium Sulfide Nanocrystals, Mater. Res. Bull. 52 (2014) 128–133. https://doi.org/10.1016/j.materresbull.2013.12.054.

[118] M.T.N. Muthukumarasamy, Quantum confinement effects in Gd-doped CdS nanoparticles prepared by chemical precipitation technique, J Mater Sci: Mater Electron (2013) 4535–4541. https://doi.org/10.1007/s10854-013-1438-1.

[119] A. Khan, M. Shkir, M.A. Manthrammel, V. Ganesh, I.S. Yahia, M. Ahmed, A.M. El-toni, A. Aldalbahi, H. Ghaithan, S. Alfaify, Effect of Gd doping on structural , optical properties , photoluminescence and electrical characteristics of CdS nanoparticles for optoelectronics, Ceram. Int. 45 (2019) 10133–10141. https://doi.org/10.1016/j.ceramint.2019.02.061.

[120] R. Zhao, P. Wang, T. Yang, Z. Li, B. Xiao, M. Zhang, Half Metallic Ferromagnetism in Eu-Doped CdS Nanoparticles, J. Appl. phy. chem. (2015). https://doi.org/10.1021/acs.jpcc.5b10444.

[121] B. Poornaprakash, U. Chalapathi, P.T. Poojitha, S.V.P. Vattikuti, S. Park, Influence of gadolinium (III) doping on the structural, optical, magnetic and photocatalytic properties of CdS quantum dots, Mater. Sci. Semicond. Process. 100 (2019) 73–78. https://doi.org/10.1016/j.mssp.2019.04.043.

[122] B. Poornaprakash, U. Chalapathi, P.T. Poojitha, S. V. Prabhakar Vattikuti, S.H. Park, CdS:Eu quantum dots for spintronics and photocatalytic applications, J. Mater. Sci. Mater. Electron. 30 (2019) 8220–8225. https://doi.org/10.1007/s10854-019-01137-y.

[123] B. Poornaprakash, R. Mangiri, A.A. Al-Kheraif, D.D. Divakar, Y.L. Kim, M. Kumar, M.S.P. Reddy, Tunable room temperature ferromagnetism and optical bandgap of CdS:Er nanoparticles, Appl. Phys. A Mater. Sci. Process. 127 (2021) 1–7. https://doi.org/10.1007/s00339-021-04508-7.

[124] M. Ren, C. Zhang, P. Li, Z. Song, X. Liu, The origin of ferromagnetism in Pd-doped CdS, J. Magn. Magn. Mater. 324 (2012) 2039–2042. https://doi.org/10.1016/j.jmmm.2012.02.006.

[125] S.M. Mahdavi, A. Irajizad, A. Azarian, R.M. Tilaki, Optical and Structural Properties of Copper Doped CdS Thin Films Prepared by Pulsed Laser Deposition, Sci. Iran. 15 (2008) 360–365.

[126] A. Jafari, A. Zakaria, Z. Rizwan, M. Sabri, M. Ghazali, Effect of Low Concentration Sn Doping on Optical Properties of CdS Films Grown by CBD Technique, Int. J. Mol. Sci. 12 (2011) 6320–6328. https://doi.org/10.3390/ijms12096320.

[127] S. Chandramohan, A. Kanjilal, S.N. Sarangi, S. Majumder, R. Sathyamoorthy, C.-

H. Hong, T. Som, Effect of substrate temperature on implantation doping of Co in CdS nanocrystalline thin films, Nanoscale. 2 (2010) 1155–1159. https://doi.org/10.1039/c005273f.

[128] M. El-Hagary, S. Soltan, Magnetic behaviour of Fe-doped CdS diluted magnetic semiconducting nanocrystalline thin films, J. Appl. Phys. 112 (2012) 043907. https://doi.org/10.1063/1.4748270.

[129] R. Premarani, J.J. Devadasan, S. Saravanakumar, R. Chandramohan, T. Mahalingam, Structural , optical and magnetic properties of Ni-doped CdS thin films prepared by CBD, (2015) 2059–2065. https://doi.org/10.1007/s10854-014-2647-y.

[130] S. Kumar, P. Sharma, V. Sharma, Red shift in absorption edge of $Cd_{1-x}Ni_xS$ dilute magnetic semiconductor nanofilms, J Nanopart Res. 15 (2013) 1662 https://doi.org/10.1007/s11051-013-1662-x.

[131] S. Kumar, P. Sharma, V. Sharma, Red shift in Absorption Edge of $Cd_{1-x}Co_xS$ Nanofilms, IEEE Trans. Nano. Technol., 13 (2014) 343-348

[132] S. Kumar, N.S. Negi, S.C. Katyal, P. Sharma, V. Sharma, Structural , morphological and magnetic analysis of Cd–Co–S dilute magnetic semiconductor nano films, J. Magn. Magn. Mater. 367 (2014) 1–8. https://doi.org/10.1016/j.jmmm.2014.04.065.

[133] S. Saravanakumar, R. Chandramohan, R.P.J. Jebaraj, Studies on Dilute Magnetic Semiconducting Co-Doped CdS Thin Films Prepared by Chemical Bath Deposition method, J. Mater. Sci. Mater. Electron. 28 (2017) 12092–12099. https://doi.org/10.1007/s10854-017-7022-3.

[134] M. Tomakin, Y. Öncel, E. F. Keskenler, V. Nevruzog, Z. Onuk, O. Görür, Investigation of $Cd_{1-x}Co_xS$ diluted magnetic semiconductor thin films fabricated by chemical bath deposition method, J. Alloys Compd. 616 (2014) 166-172.

[135] H. Khallaf, G. Chai, O. Lupan, L. Chow, S. Park, A. Schulte, Characterization of gallium-doped CdS thin films grown by chemical bath deposition, Appl. Surf. Sci. 255 (2009) 4129–4134. https://doi.org/10.1016/j.apsusc.2008.10.115.

[136] K. Zou, R. Li, Y. Liu, L. Tian, S. Feng, Structure and photoelectric properties of Dy doped CdS polycrystalline thin films, Adv. Mater. Res. Vols. 752 (2013) 1901–1905. https://doi.org/10.4028/www.scientific.net/AMR.750-752.1901.

[137] S.Y.İ. Polat, M.T.S.B. Töreli, T.K.E. Bacaksız, Optical and electrical optimization of dysprosium-doped CdS thin films, J. Mater. Sci. Mater. Electron. 29 (2018)

14774–14782. https://doi.org/10.1007/s10854-018-9613-z.

[138] Y. Wu, Y. Shao, L.G. Jacobsohn, Luminescence of ZnS:Ag scintillator prepared by the hydrothermal reaction method: Effects of reaction temperature and time, Ag concentration, and co-doping with Al, Opt. Mater. (Amst). 107 (2020). https://doi.org/10.1016/j.optmat.2020.110015.

[139] R.N. Bhargava, D. Gallagher, X. Hong, A. Nurmikko, Optical properties of manganese-doped nanocrystals of ZnS, Phys. Rev. Lett. 72 (1994) 416–419. https://doi.org/10.1103/PhysRevLett.72.416.

[140] J. P.Borah, J.Barman, K.C.Sarma, Structural and optical properties of ZnS nanoparticles, Chalcogenide Lett. 5 (2008) 201–208.

[141] K.S. Rathore, D. Patidar, Y. Janu, N.S. Saxena, K. Sharma, T.P. Sharma, Structural and optical charcterization of chemically synthesized ZnS nanoparticles, Chalcogenide Lett. 5 (2008) 105–110.

[142] G. Murali, D.A. Reddy, B. Poornaprakash, R.P. Vijayalakshmi, N.M. Rao, Effect of annealing on structural and optical properties of ZnS nanocrystals, Optoelectron. Adv. Mater. – RAPID Commun. 5 (2011) 928–931. https://doi.org/10.1016/j.solidstatesciences.2017.04.006.

[143] D. Ghica, S. V. Nistor, L.C. Nistor, M. Stefan, C.D. Mateescu, Structural phase transformations in annealed cubic ZnS nanocrystals, J. Nanoparticle Res. 13 (2011) 4325–4335. https://doi.org/10.1007/s11051-011-0379-y.

[144] N. Shanmugam, S. Cholan, N. Kannadasan, K. Sathishkumar, G. Viruthagiri, Effect of annealing on the ZnS nanocrystals prepared by chemical precipitation method, J. Nanomater. 2013 (2013). https://doi.org/10.1155/2013/351798.

[145] N. Prasad, B. Karthikeyan, Phase-dependent structural, optical, phonon and UV sensing properties of ZnS nanoparticles, Nanotechnology. 30 (2019). https://doi.org/10.1088/1361-6528/ab3cbf.

[146] Q. Liu, M. Guobing, A. Jianping, Chemical bath-deposited ZnS thin films: Preparation and characterization, Appl. Surf. Sci. 254 (2008) 5711–5714. https://doi.org/10.1016/j.apsusc.2008.03.059.

[147] P.H. Borse, N. Deshmukh, Luminescence quenching in ZnS nanoparticles due to Fe and Ni doping, J. Mater. Sci. 4 (1999) 6087–6093.

[148] N. Tsujii, H. Kitazawa, G. Kido, Magnetic properties of Mn and Eu-doped ZnS nanocrystals, J. Appl. Phys. 93 (2003) 6957–6959. https://doi.org/10.1063/1.1540034.

[149] H.J. Yuan, X.Q. Yan, Z.X. Zhang, D.F. Liu, Z.P. Zhou, L. Cao, J.X. Wang, Y. Gao, L. Song, L.F. Liu, X.W. Zhao, X.Y. Dou, W.Y. Zhou, S.S. Xie, Synthesis, optical, and magnetic properties of $Zn_{1-x}Mn_xS$ nanowires grown by thermal evaporation, J. Cryst. Growth. 271 (2004) 403–408. https://doi.org/10.1016/j.jcrysgro.2004.08.001.

[150] S. Biswas, S. Kar, S. Chaudhuri, Optical and magnetic properties of manganese-incorporated zinc sulfide nanorods synthesized by a solvothermal process, J. Phys. Chem. B. 109 (2005) 17526–17530. https://doi.org/10.1021/jp053138i.

[151] C.S. Pathak, M.K. Mandal, Characterization and optical properties of Ni^{2+} doped ZnS nanoparticles, J. Ovonic Res. 8 (2012) 15–20.

[152] C.S. Pathak, M.K. Mandal, V. Agarwala, Optical properties of undoped and cobalt doped ZnS nanophosphor, Mater. Sci. Semicond. Process. 16 (2013) 467–471. https://doi.org/10.1016/j.mssp.2012.07.009.

[153] S. Kumar, C.L. Chen, C.L. Dong, Y.K. Ho, J.F. Lee, T.S. Chan, R. Thangavel, T.K. Chen, B.H. Mok, S.M. Rao, M.K. Wu, Room temperature ferromagnetism in Ni doped ZnS nanoparticles, 554 (2013) 357–362. https://doi.org/10.1016/j.jallcom.2012.12.001.

[154] V. Ramasamy, K. Praba, G. Murugadoss, Synthesis and study of optical properties of transition metals doped ZnS nanoparticles, Spectrochim. Acta Part A Mol. Biomol. Spectrosc. 96 (2012) 963–971. https://doi.org/10.1016/j.saa.2012.07.125.

[155] R. Sarkar, C.S. Tiwary, P.Ã. Kumbhakar, A.K. Mitra, Enhanced visible light emission from Co^{2+} doped ZnS nanoparticles, Phys. B Phys. Condens. Matter. 404 (2009) 3855–3858. https://doi.org/10.1016/j.physb.2009.07.106.

[156] T.M. Hammad, J.K. Salem, S.K. Mohammed, A. Draaz, R.H.F.S. Kodeh, Optical properties of Cu^{2+} and Fe^{2+} doped ZnS semiconductor nanoparticles synthesized by co-precipitation method, J. Mater. Sci. Mater. Electron. (2015) 5495–5501. https://doi.org/10.1007/s10854-015-3106-0.

[157] S. Bhattacharya, D. Chakravorty, Electrical and magnetic properties of cold compacted iron-doped zinc sulfide nanoparticles synthesized by wet chemical method, Chem. Phys. Lett. 444 (2007) 319–323. https://doi.org/10.1016/j.cplett.2007.07.040.

[158] S. Sambasivam, D.P. Joseph, D.R. Reddy, B.K. Reddy, C.K. Jayasankar, Synthesis and characterization of thiophenol passivated Fe-doped ZnS nanoparticles, Mater. Sci. Eng. B. 150 (2008) 125–129. https://doi.org/10.1016/j.mseb.2008.03.009.

[159] N. Eryong, L. Donglai, Z. Yunsen, B. Xue, Y. Liang, J. Yong, J. Zhifeng, S. Xiaosong, Photoluminescence and magnetic properties of Fe-doped ZnS nano-particles synthesized by chemical co-precipitation, Appl. Surf. Sci. 257 (2011) 8762–8766. https://doi.org/10.1016/j.apsusc.2011.03.114.

[160] S. Sambasivam, B.K. Reddy, A. Divya, N. Madhusudhana Rao, C.K. Jayasankar, B. Sreedhar, Optical and ESR studies on Fe doped ZnS nanocrystals, Phys. Lett. A. 373 (2009) 1465–1468. https://doi.org/10.1016/j.physleta.2009.02.032.

[161] S. Sambasivam, D.P. Joseph, J.G. Lin, C. Venkateswaran, Doping induced magnetism in Co–ZnS nanoparticles, J. Solid State Chem. 182 (2009) 2598–2601. https://doi.org/10.1016/j.jssc.2009.07.015.

[162] K. Patel, M.P.D.S.H. Chaki, Effect of Cobalt doping on ZnS nanoparticles synthesized by microwave irradiation, J. Mater. Sci. Mater. Electron. 28 (2017) 5029–5036. https://doi.org/10.1007/s10854-016-6159-9.

[163] B. Poornaprakash, D.A. Reddy, G. Murali, R.P. Vijayalakshmi, B.K. Reddy, Defect induced paramagnetism in lightly doped ZnS : Fe nanoparticles, Phys. E Low-Dimensional Syst. Nanostructures. 73 (2015) 63–68. https://doi.org/10.1016/j.physe.2015.05.017.

[164] Y. Li, C. Cao, Z. Chen, Magnetic and optical properties of Fe doped ZnS nanoparticles synthesized by microemulsion method, Chem. Phys. Lett. 517 (2011) 55–58. https://doi.org/10.1016/j.cplett.2011.09.048.

[165] D. Saikia, R. Raland, J.P. Borah, Influence of Fe doping on the structural, optical and magnetic properties of ZnS diluted magnetic semiconductor, Phys. E Low-Dimensional Syst. Nanostructures. 83 (2016) 56–63. https://doi.org/10.1016/j.physe.2016.04.016.

[166] D. Saikia, R.D. Raland, J.P. Borah, In fluence of Fe doping on the structural , optical and magnetic properties of ZnS diluted magnetic semiconductor, Phys. E. 83 (2016) 56–63. https://doi.org/10.1016/j.physe.2016.04.016.

[167] B. Poornaprakash, U. Chalapathi, S.V.P. Vattikuti, Compositional, morphological, structural, microstructural, optical, and magnetic properties of Fe, Co, and Ni doped ZnS nanoparticles, Appl. Phys. A. 123 (2017) 1–10. https://doi.org/10.1007/s00339-017-0865-x.

[168] B. Poornaprakash, D.A. Reddy, G. Murali, N.M. Rao, R.P. Vijayalakshmi, B.K. Reddy, Composition dependent room temperature ferromagnetism and PL intensity of cobalt doped ZnS nanoparticles, J. Alloys Compd. 577 (2013) 79–85.

https://doi.org/10.1016/j.jallcom.2013.04.106.

[169] B. Poornaprakash, S. Sambasivam, D.A. Reddy, G. Murali, Dopant induced RTFM and enhancement of fl uorescence efficiencies in spintronic ZnS : Ni nanoparticles, 40 (2014) 2677–2684. https://doi.org/10.1016/j.ceramint.2013.10.056.

[170] B. Poornaprakash, P.T. Poojitha, U. Chalapathi, K. Subramanyam, S. Park, Synthesis, structural, optical, and magnetic properties of Co doped, Sm doped and Co+Sm co-doped ZnS nanoparticles, Phys. E. 83 (2016) 180–185. https://doi.org/10.1016/j.physe.2016.05.025.

[171] S. Kumar, N.K. Verma, Room Temperature Magnetism in Co-Doped ZnS Nanoparticles, J Supercond Nov Magn. 28 (2015) 137–142. https://doi.org/10.1007/s10948-014-2823-6.

[172] R. Wang, H. Liang, J. Hong, Z. Wang, Journal of Photochemistry and Photobiology A : Chemistry Hydrothermal synthesis of cobalt-doped ZnS for ef fi cient photodegradation of methylene blue, J. Photochem. Photobiol. A Chem. 325 (2016) 62–67. https://doi.org/10.1016/j.jphotochem.2016.03.036.

[173] S. Kumar, N.K. Verma, Room temperature investigations on optical and magnetic studies of $Co_xZn_{1-x}S$ nanorods, J. Magn. Magn. Mater. 374 (2015) 548–552. https://doi.org/10.1016/j.jmmm.2014.08.100.

[174] W. Zhao, Z. Wei, L. Zhang, X. Wu, X. Wang, J. Jiang, Optical and magnetic properties of Co and Ni co-doped ZnS nanorods prepared by hydrothermal method, J. Alloys Compd. (2016). https://doi.org/10.1016/j.jallcom.2016.12.127.

[175] M. Wu, Z. Wei, W. Zhao, X. Wang, J. Jiang, Optical and Magnetic Properties of Ni Doped ZnS Diluted Magnetic Semiconductors Synthesized by Hydrothermal Method, J. Nanomater. 2017 (2017).

[176] W. Zhao, Z. Wei, L. Zhang, X. Wu, X. Wang, J. Jiang, Room Temperature Ferromagnetic and Optical Properties of Chrome Doped ZnS Nanorods Prepared by Hydrothermal Method, J. Nanomater. (2017).

[177] P. Chandra, P.P.C. Srivastava, Fe doping in ZnS for realizing nanocrystalline-diluted magnetic semiconductor phase, J Mater Sci. 49 (2014) 6012–6019. https://doi.org/10.1007/s10853-014-8321-1.

[178] P. Chandra, P. Surajit, G.P.C. Srivastava, Antiferromagnetic coupling in Co-doped ZnS, J. Mater. Sci. 50 (2015) 7919–7929. https://doi.org/10.1007/s10853-015-9356-7.

[179] P.C. Patel, S. Ghosh, P.C. Srivastava, Bound magnetic polaron driven room-temperature ferromagnetism in Ni doped ZnS nanoparticles, Mater. Chem. Phys. 216 (2018) 285–293. https://doi.org/10.1016/j.matchemphys.2018.05.065.

[180] S. Kumar, P. Mandal, A. Singh, S. Husain, D. Kumar, V.K. Malik, S. Sharma, Magnetization properties of Co incorporated ZnS nanocrystals synthesized at low temperature via chemical route, J. Alloys Compd. 830 (2020) 154640. https://doi.org/10.1016/j.jallcom.2020.154640.

[181] V. V. Jadhavar, V.D. Mote, B.S. Munde, Study of structural, optical, and paramagnetic properties of $Zn_{1-x}Co_xS$ nanoparticles prepared via co-precipitation, J. Mater. Sci. Mater. Electron. 31 (2020) 17297–17306. https://doi.org/10.1007/s10854-020-04284-9.

[182] Y. Li, Z. Zhou, P. Jin, Y. Chen, S.B. Zhang, Z. Chen, Achieving ferromagnetism in single-crystalline ZnS wurtzite nanowires via chromium doping, J. Phys. Chem. C. 114 (2010) 12099–12103. https://doi.org/10.1021/jp102875p.

[183] H. Chen, D. Shi, J. Qi, Comparative studies on the magnetic properties of ZnS nanowires doped with transition metal atoms, J. Appl. Phys. 109 (2011). https://doi.org/10.1063/1.3573388.

[184] G. Gurung, T.K. Ekanayaka, A.J. Yost, T.R. Paudel, Absorption enhancement by transition metal doping in ZnS, Mater. Res. Express. 6 (2019). https://doi.org/10.1088/2053-1591/ab56d6.

[185] A.A. Bol, R. Van Beek, A. Meijerink, On the Incorporation of Trivalent Rare Earth Ions in II-VI Semiconductor Nanocrystals, (2002) 1121–1126.

[186] X. Tian, Z. Chen, J. Wen, Y. Du, J. Hu, S. Wang, H. Peng, Bio-inspired synthesis and optical properties of Dy^{3+} -doped ZnS nanoparticles, J. Ceram. Process. Res. 18 (2017) 116–121.

[187] M. Ihara, T. Igarashi, T. Kusunoki, K. Ohno, Preparation and Characterization of Rare Earth Activators Doped Nanocrystal Phosphors, 147 (2000) 2355–2357.

[188] P. Mukherjee, C.M. Shade, A.M. Yingling, D.N. Lamont, D.H. Waldeck, Lanthanide Sensitization in II - VI Semiconductor Materials : A Case Study with Terbium (III) and Europium (III) in Zinc Sulfide Nanoparticles, J. Phys. Chem. A. 115 (2011) 4031–4041.

[189] P. Mukherjee, Controlled Terbium (III) Luminescence in Zinc Sulfide Nanoparticles: An Assessment of Competitive Photophysical Processes, (2015). https://doi.org/10.1021/acs.jpcc.5b07182.

[190] B. Poornaprakash, P.T. Poojitha, U. Chalapathi, S. Ramu, R.P. Vijayalakshmi., S.-H. Park, Chemical synthesis, compositional, morphological, structural, optical and magnetic properties of $Zn_{1-x}Dy_xS$ nanoparticles, Ceram. Int. 42 (2016) 8092–8097.

[191] B. Poornaprakash, P.T. Poojitha, U. Chalapathi, S. Park, Achieving room temperature ferromagnetism in ZnS nanoparticles via Eu^{3+} doping, Mater. Lett. 181 (2016) 227–230. https://doi.org/10.1016/j.matlet.2016.06.033.

[192] B. Poornaprakash, U. Chalapathi, M. Reddeppa, S. Park, Effect of Gd doping on the structural , luminescence and magnetic properties of ZnS nanoparticles synthesized by the hydrothermal method, Superlattices Microstruct. 97 (2016) 104–109. https://doi.org/10.1016/j.spmi.2016.06.013.

[193] P. Kaur, S. Kumar, C. Chen, K. Yang, D. Wei, C. Dong, C. Srivastava, S.M. Rao, Gd doping induced weak ferromagnetic ordering in ZnS nanoparticles synthesized by low temperature co-precipitation technique, Mater. Chem. Phys. 186 (2017) 124–130. https://doi.org/10.1016/j.matchemphys.2016.10.037.

[194] B. Poornaprakash, S. Ramu, S. Park, R.P. Vijayalakshmi, B.K. Reddy, Room temperature ferromagnetism in Nd doped ZnS diluted magnetic semiconductor nanoparticles, Mater. Lett. 164 (2016) 104–107. https://doi.org/10.1016/j.matlet.2015.10.119.

[195] B. Poornaprakash, U. Chalapathi, Y. Suh, S.V.P. Vattikuti, M.S.P. Reddy, S. Park, Terbium-doped ZnS quantum dots: Structural, morphological, optical, photoluminescence, and photocatalytic properties, Ceram. Int. 44 (2018) 11724–11729. https://doi.org/10.1016/j.ceramint.2018.03.250.

[196] B. Poornaprakash, U. Chalapathi, S. Park, Structural and magnetic properties of ZnS: Tb^{3+} nanoparticles, J. Mater. Sci. Mater. Electron. 28 (2017) 3672–3677. https://doi.org/10.1007/s10854-016-5972-5.

[197] S. Ramu, R.P. Vijayalakshmi, Effect of Terbium Doping on the Structural and Magnetic Properties of ZnS Nanoparticles, J. Supercond. Nov. Magn. 30 (2017) 1921–1925. https://doi.org/10.1007/s10948-016-3960-x.

[198] S.M. El-hamidy, The optical behavior of multi-emission quantum dots based on Tb- doped ZnS developed via solvothermal route for bioimaging applications, Opt. Int. J. Light Electron Opt. 207 (2020) 163868. https://doi.org/10.1016/j.ijleo.2019.163868.

[199] K. Thyagarajana, Effect of (Mn, Dy) doped ZnS and (Mn, Dy) co-doped ZnS on structural , morphological and magnetic properties of ZnS, J. Inf. Comput. Sci. 10

(2020) 109–115.

[200] K.R. NEMADE, Gas Sensors Based on Inorganic Materials: An Overview, Sensors Transducers J. 132 (2011) 1–13.

[201] D.A. Johnston, M.H. Carletto, K.T.R. Reddy, I. Forbes, R.W. Miles, Chemical bath deposition of zinc sulfide based buffer layers using low toxicity materials, 404 (2002) 102–106.

[202] Q.I. Liu, G. Mao, Comparison of CdS and ZnS thin films prepared by chemical bath deposition, 16 (2009) 469–474.

[203] S.P. Patel, J.C. Pivin, A.K. Chawla, R. Chandra, D. Kanjilal, L. Kumar, Room temperature ferromagnetism in $Zn_{1-x}Co_xS$ thin films with wurtzite structure, J. Magn. Magn. Mater. 323 (2011) 2734–2740. https://doi.org/10.1016/j.jmmm.2011.05.057.

[204] S.P. Patel, J.C. Pivin, M.K. Patel, J. Won, R. Chandra, D. Kanjilal, L. Kumar, Defects induced magnetic transition in Co doped ZnS thin films: Effects of swift heavy ion irradiations, J. Magn. Magn. Mater. 324 (2012) 2136–2141. https://doi.org/10.1016/j.jmmm.2012.02.031.

[205] F. Haque, K.S. Rahman, M.A. Islam, M.J. Rashid, M. Akhtaruzzaman, M.M. Alam, Z.A. Alothman, K. Sopian, N. Amin, Growth optimization of ZnS thin films by RF magnetron sputtering as prospective buffer layer in thin film solar cells, Chalcogenide Lett. 11 (2014) 189–197.

[206] A. Goktas, Sol–gel derived $Zn_{1-x}Fe_xS$ diluted magnetic semiconductor thin films Compositional dependent room or above room temperature ferromagnetism, Appl. Surf. Sci. 340 (2015) 151–159.

[207] A. Goktas, Structural , Optical , and Magnetic Properties of Solution-Processed Co-Doped ZnS Thin Films, 45 (2016) 5709–5720. https://doi.org/10.1007/s11664-016-4771-3.

[208] R. Sahraei, S. Darafarin, An investigation on optical characteristics of nanocrystalline ZnS: Ni thin films prepared by chemical deposition method, Spectrochim. Acta. Part A Mol. Biomol. Spectrosc. 149 (2015) 941–948. https://doi.org/10.1016/j.saa.2015.05.036.

[209] K.S. Wanjala, W.K. Njoroge, J.M. Ngaruiya, Optical and Electrical Characterization of ZnS : Sn Thin Films for Solar Cell Application, 6 (2016) 1–7. https://doi.org/10.5923/j.ijee.20160601.01.

[210] A. Jrad, W. Naffouti, C. Nefzi, T. Ben, Effect of copper concentration on the

physical properties of ZnS : Cu alloys prepared by chemical bath deposition, J. Mater. Sci. Mater. Electron. 27 (2016) 10684–10695. https://doi.org/10.1007/s10854-016-5168-z.

[211] I. Lopez-Quintas, E. Rebollar, D. Ávila-Brande, J.G. Izquierdo, L. Bañares, C. Díaz-Guerra, A. Urbieta, M. Castillejo, R. de Nalda, M. Martín, Femtosecond double-pulse laser ablation and deposition of co-doped ZnS thin films, Nanomaterials. 10 (2020) 1–15. https://doi.org/10.3390/nano10112229.

[212] S. Kumar, N.. Verma, Structural, optical and magnetic investigations on Fe-doped ZnS nanoparticles, J Mater Sci Mater Electron. 26 (2015) 2754–2759. https://doi.org/10.1007/s10854-015-2755-3.

[213] N. Eryong, L. Donglai, Z. Yunsen, B. Xue, Y. Liang, J. Yong, J. Zhifeng, S. Xiaosong, Photoluminescence and magnetic properties of Fe-doped ZnS nanoparticles synthesized by chemical co-precipitation, Appl. Surf. Sci. 257 (2011) 8762–8766. https://doi.org/10.1016/j.apsusc.2011.03.114.

[214] S.P. Patel, J.C.P.G. Maity, R.P.Y.R. Chandra, D.K. Lokendra, Microstructural and surface morphological studies on Co doped ZnS diluted magnetic semiconductor thin films, J. Mater. Sci. Mater. Electron. 29 (2018) 13541–13550. https://doi.org/10.1007/s10854-018-9482-5.

[215] M.S. Akhtar, M.A. Malik, S. Riaz, S. Naseem, P. O'Brien, Optimising conditions for the growth of nanocrystalline ZnS thin films from acidic chemical baths, Mater. Sci. Semicond. Process. 30 (2015) 292–297. https://doi.org/10.1016/j.mssp.2014.10.019.

[216] B.D. Cullity and S.R.Stock, Elements of X-Ray Diffraction, 1978. https://doi.org/10.1088/0031-9112/8/7/008.

[217] G.A. Kumar, V. Thomas, G. Jose, N. V Unnikrishnan, V.P.N. Nampoori, Optical properties of porphyrins in borate glassy matrix, Mater. Chem. Phys. 73 (2002) 206–211.

[218] M. Navaneethan, J. Archana, K.D. Nisha, Y. Hayakawa, S. Ponnusamy, C. Muthamizhchelvan, Temperature dependence of morphology, structural and optical properties of ZnS nanostructures synthesized by wet chemical route, J. Alloys Compd. 506 (2010) 249–252. https://doi.org/10.1016/j.jallcom.2010.07.002.

[219] M. Thambidurai, N. Muthukumarasamy, S. Agilan, N. Murugan, S. Vasantha, R. Balasundaraprabhu, T.S. Senthil, Strong quantum confinement effect in

nanocrystalline CdS, (2010) 3254–3258. https://doi.org/10.1007/s10853-010-4333-7.

[220] C.B. Murray, D.J. Noms, M.G. Bawendi, Synthesis and characterization of nearly monodisperse CdE (E=S, Se, Te) semiconductor nanocrystallites, J. Am. Chem. Soc. 115 (1993) 8706–8715. https://doi.org/10.1021/ja00072a025.

[221] B. Liu, G.Q. Xu, L.M. Gan, C.H. Chew, W.S. Li, Z.X. Shen, Photoluminescence and structural characteristics of CdS nanoclusters synthesized by hydrothermal microemulsion, J. Appl. Phys. 89 (2001) 1059–1063. https://doi.org/10.1063/1.1335642.

[222] J.I. Kim, J. Kim, J. Lee, D.R. Jung, H. Kim, H. Choi, S. Lee, S. Byun, S. Kang, B. Park, Photoluminescence enhancement in CdS quantum dots by thermal annealing, Nanoscale Res. Lett. 7 (2012) 1–7. https://doi.org/10.1186/1556-276X-7-482.

[223] C.P. Bean, J.D. Livingston, Superparamagnetism, J. Appl. Phys. 30 (1959) 120–129. https://doi.org/10.1063/1.2185850.

[224] K. Sooklal, B.S. Cullum, S.M. Angel, C.J. Murphy, Photophysical properties of ZnS nanoclusters with spatially localized Mn^{2+}, J. Phys. Chem. 100 (1996) 4551–4555. https://doi.org/10.1021/jp952377a.

[225] D. Denzler, M. Olschewski, K. Sattler, Luminescence studies of localized gap states in colloidal ZnS nanocrystals, J. Appl. Phys. 84 (1998) 2841–2845. https://doi.org/10.1063/1.368425.

[226] D. V. Dake, N.D. Raskar, V.A. Mane, R.B. Sonpir, E. Stathatos, K. Asokan, P.D. Babu, B.N. Dole, Exploring the role of defects on diverse properties of Cr-substituted ZnS nanostructures for photocatalytic applications, Appl. Phys. A Mater. Sci. Process. 126 (2020) 1–15. https://doi.org/10.1007/s00339-020-03669-1.

[227] J. Tang, L. Wang, H. Luo, W. Xiao, Magnetic properties in zinc-blende CdS induced by Cd vacancies, Phys. Lett. A. 377 (2013) 572–576. https://doi.org/10.1016/j.physleta.2012.12.038.

[228] C. Prabakar, S. Muthukumaran, V. Raja, Structural , magnetic and photoluminescence behavior of Ni/Fe doped ZnO nanostructures prepared by co-precipitation method, Opt. Int. J. Light Electron Opt. 202 (2020) 163714. https://doi.org/10.1016/j.ijleo.2019.163714.

[229] V. Singh, P. Chauhan, Structural and optical characterization of CdS nanoparticles prepared by chemical precipitation method, J. Phys. Chem. Solids. 70 (2009)

1074–1079. https://doi.org/10.1016/j.jpcs.2009.05.024.

[230] P. Yanga, M.LuÈ, D. XuÈ, D. Yuana, C. Songa, G. Zhoub, The effect of Co^{2+} and Co^{3+} on photoluminescence characteristics of ZnS nanocrystallines, J. Phys. Chem. Solids 62. 62 (2001) 1181–1184.

[231] Y. Li, P.A. Montano, B. Barbiellini, P.E. Mijnarends, S. Kaprzyk, A. Bansil, Spin moment over 10–300 K and delocalization of magnetic electrons above the Verwey transition in magnetite, J. Phys. Chem. Solids. 68 (2007) 1556–1560. https://doi.org/10.1016/j.jpcs.2007.03.037.

[232] R.S. Turtelli, M. Atif, N. Mehmood, F. Kubel, K. Biernacka, W. Linert, R. Grössinger, C. Kapusta, M. Sikora, Interplay between the cation distribution and production methods in cobalt ferrite, Mater. Chem. Phys. 132 (2012) 832–838. https://doi.org/10.1016/j.matchemphys.2011.12.020.

[233] L. Brus, Electronic Wave Functions in Semiconductor Clusters : Experiment and Theory, J. Phys. Chem. 90 (1986) 2555–2560.

[234] N. Khorasanipoor, P. Iranmanesh, S.T. Yazdi, S. Saeednia, Synthesis and characterization of EDTA-assisted ZnS:Hg nanoparticles, J. Lumin. 219 (2020) 116948. https://doi.org/10.1016/j.jlumin.2019.116948.

[235] A.A. Dakhel, Influence of dysprosium doping on the electrical and optical properties of CdO thin films, Sol. Energy. 83 (2009) 934–939. https://doi.org/10.1016/j.solener.2008.12.015.

[236] G.S. Lotey, J. Singh, N.K. Verma, Room temperature ferromagnetism in Tb-doped ZnO dilute magnetic semiconducting nanoparticles, J Mater Sci Mater Electron. 24 (2013) 3611–3616. https://doi.org/10.1007/s10854-013-1292-1.

[237] G. Pandey, S. Dixit, A.K. Shrivastava, Effect of Gd^{3+} doping and reaction temperature on structural and optical properties of CdS nanoparticles, Mater. Sci. Eng. B Solid-State Mater. Adv. Technol. 200 (2015) 59–66. https://doi.org/10.1016/j.mseb.2015.06.007.

[238] R.E.G. Chandrasekaran, Influence of Co-doping on the structural , optical and magnetic properties of ZnO nanoparticles synthesized using auto-combustion method, J Mater Sci Mater Electron. 24 (2013) 96–105. https://doi.org/10.1007/s10854-012-0893-4.

[239] P. Photobiol, Controlled surface trap state photoluminescence from CdS QDs impregnated in poly(methyl methacrylate), Photochem. Photobiol. Sci. 11 (2012) 1220. https://doi.org/10.1039/c2pp25023c.

[240] B. Grobelna, A. Synak, P. Bojarski, The luminescence properties of dysprosium ions in silica xerogel doped with $Gd_{1.6}Dy_{0.4}(WO_4)_3$, Opt. Appl. XLII (2012) 2–9. https://doi.org/10.5277/oa120211.

[241] J.H. Park, M.G. Kim, H.M. Jang, S. Ryu, Y.M. Kim, Y.M. Kim, Co-metal clustering as the origin of ferromagnetism in Co-doped ZnO thin films, Appl. Phys. Lett. 84 (2004) 2002–2005. https://doi.org/10.1063/1.1650915.

[242] D.P. Norton, M.E. Overberg, S.J. Pearton, K. Pruessner, Ferromagnetism in cobalt-implanted ZnO, Appl. Phys. Lett. 83 (2003) 5488–5490. https://doi.org/10.1063/1.1637719.

[243] S. Paul, D. Banik, G.A. Ahmed, A. Choudhury, Magnetic Property Study in Eu Doped TiO_2 Nanoparticles, J. Mater. Sci. Mech. Eng. 3 (2016) 515–517.

[244] A.E. Clark, B.F. Desavage, R. Bozorth, Anomalous thermal expansion and magnetostriction of single-crystal dysprosium, Phys. Rev. 138 (1965) A216–A224.

[245] C. Jayachandraiah, K.S. Kumar, G. Krishnaiah, N.M. Rao, Influence of Dy dopant on structural and photoluminescence of Dy-doped ZnO nanoparticles, J. Alloys Compd. 623 (2015) 248–254. https://doi.org/10.1016/j.jallcom.2014.10.067.

[246] A. Kathalingam, S. Valanarasu, T. Ahamad, S.M. Alshehri, H.S. Kim, Spray pressure variation effect on the properties of CdS thin films for photodetector applications, Ceram. Int. 47 (2021) 7608–7616. https://doi.org/10.1016/j.ceramint.2020.11.100.

[247] B. Pejjai, V.R. Minnam Reddy, K. Seku, T.R.R. Kotte, C. Park, Chemical bath deposition of Mn-doped ZnS thin films using greener complexing agents: Effect of Mn-doping on the optical properties, Optik (Stuttg). 130 (2017) 608–618. https://doi.org/10.1016/j.ijleo.2016.10.083.

Journal of Alloys and Compounds 879 (2021) 160383

Contents lists available at ScienceDirect

Journal of Alloys and Compounds

journal homepage: www.elsevier.com/locate/jalcom

Magnetic and optical properties of transition metal (Fe, Co) and rare-earth (Tb, Dy) doped ZnS nanoparticles

Shivani Jindal, Puneet Sharma*

School of Physics & Materials Science, Thapar Institute of Engineering & Technology, Patiala 147004, India

ARTICLE INFO

Article history:
Received 23 February 2021
Received in revised form 3 May 2021
Accepted 10 May 2021
Available online 15 May 2021

Keywords:
ZnS
Transition metal
Rare earth
Magnetic properties
Dilute magnetic semiconductors

ABSTRACT

In the present work, hydrothermally synthesized transition metal (*TM* = Fe, Co) and rare earth (*RE* = Tb, Dy) doped ZnS nanoparticles were investigated for its structural, morphological, optical and magnetic properties. Phase and microstructural analysis confirmed cubic phase of ZnS having spherical shaped nanoparticles. *TM* doped showed relatively smaller crystallite size (~3.61 nm) compared to *RE* (~5.23 nm). The optical band gap found tunable in the range of 3.69–3.86 eV with doping. All nanoparticles were ferromagnetic in nature and highest value of saturation magnetization was observed for Fe doped ZnS. The tunable optical and ferromagnetic properties in *RE* and *TM* doped ZnS suggests their potential use in optoelectronic and spintronic devices.

1. Introduction

II-VI group (ZnS, CdS & ZnO) semiconductors have gained attention for various optoelectronic and spintronics device applications due to their size dependent optical, electronic and magnetic properties [1–3]. In solar cells, ZnO is primarily used as transparent conducting layer whereas, CdS and ZnS are used as window layer deposited on Cu (III-IV)$_2$ absorber layer [4,5]. Compared to CdS; ZnS is more potentially used because of its non-toxicity and better lattice matching with absorber layer. Also its higher optical band gap (E_g = 3.67 eV) than CdS (2.42 eV) allows high energy incident photons on window-absorber junction that enhance the blue response and thus contribute to better cell performance [5]. Apart from optical properties, ZnS at nano scale shows weak room temperature (*RT*) ferromagnetism due to uncompensated spins that arises from vacancies, interstitial/substitution impurity and surface defects [6]. Particle size plays a crucial role in determining their magnetization; it increases with decrease in particle size, while suppressed surface spins in larger particles cause low magnetization. However, magnetization diminishes below a critical size due to superparamagnetic effect [7].

To induce optimal magnetization along with suitable E_g could be of prime importance for various applications based on magnetic and optical properties. One of the major approaches to tune optical E_g and magnetization is by suitable doping of transition (*TM*) and rare earth (*RE*) metals. Over the past few years, considerable efforts have been made to evolve ZnS with *TM* and *RE* doping [8–15]. It is found that magnetization increases with doping of *TM* or *RE* due to increased surface defects and vacancies. Whereas, optical absorption and variation in E_g depends upon the type of dopants; higher E_g was obtained in *TM* doped (Fe, Ni, Co, Cr, Mn) due to smaller ionic radii compared to Zn^{2+} and *sp-d* spin exchange interactions [16–20]. On contrary, larger ionic radii of *RE* dopants (Tb, Dy, Sm) and *sp-f* spin exchange interactions results in decreased E_g [21,22]. The effect of *TM* and *RE* doping on optical properties are comparable among the studies with few exceptions [23,24]; whereas magnetic behaviour were contrary for same dopants and concentration. A few studies reported the paramagnetic behaviour whereas, decrease in magnetic saturation (M_s) has been observed due antiferromagnetic contribution. Li *et al.* (x = 0.30) and Saikia *et al.* (x = 0.10) synthesized Fe doped ZnS nanoparticles of 2–7 nm via microemulsion and co-precipitation method and showed paramagnetic behaviour [25,26]. On contrary, Sambasivam *et al.* and Eryong *et al.* prepared nanoparticles of size 3–7 nm via co-precipitation method and observed superparamagnetism for same composition (x = 0.10) [8,27]. It is interesting to note that Sambasivam *et al.* and Patel *et al.* showed ferromagnetism in Co doped ZnS nanoparticles, whereas Patel *et al.* reported paramagnetic behaviour [24,28,29]. In another study, Pooranprakash *et al.* showed ferromagnetism in Co doped and paramagnetism in Fe doped ZnS nanoparticle for same concentration despite lower magnetic moment of Co [30]. Kumar *et al.* has synthesized Co and Fe doped ZnS nanoparticles of cubic and

* Corresponding author.
E-mail address: puneet.sharma@thapar.edu (P. Sharma).

https://doi.org/10.1016/j.jallcom.2021.160383
0925-8388/

hexagonal phase respectively and showed diamagnetic to paramagnetic and ferromagnetic transition with doping concentration [31,32]. Further, magnetic behaviour were found to be different in Fe and Co doped ZnS nanorods, where only diamagnetic to ferromagnetic transition were observed [33,34]. Patel *et al.* reported ferromagnetic ordering in Co doped ZnS thin films [35].

The *RE* doped ZnS has also been investigated by Pooranprakash *et al.* and observed the transformation from ferromagnetism to superparamagnetism with increasing Tb dopant concentration, whereas Dy doped ZnS showed only weak ferromagnetic behaviour [13,36]. Ramu *et al.* reported paramagnetism in Tb doped ZnS [37].

The above mentioned ambiguities are largely associated to different processing methods, conditions and dopant concentration adopted by researchers. In order to understand this, a comparative study of *TM* (Fe, Co) and *RE* (Dy, Tb) doped ZnS nanoparticles at different concentration (0.05, 0.10 and 0.15) on structural, optical and magnetic property processed under similar condition has been carried thoroughly.

2. Experimental details

Laboratory grade zinc chloride ($ZnCl_2{\cdot}xH_2O$), sodium sulphide (Na_2S), cobalt chloride hexahydrate ($CoCl_2{\cdot}6H_2O$), ferric chloride hexahydrate ($FeCl_3{\cdot}6H_2O$), dysprosium (III) nitrate hydrate ($Dy(NO_3)_3{\cdot}xH_2O$) and terbium chloride hexahydrate ($TbCl_3{\cdot}6H_2O$) of 99.9% purity from sigma-aldrich were used to synthesized ZnS, $Zn_{1-x}Fe_xS$, $Zn_{1-x}Co_xS$, $Zn_{1-x}Dy_xS$ and $Zn_{1-x}Tb_xS$ (x = 0.05, 0.10 and 0.15) ZnS nanoparticles via hydrothermal method. 0.25 M of $ZnCl_2{\cdot}xH_2O$ and appropriate concentration of dopant were dissolved in distilled water. Then 0.25 M of Na_2S was added dropwise into the above solution and stirred for 30 min. The solution was transferred into a teflon lined stainless steel autoclave and placed in oven at 170 °C for 6 h. The autoclave was allowed to cool at *RT*. The obtained white colour precipitates were collected and washed with distilled water and ethanol for several times to remove impurities. The samples were finally dried in hot air oven at 60 °C. The obtained powders were annealed at 300 °C in argon atmosphere for 1 h.

The phase analysis of nanopowders was done using X-ray diffractometer (XRD) of PANalytical X'Pert PRO MRD with Cu-K_a (λ = 1.5418 Å). The morphological features and selected area electron diffraction (SAED) patterns of nanopowder was recorded by high resolution transmission electron microscopy (HR-TEM) (Hitachi H-7650). The elemental analysis was carried out by energy dispersive spectroscopy (EDS) model JEOL (JSM-1T100). Perkin Elmer Lambda 45 spectrophotometer and Agilent Carry Eclipse fluorescence spectrophotometer (G9800A) were used to determine UV–visible absorption spectra and *RT* photoluminescence (PL) spectrum, respectively of nanopowders. The *RT* magnetic studies were done using vibrating sample magnetometer (VSM) of Lake Shore of model 7404.

3. Results and discussion

3.1. Structural analysis

The representative X-ray diffraction (XRD) patterns of undoped and doped ZnS (x = 0.10) nanoparticles are shown in Fig. 1(a). The diffraction peaks corresponds to (111), (220) and (311) planes of cubic ZnS with space group *F*-43*m* (JCPDS file no. 00-002-0564). The average crystallite size was calculated by Debye-Scherrer equation [38]. The decrease in crystallite size with *TM* doping is due to smaller ionic radii of Co^{2+} (0.72 Å) and Fe^{3+} (0.64 Å) compared to Zn^{2+} (0.74 Å). On contrary, the marginal increase (4.80–5.23 nm) in crystallite size with *RE* doping is due to larger Tb^{3+} (1.25 Å) and Dy^{3+} (0.91 Å) ions. Further, the obtained shift in the peak (Fig. 1(b)) confirms that the cationic sites are well substituted in host ZnS. The

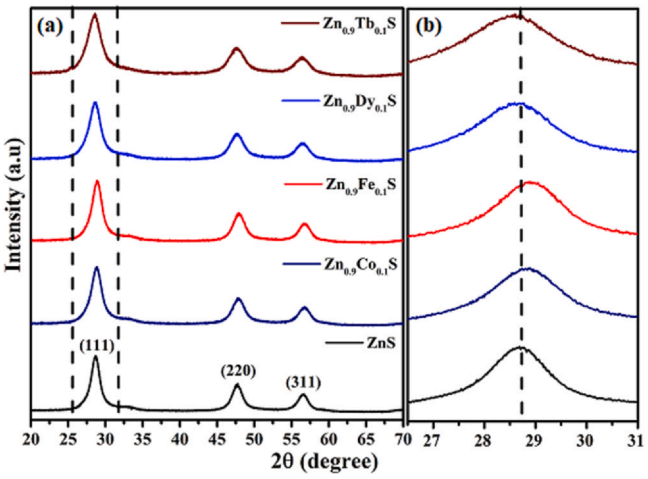

Fig. 1. (a) XRD patterns of doped nanoparticles (b) Magnified plot depicts peak shift.

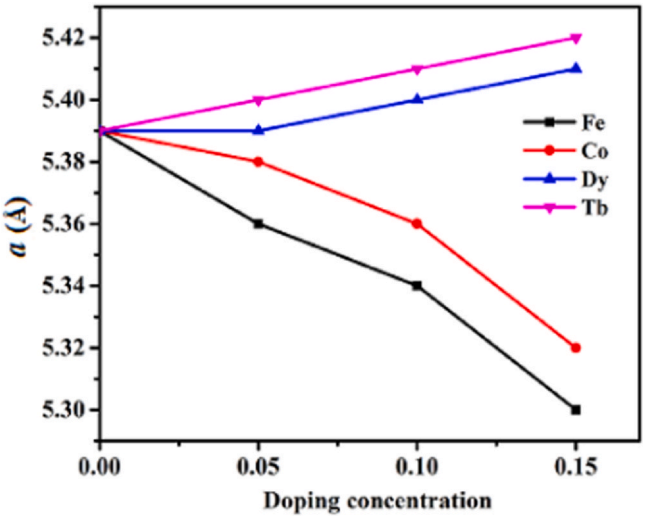

Fig. 2. Variation of lattice parameter '*a*' with doping.

change in lattice constant *'a'* with dopants is (Fig. 2) ascribed to different ionic radii of dopant and in agreement with the crystallite size variation.

3.2. Morphological studies

HR-TEM micrographs along with particle size distribution histogram of nanoparticles are shown in Fig. 3(a-k). All doped nanoparticles showed spherical morphology irrespective to type of dopant. A broad particle size distribution (4–11 nm) was observed for ZnS, which become narrower with doping. The average particle diameter of nanoparticles is given in Table 1 are comparable to crystallite size as calculated from Debye-Scherrer equation. It is clear that with *TM* doping particle size shrinks whereas with *RE* doping it increases. The size and shape of particles strongly depends upon the processing method. H. Hu *et al.* has given extensive comparative analysis of processing method and obtained particles size [39]. It was observed that for same processing method the particle size can be varied by changing the process parameters. Also same particle size can be obtained by different processing method. Since the objective of present study was to investigate the effect of dopants and their concentration, therefore same processing conditions were adopted to keep narrow particle size distribution. The *d*-spacing value measured from lattice fringe pattern (inset Fig. 3(a-e)) are about

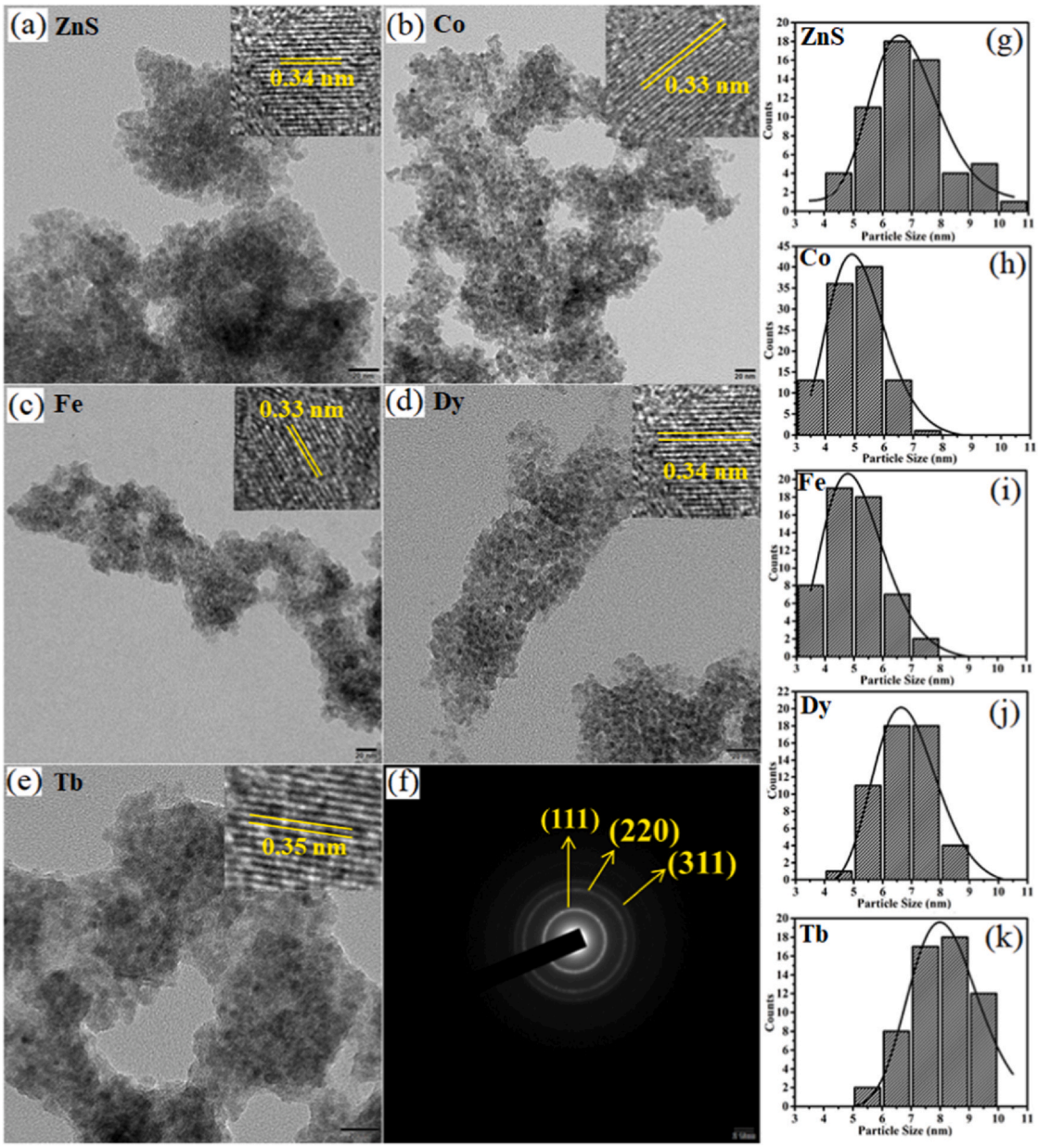

Fig. 3. (a–e) TEM micrographs of doped nanoparticles (f) SAED pattern of ZnS nanoparticles and (g–k) are particle size distribution histogram. Inset shows the lattice fringe patterns.

Table 1
Structural parameters and E_g of doped nanoparticles.

Sample	Concentration (x)	Crystallite/particle size (nm)			Optical bandgap (eV)
		XRD	TEM	UV- Vis	
ZnS	0	4.80	6.77	6.76	3.74
Co	0.05	4.25		5.52	3.77
	0.10	4.01	5.09	4.99	3.79
	0.15	3.90		4.42	3.82
Fe	0.05	4.08		4.77	3.80
	0.10	3.67	5.02	4.27	3.83
	0.15	3.61		3.90	3.86
Dy	0.05	4.85		7.40	3.73
	0.10	4.92	6.82	8.27	3.72
	0.15	4.97		9.56	3.71
Tb	0.05	5.17		9.56	3.71
	0.10	5.21	8.16	11.70	3.70
	0.15	5.23		16.55	3.69

~0.34 nm that corresponds to (111) plane of ZnS cubic structure. Fig. 3(f) shows the representative SAED patter for undoped ZnS nanoparticle that depicts continuous diffraction rings of (111), (220) and (311) planes, and in lines with XRD result. The similar SAED pattern has been observed for other samples. The presence of sharp well distinguished rings indicates the formation of small size nanoparticles.

EDS patterns of synthesized nanoparticles shown in Fig. 4 confirms the presence of Zn, S, Co, Fe, Dy and Tb without any contamination.

3.3. Optical analysis

3.3.1. UV–visible spectra

Fig. 5(a-c) depicts Tauc's plot ($(\alpha hv)^2$ vs hv) calculated from the UV–visible absorbance spectra recorded in the wavelength range of 250–500 nm (Inset). The estimated E_g from Tauc's plot are given in

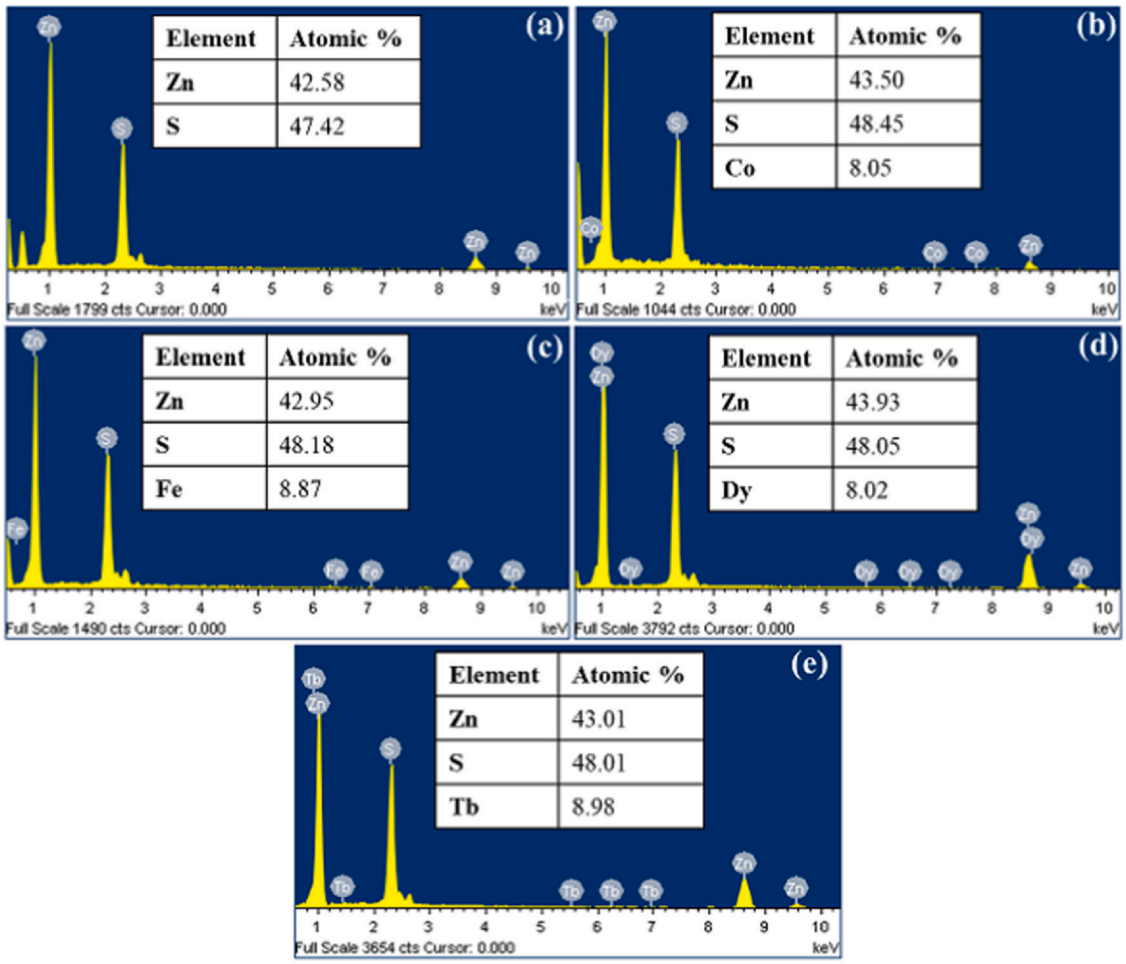

Fig. 4. EDS spectra of (a) ZnS (b) $Zn_{0.9}Co_{0.1}S$ (c) $Zn_{0.9}Fe_{0.1}S$ (d) $Zn_{0.9}Dy_{0.1}S$ (e) $Zn_{0.9}Tb_{0.1}S$ nanoparticles.

Table 1. The observed slight increase in E_g of undoped ZnS (3.74 eV) nanoparticles than its bulk (3.67 eV) counterpart can be ascribed to quantum confinement effect [36]. The comparable particle size with Bohr-exciton radii (2.5 nm), increases the separation between valence and conduction bands that consequently increases the optical E_g [37]. The E_g found to increase with TM doping concentration, whereas with *RE* doping it decreases marginally. The maximum E_g (3.86 eV) was observed for Fe doped and minimum (3.69 eV) for Tb doped ZnS nanoparticles. This variation in E_g is due to defect induced intermediate bands originated from different ionic radii and valance state of dopants that tune the electronic band structure of ZnS nanoparticles [40]. Using the obtained E_g, the particle size was further confirmed by Brus effective mass approximations (*EMA*) formula [41].

$$\Delta E_g = E_g^{nano} - E_g^{bulk} = \frac{h^2}{8R^2}\left(\frac{1}{m_e^*} + \frac{1}{m_h^*}\right) - \frac{1.8e^2}{\varepsilon R} \quad (1)$$

Where E_g^{nano} and E_g^{bulk} are optical band gap energy of nanoparticles and bulk in Joules, respectively. h is the plank's constant, R is radius of nanoparticle, $m_e^* = 0.34\ m_0$ and $m_h^* = 0.23\ m_0$ are effective mass of electrons and holes, respectively, where m_0 is free electron mass, e is the electronic charge and ε is dielectric constant of ZnS i.e. 8.76 [42]. The calculated particle size using Brus formula (Table 1) is in good agreement with XRD and TEM.

3.3.2. Photoluminescence spectra

The representative PL spectra of $x = 0.10$ obtained at excitation wavelength of 260 nm are represented in Fig. 6. All samples showed the peaks at ~359 nm, 423 nm, 451 nm, 484 nm, 528 nm and 567 nm with varied intensity. The peak at 359 nm is band to band edge transitions originating from the recombination of free excitons of ZnS nanoparticles [29]. According to defect distribution energy diagram of ZnS, the PL emission consist of two parts: first zinc vacancy (V_{Zn}) and interstitial sulphur atoms (I_S) as acceptor states located closer to valance band edge, and second sulphur vacancies (V_S) and interstitial zinc atoms (I_{Zn}) as donor states located closer to conduction band edge. The violet emission at 423 nm is attributed to transition from V_S to valence band edge of ZnS [43]. The two peaks at 451 nm and 484 nm are blue emissions associated with recombination of free charge carriers in shallow traps, at the surface of nanoparticles [44]. The two small humps at 528 nm and 567 nm are related to native defects of pure ZnS such as V_{Zn} [45,46]. No peaks related to dopant has been observed. The *RE* doped ZnS showed higher emission intensity than *TM*, which is favourable for their potential use in light emitting diodes [47].

3.4. Magnetic analysis

RT magnetization (*M-H*) loops of doped nanoparticles at different concentrations are shown in Fig. 7. The obtained measurable coercivity (H_c) and residual magnetization (M_r) (inset Fig. 7) confirms the presence of ferromagnetism in all samples. In previous studies undoped ZnS showed diamagnetic and paramagnetic behaviour. The observed ferromagnetic behaviour in ZnS can be ascribed to the presence of sulphur vacancies and higher surface to volume ratio of

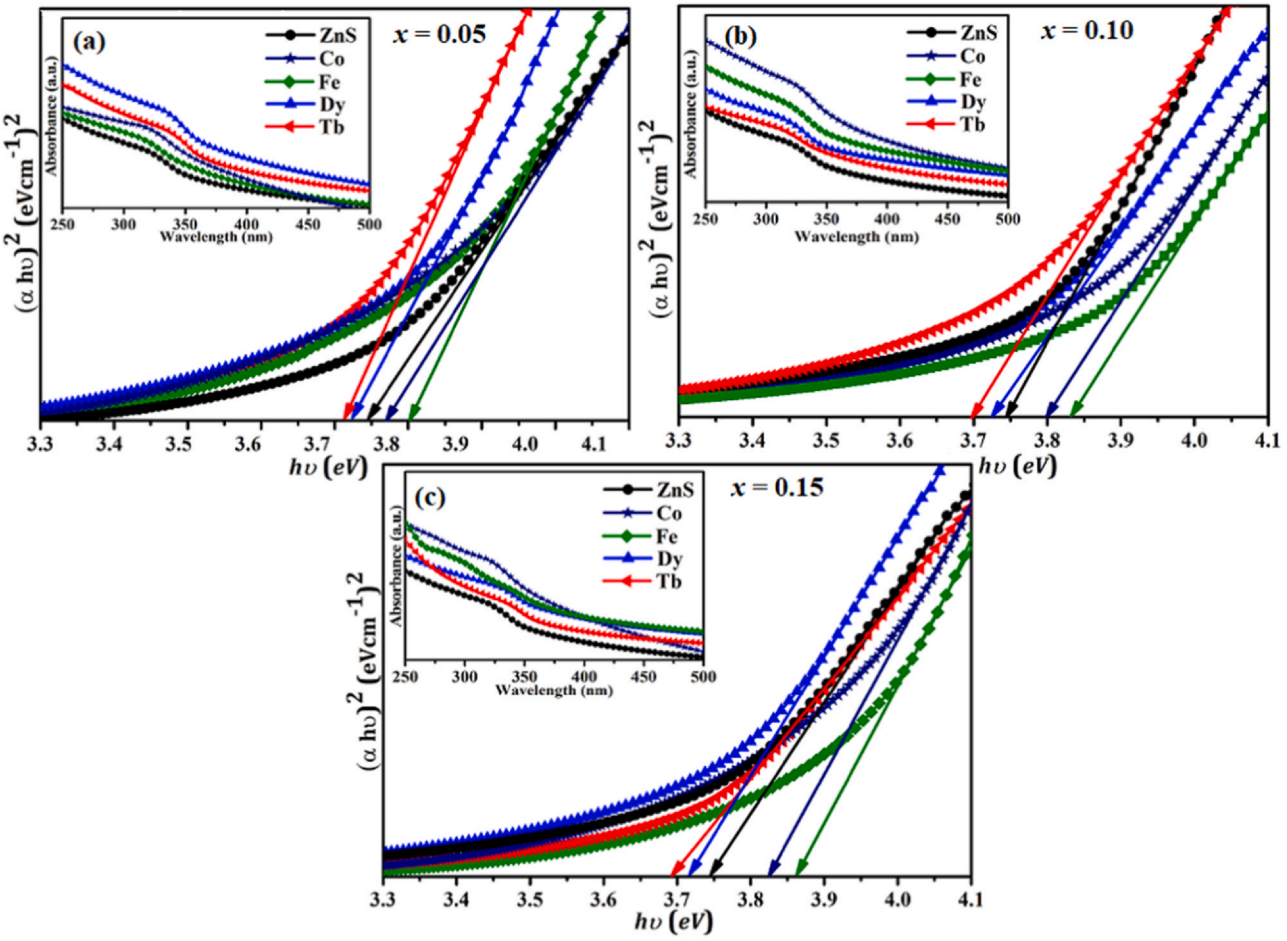

Fig. 5. (a–c) Tauc's plot of doped nanoparticles. Inset is UV–visible absorption spectra.

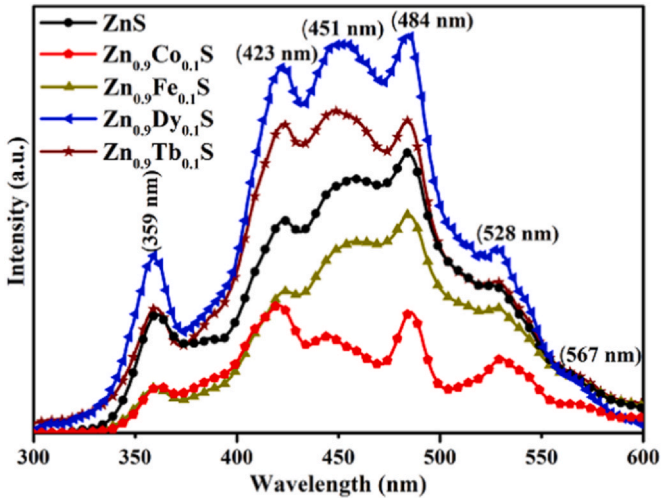

Fig. 6. PL spectra of doped nanoparticles.

nanoparticles which causes large number of uncompensated magnetic moments [6].

Table 2 shows that M_s and M_r are increasing with doping concentration for both *TM* and *RE* doped ZnS nanoparticle. The *TM* (Fe, Co) doped ZnS showed higher M_s than *RE* (Dy, Tb) due to higher magnetic moment of Fe^{3+} and Co^{2+} ion. On contrary, the lower H_c in *TM* doped suggest that inherit moment of Fe and Co contributes to swift demagnetization at lower magnetic field despite smaller particles. Also, low H_c of *RE* doped ZnS than undoped nanoparticle is due higher particle size (Table 1). Basically, the magnetic properties of DMS materials are interplay of particle size and type of dopant and its concentration. It has been observed that with decreasing particle size magnetization increases, however below a critical particle diameter, the ferromagnetism disappear and particle acquire superparamagnetism [7]. To understand the role of dopants, it is mandatory to isolate the size effect by keeping size distribution in narrow range. As discussed in introduction, *TM* doped ZnS showed different magnetization behaviour. A few studies showed that with increasing *TM* concentration, initially M_s increases and then decreases, due to dominant antiferromagnetic coupling at higher concentration [24]. In another study, Bhattacharya *et al.* has reported the signature of Fe^{2+} formation by magnetization vs temperature curve and showed the decrease in M_s due to anti ferromagnetic coupling between Fe^{3+} and Fe^{2+} ions. In the present work, M_s found to increase gradually which suggest that no antiferromagnetic coupling is present due to low doping concentration. The presence of any Fe^{2+} ion formation is also ignored due observed decrease in lattice parameter [48]. The observed high magnetization at low doping concentration suggests that doped ZnS nanoparticles are useful in data storage devices in field of spintronics.

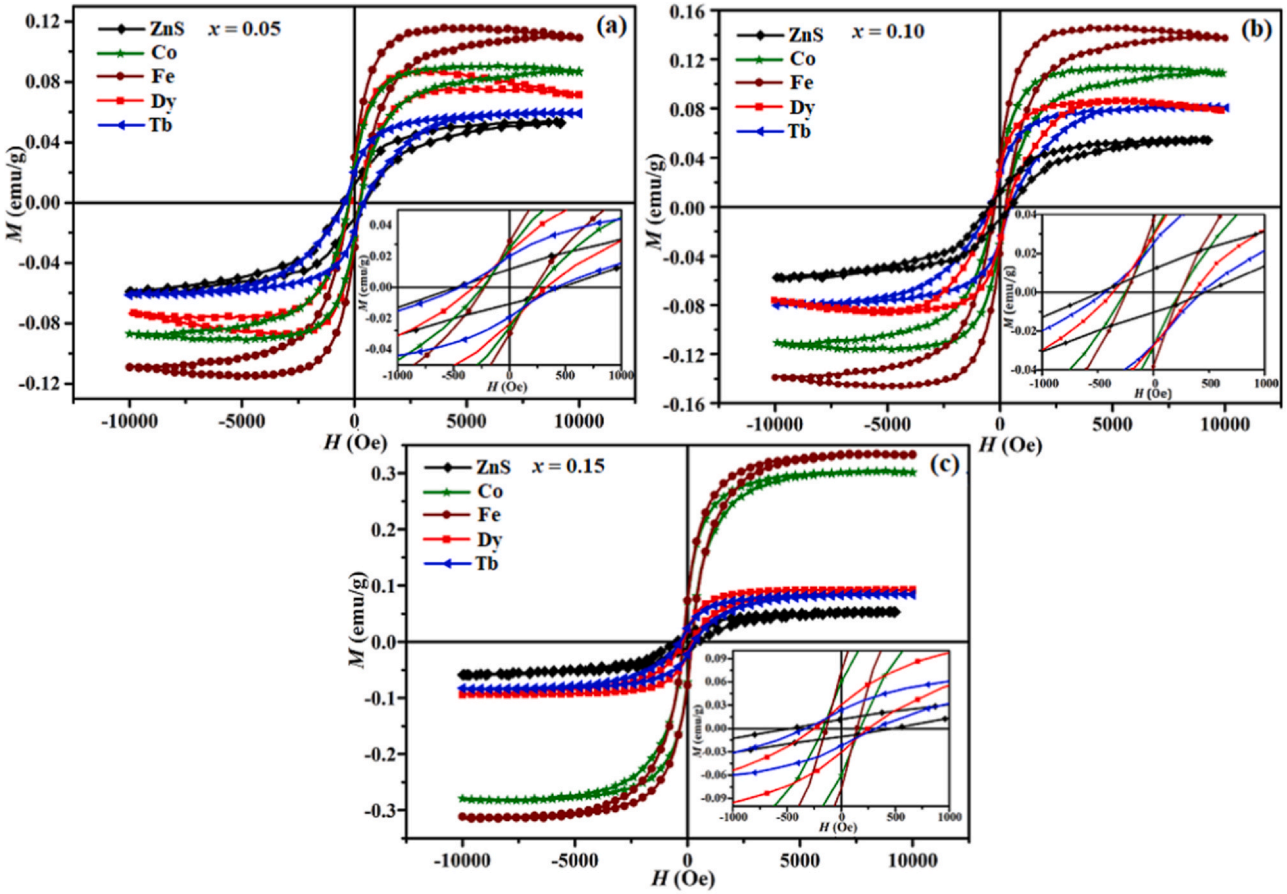

Fig. 7. *M-H* loops of doped nanoparticles. Inset shows the magnified view of *M-H* loops.

Table 2
Magnetic parameters of doped nanoparticles.

Sample	Concentration (x)	M at 1 T (emu/g)	M_r (emu/g)	H_c (Oe)
ZnS	0	0.057	0.011	471.1
Co	0.05	0.090	0.023	248.4
	0.10	0.108	0.029	247.5
	0.15	0.290	0.074	192.4
Fe	0.05	0.112	0.029	246.2
	0.10	0.137	0.037	243.5
	0.15	0.322	0.077	172.0
Dy	0.05	0.072	0.022	350.0
	0.10	0.084	0.028	367.7
	0.15	0.092	0.032	369.9
Tb	0.05	0.061	0.019	432.0
	0.10	0.078	0.026	443.4
	0.15	0.083	0.027	449.1

4. Conclusions

Series of Fe, Co, Dy and Tb doped ZnS nanoparticles were synthesized by hydrothermal technique. Effect of doping on structural, morphological, optical and magnetic properties were investigated and compared. Phase and microstructural analysis of nanoparticles confirmed cubic phase with spherical morphology. The particle size found to decrease with *TM* doping, whereas higher particle size has been obtained with *RE* doped ZnS. The tunable E_g from 3.69 to 3.86 eV has been observed in doped nanoparticles. *M-H* loops confirm *RT* ferromagnetism in all samples, where *TM* doped ZnS showed low H_c and higher M_s with a maximum value of 0.322 emu/g (Fe-doped). The present study revealed that optical and magnetic properties can be suitably tuned by *TM* or *RE* doping which could be used for both solar cells and data storage device applications.

CRediT authorship contribution statement

Shivani Jindal: Conceptualization, Methodology, Data curation, Writing - original draft, Resources, Visualization, Investigation, Validation, Writing - review & editing. **Puneet Sharma:** Supervision, Writing - review & editing.

Declaration of Competing Interest

The authors declare that they have no known competing financial interests or personal relationships that could have appeared to influence the work reported in this paper.

Acknowledgments

The author would like to acknowledge research fellowship by Thapar Institute of Engineering & Technology and DST-FIST for VSM facility.

References

[1] T. Dietl, A ten-year perspective on dilute magnetic semiconductors and oxides, Nat. Mater. 9 (2010) 965–974, https://doi.org/10.1038/nmat2898
[2] I. Zutic, J. Fabian, S. Das Sarma, Spintronics: fundamentals and applications, Rev. Mod. Phys. 76 (2004) 323–410.
[3] M. Ohno, K. Yoh, Datta-Das-type spin-field-effect transistor in the nonballistic regime, Phys. Rev. B 77 (2008) 1–7, https://doi.org/10.1103/PhysRevB.77.045323
[4] J. Perrenoud, L. Kranz, S. Buecheler, F. Pianezzi, A.N. Tiwari, The use of aluminium doped ZnO as transparent conductive oxide for CdS/CdTe solar cells, Thin Solid Films 519 (2011) 7444–7448, https://doi.org/10.1016/j.tsf.2010.12.234
[5] F. Haque, K.S. Rahman, M.A. Islam, M.J. Rashid, M. Akhtaruzzaman, M.M. Alam, Z.A. Alothman, K. Sopian, N. Amin, Growth optimization of ZnS thin films by RF magnetron sputtering as prospective buffer layer in thin film solar cells, Chalcogenide Lett. 11 (2014) 189–197.

[6] R. Singh, Unexpected magnetism in nanomaterials, J. Magn. Magn. Mater. 346 (2013) 58–73, https://doi.org/10.1016/j.jmmm.2013.07.005
[7] C.P. Bean, J.D. Livingston, Superparamagnetism, J. Appl. Phys. 30 (1959) 120–129, https://doi.org/10.1063/1.2185850
[8] N. Eryong, L. Donglai, Z. Yunsen, B. Xue, Y. Liang, J. Yong, J. Zhifeng, S. Xiaosong, Photoluminescence and magnetic properties of Fe-doped ZnS nano-particles synthesized by chemical co-precipitation, Appl. Surf. Sci. 257 (2011) 8762–8766, https://doi.org/10.1016/j.apsusc.2011.03.114
[9] F.A. La Porta, J. Andre, M.S. Li, J.R. Sambrano, J.A. Varela, E. Longo, Zinc blende versus wurtzite ZnS nanoparticles: control of the phase and optical properties by tetrabutylammonium hydroxide, Phys. Chem. Chem. Phys. 16 (2014) 20127–20137, https://doi.org/10.1039/c4cp02611j
[10] V. Ramasamy, K. Praba, G. Murugadoss, Synthesis and study of optical properties of transition metals doped ZnS nanoparticles, Spectrochim. Acta Part A Mol. Biomol. Spectrosc. 96 (2012) 963–971, https://doi.org/10.1016/j.saa.2012.07.125
[11] P. Chandra, P.P.C. Srivastava, Fe doping in ZnS for realizing nanocrystalline-diluted magnetic semiconductor phase, J. Mater. Sci. 49 (2014) 6012–6019, https://doi.org/10.1007/s10853-014-8321-1
[12] S. Kumar, P. Mandal, A. Singh, S. Husain, D. Kumar, V.K. Malik, S. Sharma, Magnetization properties of Co incorporated ZnS nanocrystals synthesized at low temperature via chemical route, J. Alloy. Compd. 830 (2020) 154640, https://doi.org/10.1016/j.jallcom.2020.154640
[13] B. Poornaprakash, U. Chalapathi, S. Park, Structural and magnetic properties of ZnS: Tb^{3+} nanoparticles, J. Mater. Sci. Mater. Electron. 28 (2017) 3672–3677, https://doi.org/10.1007/s10854-016-5972-5
[14] I. Lopez-Quintas, E. Rebollar, D. Ávila-Brande, J.G. Izquierdo, L. Bañares, C. Díaz-Guerra, A. Urbieta, M. Castillejo, R. de Nalda, M. Martín, Femtosecond double-pulse laser ablation and deposition of co-doped ZnS thin films, Nanomaterials 10 (2020) 1–15, https://doi.org/10.3390/nano10112229
[15] F.J. Rodriguez, J. Reyes, D.Y. Medina, M.A. Barron, C. Haro-Perez, Synthesis of ZnS:Tm3+ nanoparticles by the polyol method, Open J. Appl. Sci. 09 (2019) 613–619, https://doi.org/10.4236/ojapps.2019.97049
[16] S. Sambasivam, B.K. Reddy, A. Divya, N. Madhusudhana Rao, C.K. Jayasankar, B. Sreedhar, Optical and ESR studies on Fe doped ZnS nanocrystals, Phys. Lett. A 373 (2009) 1465–1468, https://doi.org/10.1016/j.physleta.2009.02.032
[17] X. Zeng, J. Zhang, F. Huang, X. Zeng, J. Zhang, F. Huang, Optical and magnetic properties of Cr-doped ZnS nanocrystallites, J. Appl. Phys. 111 (2012) 123525, https://doi.org/10.1063/1.4729877
[18] K. Sharma, P. Kumar, G. Verma, A. Kumar, Optical properties of transition metal doped ZnS nanoparticles in PVK based nanocomposite films, Optik 206 (2020) 164357, https://doi.org/10.1016/j.ijleo.2020.164357
[19] D. Sridevi, K.V. Rajendran, Enhanced photoluminescence of ZnS nanoparticles doped with transition and rare earth metallic ions, Chalcogenide Lett. 7 (2010) 397–401.
[20] G. Gurung, T.K. Ekanayaka, A.J. Yost, T.R. Paudel, Absorption enhancement by transition metal doping in ZnS, Mater. Res. Express 6 (2019) 126550, https://doi.org/10.1088/2053-1591/ab56d6
[21] B. Poornaprakash, P.T. Poojitha, U. Chalapathi, K. Subramanyam, S. Park, Synthesis, structural, optical, and magnetic properties of Co doped, Sm doped and Co+Sm co-doped ZnS nanoparticles, Physica E 83 (2016) 180–185, https://doi.org/10.1016/j.physe.2016.05.025
[22] P. Mukherjee, C.M. Shade, A.M. Yingling, D.N. Lamont, D.H. Waldeck, Lanthanide sensitization in II - VI semiconductor materials: a case study with terbium (III) and europium (III) in zinc sulfide nanoparticles, J. Phys. Chem. A 115 (2011) 4031–4041.
[23] R. Sarkar, C.S. Tiwary, P.Ã. Kumbhakar, A.K. Mitra, Enhanced visible light emission from Co^{2+} doped ZnS nanoparticles, Phys. B Phys. Condens. Matter 404 (2009) 3855–3858, https://doi.org/10.1016/j.physb.2009.07.106
[24] S. Sambasivam, D.P. Joseph, J.G. Lin, C. Venkateswaran, Doping induced magnetism in Co–ZnS nanoparticles, J. Solid State Chem. 182 (2009) 2598–2601, https://doi.org/10.1016/j.jssc.2009.07.015
[25] Y. Li, C. Cao, Z. Chen, Magnetic and optical properties of Fe doped ZnS nanoparticles synthesized by microemulsion method, Chem. Phys. Lett. 517 (2011) 55–58, https://doi.org/10.1016/j.cplett.2011.09.048
[26] D. Saikia, R.D. Raland, J.P. Borah, In fluence of Fe doping on the structural, optical and magnetic properties of ZnS diluted magnetic semiconductor, Physica E 83 (2016) 56–63, https://doi.org/10.1016/j.physe.2016.04.016
[27] S. Sambasivam, D.P. Joseph, D.R. Reddy, B.K. Reddy, C.K. Jayasankar, Synthesis and characterization of thiophenol passivated Fe-doped ZnS nanoparticles, Mater. Sci. Eng. B 150 (2008) 125–129, https://doi.org/10.1016/j.mseb.2008.03.009
[28] P. Chandra, P. Surajit, G.P.C. Srivastava, Antiferromagnetic coupling in Co-doped ZnS, J. Mater. Sci. 50 (2015) 7919–7929, https://doi.org/10.1007/s10853-015-9356-7
[29] K. Patel, M.P.D.S.H. Chaki, Effect of Cobalt doping on ZnS nanoparticles synthesized by microwave irradiation, J. Mater. Sci. Mater. Electron. 28 (2017) 5029–5036, https://doi.org/10.1007/s10854-016-6159-9
[30] B. Poornaprakash, U. Chalapathi, S.V.P. Vattikuti, Compositional, morphological, structural, microstructural, optical, and magnetic properties of Fe, Co, and Ni doped ZnS nanoparticles, Appl. Phys. A 123 (2017) 1–10, https://doi.org/10.1007/s00339-017-0865-x
[31] S. Kumar, N.K. Verma, Room temperature magnetism in Co-doped ZnS nanoparticles, J. Supercond. Nov. Magn. 28 (2015) 137–142, https://doi.org/10.1007/s10948-014-2823-6
[32] S. Kumar, N. Verma, Structural, optical and magnetic investigations on Fe-doped ZnS nanoparticles, J. Mater. Sci. Mater. Electron. 26 (2015) 2754–2759, https://doi.org/10.1007/s10854-015-2755-3
[33] S. Kumar, N.K. Verma, Investigation of the magnetic and optical properties of wurtzite Fe-doped ZnS nanorods, J. Electron. Mater. 44 (2015) 2829–2834, https://doi.org/10.1007/s11664-015-3688-6
[34] S. Kumar, N.K. Verma, Room temperature investigations on optical and magnetic studies of $Co_xZn_{1-x}S$ nanorods, J. Magn. Magn. Mater. 374 (2015) 548–552, https://doi.org/10.1016/j.jmmm.2014.08.100
[35] S.P. Patel, J.C. Pivin, A.K. Chawla, R. Chandra, D. Kanjilal, L. Kumar, Room temperature ferromagnetism in $Zn_{1-x}Co_xS$ thin films with wurtzite structure, J. Magn. Magn. Mater. 323 (2011) 2734–2740, https://doi.org/10.1016/j.jmmm.2011.05.057
[36] B. Poornaprakash, P.T. Poojitha, U. Chalapathi, S. Ramu, R.P. Vijayalakshmi, S.-H. Park, Chemical synthesis, compositional, morphological, structural, optical and magnetic properties of $Zn_{1-x}Dy_xS$ nanoparticles, Ceram. Int. 42 (2016) 8092–8097.
[37] S. Ramu, R.P. Vijayalakshmi, Effect of terbium doping on the structural and magnetic properties of ZnS nanoparticles, J. Supercond. Nov. Magn. 30 (2017) 1921–1925, https://doi.org/10.1007/s10948-016-3960-x
[38] B.D. Cullity S.R. Stock, Elements of X-RAY Diffraction, second ed., 1978.
[39] H. Hu, W. Zhang, Synthesis and properties of transition metals and rare-earth metals doped ZnS nanoparticles, 28 (2006) 536–550, https://doi.org/10.1016/j.optmat.2005.03.015
[40] C.B. Murray, D.J. Noms, M.G. Bawendi, Synthesis and characterization of nearly monodisperse CdE (E=S, Se, Te) semiconductor nanocrystallites, J. Am. Chem. Soc. 115 (1993) 8706–8715, https://doi.org/10.1021/ja00072a025
[41] L. Brus, Electronic wave functions in semiconductor clusters: experiment and theory, J. Phys. Chem. 90 (1986) 2555–2560.
[42] N. Khorasanipoor, P. Iranmanesh, S.T. Yazdi, S. Saeednia, Synthesis and characterization of EDTA-assisted ZnS:Hg nanoparticles, J. Lumin. 219 (2020) 116948, https://doi.org/10.1016/j.jlumin.2019.116948
[43] V.P. Devarajan, D. Nataraj, T. Pazhanivel, K. Senthil, M. Seol, K. Yong, J. Hermannsdorfer, R. Kempe, Molecular conformation dependent emission behaviour (blue, red and white light emissions) of all-trans-β-carotene-ZnS quantum dot hybrid nanostructures, J. Mater. Chem. 22 (2012) 18454–18462, https://doi.org/10.1039/c2jm32982d
[44] K. Sooklal, B.S. Cullum, S.M. Angel, C.J. Murphy, Photophysical properties of ZnS nanoclusters with spatially localized Mn2+, J. Phys. Chem. 100 (1996) 4551–4555, https://doi.org/10.1021/jp952377a
[45] D. Denzler, M. Olschewski, K. Sattler, Luminescence studies of localized gap states in colloidal ZnS nanocrystals, J. Appl. Phys. 84 (1998) 2841–2845, https://doi.org/10.1063/1.368425
[46] D.V. Dake, N.D. Raskar, V.A. Mane, R.B. Sonpir, E. Stathatos, K. Asokan, P.D. Babu, B.N. Dole, Exploring the role of defects on diverse properties of Cr-substituted ZnS nanostructures for photocatalytic applications, Appl. Phys. A Mater. Sci. Process. 126 (2020) 1–15, https://doi.org/10.1007/s00339-020-03669-1
[47] C. Jayachandraiah, K.S. Kumar, G. Krishnaiah, N.M. Rao, Influence of Dy dopant on structural and photoluminescence of Dy-doped ZnO nanoparticles, J. Alloy. Compd. 623 (2015) 248–254, https://doi.org/10.1016/j.jallcom.2014.10.067
[48] S. Bhattacharya, D. Chakravorty, Electrical and magnetic properties of cold compacted iron-doped zinc sulfide nanoparticles synthesized by wet chemical method, Chem. Phys. Lett. 444 (2007) 319–323, https://doi.org/10.1016/j.cplett.2007.07.040

J Mater Sci: Mater Electron

Ferromagnetic transition metal-doped CdS nanoparticles: a comparative study

Shivani Jindal[1] and Puneet Sharma[1,*]

[1] School of Physics & Materials Science, Thapar Institute of Engineering & Technology, Patiala 147004, India

Received: 9 June 2020
Accepted: 24 September 2020

ABSTRACT

In the present work, series of ferromagnetic transition metal-doped (Fe, Co) CdS nanoparticles were synthesized via hydrothermal technique. The particles were characterized for structural, morphological, optical and magnetic properties. The X-ray diffraction confirmed the single wurtzite phase for all compositions. The relatively smaller crystallite size (~ 11.50 nm) was obtained with Fe (x = 0.15) compared to Co doping (~ 13.88 nm). The HR-TEM micrographs revealed spherical morphology of nanoparticles with decrease in average particle size. The increase in optical band gap was observed with doping. In photoluminescence spectra, the main emission peak at 529 nm corresponds to green emission due to *d-d* intra ion transition. The magnetic analysis confirmed room temperature ferromagnetism in all the compositions and highest value of saturation magnetization has been observed for Fe-doped nanoparticles.

1 Introduction

Dilute magnetic semiconductors (DMS) have gained remarkable attention due to their potential application in spintronic devices, solar cells, light emitting diodes and gas sensors [1–5]. These materials exhibit entirely different properties at nanoscale regime compared to their bulk counterpart. The two foremost important properties of these nano materials are existence of suitable bandgap (E_g) which is well exploited for solar cell applications and weak ferromagnetism which is yet to be explored for storage devices. The origin of ferromagnetism in these materials is controversial and has been explained by various types of exchange interactions, i.e., super exchange, double exchange and RKKY interactions [6]. It is also reported that presence of secondary phases and defects were also contribute to ferromagnetism [7, 8]. However, existence of weak room temperature (*RT*) magnetization restricts their application in realized devices.

Among various II-VI DMS materials, CdS with direct optical E_g of 2.42 eV have been extensively investigated. Various techniques have been employed to synthesize CdS nanostructures such as sol-gel, hydrothermal, chemical co-precipitation, etc. to control particle sizes by suitable process parameter [9–11]. In one of the focuses, the effect of particle size and its distribution were extensively investigated and well established [12, 13]. In another approach, the magnetic and optical properties were tuned by suitable cation doping. The major investigations were

Address correspondence to E-mail: puneet.sharma@thapar.edu

https://doi.org/10.1007/s10854-020-04549-3
Published online: 06 October 2020

related to rare earth (*RE*) (Dy, Gd, Tb, Eu etc.) and transition metals (*TM*) (Fe, Cr, Co etc.) doping using different synthesis techniques [14–20]. Among the *RE* and *TM*, *RE* reportedly enhances magnetization and luminescent properties. However, their low Curie temperature (below *RT*) can be a disadvantage for any application where *RT* magnetization is of primary importance. Therefore, doping of *TM* (Fe, Co) with high magnetic moment at *RT* may contribute to higher magnetization. Also, their smaller ionic radii compared to Cd^{2+} will provide lattice stress, which may help to tune optical E_g. The Fe- and Co-doped CdS nanostructures has been reported by several researchers, but the comparative study on optical and magnetic properties at higher doping concentration is limited [21, 22]. A few studies reported the paramagnetic behaviour of CdS nanoparticles upon doping with Fe and Co [23–25], whereas a decreased magnetization with doping concentration was observed due to antiferromagnetic coupling [26]. Therefore, to understand this ambiguity, a comparative study of Fe- and Co-doped nanostructures processed under similar condition may give a deep insight for better understanding.

Among various techniques employed to synthesize CdS nanoparticles, hydrothermal method is more advantageous because of easy control on processing parameters to produce particles of finite size, good chemical homogeneity and high purity at low temperature. In the present work, Fe- and Co-doped CdS nanoparticles at $x = 0$, 0.05, 0.10 and 0.15 have been synthesized by hydrothermal method. A systematic investigation on dopant induced variations in structural, optical, and magnetic properties was carried out.

2 Experimental details

Laboratory grade cadmium chloride monohydrate ($CdCl_2{\cdot}xH_2O$), sodium sulphide (Na_2S), ferric chloride hexahydrate ($FeCl_3{\cdot}6H_2O$) and cobalt chloride hexahydrate ($CoCl_2{\cdot}6H_2O$) of 99.9% purity from sigma-aldrich were used to synthesized $Cd_{1-x}Fe_xS$ and $Cd_{1-x}Co_xS$ ($x = 0.0$, 0.05, 0.10 and 0.15) nanoparticles via hydrothermal method. 0.25 M of $CdCl_2{\cdot}xH_2O$ and appropriate concentration of dopant were dissolved in distilled water. The colour of solutions changes from transparent to pale yellow (Fe-doping) and purplish pink (Co doping) with doping. Then, 0.25 M of Na_2S was added dropwise into the above solution and stirred for 1 h. The solution was transferred into 100 ml teflon-lined stainless steel autoclave with 80% of the total volume and placed in oven at 160 °C for 5 h. The autoclave was allowed to cool at *RT*. The obtained yellow colour precipitates were collected and washed with ethanol and distilled water for several times to remove impurities. The samples were finally dried in hot air oven at 60 °C. The powders were annealed at 300 °C in argon atmosphere for 1 h.

The X-ray diffractometer (XRD) of PANalytical X'Pert PRO MRD with CuK_α ($\lambda = 1.5418$ Å) was used to confirm the phase formation. The morphological features and selected area electron diffraction (SAED) patterns were recorded by high-resolution transmission electron microscopy (HR-TEM) (Hitachi H-7650). The elemental analysis was carried out by energy dispersive spectroscopy (EDS) model JEOL (JSM-1T100). Perkin Elmer Lambda 45 spectrophotometer and Agilent Carry Eclipse fluorescence spectrophotometer (G9800A) were used to determine UV-visible absorption spectra and *RT* photoluminescence (PL) spectrum, respectively, of nanopowders. The *RT* magnetic measurements were done using vibrating sample magnetometer (VSM) of Lake Shore model 7404.

3 Results and discussion

3.1 Structural analysis

The XRD patterns of synthesized nanopowders are illustrated in Fig. 1. that indicates the polycrystalline nature of powders. All XRD patterns were refined by Rietveld method using fullprof software with hexagonal symmetry (space group $P6_3mc$). The refinements were best fitted as χ^2 values were well below 2. Table 1 shows the structural parameters as obtained from refinement. The peak shift (inset Fig. 1) towards higher diffraction angle is due to stresses in the lattice as a consequence of smaller ionic radii of Fe^{3+} ion (0.64 Å) and Co^{2+} ion (0.74 Å) compared to Cd^{2+} ion (0.97 Å) [26, 27]. The c/a ratio is 1.63 which confirms the hexagonal symmetry of nanoparticles. The crystallite sizes (*D*) of nanoparticles were calculated using the Debye-Scherrer formula [28].

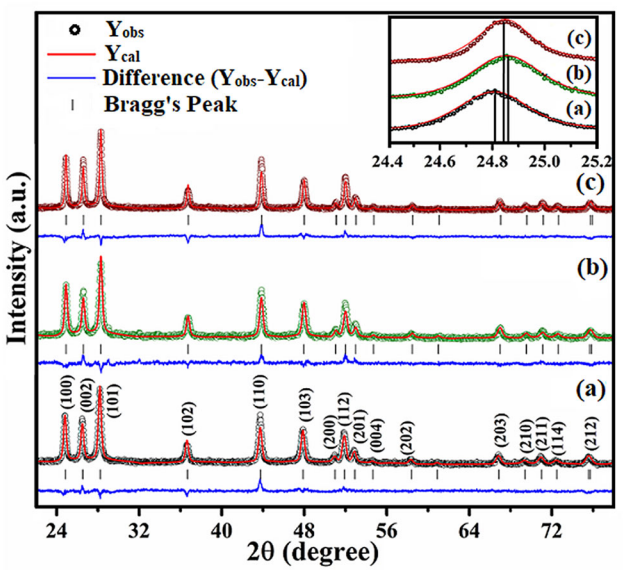

Fig. 1 Refined XRD pattern of **a** CdS, **b** $Cd_{1-x}Fe_xS$ and **c** $Cd_{1-x}Co_xS$ ($x = 0.15$) nanoparticles. Inset shows the enlarged view of (100) plane

$D = \frac{0.9\lambda}{\beta Cos\theta}$ where, λ is wavelength of X-ray, θ is the Bragg's angle, β is full width at half maximum (FWHM) calculated from Caglioti equation $(u\tan^2\theta + v\tan\theta + w)^{1/2}$, function u, v and w are the shape parameters obtained from refinement. A consistent decrease in lattice parameters and D (Table 1) with doping concentration confirms that cationic sites are well substituted in host CdS lattice.

3.2 Morphological analysis

HR-TEM micrographs of $Cd_{1-x}Fe_xS$ and $Cd_{1-x}Co_xS$ nanoparticles for $x = 0.0$ and 0.10 are shown in Fig. 2a–c. The particle size distribution and corresponding Gaussian curve fitting of samples are representing in Fig. 2e–g. The average particle diameter of undoped CdS is 37.69 nm which decreased to 13.06 nm (Fe) and 19.14 nm (Co). The particle size as obtained from TEM was reduced by more than half for the doped system. The measured d-spacing value from lattice fringe pattern is ~ 0.38 nm, 0.33 nm and 0.35 nm as shown in inset, corresponds to (002) plane of hexagonal structure of CdS. The decrease in d-spacing can be ascribed to lattice shrinkage with doping. The SAED pattern for CdS (Fig. 2d) is not sharp indicating the nano crystalline nature of nanoparticles.

Figure 3 represents EDS pattern of $Cd_{1-x}Fe_xS$ and $Cd_{1-x}Co_xS$ ($x = 0.10$) nanoparticles that confirms the presence of Cd, S, Fe and Co without any contamination.

3.3 Optical analysis

3.3.1 *UV- visible spectra*

Figure 4a, b shows the UV–visible absorption spectra of $Cd_{1-x}Fe_xS$ and $Cd_{1-x}Co_xS$ nanoparticles recorded from 450 to 700 nm. The blue shift in absorbance wavelength was observed with doping. The optical E_g was determined using the following Tauc's equation [29]:

Table 1 Structural parameters and E_g of $Cd_{1-x}Fe_xS$ and $Cd_{1-x}Co_xS$ nanoparticles

Doping concentration (x)	Lattice parameters ($Å$)		Crystallite Size D (nm)	Optical bandgap E_g (eV)
	a	c		
CdS				
0.0	4.135	6.715	19.67	2.48
$Cd_{1-x}Fe_xS$				
0.05	4.133	6.713	14.81	2.53
0.10	4.131	6.710	13.80	2.55
0.15	4.130	6.709	11.50	2.56
$Cd_{1-x}Co_xS$				
0.05	4.134	6.715	17.07	2.49
0.10	4.133	6.712	15.53	2.51
0.15	4.131	6.710	13.88	2.53

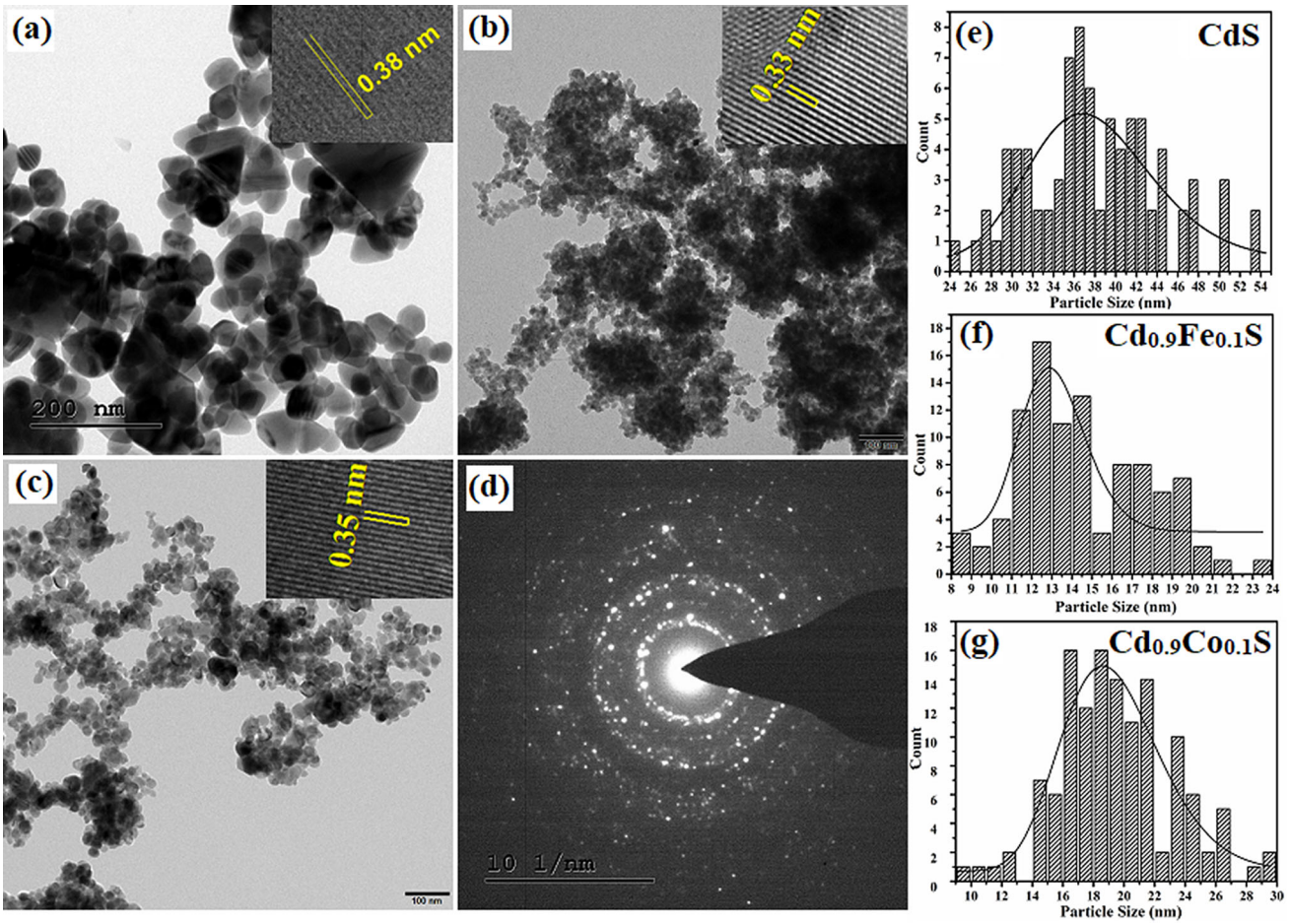

Fig. 2 TEM micrographs of **a** CdS **b** $Cd_{0.9}Fe_{0.1}S$ **c** $Cd_{0.9}Co_{0.1}S$ **d** SAED pattern for CdS and **e**–**g** are particle size distribution histogram. Inset shows lattice fringe pattern

$$\alpha h\upsilon = A(h\upsilon - E_g)^n$$

where α is absorption coefficient, υ is frequency, constant A is function of electronic transition probability, h is Plank's constant and n is type of transition (for direct transition $n = 1/2$). E_g was determined by extrapolating the plot of $(\alpha h\upsilon)^2$ vs. $h\upsilon$.

The variation in Eg with Fe and Co doping is shown in Fig. 4(c, d) and tabulated in Table 1. The Eg for undoped CdS is 2.48 eV increased with doping to 2.56 eV (Fe) and 2.53 eV (Co). The change in Eg can be attributed to various factors such as formation of defects, quantum confinement effect etc. Since, the size of nanoparticles in our system is much higher than Bohr-exciton radii (5 nm) therefore the size effect has no role in the modification of E_g. The widening of E_g with doping content can be ascribed to Burstein–Moss effect. According to which, when excess carriers are introduced in host lattice, the Fermi level shifts in conduction band because of *sp-d* exchange interaction between the band electrons and localized spin of Co and Fe [30]. This exchange interaction produces the excess carriers which occupy the states closer to Fermi level in conduction band, resulting in shifting of E_g to higher levels. Further, formation of various sulphur related defects with doping, tends to change the electronic band structure of host lattice [31].

3.3.2 *Photoluminescence spectra*

RT-photoluminescence spectra of the synthesized nanoparticles are represented in Fig. 5 obtained at excitation wavelength of 380 nm. Four peaks are observed at 490 nm, 529 nm, 540 nm and 571 nm in all compositions. The peak at 490 nm correspond to blue emissions. The main emission band at around 529 nm is due to green emission, which can be

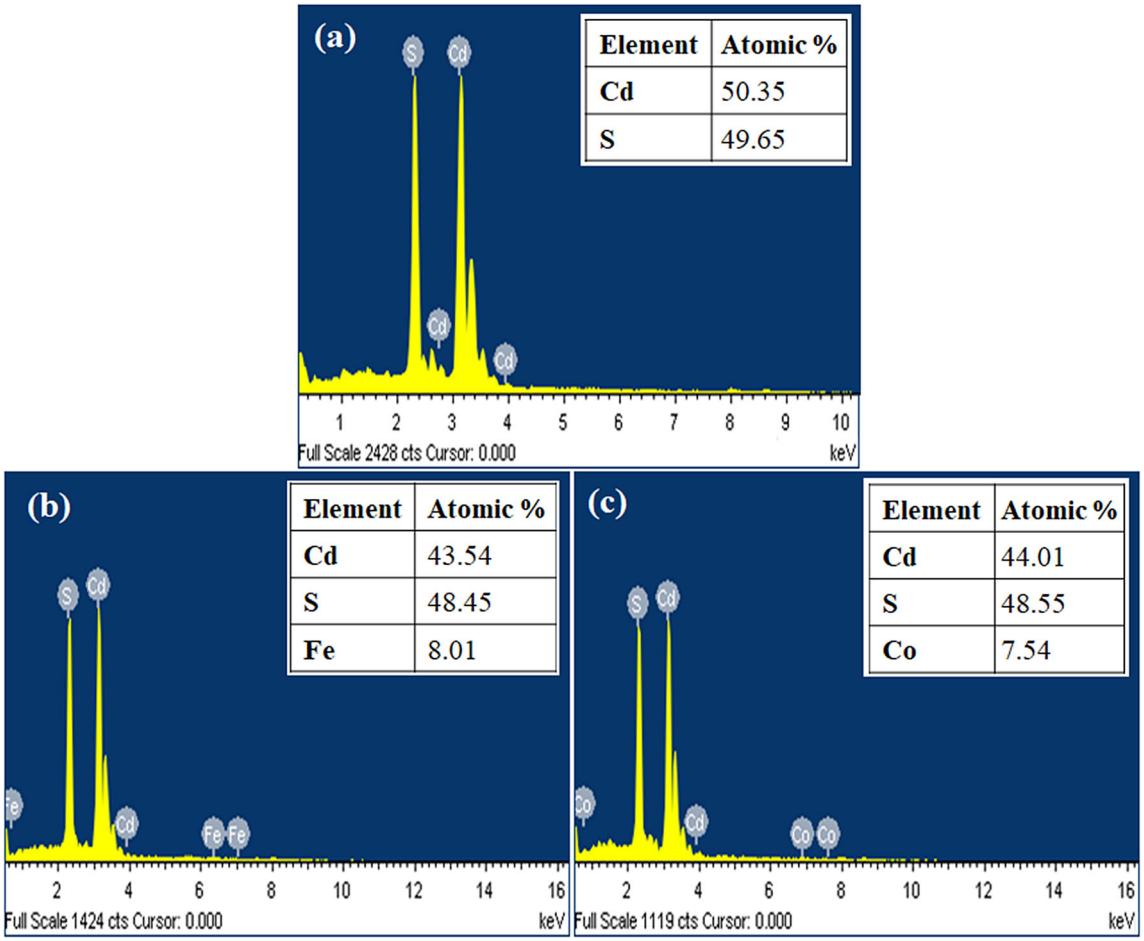

Fig. 3 EDS spectra of **a** CdS, **b** $Cd_{0.9}Fe_{0.1}S$, **c** $Cd_{0.9}Co_{0.1}S$ nanoparticles

attributed to surface donor-acceptor pair recombination and also to *d–d* intra ion transitions [32]. Two small peaks at 540 nm and 571 nm are due to presence of surface traps. On doping, the peak at 540 nm slightly shifts to higher wavelength ~ 544 nm. This can be ascribed to increase surface or trap defects due to formation of sulphur or cadmium vacancies with increasing doping content. No dopant related peaks has been observed. However, the intensity of peaks gets quenched with doping. The quenching of PL intensity can be attributed to formation of deep centers or defects that inhibit more number of electrons / holes to get excited and give rise to non-radiative transitions. However, intensity of Fe-doped CdS is higher than Co, as doping of Fe^{3+} may create more Cd^{2+} vacancies as compared to Co^{2+} to maintain the charge neutrality. This causes high donor-acceptor pair recombination in Fe-doped CdS than in Co-doped CdS. Similar type of quenching has been reported in literature [26, 33].

3.4 Magnetic analysis

RT magnetic hysteresis (*M–H*) loops of Fe- and Co-doped CdS nanoparticles are shown in Fig. 6. All composition shows measurable coercivity (H_c) and residual magnetization (M_r) (inset Fig. 6) which confirms ferromagnetic ordering. The origin of ferromagnetism in DMS can be ascribed to various reasons firstly; the formation of ion vacancies and defects [34]. Secondly; the higher surface to volume ratio of nanoparticles causes larger number of magnetic moment; the exchange interaction between them favours parallel alignment of spin magnetic moment that results in higher saturation magnetization (M_s) [6]. The observed ferromagnetism in undoped CdS can be attributed to above mentioned reasons. Beside the own magnetization of CdS nanoparticles, doping with Fe and Co further contribute to ferromagnetism, which is well evident from Fig. 6. The M_s is linearly increasing with doping

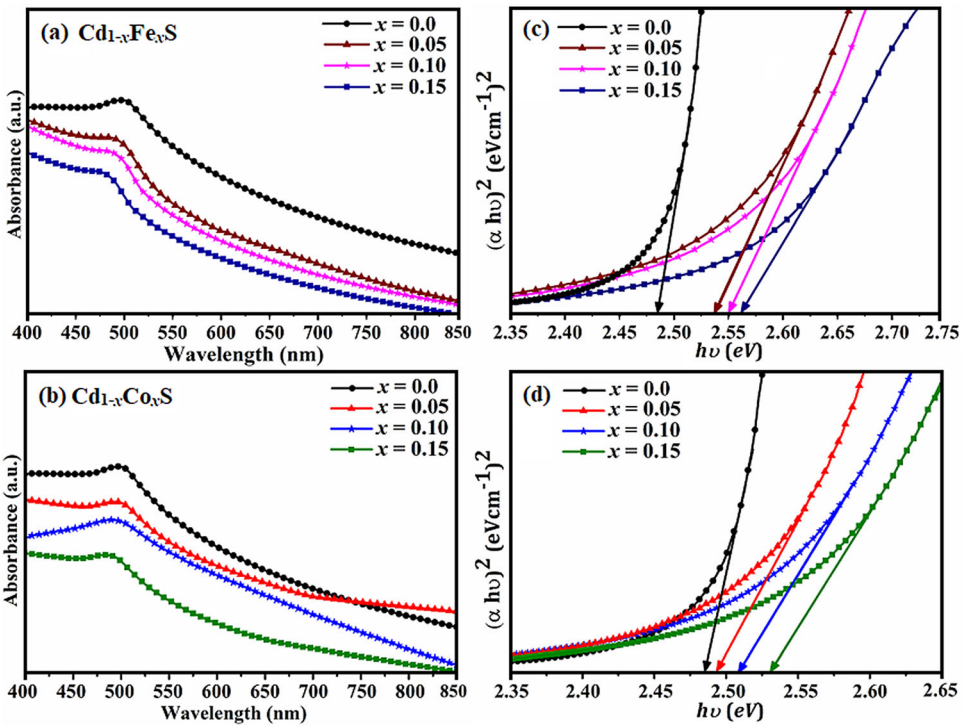

Fig. 4 **a** and **b** UV–visible absorption spectra, **c** and **d** Tauc's plot of $Cd_{1-x}Fe_xS$ and $Cd_{1-x}Co_xS$ nanoparticles

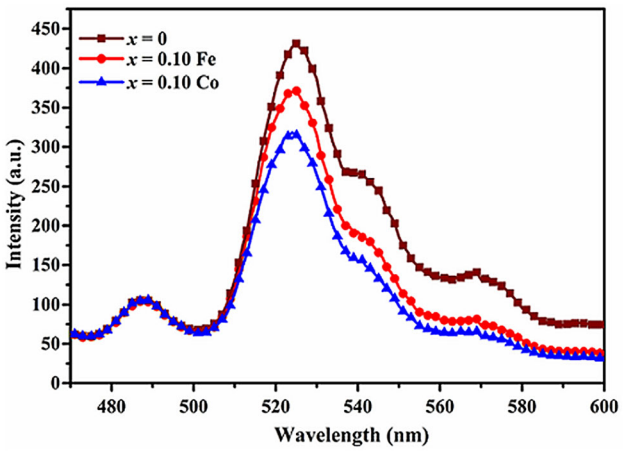

Fig. 5 PL spectra of $Cd_{1-x}Fe_xS$ and $Cd_{1-x}Co_xS$ ($x = 0.10$) nanoparticles

concentration. Also, as reflected from PL spectra due to higher surface donor-acceptor pair recombination, $Cd_{1-x}Fe_xS$ should have a weak magnetism. However, the higher M_s in Fe-doped nanoparticles is due to higher magnetic moment of Fe^{3+} ion compared to Co^{2+} ion that may have obscure the weak magnetism caused by donor-acceptor pair recombination in Fe-doped CdS nanoparticles. The decrease in H_c with doping is consequence of soft magnetic nature of *TM* ions (Fe, Co) (Table 2). Comparing the magnetic nature of Fe and Co, Co is hexagonal in nature and magnetization vector remain along c axis, whereas Fe is cubic with magnetization vector along $< 100 >$ direction [35, 36]. Moreover, relative higher magnetocrystalline anisotropy of Co results in higher

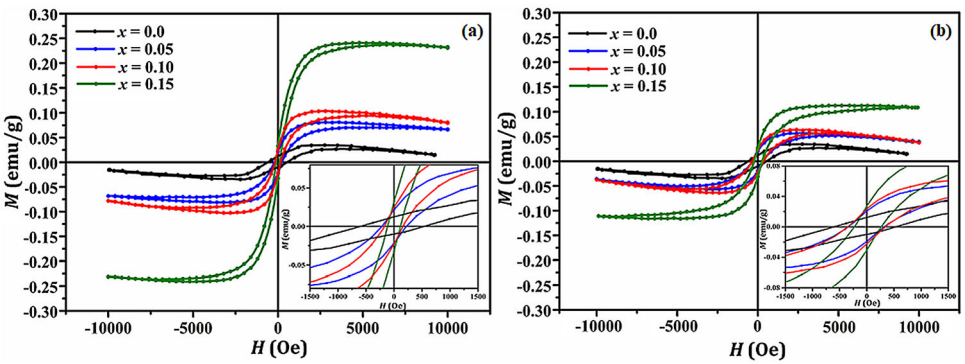

Fig. 6 *M–H* loops of **a** $Cd_{1-x}Fe_xS$, **b** $Cd_{1-x}Co_xS$ nanoparticles. Inset shows the magnified view of *M–H* loop

Table 2 Magnetic parameters of $Cd_{1-x}Fe_xS$ and $Cd_{1-x}Co_xS$ nanoparticles

Doping concentration (x)	$Cd_{1-x}Fe_xS$			$Cd_{1-x}Co_xS$		
	M_s (emu/g)	M_r (emu/g)	H_c (Oe)	M_s (emu/g)	M_r (emu/g)	H_c (Oe)
0.0	0.015	0.012	534.2	0.015	0.012	534.2
0.05	0.067	0.021	225.0	0.037	0.021	335.1
0.10	0.080	0.025	162.7	0.038	0.023	340.0
0.15	0.236	0.032	114.2	0.109	0.028	263.7

H_c. Hence Co-doped CdS shows higher H_c than Fe-doped nanoparticles. The observed M_s value are comparable to highest reported in the literature for given compositions [15, 23, 26, 37].

4 Conclusions

Series of Fe- and Co-doped CdS nanoparticles were synthesized by hydrothermal technique. Effect of Fe and Co doping on structural, morphological, optical and magnetic properties was investigated and compared. Phase and microstructural analysis confirmed wurtzite phase of nanoparticles having spherical morphology. The crystallite size of Fe-doped CdS ($\sim$ 11.50 nm) was relatively smaller than Co doping ($\sim$ 13.88 nm). The E_g for undoped CdS was 2.48 eV which increased with doping to 2.56 eV (Fe) and 2.53 eV (Co). In photoluminescence spectra, the major peak at 529 nm corresponds to green emission; however, no dopant related emissions were observed. *M–H* loops confirm *RT* ferromagnetism in all the compositions with a maximum value of M_s (0.236 emu/g) was observed for Fe. The present study revealed that Fe-doped(x = 0.15) CdS nanoparticles showed enhanced optical and magnetic properties that which makes it potential candidate to use as a buffer layer in solar cells and magneto-optical device applications.

Acknowledgements

The author would like to acknowledge research fellowship by Thapar Institute of Engineering & Technology and DST-FIST for VSM facility.

References

1. C. Liu, F. Yun, H. Morkoc, J. Mater. Sci. Mater. Electron. **16**, 555–597 (2005)
2. I. Zutic, J. Fabian, S.D. Sarma, Rev. Mod. Phys. **76**, 323–410 (2004)
3. A. Hartley, S.J.C. Irvine, J. Mater. Sci. Mater. Electron. **11**, 569–573 (2000)
4. F. Li, C. Nie, L. You, X. Jin, Q. Zhang, Y. Qin, F. Zhao, Y. Song, Z. Chen, Q. Li, Nanotechnology **29**, 205701 (2018)
5. S.T. Navalea, A.T. Manea, M.A. Chougulea, N.M. Shindeb, J.H. Kimb, V.B. Patila, RSC Adv. **4**, 44547–44554 (2014)
6. R. Singh, J. Magn. Magn. Mater. **346**, 58–73 (2013)
7. E. Biegger, L. Staheli, M. Fonin, U. Rudiger, Y.S. Dedkov, J. Appl. Phys. **101**, 103912 (2007)
8. B. Pal, P.K. Giri, J. Nanosci. Nanotechnol. **11**, 1–8 (2011)
9. V.I. Boev, A. Soloviev, B. Rodríguez-González, C.J.R. Silva, M.J.M. Gomes, Mater. Lett. **60**, 3793–3796 (2006)
10. J. Zang, G. Zhao, G. Han, Front. Chem. China **2**, 98–101 (2007)
11. B.S. Rao, B.R. Kumar, V.R. Reddy, T.S. Rao, Chalcogenide Lett. **3**, 177–185 (2011)
12. R. Banerjee, R. Jayakrishnan, P. Ayyub, J. Phys.: Condens. Matter. **12**, 10647–10654 (2000)
13. A. Datta, A. Priyam, S.N. Bhattacharyya, K.K. Mukherjea, A.Saha, J. Colloid. Interf. Sci. **322**, 128–135 (2008)
14. C. Dey, B. Karmakar, Phys. Status Solidi A **8**, 1700105 (2017)
15 B. Poornaprakasha, U. Chalapathia, P.T. Poojithab, S.V. Prabhakar, Vattikutic, Mater. Sci. Semicond. Proc. **100**, 73–78 (2019)
16. S. Rai, L. Bokatial, Bull. Mater. Sci. **34**, 227–231 (2011)
17. S.T. Selvan, T. Hayakawa, M. Nogami, J. Non-Cryst. Solids **137**, 137–141 (2001)
18. A. Ghosh, S. Paul, S. Raj, J. Magn. Magn. Mater. **405**, 238–243 (2016)
19. M. Thambidurai, N. Muthukumarasamy, D. Velauthapillai, N. Murugan, J. Chaudhuri, S. Parameswaran, A. Marathe, S. Agilan, R. Balasundaraprabhu, J. Mater. Sci. Mater. Electron. **23**, 618–624 (2012)

20. S. Kumar, N.S. Negi, S.C. Katyal, P. Sharma, V. Sharma, J. Magn. Magn. Mater. **367**, 1–8 (2014)
21. L.K. Sharma, M.S. Inpasalini, S. Mukherjee, J. Mater. Sci.: Mater. Electron. **26**, 7621–7628 (2015)
22 A.M.B. Leena, K. Raji, Mater. Today **8**, 362–370 (2019)
23. G. Murali, D.A. Reddy, B. PoornaPrakash, R.P. Vijayalakshmi, B.K. Reddy, R. Venugopal, Phys. B **407**, 2084–2088 (2012)
24. F. Ibraheem, M.A. Mahdy, E.A. Mahmoud, J.E. Ortega, C. Rogero, I.A. Mahdy, A. El-Sayed, J. Alloy Compd. **834**, 155196 (2020)
25. N.H. Patel, M.P. Deshpande, S.H. Chaki, J. Mater. Sci. Mater. Electron. **29**, 11394–11403 (2018)
26. G. Giribabu, G. Murali, D.Amaranatha Reddy, C. Liu, R.P. Vijayalakshmi, J. Alloy Compd. **581**, 363–368 (2013)
27. H. Sekhar, D.N. Rao, J. Alloy Compd. **517**, 103–110 (2012)
28 B.D. Cullity, S.R. Stock, *Elementary of X-Ray Diffraction*, 3rd edn. (Prentice-Hall, Englewood Cliffs, 2001)
29. G.A. Kumara, V. Thomas, G. Jose, N.V. Unnikrishnan, V.P.N. Nampoori, Mater. Chem. Phys. **73**, 206–211 (2002)
30 C. Prabakar, S. Muthukumaran, V. Raja, Optik **202**, 163714 (2020)
31. V. Singh, P. Chauhan, J. Phys, Chem. Solids **70**, 1074–1079 (2009)
32. C.B. Murray, D.J. Norris, M.G. Bawendi, J. Am. Chem. Soc. **115**, 8706–8715 (1993)
33 P. Yang, M. Lu, D. Xu, D. Yuan, C. Song, G. Zhou, J. Phys. Chem. Solids **62**, 11811–1184 (2001)
34. J.P. Tang, L. Wang, H.J. Luoc, W.Z. Xiao, Phys. Lett. A **377**, 572 (2013)
35. Y. Lia, P.A. Montanoa, B. Barbiellinid, P.E. Mijnarendsd, S. Kaprzykd, A. Bansil, J. Phys. Chem. Solids **68**, 1556–1560 (2007)
36. R.S. Turtelli, M. Atif, N. Mehmooda, F. Kubel, K. Biernacka, W. Linert, R. Grossinger, C. Kapusta, M. Sikora, Mater. Chem. Phys. **132**, 832–838 (2012)
37. R. Zhao, P. Wang, T. Yang, Z. Li, B. Xiao, M. Zhang, J. Phys. Chem. C **119**, 28679–28684 (2015)

Materials Science in Semiconductor Processing 108 (2020) 104884

Contents lists available at ScienceDirect

Materials Science in Semiconductor Processing

journal homepage: http://www.elsevier.com/locate/mssp

Optical and magnetic properties of Dy^{3+} doped CdS dilute magnetic semiconductor nanoparticles

Shivani Jindal, Puneet Sharma *

School of Physics and Materials Science, Thapar Institute of Engineering and Technology, Patiala, 147004, India

ARTICLE INFO

Keywords:
CdS
Dilute magnetic semiconductors
Magnetic properties
Optical properties

ABSTRACT

Hydrothermally synthesized $Cd_{1-x}Dy_xS$ ($x = 0.0$, 0.05 and 0.10) nanoparticles were investigated for its structural, morphological, optical and magnetic properties. The single wurtzite phase was confirmed for all compositions. HR-TEM micrographs revealed spherical morphology of nanoparticles. The average particle size found to decrease from 40 nm to 30 nm with Dy^{3+} doping. The optical band gap was increased from 2.44 eV ($x = 0.0$) to 2.55 eV ($x = 0.10$). The luminescence peak at 568 nm due to Dy^{3+} transition ($^4F_{9/2} \rightarrow {}^6H_{13/2}$) was observed. Magnetic analysis confirmed room temperature ferromagnetism in all the samples.

M-H loop of doped nanoparticle showed enhanced magnetization with paramagnetic contribution.

1. Introduction

Owing to unique size dependent optical, electronic and magnetic properties, II-VI group (CdS, ZnO & ZnS) semiconductors have gained considerable attention in various optoelectronic and spintronic applications [1]. Also, their wide band gap (E_g) in visible range makes them suitable candidate for solar cell application [2]. At nanoscale regime, these materials exhibit entirely different properties as compared to their bulk counterpart due to large surface to volume ratio and quantum-confinement effects [3,4]. Further, the properties of these materials can be altered by tailoring the particle size and suitable cationic doping [5].

Among II-VI group, CdS with direct E_g of 2.42 eV has been extensively used in photodetectors, photocatalyst, light emitting diodes, gas detectors and n-type window layer in solar cells [2,6–9]. In the last few years, size dependent properties of CdS nanoparticles were extensively investigated [10,11]. An adequate amount of work has been carried out for transition metal (TM) doped CdS nanostructures, which reportedly enhances magnetization and optical E_g [12–14]. In contrary to TM, the studies pertaining to rare earth (RE) doped are very limited. The RE elements exhibit interesting magnetic and optoelectronic properties in many functional materials [15,16]. Their highly localized 4f electrons results in weak f-f interactions between the neighbouring atoms causes larger magnetic moments than 3d TMs. Also, excitation of RE doped semiconductors results in sharp line emission due to intra $4f^n$ transitions, which covers the ultra violet (UV), visible and infrared regions of energy spectrum [17]. In past, magnetic and optical properties of RE doped (Gd, Eu, Ce and Tb) CdS nanoparticles were investigated [15,18–20]. A few studies on Dy^{3+} doped CdS nanoparticles/thin films were also reported, however, the investigations were restricted to structural and optical properties only [21–23]. In the present work, the effect of Dy^{3+} doping on CdS nanoparticles were systematically studied for it structural, morphological, optical and magnetic properties.

2. Experimental details

Laboratory grade Cadmium Chloride Monohydrate ($CdCl_2 \cdot xH_2O$), Dysprosium (III) nitrate hydrate ($Dy(NO_3)_3 \cdot xH_2O$) and Sodium Sulphide (Na_2S) of 99.9% purity from Sigma-Aldrich were used to synthesized $Cd_{1-x}Dy_xS$ ($x = 0.0$, 0.05 and 0.10) nanoparticles via hydrothermal method. 0.25 M of $CdCl_2 \cdot xH_2O$, 0.25 M of Na_2S were dissolved in distilled water and stirred for 30 min. The solution was transferred into a Teflon lined stainless steel autoclave and kept in a furnace at 160°C for 5 h. The obtained precipitates were collected and washed with distilled water and ethanol for several times to remove impurities. The samples were finally dried in hot air oven to obtain the powder.

The phase analysis of nanopowders was done using X-ray diffractometer (XRD) of PANalytical X'Pert PRO MRD with Cu–Kα ($\lambda = 1.5418$ Å). The morphological features and selected area electron diffraction (SAED) patterns of nanopowder was recorded by high resolution transmission electron microscopy (HR-TEM) (Hitachi H-7650). The elemental analysis was carried out by energy dispersive spectroscopy

* Corresponding author.
E-mail address: puneet.sharma@thapar.edu (P. Sharma).

https://doi.org/10.1016/j.mssp.2019.104884
Received 17 July 2019; Received in revised form 12 December 2019; Accepted 12 December 2019
Available online 18 December 2019
1369-8001/

(EDS) model JEOL (JSM-1T100). PerkinElmer Lambda 45 spectrophotometer and Agilent Carry Eclipse fluorescence spectrophotometer (G9800A) were used to determine UV–visible absorption spectra and room temperature (*RT*) photoluminescence (PL) spectrum, respectively of nanopowders. The *RT* magnetic studies were done using vibrating sample magnetometer (VSM) of Lake Shore of model 7404.

3. Results and discussion

3.1. Structural analysis

Fig. 1 shows XRD patterns of nanopowders indicating the polycrystalline nature for all compositions. All XRD patterns were refined by Rietveled refinement using fullproof software with hexagonal symmetry (space group $P6_3mc$). The χ^2 values were below 2 which suggest that refinements were best fitted. Table 1 shows the structural parameters as obtained from refinement for all compositions. The 2θ values are shifting towards higher diffraction angle due to smaller ionic radii of Dy^{3+} ion (0.91 Å) as compared to Cd^{2+} ion (0.97 Å) [24]. The crystallite sizes (*D*) of nanoparticles were calculated using the Debye-Scherrer formula [25].

$$D = \frac{0.9\,\lambda}{\beta Cos\theta}$$

where, λ is wavelength of X-ray, θ is the Bragg's angle, β is full width at half maximum (FWHM) calculated from Caglioti equation $(u\tan^2\theta + v\tan\theta + w)^{1/2}$, function *u*, *v* and *w* are the shape parameters obtained from refinement.

The *D* found to decrease with doping. The marginal shrinkage in lattice parameters with doping is ascribed to lower ionic radii of Dy^{3+}.

3.2. Morphological studies

HR-TEM images and SAED pattern of $Cd_{1-x}Dy_xS$ nanoparticles for $x = 0.0$ and 0.10 are shown in Fig. 2(a–d). The spherical morphology with an average particle diameter of 40 nm ($x = 0.0$) and 30 nm ($x = 0.10$) were observed. The decrease in particle size with doping may ascribed to different reasons. The lower ionic radii of Dy^{3+} than Cd^{2+} causes shrinkage in the unit cell which resulted in smaller particle size.

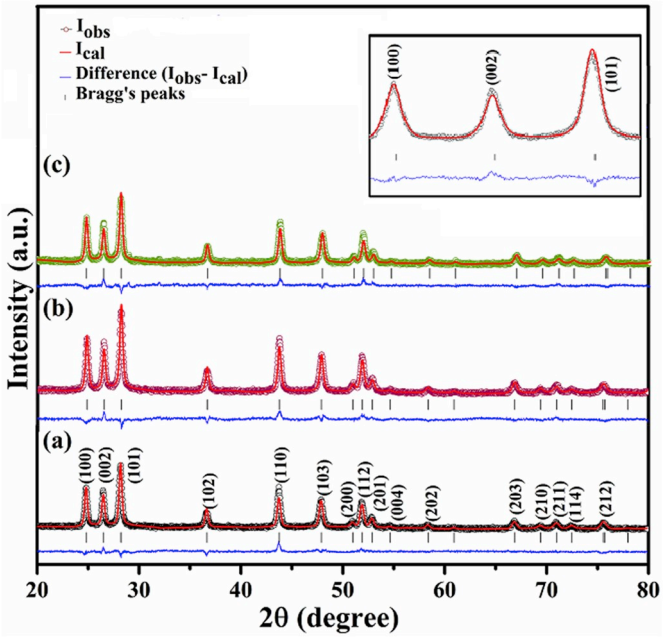

Fig. 1. Refined XRD patterns of $Cd_{1-x}Dy_xS$ nanoparticles (a) $x = 0.0$, (b) $x = 0.05$, (c) $x = 0.10$. Inset shows the representative enlarged view of fit.

Table 1
Structural parameters and optical E_g of $Cd_{1-x}Dy_xS$ nanoparticles.

Doping Concentration (*x*)	*a* (Å)	*c* (Å)	2θ (degree) (101)	*D* (nm)	E_g (eV)
0.0	4.135	6.715	24.845	29.03	2.44
0.05	4.133	6.713	24.867	22.14	2.54
0.10	4.131	6.710	24.873	19.91	2.55

However, the contribution of this shrinkage is marginal. Also, it may possible that a small fraction of Dy^{3+} ions remain unsubstituted which may provide pinning action on particle growth. The other reason could be the different thermodynamic conditions of crystal growth of doped and undoped one. The doped CdS may require a higher synthesis temperature to achieve similar particle size. The measured *d*-spacing value from lattice fringe pattern is ~0.33 nm (Fig. 2(c)), that corresponds to (002) plane of hexagonal structure of CdS. The corresponding SAED pattern (Fig. 2(d)) is not sharp, depicting the nano-crystalline nature of particles.

Fig. 3 depicts EDS pattern of $Cd_{1-x}Dy_xS$ ($x = 0.0$, 0.05 and 0.10) nanoparticles that confirms the presence of Cd, S and Dy without any contamination.

3.3. Optical analysis

3.3.1. UV–visible spectra

Fig. 4(a) shows the UV–visible absorption spectra of $Cd_{1-x}Dy_xS$ nanoparticles recorded from 400 to 700 nm. The blue shift was observed with Dy^{3+} doping. The optical E_g was determined from Tauc's relation using the following equation [26]:

$$\alpha h\nu = A(h\nu - E_g)^n$$

where, *v* is frequency, α is absorption coefficient, constant *A* is function of electronic transition probability, *h* is Plank's constant and *n* is type of transition (for direct transition $n = 1/2$). Fig. 4(b) shows the Tauc's plot, where E_g was determined by extrapolating the plot of $(\alpha h\nu)^2$ versus $h\nu$.

Table 1 displays the E_g of synthesized nanoparticles. It also shows that the doping of Dy^{3+} in CdS enhances the E_g from 2.44 eV to 2.55 eV. When the dimensions of the semiconductor materials are comparable to exciton-Bohr radius, the excitons are confined, which means that their motion in the crystal is restricted. Such physical confinement of excitons causes changes in the energetic spectrum of semiconductor. The decrease in particle size increases the separation between valence and conduction bands which enhances the optical E_g [27,28]. However, in our system the measured particle size is quite higher than exciton-Bohr radii (5 nm), hence, the variation in E_g cannot be ascribed to confinement effect. Therefore, the decrease in particle size with doping may be the reason for higher E_g [29]. The reason for decrease in particle size is already explained in section 3.2. Also, the formation of sulphur vacancies due to charge imbalance between Cd^{2+} and Dy^{3+} may be the reason for increase in E_g.

3.3.2. Photoluminescence spectra

The PL-spectra of $Cd_{1-x}Dy_xS$ nanoparticles with excitation wavelength of 380 nm and de-convoluted spectra for $x = 0.0$ and 0.10 are shown in Fig. 5. The peaks at around 486 nm is band to band edge transition whereas, peaks at 520 nm and 536 nm corresponds to defect states in undoped CdS (Fig. 5(b)). The major peak at around 520 nm is attributed to green emission ascribed to surface donor-acceptor pair recombination. After excitation across band-edge, the electrons and holes trickle down non-radiatively to deep-traps where two recombination processes occurs in d-d intra ion transitions. Firstly, recombination of trapped holes in acceptor level with free electrons from conduction band and secondly, with electrons from donor level that results in green emission [28]. In doped CdS (Fig. 5), the peak at 536 nm ($x = 0$) slightly shifted to 538 nm due to sulphur vacancies which easily

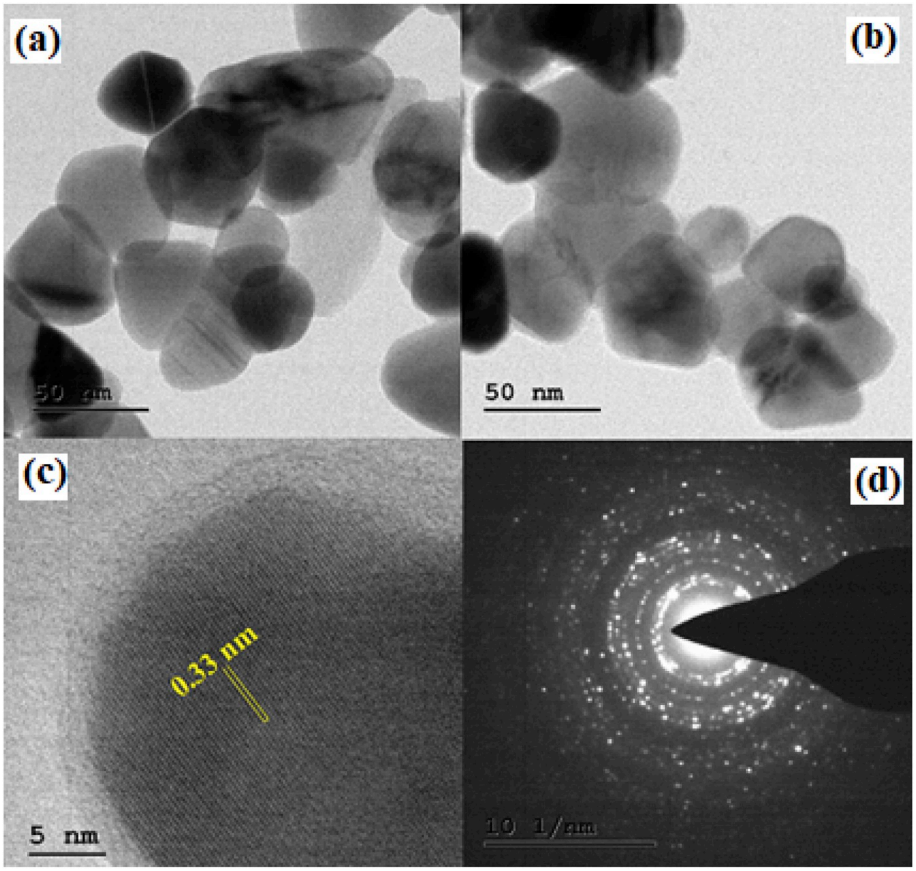

Fig. 2. TEM micrographs of $Cd_{1-x}Dy_xS$ nanoparticles (a) $x = 0.0$, (b) $x = 0.10$, (c) lattice fringe pattern for $x = 0.10$, (d) SAED pattern for $x = 0.10$.

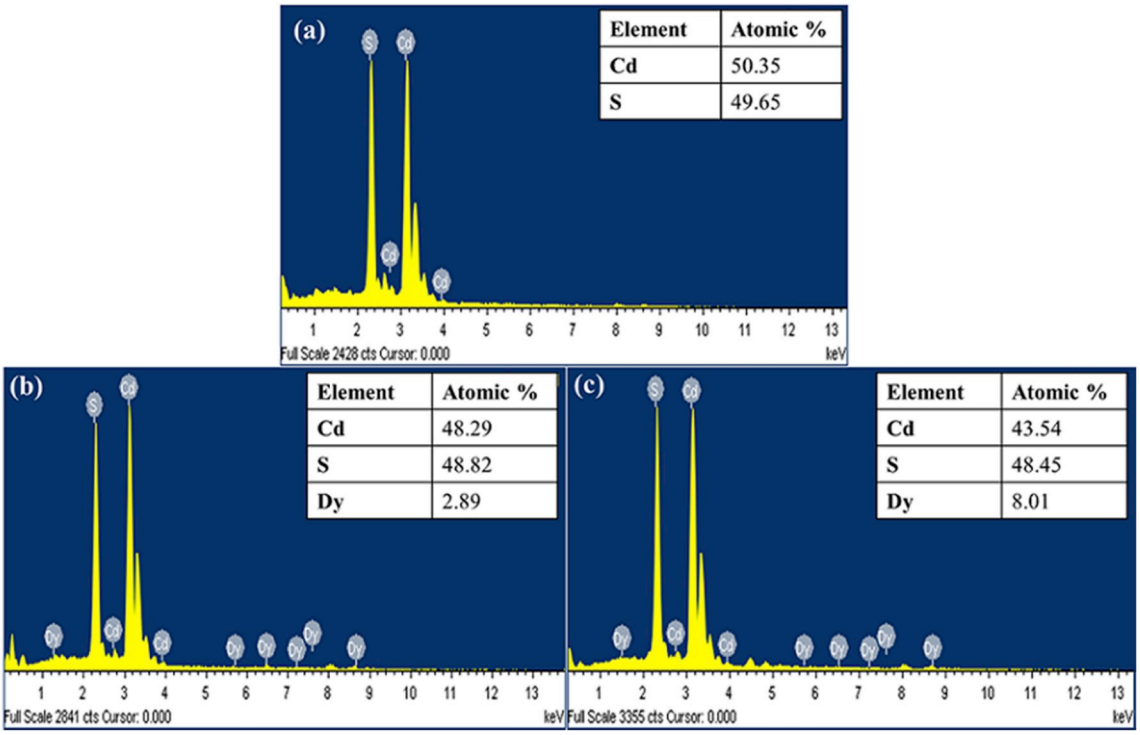

Fig. 3. EDS spectra of $Cd_{1-x}Dy_xS$ nanoparticles (a) $x = 0.0$, (b) $x = 0.05$, (c) $x = 0.10$.

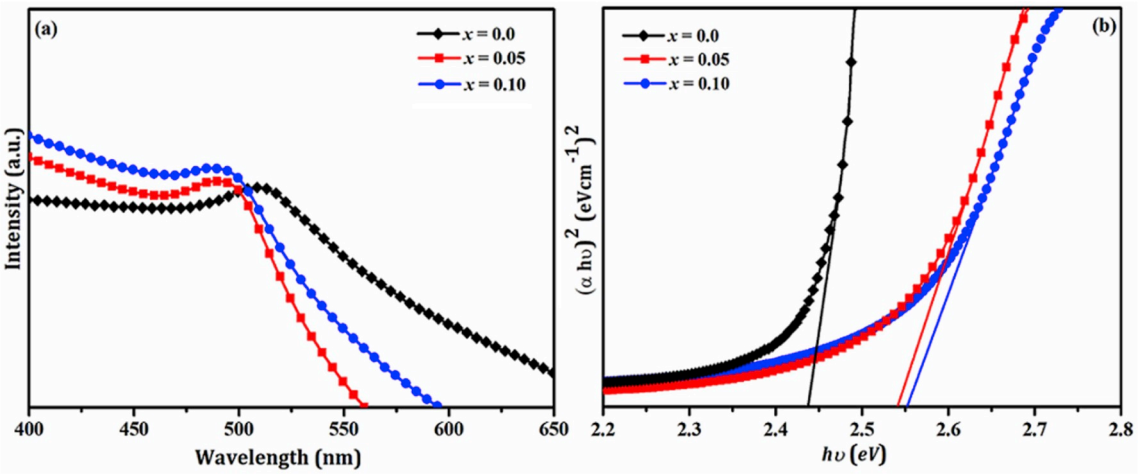

Fig. 4. (a) UV–visible absorption spectra, (b) Tauc's plot of $Cd_{1-x}Dy_xS$ nanoparticles.

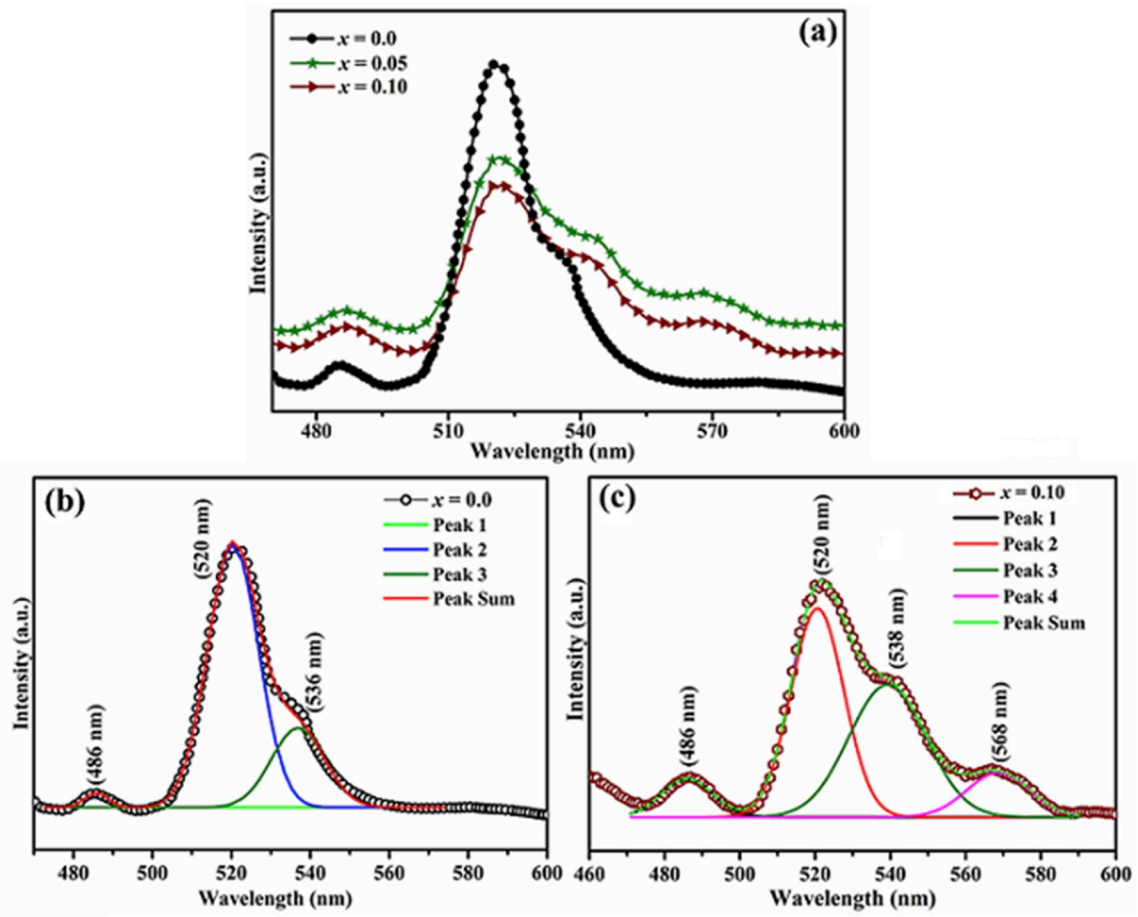

Fig. 5. (a) PL spectra of $Cd_{1-x}Dy_xS$ nanoparticles (vertically shifted). De-convoluted spectra $Cd_{1-x}Dy_xS$ nanoparticles (b) $x = 0.0$, (c) $x = 0.10$.

forms in CdS. These sulphur vacancies acts as trap states for photo-generated electrons resulting in yellow emission [30]. The doping of Dy^{3+} in CdS introduces new energy levels within its E_g. The peak at 568 nm is ascribed to Dy^{3+} $^4F_{9/2} \rightarrow {}^6H_{13/2}$ (yellow emission) magnetic dipole transitions. The Dy^{3+} ions also show emission peak at 486 nm due to force electric dipole $^4F_{9/2} \rightarrow {}^6H_{15/2}$ (blue emission) transition that is overlapping with band to band edge transition [31]. The yellow luminescence caused by Dy^{3+} doping, make them good candidate for yellow laser and for white light emitting diode (pc-WLED) [32].

3.4. Magnetic analysis

Fig. 6 shows *RT* magnetic behaviour of $Cd_{1-x}Dy_xS$ nanoparticles. The magnified image of *M-H* loop (Inset II) shows the presence of residual magnetization (M_r) and coercivity (H_c) in CdS nanoparticles. The measured magnetic properties of nanoparticles are given in Table 2. The large surface to volume ratio of nanoparticles generates uncompensated surface magnetic moments which interact ferromagnetically with their nearest neighbouring moments and causes weak ferromagnetism [33].

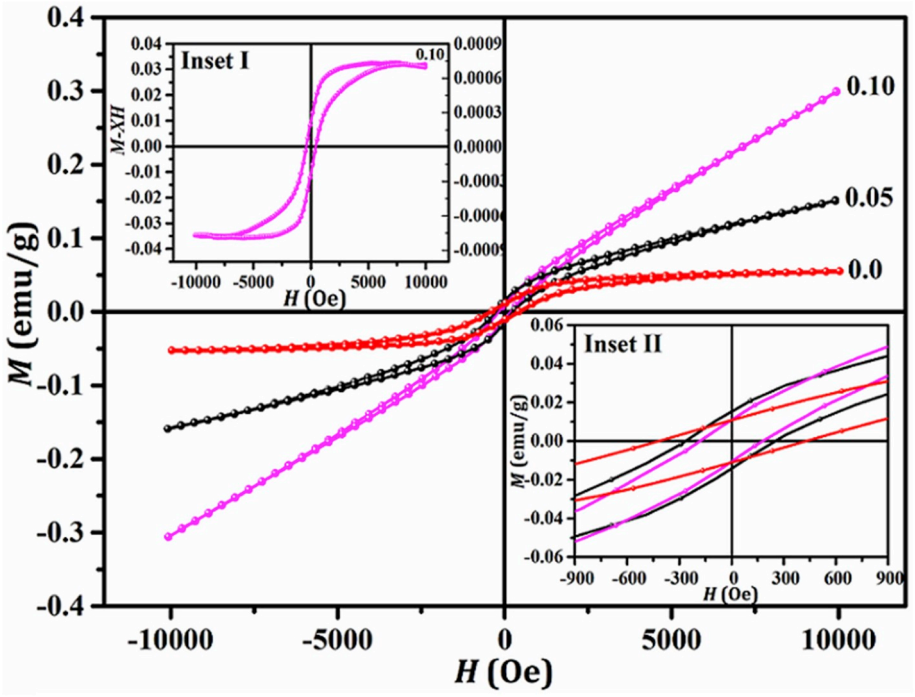

Fig. 6. *M-H* loops of $Cd_{1-x}Dy_xS$ nanoparticles. Inset I shows (M-χH) vs H loop for x = 0.10and Inset II shows magnified view of *M-H* loop.

Table 2
Magnetic parameters of $Cd_{1-x}Dy_xS$ nanoparticles.

Doping Concentration (*x*)	*M* at 1 T (emu/g)	M_r (emu/g)	H_c (Oe)
0.0	0.05	0.011	426.9
0.05	0.15	0.015	258.4
0.10	0.30	0.010	179.4

The magnetization (*M*) found to increase with doping, however *M-H* loop are non-saturating in nature. The non-saturating *M-H* behaviour is a characteristic feature of paramagnetic, anti-ferromagnetic or super-paramagnetic contributions. Since the particle size of CdS nanparticles are above 19 nm, therefore, possibility of superparamagnetic contribution can be neglected. Similar, non-saturating behaviour was observed in Co doped ZnO nanostructures, where fine nanoclusters of Co contributed to superparamagnetism [34,35]. Also antiferromagnetic coupling between neighbouring ferromagnetic ions showed non saturating behaviour [36]. Since Dy^{3+} is paramagnetic at *RT* with Curie temperature of 85K [37], therefore their nanoclusters will not contribute to superparamagnetism. Hence, non-saturation of *M-H* curve may ascribe to paramagnetic contribution from Dy^{3+} ions. It is also found to increases with Dy^{3+} concentration. Subtracting paramagnetic contribution from magnetization (*M* - *χH*, *χ* is susceptibility); well saturated *M-H* loops were observed. The representative figure (*x* = 0.10) is shown in Inset-I Fig. 6.

4. Conclusions

$Cd_{1-x}Dy_xS$ (x = 0.0, 0.05 and 0.10) nanoparticles were synthesized by hydrothermal technique. The refined XRD patterns confirmed wurtzite phase in all compositions. HR-TEM micrographs revealed the spherical morphology of the particles. The average particle size was decreased from 40 nm to 30 nm with Dy^{3+} doping. The optical E_g enhanced from 2.44 eV (*x* = 0.0) to 2.55 eV (*x* = 0.10). In PL-spectra, Dy^{3+} related $^4F_{9/2} \rightarrow {}^6H_{13/2}$ transition (yellow emission) was observed at 568 nm. The *M-H* loop of doped CdS nanoparticles showed enhanced magnetization with an evidence of paramagnetic contribution. This study revealed that optical and magnetic properties can be tuned by suitable Dy^{3+} doping.

Declaration of competing interest

The authors declare that they have no known competing financial interests or personal relationships that could have appeared to influence the work reported in this paper.

CRediT authorship contribution statement

Shivani Jindal: Conceptualization, Methodology, Data curation, Writing - original draft, Resources, Visualization, Investigation, Validation, Writing - review & editing. **Puneet Sharma:** Supervision, Writing - review & editing.

Acknowledgement

The author would like to acknowledge research fellowship by Thapar Institute of Engineering & Technology.

Appendix A. Supplementary data

Supplementary data to this article can be found online at https://doi.org/10.1016/j.mssp.2019.104884.

References

[1] S.D. Sarma, E.H. Hwang, A. Kaminski, How to make semiconductors ferromagnetic: a first course on spintronics, Solid State Commun. 127 (2003) 99–107.
[2] S. Shirakata, K. Ohkubo, Y. Ishii, T. Nakada, Effects of CdS buffer layers on photoluminescence properties of Cu (In, Ga) Se_2 solar cells, Sol. Energy Mater. Sol. Cells 93 (2009) 988–992.
[3] D.P. Norton, S.J. Pearton, A.F. Hebard, N. Theodoropoulou, L.A. Boatner, R. G. Wilson, Ferromagnetism in Mn-implanted ZnO:Sn single crystals, Appl. Phys. Lett. 82 (2003) 239–241.
[4] T. Dietl, A ten-year perspective on dilute magnetic semiconductors and oxides, Nat. Mater. 9 (2010) 965–974.
[5] Y.C. Cao, Science, Impurities enhance semiconductor nanocrystal performance, Science 332 (2011) 48–49.

[6] F. Cao, L. Meng, M. Wang, W. Tian, L. Li, Gradient energy band driven high-performance self-powered perovskite/CdS photodetector, Adv. Mater. 31 (2019) 1806725.
[7] Y. Huang, F. Sun, T. Wu, Q. Wu, Z. Huang, H. Su, Z. Zhang, Photochemical preparation of CdS hollow microspheres at room temperature and their use in visible-light photocatalysis, J. Solid State Chem. 184 (2011) 644–648.
[8] F. Li, C. Nie, L. You, X. Jin, Q. Zhang, Y. Qin, F. Zhao, Y. Song, Z. Chen, Q. Li, White light emitting device based on single-phase CdS quantum dots, Nanotechnology 29 (2018) 205701.
[9] S.T. Navalea, A.T. Manea, M.A. Chougulea, N.M. Shindeb, J.H. Kimb, V.B. Patila, Highly selective and sensitive CdS thin film sensor for detection of NO_2 gas, RSC Adv. 4 (2014) 44547–44554.
[10] J. Zhang, L. Sun, C. Liao, C. Yan, Size control and photoluminescence enhancement of CdS nanoparticles prepared via reverse micelle method, Solid State Commun. 124 (2002) 45–48.
[11] G. Maa, S.H. Tanga, W. Suna, Z. Shena, W. Huangb, J. Shi, Size-dependent excited state properties of CdS nanocrystals, Phys. Lett. A 299 (2002) 581–585.
[12] N.H. Patel, M.P. Deshpande, S.H. Chaki, Study on structural, magnetic properties of undoped and Ni doped CdS nanoparticles, Mater. Sci. Semicond. Process. 31 (2015) 272–280.
[13] T. Sivaraman, A.R. Balu, V.S. Nagarethinam, Effect of magnesium incorporation on the structural, morphological, optical and electrical properties of CdS thin films, Mater. Sci. Semicond. Process. 27 (2014) 915–923.
[14] K. Deka, M.P.C. Kalita, Structural phase controlled transition metal (Fe, Co, Ni, Mn) doping in CdS nanocrystals and their optical, magnetic and photocatalytic properties, J. Alloy. Comp. 757 (2018) 209–220.
[15] B. Poornaprakasha, U. Chalapathia, P.T. Poojithab, S.V. Prabhakar Vattikutic, Influence of gadolinium (III) doping on the structural, optical, magnetic, and photocatalytic properties of CdS quantum dots, Mater. Sci. Semicond. Process. 100 (2019) 73–78.
[16] P. Kaur, S. Kumar, C. L Chen, K.S. Yang, D.H. Wei, C.L. Dong, C. Srivastava, S. M. Rao, Gd doping induced weak ferromagnetic ordering in ZnS nanoparticles synthesized by low temperature co-precipitation technique, Mater. Chem. Phys. 186 (2017) 124–130.
[17] R.N. Bhargava, Doped nanocrystalline materials- physics and applications, J. Lumin. 70 (1996) 85–94.
[18] S.T. Selvan, T. Hayakawa, M. Nogami, Enhanced fluorescence from Eu^{3+}-doped silica gels by absorbed CdS nanoparticles, J. Non-Cryst. Solids 137 (2001) 137–141.
[19] L. Saravanan, A. Pandurangan, R. Jayavel, Synthesis and luminescence enhancement of cerium doped CdS nanoparticles, Mater. Lett. 343 (2012) 343–345.
[20] S. Rai, L. Bokatial, Effect of CdS nanoparticles on photoluminescence spectra of Tb^{3+} in sol–gel-derived silica glasses, Bull. Mater. Sci. 34 (2011) 227–231.
[21] S. Yılmaz, Polat, M. Tomakin, S.B. Toreli, T. Kucukomeroglu, E. Bacaks, Optical and electrical optimization of dysprosium-doped CdS thin films, J. Mater. Sci. Mater. Electron. 29 (2018) 14774–14782.
[22] P.V. Jyothy, K.A. Amrutha, J. Xavier, N.V. Unnikrishnan, Fluorescence characteristics of Dy^{3+}/CdS nanocrystals doped silica xerogel, J. Phys. Chem. Solids 70 (2009) 927–930.
[23] C. Dey, B. Karmakar, In situ generated CdS nanostructure induced enhanced photoluminescence from Dy^{3+} ions doped dielectric nanocomposites, Phys. Status Solidi A 8 (2017) 1700105.
[24] A.A. Dakhel, Influence of dysprosium doping on the electrical and optical properties of CdO thin films, Sol. Energy 83 (2009) 934–939.
[25] B.D. Cullity, S.R. Stock, Elementary of X-Ray Diffraction, third ed., Prentice-Hall, Englewood Cliffs, 2001.
[26] G.A. Kumara, V. Thomas, G. Jose, N.V. Unnikrishnan, V.P.N. Nampoori, Optical properties of porphyrins in borate glassy matrix, Mater. Chem. Phys. 73 (2002) 206–211.
[27] M. Bangal, S. Ashtaputre, S. Marathe, A. Ethiraj, N. Hebalkar, S.W. Gosavi, J. Urban, S.K. Kulkarni, Semiconductor nanoparticle, Hyperfine Interact. 160 (2005) 81.
[28] C.B. Murray, D.J. Norris, M.G. Bawendi, Synthesis and characterization of nearly monodisperse CdE (E = S, Se, Te) semiconductor nanocrystallites, J. Am. Chem. Soc. 115 (1993) 8706–8715.
[29] M. Thambidurai, N. Muthukumarasamy, S. Agilan, N. Murugan, S. Vasantha, R. Balasundaraprabhu, T.S. Senthil, Strong quantum confinement effect in nanocrystalline CdS, J. Mater. Sci. 45 (2010) 3254–3258.
[30] S. Karan, M. Majumder, B. Mallik, Controlled surface trap state photoluminescence from CdS QDs impregnated in poly (methyl methacrylate), Photochem. Photobiol. Sci. 11 (2012) 1220–1232.
[31] B. Grobelna, A. Synak, P. Bojarski, The luminescence properties of dysprosium ions in silica xerogel doped with $Gd_{1.6}Dy_{0.4}(WO_4)_3$, Opt. Appl. 2 (2012) 337–344.
[32] E.I. Anila, M.K. Jayaray, Effect of dysprosium doping on the optical properties of SrS:Dy, Cl phosphor, J. Alloy. Comp. 504 (2010) 257–260.
[33] R. Singh, Unexpected magnetism in nanomaterials, J. Magn. Magn. Mater. 346 (2013) 58–73.
[34] J.H. Park, M.G. Kim, H.M. Jang, S. Ryu, Co-metal clustering as the origin of ferromagnetism in Co-doped ZnO thin films, Appl. Phys. Lett. 84 (2004) 1338–1340.
[35] D.P. Norton, M.E. Overberg, S.J. Pearton, K. Pruessner, Ferromagnetism in cobalt-implanted ZnO, Appl. Phys. Lett. 83 (2003) 5488–5490.
[36] Susmita Paul, Dhiman Banik, G.A. Ahmed, Amarjyoti Choudhury, Magnetic property study in Eu doped TiO_2 nanoparticles, J. Mater. Sci. Mech. Eng. 8 (2016) 515–517.
[37] A.E. Clark, B.F. Desavage, R. Bozorth, Anomalous thermal expansion and magnetostriction of single-crystal dysprosium, Phys. Rev. 138 (1953) A216–A224.

J Mater Sci: Mater Electron
DOI 10.1007/s10854-017-7891-5

Effect of Tb^{3+} ion substitution on structural, optical and magnetic properties of CdS nanoparticles

Shivani Jindal[1] · Kamaldeep Kaur[1] · N. K. Verma[1] · Puneet Sharma[1]

Received: 7 June 2017 / Accepted: 20 September 2017

Abstract $Cd_{1-x}Tb_xS$ ($x=0.00, 0.05, 0.10, 0.15$) nanoparticles were synthesized by hydrothermal technique. The effect of Tb-doping on structural, optical and magnetic properties were studied. The X-ray diffraction (XRD) confirmed wurtzite phase without any impurity. HR-TEM micrographs revealed the particle size of ~18 nm with spherical morphology. Band gap calculated from UV–Visible absorption spectra showed an initial decrease from 2.49 eV ($x=0$) to 2.45 eV ($x=0.10$). Further, increasing Tb-doping to $x=0.15$ band gap increased to 2.54 eV. Photoluminescence emission spectra showed peaks at 430 and 490 nm for $x=0$ and 0.05 which corresponds to blue emission. Further increase in Tb doping, peaks found to be quenched. Peak at 530 nm is due to green emission and shifted to higher wavelength with Tb-doping. Magnetic analysis confirmed ferromagnetism in both undoped and Tb-doped nanoparticles. Saturation magnetization found to decrease upto $x=0.10$ and increased for $x=0.15$.

1 Introduction

Rare earth or transition metal doped group IV–VI, III–V and II–VI semiconductors are known as dilute magnetic semiconductors (DMS). These DMS materials are promising candidates for spintronic applications, in which they allow the manipulation of carrier spins [1]. These materials possess unique electronic and magnetic properties as compared to their bulk counterparts due to quantum effect at nanoscale [2, 3]. The origin of ferromagnetism in nanomaterials is a controversial topic and is still under investigation [4]. The observed ferromagnetism were explained by various types of exchange interactions i.e. double-exchange, RKKY and super-exchange in these materials [5, 6]. It is also attributed to the reduction of one or more dimensions at nanoscale that decreases the atomic coordination number. This reduces the hoping tendency of electrons and hence increases coulomb interaction to bandwidth ratio which increases the magnetic tendency [7]. Whereas, secondary phases or defects are also found responsible for their magnetic behaviour [8, 9]. In the recent years, the observation of ferromagnetic ordering at room temperature (*RT*) accompanied by high Curie temperature in II-VI and III-V semiconductors has gained a significant attention for future device applications.

Among various II–VI semiconductors, CdS is of greater interest due to its wide band gap (E_g) of 2.42 eV with high electronic transport, high mobility as well as its good magneto-optical properties [10]. Therefore, it is considered to be a promising host material for application in solar cell, light emitting diodes, photocatalysis and photo detectors [11–14]. Recently, II–VI semiconductor materials doped with rare earth ions are in focus as they are potential candidates for optical display devices [15]. These ions have partially filled $4f^n$ shells due to which they exhibit longer fluorescence lifetime, large excitation emission separation and very narrow intense emission lines [16]. There are various reports on rare earth (Gd, Pr, Eu, Ce) doped CdS nanoparticles [17–20]. However, there are few reports on Tb-doped CdS nanoparticles that focused to their fluorescence and photoluminescence properties but not on their magnetic properties [21, 22]. In this communication, we systematically investigated the structural, optical and magnetic properties of Tb-doped CdS nanoparticles.

✉ Puneet Sharma
puneet.sharma@thapar.edu

[1] School of Physics and Materials Science, Thapar University, Patiala 147004, India

Published online: 03 October 2017

2 Experimental details

$Cd_{1-x}Tb_xS$ ($x = 0.00, 0.05, 0.10, 0.15$) nanoparticles were synthesized by hydrothermal technique. Stoichiometric composition of cadmium chloride ($CdCl_2{\cdot}2H_2O$) and terbium chloride hexa-hydrate ($Cl_3Tb{\cdot}6H_2O$) of 99.99% purity were used for synthesis. 0.25 M of cadmium chloride, 0.25 M of sodium sulphide (Na_2S) and 0.05 mg of Cetyl Trimethyl Ammonium Bromide (CTAB) were added in distilled water as a solvent, and stirred for 30 min. The final solution was transferred into a Teflon lined stainless steel autoclave and kept in a furnace at 160 °C for 5 h. The obtained precipitates were washed with distilled water and ethanol for 3–4 times to remove impurities. The samples were finally dried in hot air oven to obtain the powder.

The phase analysis of synthesized nanoparticles was done using X-ray diffractometer (XRD) (PANalytical X'Pert PRO MRD) with Cu-$K\alpha_1$ (1.54 Å). The morphological features and selected area electron diffraction (SAED) patterns of nanopowders were recorded by high resolution transmission electron microscopy (HR-TEM) (Hitachi H-7650). Perkine Elmer Lambda 45 spectrophotometer and Perkin Elmer fluorescence spectrometer were used to determine UV–Visible absorption spectra and *RT*-photoluminescence spectrum respectively. The *RT* magnetic studies were carried out using vibrating sample magnetometer (VSM) (Lake Shore model-7404).

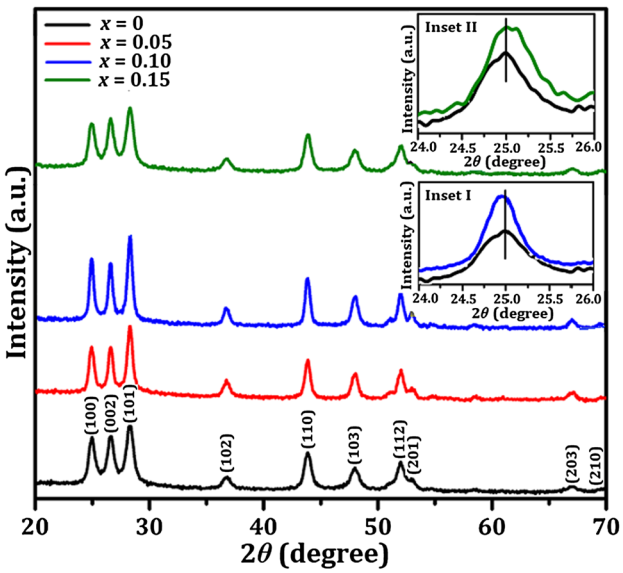

Fig. 1 XRD patterns of $Cd_{1-x}Tb_xS$ nanoparticles. Inset shows the enlarged view of (100) plane

Table 1 Structural parameters and optical bandgap of $Cd_{1-x}Tb_xS$ nanoparticles for $x = 0, 0.05, 0.10, 0.15$

Doping concentration (x)	Lattice parameters		Crystallite size (nm)		Optical bandgap (eV)
	a (Å)	c (Å)	XRD	UV–Vis	
0	4.127	6.670	13.34	11.38	2.49
0.05	4.124	6.683	16.63	15.65	2.46
0.10	4.120	6.690	17.68	18.00	2.45
0.15	4.126	6.692	12.08	9.03	2.54

3 Results and discussion

3.1 Structural analysis

X-ray diffraction (XRD) patterns of synthesized nanoparticles have been illustrated in Fig. 1. The sharp diffraction peaks indicate the polycrystalline nature of powders. All diffraction peaks corresponds to the hexagonal wurtzite phase with space group $P6_3mc$ (JCPDS file no. 41-1049). CdS has two structural phases, i.e. hexagonal wurtzite and rock-salt phase. Rock-salt phase of CdS is high pressure phase and is difficult to keep under ambient conditions [23].

No impurity peak was observed in XRD patterns. The crystallite size (D) is calculated by the Debye–Scherrer formula [24]:

$$D = \frac{0.9\,\lambda}{\beta\cos\theta} \tag{1}$$

where λ is wavelength of X-ray used, β is full width at half maximum, and θ is the Bragg angle. The crystallite size for $Cd_{1-x}Tb_xS$ nanoparticles for $x = 0$, 0.05, 0.10 and 0.15 are given in Table 1 and found to increased up to $x = 0.10$. Inset I shows a clear peak shift towards lower diffraction angle, which is a consequence of stresses in lattice due to larger atomic radii of Tb^{3+} ion (1.25 Å) compared to Cd^{2+} ion (0.97 Å) [25]. However, for $x = 0.15$, reverse trend has been observed i.e., peak shift towards higher diffraction angle (Inset II), which suggest that the excess Tb^{3+} remained unsubstituted and creates pining action to lattice expansion. To verify Tb^{3+} ion effect, lattice parameters (a, c) have been calculated (as shown in Table 1) by the following relation [24]:

$$\frac{1}{d_{hkl}^2} = \frac{4}{3}\left[\frac{h^2 + hk + k^2}{a^2}\right] + \frac{l^2}{c^2} \tag{2}$$

where d is inter-planar spacing and (hkl) are miller indices of plane. The lattice parameters a and c were calculated using (002) and (101) planes. An expansion in 'c' with doping

content is observed upto $x = 0.10$ without any measurable change in *'a'* values. Further on increasing doping to $x = 0.15$, no further change is observed.

3.2 Morphological studies

Figure 2a–d shows HR-TEM images and SAED pattern of $Cd_{1-x}Tb_xS$ nanoparticles for $x = 0$ and 0.15. Nanopowder shows spherical morphology with uniform particle size. The average particle diameter (~18 nm) was measured in both the powders, which indicate Tb^{3+} ion has no visible effect on the particle size and morphology. The thin layer around the particle is due to addition of CTAB during synthesis. The *d*-spacing value of lattice planes measured from HR-TEM image (Fig. 2c) is about 0.336 nm, which corresponds to (002) plane. The corresponding SAED pattern in Fig. 2d is not sharp indicating the nanocrystalline nature of nanopowder.

3.3 Optical analysis

3.3.1 UV–Visible spectra

The optical studies of $Cd_{1-x}Tb_xS$ were carried out by UV–Visible absorption spectra shown in Fig. 3. The E_g of nanoparticles was determined by following equation [26]:

$$(\alpha hv)^2 = A(hv - E_g)^n \quad (3)$$

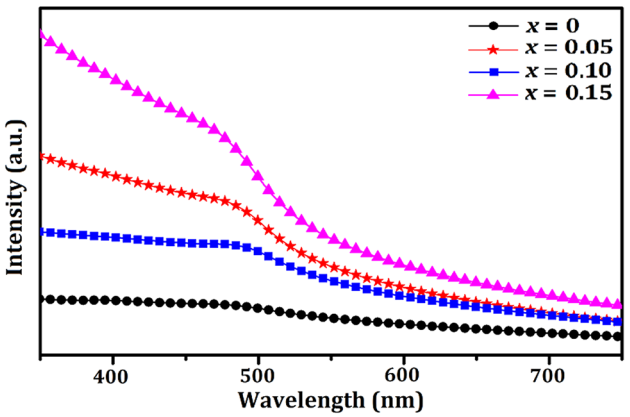

Fig. 3 UV–Visible absorption spectra of $Cd_{1-x}Tb_xS$ nanoparticles

where α is absorption coefficient, v is frequency, constant A is function of electronic transition probability, E_g is the optical band gap, h is Planck's constant and n depends on the type of transition. The CdS nanoparticles have direct transition i.e. $n = 1/2$. E_g was determined by Tauc's plot as shown in Fig. 4.

The variation of E_g with Tb-doping is shown in Table 1. The calculated E_g of undoped CdS nanoparticles is 2.49 eV, which is higher than bulk CdS (2.42 eV). The blue shift in energy band is the consequence of quantum confinement effect [27]. This will lead to change in the electronic band structure of the CdS nanoparticles, and consequently, higher

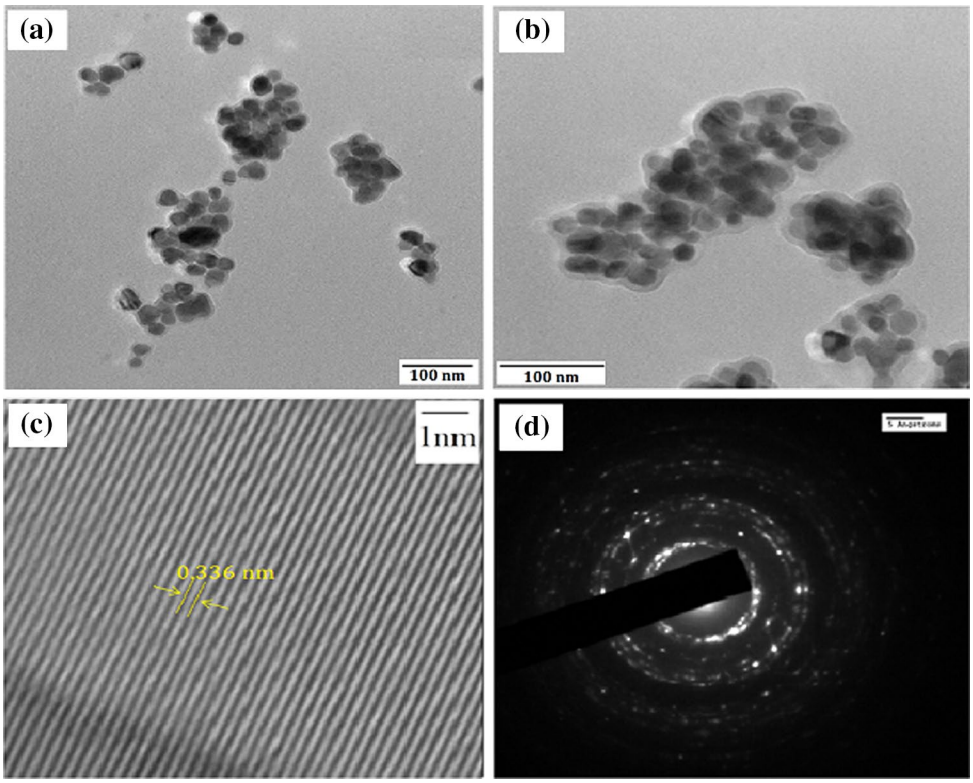

Fig. 2 TEM micrograph of $Cd_{1-x}Tb_xS$ nanoparticles **a** $x = 0$, **b** $x = 0.15$, **c** HR-TEM for $x = 0.15$, **d** SAED pattern for $x = 0.15$

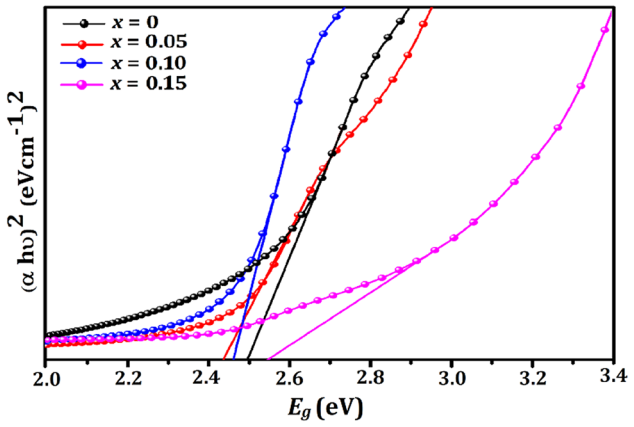

Fig. 4 The Tauc's plot of $Cd_{1-x}Tb_xS$ nanoparticles

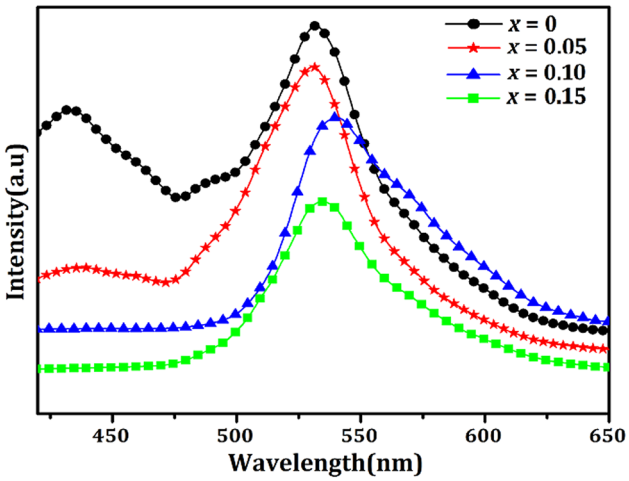

Fig. 5 *RT*- Photoluminescence spectra of $Cd_{1-x}Tb_xS$ nanoparticles

E_g is observed as compared to their bulk counterpart [28]. For $x = 0.05$ and 0.10 compositions, there is a decrease in E_g showing the red shift and the absorption edge shifts towards the higher wavelength indicates the increase in particle size, as obtained from XRD [17]. Also, the decrease in E_g can be attributed to the introduction of new energy levels in the host lattice with doping [29]. At $x = 0.15$, more defect centers may be created due to decrease in crystallite size (12.08 nm), which in turn increaseE_g to 2.54 eV.

The relation of optical band gap of nanoparticle as a function of particle radius was explained by Brus using effective mass approximations (EMA) formula [30].

$$\Delta E_g = E_g^{nano} - E_g^{bulk} = \frac{h^2}{8R^2}\left(\frac{1}{m_e^*} + \frac{1}{m_h^*}\right) - \frac{1.8e^2}{\epsilon R} \quad (4)$$

where E_g^{nano} and E_g^{bulk} are optical band gap energy of nanoparticles and bulk in Joules, respectively. R is radius of nanoparticle, $m_e^* = 0.19m_0$ and $m_h^* = 0.8m_0$ are effective mass of electrons and holes respectively, where m_0 is free electron mass, e is the electronic charge and ϵ is dielectric constant of CdS i.e. 5.7 [31].

The size of the nanoparticles calculated using EMA formula is tabulated in Table 1. Variation in particle size with Tb-doping is comparable with the crystallite size as calculated by Debye–Scherre formula.

3.3.2 Photoluminescence spectra

Figure 5 shows the *RT*-photoluminescence spectra of the synthesized nanoparticles obtained at excitation wavelength of 380 nm. Three peaks are observed at 430, 490 and 530 nm in undoped CdS. The peaks at 430 and 490 nm for $x = 0$ and 0.05 can be due to blue emissions. However, with increasing doping concentration, intensity of these peaks quenched and peaks are not observable for $x = 0.10$ and 0.15. The main excitonic emission band around 530 nm is due to green emission, which can be ascribed to surface donor–acceptor pair recombination and also to *d-d* intra ion transitions [28]. For $x = 0.10$ and 0.15, the green emission peak slightly shifted to higher wavelength ~ 540 nm. This can be attributed to increase in surface or trap defects on increasing doping concentration [32].

3.4 Magnetic analysis

RT magnetic hysteresis loops of $Cd_{1-x}Tb_xS$ nanoparticles for $x = 0$, 0.05, 0.10 and 0.15 are shown in Fig. 6. The undoped CdS nanoparticles show ferromagnetism at *RT*. Ferromagnetism in undoped CdS nanoparticles can be attributed to the presence of Cd vacancy that changes its electronic configuration [33]. The presence of magnetic moments on the surface of nanoparticles is also responsible for ferromagnetic behaviour. The exchange interaction between neighbouring

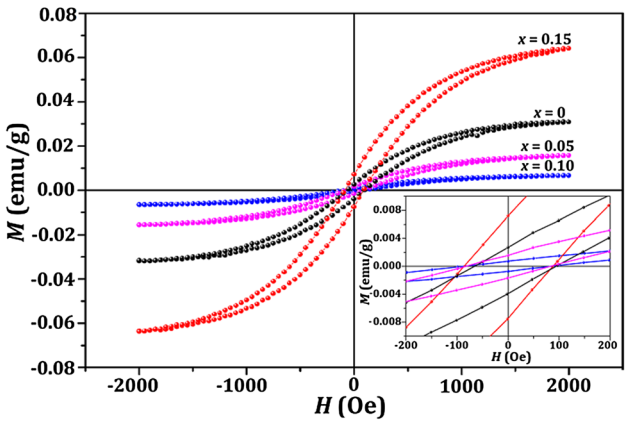

Fig. 6 *M-H* curves of $Cd_{1-x}Tb_xS$ nanoparticles and inset shows magnified view of *M-H* curve

nanoparticles results in parallel alignment of magnetic moments. The high surface to volume ratio of nanoparticles causes large number of magnetic moments in the same direction, which leads to higher magnetization [34]. The higher magnetization value for $x=0.15$ can be related to decrease in crystallite size as calculated from XRD. Also, this can be attributed to the formation of various defects or vacancies with increase in dopant concentration.

4 Conclusion

$Cd_{1-x}Tb_xS$ ($x=0.00$, 0.05, 0.10, 0.15) nanoparticles were synthesized by hydrothermal technique. X-ray studies confirmed the wurtzite phase without any impurity. HR-TEM micrographs revealed the particle size of ~18 nm with spherical morphology. E_g calculated from UV–Visible absorption spectra showed an initial decrease from 2.49 eV ($x=0$) to 2.45 eV ($x=0.10$). Further increasing Tb-doping to $x=0.15$, E_g increased to 2.54 eV. This reveals that E_g can be tuned by suitable Tb-doping. *RT*-Photoluminescence emission spectra showed peaks at 430, 490 and 530 nm for $x=0$ and 0.05. Peaks at 430 and 490 nm correspond to blue emission, which found to be quenched with further increase in Tb-doping. Peak observed around 530 nm is due to green emission and shifted to higher wavelength with Tb-doping. Magnetic analysis confirmed *RT* ferromagnetism in both undoped and Tb-doped CdS nanoparticles. Saturation magnetization found to depend on Tb concentration. These studies revealed that E_g and magnetization can be tuned by suitable Tb doping.

References

1. C. Liu, F. Yun, H. Morkoc, J. Mater. Sci. Mater. Electron. **16**, 555 (2005)
2. S.D. Bader, Rev. Mod. Phys. **78**, 1 (2006)
3. F. Baletto, R. Ferrando, Rev. Mod. Phys. **77**, 371 (2005)
4. D.P. Norton, S.J. Pearton, A.F. Hebard, N. Theodoropoulou, L.A. Boatner, R.G. Wilson, Appl. Phys. Lett. **82**, 239 (2003)
5. T. Dietl, Nat. Mater. **9**, 965 (2010)
6. K. Sato, L. Bergqvist, J. Kudrnovsky´, P.H. Dederichs, O. Eriksson, I. Turek, B. Sanyal, G. Bouzerar, H.K. Yoshida, V.A. Dinh, T. Fukushima, H. Kizaki, R. Zeller, Rev. Mod. Phys. **82**, 1633 (2010)
7. R. Singh, J. Magn. Magn. Mater. **346**, 58 (2013)
8. E. Biegger, L. Staheli, M. Fonin, U. Rudiger, Y.S. Dedkov, J. Appl. Phys. **101**, 103912 (2007)
9. B. Pal, P.K. Giri, J. Nanosci. Nanotechnol. **11**, 1 (2011)
10. Y. Hanifehpour, N. Hamnabard, B. Mirtamizdoust, J Inorg Organomet Polym. **26**, 623 (2016)
11. S. Shirakata, K. Ohkubo, Y. Ishii, T. Nakada, Sol. Energy Mat. Sol. Cells **93**, 988 (2009)
12. H. Murai, T. Abe, J. Matsuda, H. Sato, S. Chiba, Y. Kashiwaba, Appl. Surf. Sci. **244**, 351 (2005)
13. Y. Huang, F. Sun, T. Wu, Q. Wu, Z. Huang, H. Su, Z. Zhang, J. Solid State Chem. **184**, 644 (2011)
14. Y. Wang, S. Ramanathan, Q. Fan, F. Yun, H. Morkoc, S. Bandyopadhyay, J. Nanosci. Nanotechnol. **6**, 2077 (2006)
15. X.F. Duan, Y. Huang, R. Agarwal, C.M. Lieber, Nature **421**, 241 (2003)
16. L. Saravanan, R. Jayavel, A. Pandurangan, L.J. Hsin, M.H. Yuan, Mater. Res. Bull. **52**, 128 (2014)
17. G. Pandeya, S. Dixit, A.K. Shrivastava, Mater. Sci. Eng. B **200**, 59 (2015)
18. L. Bokatial, S. Rai, J. Lumin. **130**, 1857 (2010)
19. S.T. Selvan, T. Hayakawa, M. Nogami, J. Non-Cryst. Solids **291**, 137 (2001)
20. L. Saravanan, A. Pandurangan, R. Jayavel, Mater. Lett. **66**, 343 (2012)
21. P.V. Jyothy, K.A. Amrutha, J. Gijo, N.V. Unnikrishnan, J Fluoresc. **19**, 165 (2009)
22. S. Rai, L. Bokatial, Bull. Mater. Sci. **34**, 227 (2011)
23. P. Wang, B. Xiao, R. Zhao, Y. Ma, M. Zhang, ACS Appl. Mater. Interfaces **8**, 6656 (2016)
24. B.D. Cullity, S.R. Stock, *Elementary of X-ray Diffraction*, 3rd edn. (Prentice-Hall, Englewood Cliffs, 2001)
25. G.S. Lotey, J. Singh, N.K. Verma, J. Mater. Sci. Mater. Electron. **24**, 3611 (2013)
26. G.A. Kumara, V. Thomas, G. Jose, N.V. Unnikrishnan, V.P.N. Nampoori, Mater. Chem. Phys. **73**, 206 (2002)
27. M. Bangal, S. Ashtaputre, S. Marathe, A. Ethiraj, N. Hebalkar, S.W. Gosavi, J. Urban, S.K. Kulkarni, Semiconductor nanoparticle. Hyperfine Interact. **160**, 81 (2005)
28. C.B. Murray, D.J. Norris, M.G. Bawendi, J. Am. Chem. Soc. **115**, 8706 (1993)
29. R. Elilarassi, G. Chandrasekaran, J. Mater. Sci. Mater. Electron. **24**, 96 (2013)
30. L.E. Brus, J. Phys. Chem. **90**, 2555 (1986)
31. S. Muruganandam, G. Anbalagan, G. Murugadoss, Appl. Nanosci. **5**, 245 (2015)
32. V. Singh, P. Chauhan, J. Phys, Chem. Solids **70**, 1074 (2009)
33. J.P. Tang, L. Wang, H.J. Luoc, W.Z. Xiao, Phys. Lett. A **377**, 572 (2013)
34. P.K. Sharma, R.K. Dutta, A.C. Pandey, S. Layek, H.C. Verma, J. Magn. Magn. Mater. **321**, 2587 (2009)

Turnitin Originality Report

Processed on: 27-Aug-2021 11:07 +0530
ID: 1636670700
Word Count: 16453
Submitted: 1

Shivani Thesis By Shivani Shivani

Similarity Index	Similarity by Source	
14%	Internet Sources:	6%
	Publications:	9%
	Student Papers:	6%

2% match (student papers from 16-Jul-2019)
Submitted to Thapar University, Patiala on 2019-07-16

1% match (student papers from 05-Jun-2011)
Submitted to Higher Education Commission Pakistan on 2011-06-05

1% match (Internet from 15-Oct-2020)
https://worldwidescience.org/topicpages/z/zns+nanocrystalline+thin.html

< 1% match (student papers from 23-Sep-2020)
Class: Sanjay Kashyap
Assignment: Santhosh Thesis
Paper ID: 1394335628

< 1% match (student papers from 12-Jul-2019)
Submitted to Thapar University, Patiala on 2019-07-12

< 1% match (student papers from 13-Jul-2018)
Submitted to Thapar University, Patiala on 2018-07-13

< 1% match (student papers from 30-May-2016)
Submitted to Thapar University, Patiala on 2016-05-30

< 1% match (student papers from 27-Aug-2015)
Submitted to Thapar University, Patiala on 2015-08-27

< 1% match (student papers from 20-Jul-2016)
Submitted to Thapar University, Patiala on 2016-07-20

< 1% match (student papers from 07-Jul-2014)
Submitted to Higher Education Commission Pakistan on 2014-07-07

< 1% match (student papers from 15-Jul-2016)
Submitted to Higher Education Commission Pakistan on 2016-07-15

< 1% match (Internet from 29-Feb-2020)
https://worldwidescience.org/topicpages/z/zns+thin+films.html

< 1% match (Internet from 27-Apr-2020)
https://worldwidescience.org/topicpages/y/yba2cusub+3-xznsub+xosub.html

< 1% match (Internet from 05-Aug-2020)
https://worldwidescience.org/topicpages/z/zns+amorphous+thin.html

< 1% match (Internet from 18-Oct-2020)
https://worldwidescience.org/topicpages/c/core-shell+iron-iron+oxide.html